

AD-A172 482

CENTRIFUGAL AND ANALYTICAL MODELING OF A BURIED  
FLEXIBLE CONDUIT (U) COLORADO UNIV AT BOULDER DEPT OF  
CIVIL ENVIRONMENTAL AND ARCH J C NI 31 OCT 85

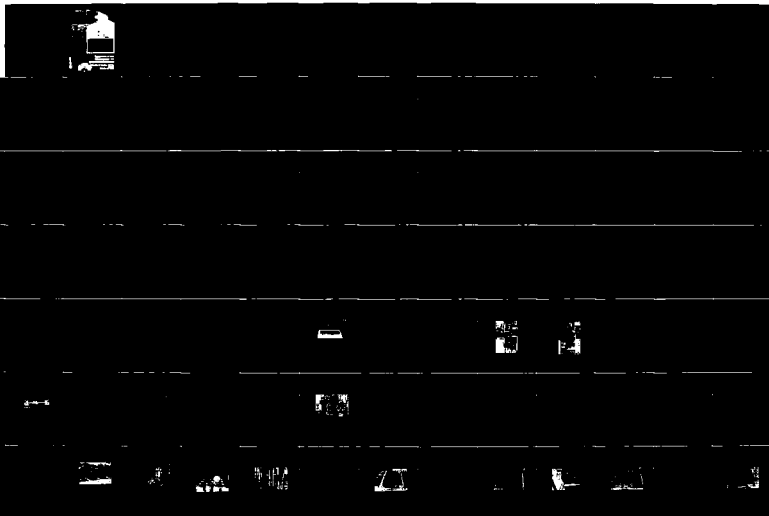
1/3

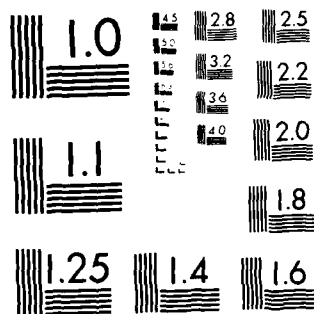
UNCLASSIFIED

AFOSR-IR-86-0850 AFOSR-84-0300

F/G 13/13

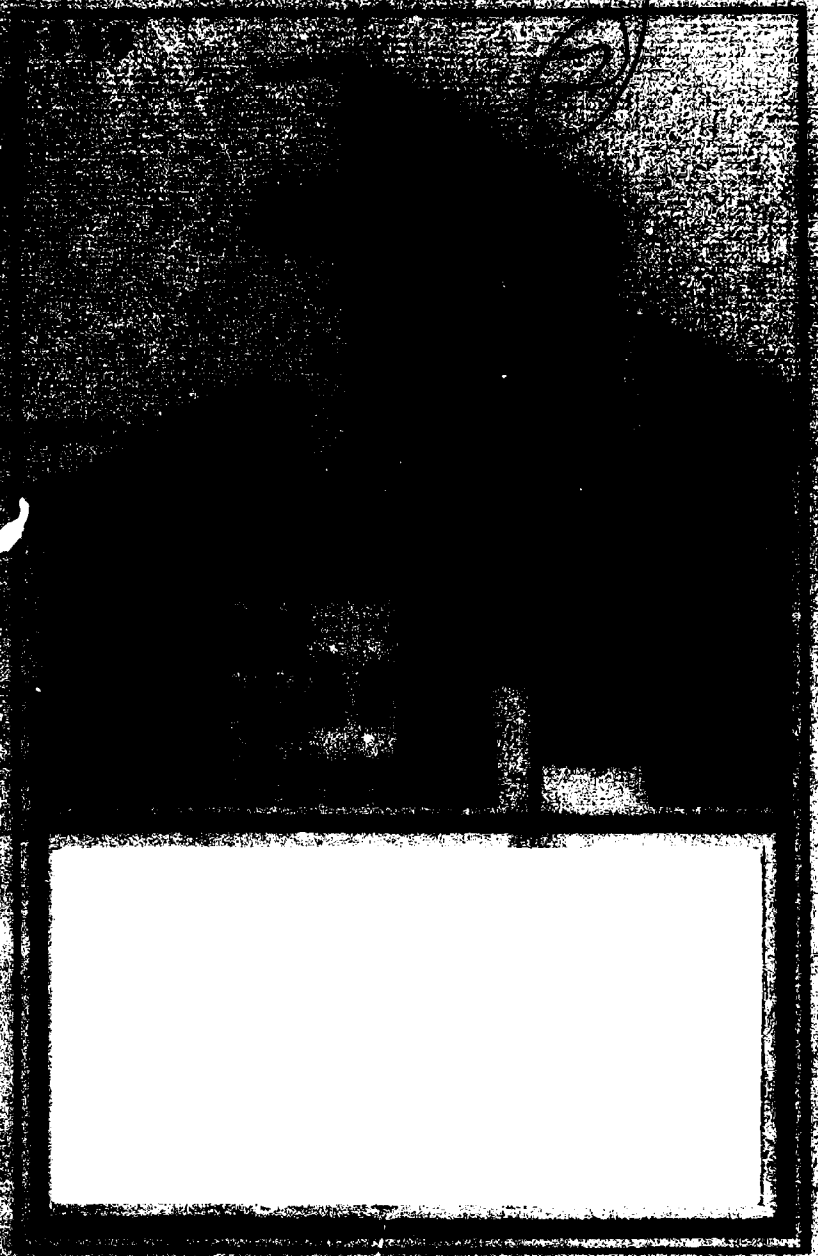
NL





XEROCOPY RESOLUTION TEST CHART  
NATIONAL BUREAU OF STANDARDS 1963-A

AD-A172 482



... of ...  
... and ...  
...  
...

470602 PM

86 10 01 13Q

UNCLASSIFIED  
SECURITY CLASSIFICATION OF THIS PAGE

h...  
18 Apr 81

# REPORT DOCUMENTATION PAGE

1a. REPORT SECURITY CLASSIFICATION UNCLASSIFIED		1b. RESTRICTIVE MARKINGS UNRESTRICTED	
2a. SECURITY CLASSIFICATION AUTHORITY		3. DISTRIBUTION AVAILABILITY OF REPORT APPROVED FOR PUBLIC RELEASE DISTRIBUTION STATEMENT	
2b. DECLASSIFICATION DOWNGRADING SCHEDULE			
4. PERFORMING ORGANIZATION REPORT NUMBER		5. MONITORING ORGANIZATION REPORT NUMBER <b>AFOSR-TR-86-0850</b>	
6a. NAME OF PERFORMING ORGANIZATION UNIVERSITY OF COLORADO	6b. OFFICE SYMBOL (If applicable) CEAE DEPT.	7a. NAME OF MONITORING ORGANIZATION <b>AFOSR</b>	
6c. ADDRESS (City, State and ZIP Code) CIVIL, ENVIRONMENTAL & ARCHITECTURAL ENGRG. CAMPS BOX 428, BOULDER, CO 80506		7b. ADDRESS (City, State and ZIP Code) <b>Same as 6c</b>	
8a. NAME OF FUNDING SPONSORING ORGANIZATION (AIR FORCE) OFFICE OF SCIENTIFIC RESEARCH	8b. OFFICE SYMBOL (If applicable) AFOSR NA	9. PROCUREMENT INSTRUMENT IDENTIFICATION NUMBER <b>AFOSR-TR-86-0850 84-0300</b>	
8c. ADDRESS (City, State and ZIP Code) CAMPS BOX 428, BOULDER, CO 80506		10. SOURCE OF FUNDING NOS. PROGRAM ELEMENT NO. PROJECT NO. TASK NO. WORK UNIT NO. <b>61525</b>	
11. TITLE (Include Project No. and Subproject No.) CENTRIFUGE AND ANALYTICAL MODELING OF A BARBED FLEXIBLE CULVERT		11. UNCLASSIFIED <b>2302 C2</b>	
12. PERSONAL AUTHOR(S) <b>JIM CHINKUAN NI</b>			
13a. TYPE OF REPORT Final	13b. TIME COVERED FROM JUL 81 TO DEC 81	14. DATE OF REPORT (Yr. Mo. Day) 10/1/81	15. PAGE COUNT 21
16. SUPPLEMENTARY NOTATION			
17. DECAT CODES FIELD GROUP SUB GR		18. SUBJECT TERMS (Continue on reverse if necessary and identify by block number) SOIL STRUCTURE INTERACTION, NUMERICAL MODELING, CENTRIFUGE MODEL TESTING, CONSTITUTIVE PROPERTIES OF SOILS	
19. ABSTRACT (Continue on reverse if necessary and identify by block number) This report summarizes one phase of the research on the modeling of buried structures by centrifuge testing and by numerical methods. Testing in the centrifuge makes it possible to simulate the gravity-induced overburden pressure effects that dictate the soil stiffness which in turn determine the soil-structure phenomena. Scaled model testing in the centrifuge is used in the project to validate analytical methods commonly used to analyze soil-structure interaction problems. The model is a 1/10 scale, 1/4 in. dia. pipe at 50 g under a static surface pressure loading. Results of radial deflections and strains measured around the pipe. These experiments were analyzed by a finite element program in which different constitutive models were incorporated, including a non-linear elastic model and an elasto-plastic model. On the basis of comparison with centrifuge test data, the suitability and accuracy of the different analyses were assessed.			
20. DISTRIBUTION AVAILABILITY OF ABSTRACT UNCLASSIFIED/UNLIMITED <input checked="" type="checkbox"/> SAME AS RPT <input type="checkbox"/> DTIC USERS <input type="checkbox"/>		21. ABSTRACT SECURITY CLASSIFICATION UNCLASSIFIED	
22a. NAME OF RESPONSIBLE INDIVIDUAL DR SPENCER WU		22b. TELEPHONE NUMBER (Include Area Code) 202/7674935	22c. OFFICE SYMBOL AFOSR/NA

2

**CENTRIFUGAL AND ANALYTICAL**

**MODELING OF A BURIED**

**FLEXIBLE CULVERT**

by

**Jim Chinkuan Ni**

Technical Report

AFOSR Grant No. 84-0390

This document has been approved  
for public release and sale; its  
distribution is unlimited.

DTIC  
ELECT  
S OCT 2 1986  
A

CENTRIFUGAL AND ANALYTICAL MODELING

OF

A BURIED FLEXIBLE CULVERT

by

Jim Chinkuan Ni

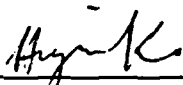
B.S., National Taiwan Institute of Technology, 1979


M.S., University of New Mexico, 1981

A thesis submitted to the  
Faculty of the Graduate School of the  
University of Colorado in partial fulfillment  
of the requirements for the degree of  
Doctor of Philosophy  
Department of  
Civil, Environmental and Architectural Engineering  
1985

not for  
distribution

This thesis for the Doctor of Philosophy degree by  
Jim Chinkuan Ni  
has been approved for the  
Department of  
Civil, Environmental and Architectural Engineering  
by

  
\_\_\_\_\_  
Hon-Yim Ko

  
\_\_\_\_\_  
Stein Sture

Date Oct 31, 1985



Accession For	
NTS	CHAI
BT	100
Version Control	
Justification	
By	
Initiation/	
Availability Codes	
Atoll and/or	
List	Special
A1	

Ni, Jim Chinkuan (Ph.D. Civil Engineering)

Centrifugal and Analytical Modeling of a Buried Flexible Culvert

Thesis directed by Professor Hon-Yim Ko

A flexible culvert depends primarily on the surrounding soil for support, and the structural stresses and deflections are controlled by the interaction between the structure and the back-fill. The finite element method is capable of simulating many of the factors which control the interaction between culvert structures and the surrounding soil. It can be used as a research tool to provide a basis for more effective and efficient simple design methods.

For the finite element method to produce useful results in analysing the buried culvert problem, a correct analytical model is required which, in turn, means a correct model of material properties is essential. The objective of this study is to investigate the suitability of the hyperbolic and Lade's constitutive relations in this buried, flexible culvert problem by comparing analytical results with centrifuge model test results.

Two series of centrifugal model tests of buried culverts under symmetrical and unsymmetrical ground surface loadings were conducted. The deflections of the culvert and the strains in the culvert induced during loading were measured.



The soil used in the centrifugal model was tested in conventional experiments to obtain the data base for the calibration of the hyperbolic and Lade's constitutive relations. An analytical model utilizing the finite element method with 4-node isoparametric element was developed to simulate the construction process and the gravitational field of the centrifugal model. The two calibrated constitutive relations for soil were implemented into the analytical model. A convergence study showed that the analytical model was correctly constructed.

The results obtained from the analytical model were compared with those from the centrifugal tests. It was found that both the hyperbolic and Lade's constitutive relations for soil showed qualitatively good results but not quantitatively, because the soil used in the centrifugal model exhibited strong stress induced anisotropy due to the layer compaction method used in preparing the centrifuge model. Only an anisotropic soil model with the ability to account for the rotation of the principal stresses will offer an accurate solution for the problem of a flexible culvert buried in a layered backfill.

## ACKNOWLEDGEMENTS

I wish to express my sincere gratitude to Professor Hon-Yim Ko, not only for his support and guidance throughout this study but also for everything he has done to make this thesis possible.

Special thanks go to Professors Stein Sture and Kaspar J. Willam for the constructive discussion which helped in finding the right solution to the problem, and to Drs. Dobroslav Znidarcic and Karl E. Gustafson for serving on the examining committee.

Appreciation is extended to Dave Jones, Frank Jancewicz and Tom Bank for their construction of the apparatus, and to Jeffry Budiman and other colleagues for their friendship. A lot of thanks go to JoAnne Hunt and Deonna Ainslie of Applied Mechanics, Inc. for their patient and wonderful typing of this thesis. Financial support provided by the Air Force Office of Scientific Research under Grant No. AFOSR84-0300 is gratefully acknowledged.

Last, but not least, my endless thanks go to my dear wife, Hwei-Ru, and my son, Jake, for all their sacrifices and deepest love during this time.

## TABLE OF CONTENTS

	PAGE
Acknowledgements . . . . .	v
List of Tables . . . . .	ix
List of Figures . . . . .	x
CHAPTER	
I. INTRODUCTION . . . . .	1
1.1 Introduction . . . . .	1
1.2 Statement of Problem . . . . .	3
1.2.1 Culvert . . . . .	3
1.2.2 Culvert-Soil System . . . . .	5
1.3 Literature Review . . . . .	6
1.3.1 Classical Methods . . . . .	6
1.3.2 Exact Solution Methods . . . . .	8
1.3.3 Finite Element Methods . . . . .	9
1.4 Objectives . . . . .	18
II. DESCRIPTION OF SOIL . . . . .	23
2.1 Index Properties . . . . .	23
2.2 Engineering Properties . . . . .	27
III. DESCRIPTION OF EQUIPMENT . . . . .	33
3.1 Description of the Centrifuge . . . . .	33
3.2 Culvert and Strain Gauges . . . . .	33
3.2.1 Culvert and Its Properties . . . . .	33
3.2.2 Selection of Gauge . . . . .	36

## CHAPTER

3.2.3	Gauge Installation . . . . .	36
3.2.4	Wiring Technique . . . . .	41
3.2.5	Gauge Circuit and Amplification . . . .	44
3.2.6	Zero Stability . . . . .	48
3.2.7	Zero Shift . . . . .	50
3.3	LVDT System . . . . .	51
3.4	Data Acquisition System and Polarity Check .	56
3.5	Line Load Test . . . . .	59
3.6	Soil Container . . . . .	63
3.7	Loading Apparatus . . . . .	63
3.8	Model Preparation . . . . .	66
3.9	Test Procedure . . . . .	77
3.10	Centrifuge Test Results . . . . .	82
IV.	CONSTITUTIVE RELATIONS . . . . .	90
4.1	General . . . . .	90
4.2	Isotropic Linear Elastic Stress-Strain Relation . . . . .	91
4.2.1	General Description . . . . .	91
4.2.2	Parameter Evaluation of Soil . . . . .	93
4.2.3	Prediction of Triaxial Test . . . . .	94
4.2.4	Parameter Evaluation of Aluminum Culvert . . . . .	97
4.3	Hyperbolic Stress-Strain Relation . . . . .	97
4.3.1	General Description . . . . .	97
4.3.2	Parameter Evaluation . . . . .	102
4.3.3	Prediction of Triaxial Test . . . . .	105

## CHAPTER

4.4	Lade's Elasto-Plastic Relation . . . . .	110
4.4.1	General Description . . . . .	110
4.4.2	Parameter Evaluation . . . . .	120
4.4.3	Prediction of Triaxial Test . . . . .	134
V.	NUMERICAL MODELING . . . . .	140
5.1	General . . . . .	140
5.2	Numerical Modeling Procedure . . . . .	140
5.3	Numerical Formulations for Constitutive Laws. . . . .	148
5.3.1	Hyperbolic Constitutive Relation . . . . .	148
5.3.2	Lade's Constitutive Relation . . . . .	150
VI.	COMPARISONS BETWEEN CENTRIFUGAL AND ANALYTICAL RESULTS . . . . .	158
6.1	Verification of the Analytical Model . . . . .	158
6.2	Convergence Studies . . . . .	165
6.3	Comparisons Between Centrifugal and Analytical Results . . . . .	176
6.3.1	Symmetrical Loading . . . . .	177
6.3.1	Unsymmetrical Loading . . . . .	189
6.4	Discussion of the Results . . . . .	197
VII.	SUMMARY, CONCLUSIONS AND RECOMMENDATIONS . . . . .	207
7.1	Summary . . . . .	207
7.2	Conclusions . . . . .	208
7.3	Recommendations for Future Work . . . . .	210
	BIBLIOGRAPHY . . . . .	212
	APPENDIX A - Centrifuge Test Results . . . . .	219
	APPENDIX B - Loading and Unloading Criteria in Hyperbolic Soil Model . . . . .	225

## LIST OF TABLES

TABLE		PAGE
1.1	Comparison Between Centrifugal and Analytical Modeling of Buried Culvert Problem . . . . .	21
2.1	Basic Characteristics of Soil . . . . .	25
3.1	University of Colorado Centrifuge Specifications .	34
3.2	Engineering Properties of Tube . . . . .	37
3.3	Amplification of Amplifiers . . . . .	49
3.4	Sign Convention of Strain Gauge and LVDT . . . . .	58
3.5	Average Compaction Effort for Centrifugal Soil Model . . . . .	71
4.1	Parameters in Hyperbolic Constitutive Relations . .	107
4.2	Parameters in Lade's Elasto-Plastic Relations . . .	136
6.1	Comparison Between Close Form and Numerical Solutions of an Idealized Problem I . . . . .	161
6.2	Comparison Between Close Form and Numerical Solutions of an Idealized Problem II . . . . .	164

## LIST OF FIGURES

FIGURE	PAGE
1.1 Pipe Definition . . . . .	4
2.1 Grain Size Distribution . . . . .	24
2.2 Modified Proctor Compaction Test Results . . . . .	26
2.3 Deviator Stress vs Axial Strain from Conventional Triaxial Compression Tests . . . . .	28
2.4 Volumetric Strain vs Axial Strain from Conventional Triaxial Compression Tests . . . . .	29
2.5 Mohr Circle Diagram . . . . .	31
2.6 Isotropic Pressure vs Volumetric Strain from Isotropic Compression Test . . . . .	32
3.1 Schematic of the Centrifuge . . . . .	35
3.2 Locations of 22 Strain Gauges . . . . .	38
3.3 Gauge Locators . . . . .	40
3.4 Wired Strain Gauge System . . . . .	42
3.5 The Tube with Strain Gauges and Wire Leads . . . . .	43
3.6 Wheatstone Bridge . . . . .	45
3.7 Amplifier, Dummy Gauge and LVDT Signal Conditioning Module Boxes . . . . .	46
3.8 Jones' Strips on the Arm in the Centrifuge . . . . .	47
3.9 Stiff Rod with 12 LVDTs . . . . .	52
3.10 Locations of 12 LVDTs . . . . .	53
3.11 Schematic of Buried Culvert . . . . .	54

## FIGURE

3.12	Data Acquisition and Computer System . . . . .	57
3.13	Schematic of Line Load Test . . . . .	60
3.14	Moment Diagram in Line Load Test . . . . .	61
3.15	Analytical Solution of Thin Ring . . . . .	62
3.16	Schematic of Two Soil Boxes . . . . .	64
3.17	Loading Apparatus . . . . .	65
3.18	Oven Dried Soil is Cooling Off . . . . .	67
3.19	Mixing Equipment . . . . .	68
3.20	Waxed Cans . . . . .	69
3.21	Soil Compaction on the Press Machine . . . . .	70
3.22	A Flat Cutter to Trim Extra Soil Away . . . . .	72
3.23	Trench Cutter for Rough Shape . . . . .	74
3.24	Trench Cutter for Precise Shape . . . . .	75
3.25	The Completed Trench . . . . .	76
3.26	The Completed Assembly . . . . .	78
3.27	Soil Crusher . . . . .	79
3.28	Deflected Culvert Under Symmetrical Loading . . . . .	84
3.29	Deflection at Crown Under Symmetrical Loading . . . . .	85
3.30	Deflection at Springline Under Symmetrical Loading . . . . .	86
3.31	Hoop Stresses Under Symmetrical Loading . . . . .	87
3.32	Bending Moments Under Symmetrical Loading . . . . .	88
3.33	Deflected Culvert Under Unsymmetrical Loading . . . . .	89
4.1a	Comparisons Between Predictions of Linear Elastic Relation and Experimental Results of Conventional Triaxial Compression Tests. $\sigma_1 - \sigma_3$ vs $\epsilon_1$ Plot . . . . .	95



## FIGURE

4.1b	Comparisons Between Predictions of Linear Elastic Relation and Experimental Results of Conventional Triaxial Compression Tests. $\epsilon_v$ vs $\epsilon_1$ Plot . . . . .	96
4.2	Hyperbolic Relation Calibration. $E_1/P_a$ vs $\sigma_3/P_a$ Plot . . . . .	103
4.3	Hyperbolic Relation Calibration. $B/P_a$ vs $\sigma_3/P_a$ Plot . . . . .	106
4.4	Comparisons Between Predictions of Hyperbolic Relation and Experimental Results of Conventional Triaxial Compression Tests. $\sigma_1$ - $\sigma_3$ vs $\epsilon_1$ Plot . .	108
4.5	Comparison Between Predictions of Hyperbolic Relation and Experimental Results of Conventional Triaxial Compression Tests. $\epsilon_v$ vs $\epsilon_1$ Plot . . .	109
4.6	Schematic Illustrations of (a) Elastic, Plastic Collapse, and Plastic Expansive Strain Components in Drained Triaxial Compression Test, and (b) Conical and Spherical Cap Yield Surfaces in Triaxial Plane (Lade, 1977) . . . . .	112
4.7	Ultimate Strength and Yield Surfaces (Lade, 1977) .	113
4.8	Translation of Principal Stress Space Along Hydrostatic Axis to Include Effect of Tensile Strength in Failure Criterion . . . . .	119
4.9	Lade's Relation Calibration. $I_1^3/I_3-27$ vs $P_a/I_1$ Plot . . . . .	121
4.10	Lade's Relation Calibration. $E_{ur}/P_a$ vs $\sigma_3/P_a$ Plot . . . . .	123
4.11	Lade's Relation Calibration. $\epsilon_v$ vs $\sigma_3/P_a$ Plot . . . . .	124
4.12	Lade's Relation Calibration. $W_c/P_a$ vs $f_c/P_a^2$ Plot . . . . .	127
4.13	Lade's Relation Calibration. $\eta_2$ vs $f_p$ Plot . . . . .	129
4.14	Lade's Relation Calibration. $S$ vs $\sqrt{\sigma_3/P_a}$ Plot . . . . .	131

## FIGURE

4.15	Lade's Relation Calibration. Intercept vs $\sqrt{\sigma_3/P_a}$ Plot . . . . .	132
4.16	Lade's Relation Calibration. $W_p$ peak/ $P_a$ vs $\sigma_3/P_a$ Plot . . . . .	133
4.17	Lade's Relation Calibration. $q$ vs $\sigma_3/P_a$ Plot . . . . .	135
4.18	Comparison Between Predictions of Lade's Relation and Experimental Results of Conventional Triaxial Compression Tests. $\sigma_1$ - $\sigma_3$ vs $\epsilon_1$ Plot . .	137
4.19	Comparison Between Predictions of Lade's Relation and Experimental Results of Conventional Triaxial Compression Tests. $\epsilon_v$ vs $\epsilon_1$ Plot . . .	138
4.20	Comparison Between Predictions of Lade's Relation and Experimental Results of Isotropic Compression Tests. $\sigma_3$ vs $\epsilon_v$ Plot . . . . .	139
5.1	Analytical Modeling of Soil-Culvert System in the Centrifuge . . . . .	142
5.2	Parasitic Shear in Linear Element . . . . .	147
6.1	Idealized Problem I . . . . .	159
6.2	Idealized Problem II . . . . .	163
6.3	Mesh 1 with 43 Elements . . . . .	166
6.4	Mesh 2 with 76 Elements . . . . .	167
6.5	Mesh 3 with 122 Elements . . . . .	168
6.6	Convergence Study on Refined Meshes. Deflection at Crown. Hyperbolic Soil Model . . .	169
6.7	Convergence Study on Refined Meshes. Deflection at Springline. Hyperbolic Soil Model.	170
6.8	Convergence Study on Refined Meshes. Deflection at Crown. Lade's Soil Model . . . . .	171
6.9	Convergence Study on Refined Meshes. Deflection at Springline. Lade's Soil Model . .	172

## FIGURE

6.10	Convergence Study on Load Increment . . . . .	173
6.11	Stiffer Elements in Mesh 3 . . . . .	175
6.12	Comparison Between Under- and Full-Integration . .	178
6.13	Comparison of Deflections. Symmetrical Load 10 psi . . . . .	179
6.14	Comparison of Deflections. Symmetrical Load 20 psi . . . . .	180
6.15	Comparison of Deflections. Symmetrical Load 30 psi . . . . .	181
6.16	Comparison of Deflections. Symmetrical Load 40 psi . . . . .	182
6.17	Hoop Stresses Under Selfweight. Hyperbolic Soil Model . . . . .	184
6.18	Hoop Stresses Under Selfweight. Lade's Soil Model . . . . .	185
6.19	Hoop Stresses Under Symmetrical Load. Hyperbolic Soil Model . . . . .	186
6.20	Hoop Stresses Under Symmetrical Load. Lade's Soil Model . . . . .	187
6.21	Gauged Tube in the Soil Trench . . . . .	188
6.22	Mesh 4 for Unsymmetrical Load . . . . .	190
6.23	Comparison of Deflections. Unsymmetrical Load 10 psi . . . . .	191
6.24	Comparison of Deflections. Unsymmetrical Load 20 psi . . . . .	192
6.25	Comparison of Deflections. Unsymmetrical Load 30 psi . . . . .	193
6.26	Comparison of Deflections. Unsymmetrical Load 40 psi . . . . .	194
6.27	Hoop Stresses Under Unsymmetrical Load. Hyperbolic Soil Model . . . . .	195

## FIGURE

6.28	Hoop Stresses Under Unsymmetrical Load. Lade's Soil Model . . . . .	196
6.29	Buckling Failure of the Flexible Culvert . . . . .	198
6.30	Stress Paths. Hyperbolic Soil Model . . . . .	199
6.31	Stress Paths. Lade's Soil Model . . . . .	200
6.32	Comparison of Deflection at Invert . . . . .	201
6.33	Comparison of Deflection at Crown. Improved Hyperbolic Soil Model . . . . .	204
6.34	Stiffer Elements in Mesh 4 . . . . .	206

## CHAPTER I

### INTRODUCTION

#### 1.1 Introduction

The complex problem of the reaction of a buried culvert to loads applied at the ground surface is studied using physical modeling in a geotechnical centrifuge. The concept of using a high gravity field to simulate body forces in reduced scale models was first suggested by James Watt during the steam engine age. In the early 1930's Bucky used the method to study models of underground openings in mining operations. In the last decade centrifugal modeling has been applied to many complicated engineering problems like excavation, reinforced embankment, soil slope stability, offshore gravity structure, offshore suction anchors, sedimentation, consolidation, pile driving, and buried culvert.

What makes centrifugal modeling so valuable to the understanding and solution of geotechnical problems is that data can be generated on the soil structure's behavior under stress conditions close to those experienced by the prototype. Soil is the most difficult engineering material to deal with due to its nonlinear, time-dependent and inelastic behavior. The increased

body forces in the centrifuge can correctly capture the initial stress state of earth structures for which self-weight is the main source of load.

There are mainly two schemes of utilization in centrifugal modeling. First, a model test structure is geometrically similar to the prototype and is constructed of the prototype material, so that the test results can be interpreted through scaling relations to represent the prototype response. In order to get the correct response, the geology of the prototype site, the construction details of the structure, and the stress history of soil material have to be faithfully duplicated in the centrifuge model. This will give the designer an opportunity for observing unexpected phenomena and failure modes of the structure to benefit the design purpose. Second, the data collected by centrifuge testing under controlled laboratory conditions are used as the basis for calibrating numerical models in which a major input component is the constitutive properties of the soil. In this scheme of centrifuge utilization there is no specific prototype to be simulated and as a result the construction of the test model can be considerably simplified. This philosophy is adopted for the research described in this dissertation.

## 1.2 Statement of Problem

### 1.2.1 Culvert

A culvert can be classified as being either rigid or flexible and the design methods used for each type are accordingly different. The meaning of the words "rigid" and "flexible" is rather relative than absolute, depending on the relative stiffness between the culvert and the surrounding soil. In general there are two types of definition based on the material and the failure mode of the culvert.

The term "rigid" is used for culverts made of concrete, reinforced concrete and cast iron, and the term "flexible" is applied to culverts made of plastic, corrugated metal plate, and steel plate. However, as far as the failure mode is concerned, a rigid culvert will normally fail by bending of the culvert wall, and a flexible culvert by buckling (Allgood et al., 1968, Luscher 1966, Whitman et al., 1962). Since the failure mode of the culvert is controlled by the geometry and the properties of soil and culvert, the latter definition is more rational.

Figure 1.1 illustrates a circular culvert cross-section with commonly defined areas identified. The crown and the invert are the top and the bottom of the pipe, respectively. The springline is an imaginary line connecting left and right extremities. The shoulder is located between the crown and springline, and the haunch resides between the invert and springline.

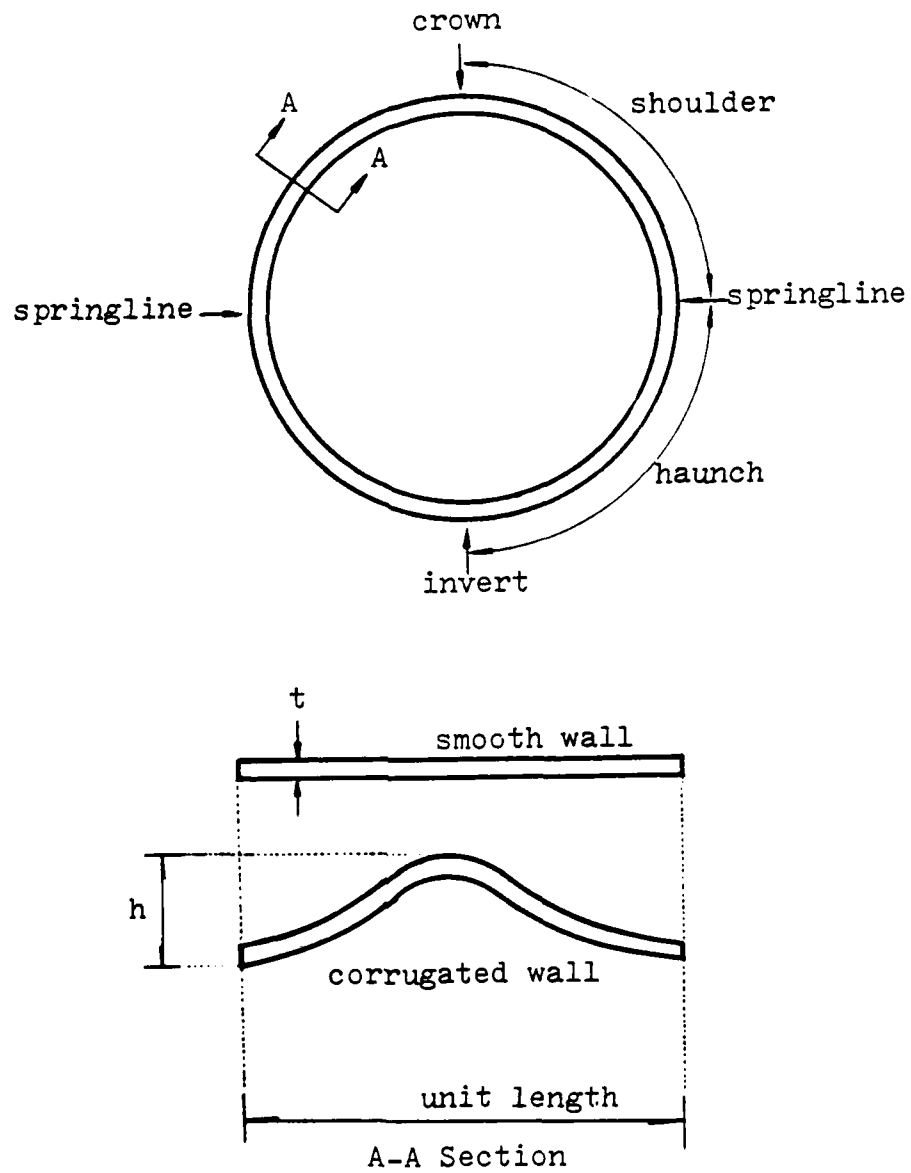


FIGURE 1.1 Pipe Definition



In the plane strain case the hoop stiffness can be expressed as  $EA/R(1-\nu^2)$ , and the bending stiffness can be represented by  $EI/R^2(1-\nu^2)$ , where  $I$  is the moment of inertia of wall per unit length,  $A$  is the thrust area of wall,  $E$  is Young's modulus,  $R$  is the radius of the culvert, and  $\nu$  is Poisson's ratio.

In general the bending stiffness is substantially less than hoop stiffness. Consequently, the culvert displacement is primarily contributed by the bending mode as opposed to the hoop compression. This illustrates the importance of correct evaluation of stresses which are acting in the culvert.

#### 1.2.2 Culvert-Soil System

There are three important aspects of the interaction between a flexible culvert and the surrounding soil, i.e., deformation restraint, stress redistribution, and arching. Because of this interaction the load-carrying capacity of the culvert-soil system exceeds far beyond the individual capacity of each component.

Deformation restraint provided by the surrounding soil increases the resistance of the culvert against buckling, because the restraint forces the culvert to buckle in higher modes. The more dense and stiff the soil is around the culvert, the more effective the deformation restraint.

Stress redistribution is the fact that the stresses around the springline of a culvert will increase above the at-rest value. When the culvert deflects under the vertical load at the surface, the side of the culvert was pushed against the adjacent soil, and the contact stresses increase. This was proved by Hoeg (1968) and Howard (1972). They found the side contact stresses against the thin flexible pipe increased with increasing flexibility of the pipe in both cohesionless and cohesive soils.

Arching is the action by which the contact stress around the crown is reduced when the culvert deflects inwardly at the crown. Rigid culverts have larger stiffnesses than the soil stiffness and induce negative arching. On the other hand, flexible culverts generally triggered positive arching. Qualitatively, positive arching is enhanced as the soil stiffness is increased and/or culvert stiffness is decreased. These were confirmed by Hoeg (1968) and Howard (1972).

### 1.3 Literature Review

#### 1.3.1 Classical Methods

Currently used design methods for buried culvert are mainly based on the work done at Iowa State University by Marston (1922, 1930) and Spangler (1928, 1941) about sixty years ago. For circular flexible pipes two design criteria have been commonly used.

First is the Iowa Formula (Spangler, 1941) in which the change in the horizontal diameter of the flexible tube is evaluated as follows:

$$\Delta X = D_1 \frac{K W_c r^3}{EI + 0.061 E_s r^3} \quad (1.1)$$

where

$\Delta X$  = the change of horizontal diameter,

$D_1$  = deflection lag factor,

$W_c$  = effective vertical load acting on the pipe from Marston's estimation,

$K$  = bedding constant,

$r$  = mean radius of the pipe,

$E$  = modulus of the pipe material,

$I$  = moment of inertia,

$E_s$  = modulus of the soil.

Design is achieved by adjusting the pipe's in-plane bending stiffness to contain the deflection within 5% of the diameter. The accuracy of the Iowa Formula is tied to the proper selection of those empirical parameters. The soil modulus is the most controversial one since it varies with so many factors, like confining pressure, soil density and strain rate, etc.

Second is the ring compression theory which was proposed by White and Layer (1960) who assumed that the wall thrust is equal to the weight of the soil column above the culvert.

$$T = \gamma H r \quad (1.2)$$

where

$T$  = wall thrust,

$\gamma$  = unit weight of soil,

$H$  = distance from the top of the pipe to the surface of the fill,

$r$  = mean radius of the tube.

The design procedure is to adjust the wall area so that the hoop stress is under the ultimate seam strength or yield stress reduced by a safety factor.

Since the 1960's many researchers based the design of flexible culverts on elastic buckling. These works were discussed in detail by Leonards and Stetkar (1978).

Generally speaking, the Iowa Formula, ring compression theory, and buckling theory are used for the design of flexible culverts. In these methods the magnitude of the vertical load or horizontal load on the culvert is assumed instead of the real load distribution. These assumptions made many parameters in the above theories or formulas so empirical that the use of these methods is seriously limited and their applicability to a special problem is almost impossible.

### 1.3.2 Exact Solution Methods

By considering the soil as a continuum and the culvert as a shell, the soil-culvert system can be treated as a boundary value problem. If linear elasticity is assumed for the soil and

the linear elastic shell or ring theory is used for the culvert then an exact solution can be found for this kind of boundary value problem. Malishev (1965), Savin (1961), Hoeg (1966), Burns (1964), and Dar and Bates (1974) all presented solutions of this kind.

The solution by Burns provides a closed form solution of linearly elastic, circular cylinder embedded in a linearly elastic, isotropic, homogeneous, and weightless medium under plane strain conditions. Uniformly distributed vertical and horizontal loads were applied on the boundaries. Free slippage and no slippage are the only options for the interface between the soil and the culvert. Although these solutions offer an assessment of the problem of soil-structure interaction, those very idealized assumptions make this method unsuitable for accounting for the irregular geometric shape, nonhomogeneity, nonlinear material properties and construction process. So their satisfactory application is still limited to a few highly specialized situations.

### 1.3.3 Finite Element Methods

The finite element method has received much attention in the field of soil-culvert interaction since the mid 1960's. There are several advantages of this numerical method over classical methods and exact solution methods, namely, (1) the ability to represent the complex nonlinear behavior of the soil and the structure; (2) the ability to represent the nonhomogeneous back-fill conditions; (3) the ability to simulate the actual sequence

of construction operations; (4) the ability to output the displacements, strains and stresses of the soil and culvert at any stage for design or analysis purposes; and (5) the ability to illustrate the effect of different parameters.

Brown et al., (1968) studied the behavior of a flexible culvert under 80 foot high hills with the finite element method in which constant strain triangular element is used to model the soil medium. The culvert member is represented by three overlapping triangular elements, whose stiffness matrices are assembled suitably so that the transformed stiffness matches exactly that of the curved member. The linear elastic and isotropic material property law is used for both soil and culvert elements. The effect on the normal pressure distribution on the culvert is studied under different conditions, like interface, culvert flexibility, and hay replacement. By comparing the analytical solutions with the field measurements the finite element prediction on the magnitude and distribution of normal pressure is found to be fairly good. Brown performed similar analyses on the rigid culvert (1967).

Doderer (1970) studied soil-culvert problems with the finite element method in which both soil and culvert were modeled by linear elasticity and constant strain triangular elements. He found that although the stresses and strains in the soil could be predicted satisfactorily, the constant strain triangular element could not predict the stresses in the culvert.

Duncan and Clough (1971) presented the finite element analyses of Port Allen Lock. The soil and the concrete culvert were represented by linear strain quadrilateral elements. Stress-dependent stress-strain behavior developed by Duncan and Chang (1970) was used to model the soil. The concrete culvert was treated as linear elastic. One-dimensional elements were employed to represent the interface between soil and concrete. The incremental finite element analyses were performed by simulating each of the actual construction operations:  $K_0$  initial condition, excavation, dewatering, placement of concrete and backfill, re-establishment of normal groundwater conditions, and filling of the lock with water. The observed rebounds during excavation, settlement during construction, earth pressures, and structural deflections agree closely with the calculated values. They also found that the finite element method with linear elastic soil behavior and simple "gravity turn-on" loading gave a poor match. Therefore, the finite element method with nonlinear material property and simulated construction sequence procedure is a very promising tool to analyze the complex soil-structure interaction problem.

Duns and Butterfield (1970) performed a series of tests on a 6 inch diameter, mild-steel cylindrical pipe instrumented with strain gauges and buried in the uniform fine sand. The axial thrust and bending moment of the cylinder were calculated from the measurements and were compared with the results from finite element analyses in which constant strain triangular elements were

used to approximate the soil medium and the straight beam elements were used to represent the cylinder. The stiffness matrix for each beam element was evaluated from the slope deflection formulation and then the rotational degrees of freedom were condensed before it was assembled into the system stiffness matrix. Full bond at the interface was assumed. The material model was linear elastic and the loading consisted of a uniform surface pressure. It was found that the bending moment in the tube wall is highly dependent upon Young's modulus of the surrounding medium. An approximate step-by-step analysis taking into account the nonlinear stress-strain law for the soil showed that the bending moment is nonlinear and is in agreement with the experimental data, although the thrust still varies linearly with surface pressure. The elastic analyses showed that the thrust at the springline exceeds the hydrostatic load by 20-30%, i.e., negative arching occurred. This difference was attributed to the assumption about full bond at the interface between soil and tube.

Trott and Gaunt (1972) used the constant strain triangular element to represent soil and the line element to approximate the steel pipe. The line elements could sustain axial load only. On the basis of a comparison with field measurements they concluded that the finite element analysis shows a promising future in this type of problem.

Abel et al., (1973) studied the stresses around a flexible elliptic pipe by using an experimental and numerical methods.



Quadrilateral elements were used to model both the pipe and soil. The displacement model chosen had a quadratic variation and hence the 4-node element was nonconforming. As a result, the convergence to exact elasticity solutions is much faster than the simple, isoparametric quadrilateral elements, particularly when flexural behavior is present. The interface between soil and pipe was assumed to be full bond and the material properties were treated as linear elastic. Based on the experimental work it was concluded that for deep pipe the normal stresses were significantly reduced and the hoop stresses were significantly increased with interface slippage. The internal stresses induced in the pipe wall were also reduced through the more even distribution and lower values of normal stresses around the pipe. For the shallow pipe, the same effect is less evident. The internal stresses in the shallow pipe wall may not be disturbed much from the varied interface condition.

Anand (1974) used the finite element method to compute the stresses at the soil-pipe interface. The reinforced concrete pipe was represented by 320 quadrilateral plane strain elements with nonlinear material properties and proper cracking mechanisms. The soil was modeled with up to 257 quadrilateral and triangular plane strain elements with nonlinear elastic properties, and Young's modulus and Poisson's ratio were determined by uniaxial strain and triaxial tests. The interface condition between the pipe and the

soil was assumed to be full bond. The measurements of normal stresses in the soil and at the soil-pipe interface and of the displacements in the soil were obtained and were used to compare with the analytical solution.

Katona (1976) developed a finite element program CANDE which stands for Culvert ANalysis and DEsign. Small strain theory and plane strain cases are assumed. The soil is modeled by quadrilateral elements and the pipe is represented by plane strain beam elements. The soil properties are modeled by linear elasticity, overburden-dependent model, and extended Hardin model. A bilinear stress-strain relationship is used to represent the steel, aluminum and concrete material properties. The soil-culvert interface is modeled by interface elements which allow for frictional sliding, separation, and rebounding. Chang, Espinoza and Selig (1980) used this program to analyze the Newtown Creek culvert. Measurements were made of bending and thrust stresses in the steel, deflection of the culvert, backfill stresses, and backfill strains and deformations. However, the validation of the CANDE's capabilities is incomplete because very little field data is available. A convergence problem was encountered when the interface elements were used.

Duncan (1977) presented a finite element analysis of buried flexible metal culvert structures. Beam elements were used to represent the culvert and the 4-node quadrilateral elements

model the soil. The hyperbolic model with Young's and Bulk moduli by Duncan, et al., (1977) was used for soil properties. Interface elements were incorporated between the culvert and the backfill to permit relative displacements. The live loads due to traffic and the incremental placement of backfill around and over the structure were simulated numerically. A trial and error procedure was used to determine what stiffness should be assigned to the upper longitudinal seam with loose bolts. The measurements of stresses and deflections of the culvert were used to calibrate the stiffness of structure. It was concluded that the effects of slip between the structure and the backfill are small, and the relative stiffness of the structure and the backfill has no significant effect on hoop stress even for shallow cover conditions. With a shallow cover, live loads on the surface of the backfill can induce unsymmetrical loads which generates larger bending moments and cannot be resisted entirely through ring compression action. Seam compression failure was believed to occur before the buckling failure in this case.

Larsen (1977) analyzed the earth pressure around the buried concrete pipe by testing scale physical models in the centrifuge to obtain measurements which were matched to the results from finite element methods. Specially designed load cells were mounted in the wall of concrete pipe so that the normal and tangential stresses on the pipe could be measured. Numerical

analyses were conducted using three computer programs, i.e., FESOL, ICES STRUDL-II and CR-FESM. The FESOL program was developed by Simpson (1973) who used simple constant strain triangles to model the soil with linear elastic and Leighton Buzzard Sand models. The results showed poor agreement with lab data. The ICES STRUDL-II program was developed at Massachusetts Institute of Technology for structural design. A variety of elements are available, ranging from constant strain triangles to isoparametric elements with 12 nodes. The material models are all linear elastic. However, the body forces have to be transformed to nodal forces by the user. Considerable stress discontinuities were observed along the interface between soil and pipe if the circular pipe is modeled by elements with straight sides. The CR-FESM program was written by Reimers (1975). Constant strain triangles were used to model the soil and beam elements were used to represent the pipe. The beam elements were introduced because the triangular elements could not model the behavior of the pipe accurately enough without using too many elements. The hyperbolic stress-strain model of Duncan and Chang (1970) was used for soil properties without making any distinction between loading and unloading. In comparison with the lab test results, this program shows promise.

Krizek and McQuade (1978) presented the studies on the behavior of buried concrete pipe. The finite element codes developed by Anderson (1974) and Wenzel (1975) were used to generate

the analytical solutions which were compared with the measurements from the field, such as the normal stresses on the pipe, the strain at the inside and outside surfaces of the pipe, the strains of the reinforcing steel, the stresses in the soil, diameter changes, and the relative displacements between the soil and the pipe. The soil was modeled with quadrilateral and triangular plane strain elements. The soil properties were modeled as piecewise linear elastic, with the moduli values determined from the uniaxial strain test, triaxial test, plane strain test, and the true triaxial test. Six concrete elements comprise the thickness of the pipe wall and two overlay steel elements represent the reinforcement. The modulus of elasticity of the concrete is a function of the major principal stress and the ultimate compressive strength of the concrete. A proper crack mechanism gets action when the tensile strength of concrete is reached and consequently increases the number of pipe elements. The soil-pipe interface was assumed to be fully bonded. Soil elements are subtracted in excavation or added in backfilling incrementally during the construction process.

McVay (1982) analyzed buried, corrugated steel culverts and reinforced concrete pipes. The culvert was modeled with straight beam elements and the adjacent soil with either subparametric triangular or quadrilateral elements. Four soil models were considered: 1) bilinear modulus with constant Poisson's ratio, 2) linear elasticity, 3) overburden-dependent model, and

4) hyperbolic model with nonlinear Young's modulus and bulk modulus. The steel properties were represented by a bilinear model and the rigid conduit by a trilinear model. The construction procedure was simulated and the boundary effect was studied. The live loads and the buckling of the conduit wall were not considered. Due to the convergence problem created by combining the nonlinear soil properties with the use of interface elements, the interface condition was not considered. However, the good agreement between the measured and calculated responses from the code with a hyperbolic soil model, indicates that the interface condition might have a minimal effect on this problem. It was concluded that the code with a hyperbolic soil model predicted the response of a soil-culvert system very well in both flexible and rigid culverts, and the overburden-dependent soil model should be abandoned since the stress path in the soil element adjacent to the culvert did not follow the path in the uniaxial compression test on which this soil model was calibrated.

#### 1.4 Objectives

From the review in the previous sections it is obvious that the classical and exact solution methods have limited success for analyzing soil-culvert system and the finite element method was regarded as the most promising device to analyze this kind of complex problem. This does not necessarily mean that a new design method should use finite element method, but the finite element

method can offer a valuable insight into this problem and lead to a new, simple and adequate design method provided that the finite element program used can be shown to predict the exact response of the system being analyzed.

The data for comparison with the results from the finite element method can be used to determine whether this code is adequate or not. In principle these data could be generated from field measurements on full scale prototypes, but this would be very time consuming and expensive. Indeed there are very few of this kind of data available (McVay, 1982). Even in cases where such data do exist, variability in field compaction, workmanship and installation make these data inaccurate to be used to calibrate the numerical finite element code (McVay, 1982). On the other hand, centrifuge model testing is a very cheap, easy and accurate way to acquire the same data as could be obtained from the full scale field tests.



The behavior of a soil-culvert system is very much dependent upon the variables such as construction process and the properties of soil, culvert, and the interface between them. It seems that the interface condition is not important for the shallow culvert. This was evident from the works of Abel et al., (1973) and Duncal (1977). In order to exclude the possible effects from the interface, a shallow buried culvert is used in this study. It

is extremely important to prepare the centrifuge model in a way to make only one variable stand out each time and to model the remaining variables faithfully.

Table 1.1 shows the comparison between the centrifuge model and numerical model in terms of how the variables are incorporated. The displacements and strains of soil and culvert are kept small by using a very stiff soil, a very flexible culvert and moderate surface loading. The discretization of the culvert and surrounding soil in the analytical model is a built-in ingredient. The associated discretization error can be minimized by using finer meshes. Many researchers recommended the  $1 \times 1$  under integration of stiffness in the thin shell and plate problems where 4-node quadrilateral elements are used to model the shell and plate (McNeal 1978, Hughes et al., 1978, and Prathap et al., 1982). So under-integration for culvert stiffness and full-integration for soil stiffness are used in this study. It turns out that under-integration is very critical in computing the response of a buried thin culvert. This will be discussed in detail in Chapter VI. The construction process and gravitational stress history experienced by the centrifugal model before the application of surface loading are also faithfully simulated in the numerical model. The kinematic boundary conditions along the interface between the soil and the model container is likely to produce only vertical movement vertically and will be modeled as such. The surface load is limited in order to maintain the stress



Table 1.1

Variable	Centrifugal Model	Numerical Model
displacement-strain	small displacement	small displacement theory
soil element	infinitely small	discrete 4-node quadrilateral finite elements with 2x2 stiffness integration
culvert element	infinitely small	discrete 4-node quadrilateral finite elements with 1x1 stiffness integration
soil	S.M. sandy silts	represented by linear elastical, hyperbolic or Lade's model
culvert	aluminum pipe	represented by linear elasticity
initial stress	gravity induced stress	faithfully simulated process
stress boundary	surface loading	faithfully simulated process
kinematic boundary		
interface slippage	insignificant i.e. full bonding	full bonding
soil density	uniform	faithfully simulated
dimension	very close to plane strain	plane strain

state in the culvert below the yield stress, so that linear elasticity can be assumed for the culvert. This leaves the constitutive model for the soil as the only variable in the numerical analysis and makes it possible to concentrate on modeling the soil properties by different constitutive models in order to determine the accuracy of such models.

The objective of this thesis is to investigate the ability of the linear elastic, hyperbolic and Lade's soil models to predict the response of a buried flexible culvert.

## CHAPTER II

### DESCRIPTION OF SOIL

#### 2.1 Index Properties

The soil used in this investigation was obtained from the valleys in the Nevada desert. Its grains shape vary from subrounded to angular, and contain calcium carbonate which is commonly identified on the basis of reaction with diluted hydrochloric acid (Fugro National, Inc., 1979).

The original soil was sieved to remove any grains larger than 4.75 mm to produce the grain size distribution shown in Figure 2.1. The coefficient of uniformity,  $C_u$ , for the resulting soil is 3.1 and the coefficient of curvature,  $C_c$ , is 1.0. With a plasticity index equal to 3.9, the soil is classified as sand silt, SM, under the Unified Soil Classification System. The specific gravity is equal to 2.66. All these values are listed in Table 2.1.

A modified Proctor compaction test was performed with a standard mold in which five layers of soil were compacted with a 5.5 pound hammer. Each layer was compacted 25 times with a 12 inch constant drop height. The maximum dry density is equal to 125.9 lb/ft<sup>3</sup> and the optimum moisture content is 10.8% as shown in Figure 2.2.

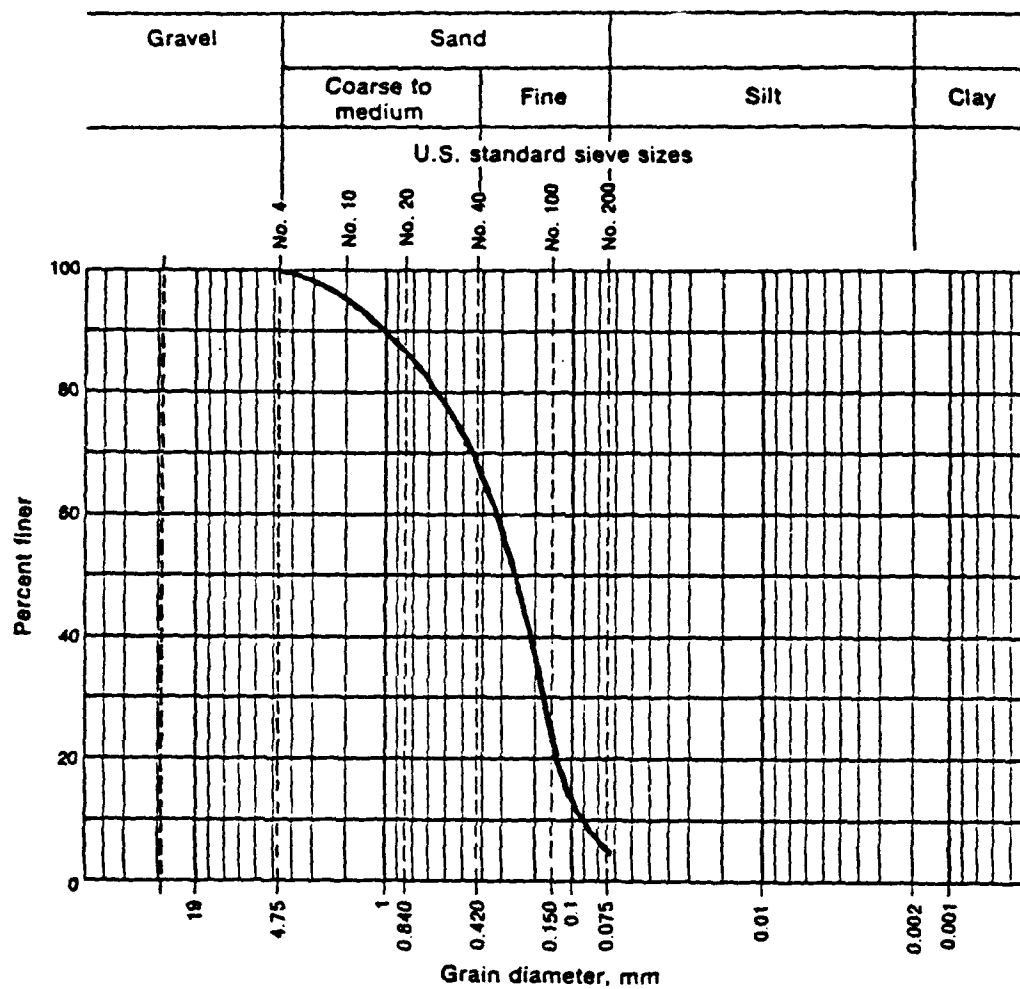


Figure 2.1 Grain Size Distribution

TABLE 2.1 - Basic Characteristics of Soil

INDEX PROPERTIES			COMPACTION RESULTS		GRADATION RESULTS						
LL	PL	PI	MAXIMUM DRY DENSITY	OPTIMUM MOISTURE CONTENT	FINES	C <sub>u</sub>	C <sub>c</sub>	D <sub>10</sub>	D <sub>30</sub>	D <sub>60</sub>	G <sub>s</sub>
(%)	(%)	(%)	(pcf)	(%)	(%)			(mm)	(mm)	(mm)	
16.1	12.2	3.9	125.9	10.8	<5	3.1	1.0	0.09	0.17	0.32	2.66

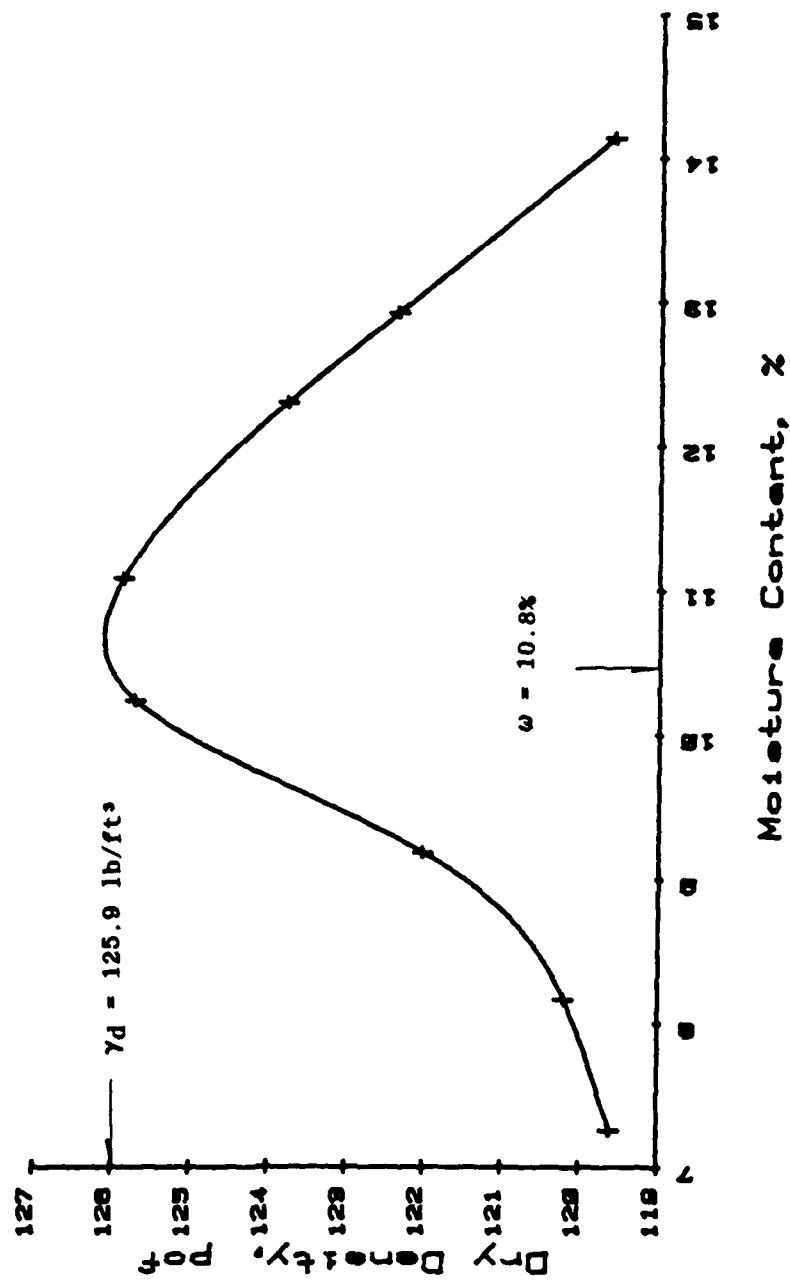


Figure 2.2 Modified Proctor Compaction Test Results

## 2.2 Engineering Properties

Soil samples were statically compacted to 90% of maximum dry density, 113.4 lb/ft<sup>3</sup>, at the optimum moisture content of 10.8% for conventional triaxial and isotropic compression tests. The soil samples were compacted in 11 layers with the undercompaction methods (Ladd, 1978) in which the degree of undercompaction for the first layer was determined by a trial and error procedure. Uniformity of the soil sample was achieved if 5% undercompaction for the first layer was used. The same degree of under compaction preparation for the centrifugal soil model.

A series of drained triaxial compression tests were conducted. The range of confining pressure used would cover the values expected to occur in the centrifugal model tests. Since the soil sample was unsaturated the volume change was measured by monitoring the volume of water flowing into or out of the triaxial cell chamber.

Figures 2.3 and 2.4 show the axial stress-axial strain relations and volumetric strain-axial strain relations from the tests at confining pressure of 2.5, 5, 15, 25 and 35 psi, respectively. The soil dilates under low confining pressures and contracts under high confining pressures. Post-peak softening for low confining pressures gradually switches to hardening without a peak value for high confining pressures. In Figure 2.4 it is

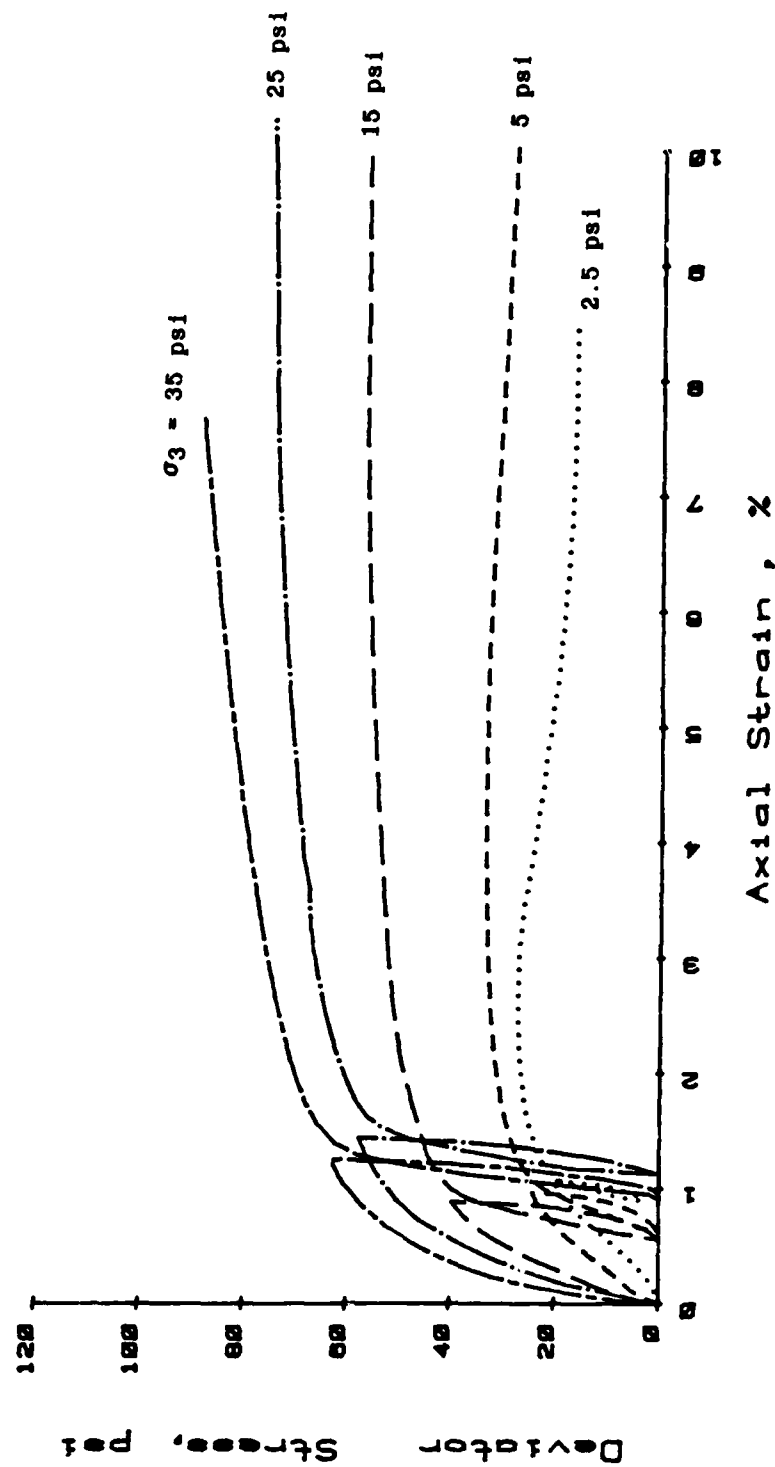


Figure 2.3 Deviator Stress vs Axial Strain from Conventional Triaxial Compression Tests



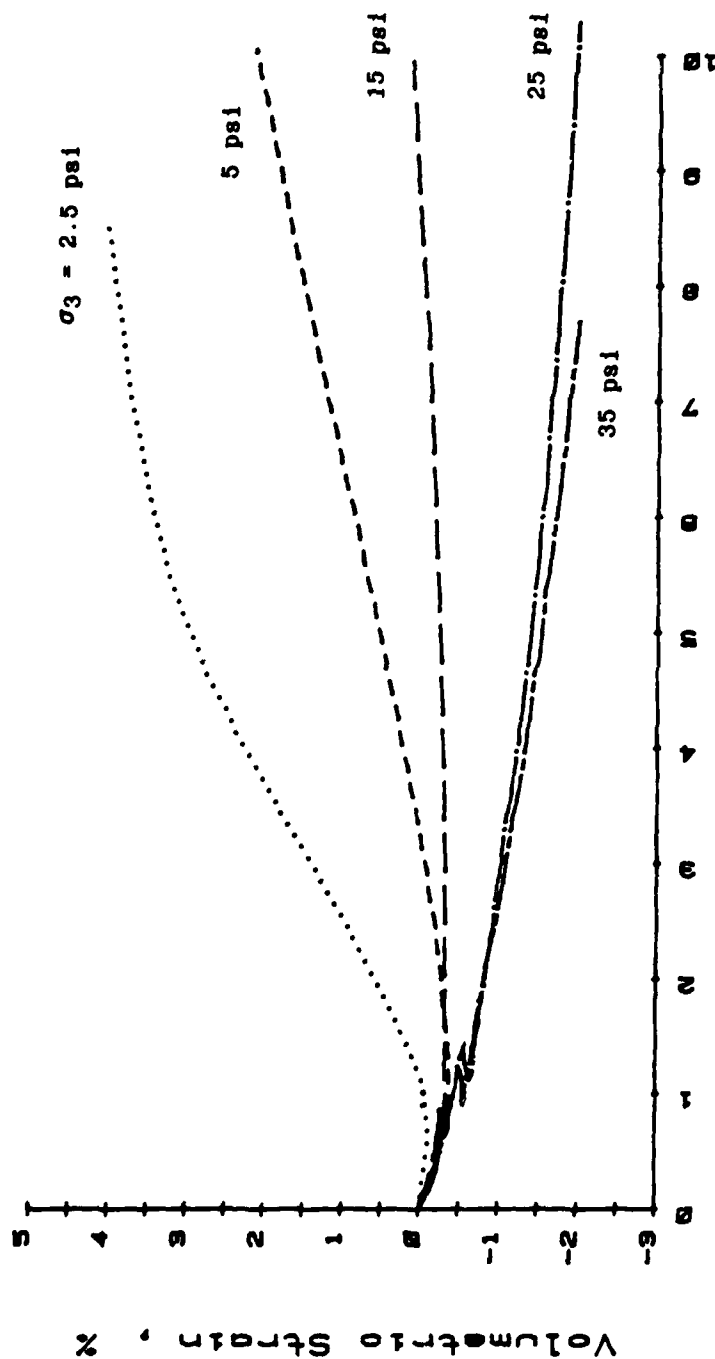


Figure 2.4 Volumetric Strain vs Axial Strain from Conventional Triaxial Compression Tests

observed that the soil continues to decrease in volume during unloading. This observation contradicts the theory of elasticity but can be explained by the theory of plasticity. In the theory of elasticity shown in the incremental form of equation 4.4, the strain increment corresponding to a stress increment must follow the direction of the stress increment. Thus, an elastic material will increase in volume upon unloading. However, in the theory of plasticity, the strain increment is a function of the stress increment and the total stress. If the total stress is compressive although the stress increment is tensile, the net influence on the strain increment could be compressive or tensile, depending on the current stress state. The observation in the triaxial tests can therefore be explained by such a theory of plasticity.

The Mohr-Coulomb failure envelope is drawn for the failure test data in Figure 2.5. The apparent cohesion,  $c$ , and the angle of shearing strength,  $\phi$ , were found to be 6.5 psi and  $30.7^\circ$ , respectively.

Finally, an isotropic compression test was performed with one cycle of loading and unloading. Figure 2.6 shows the test results.

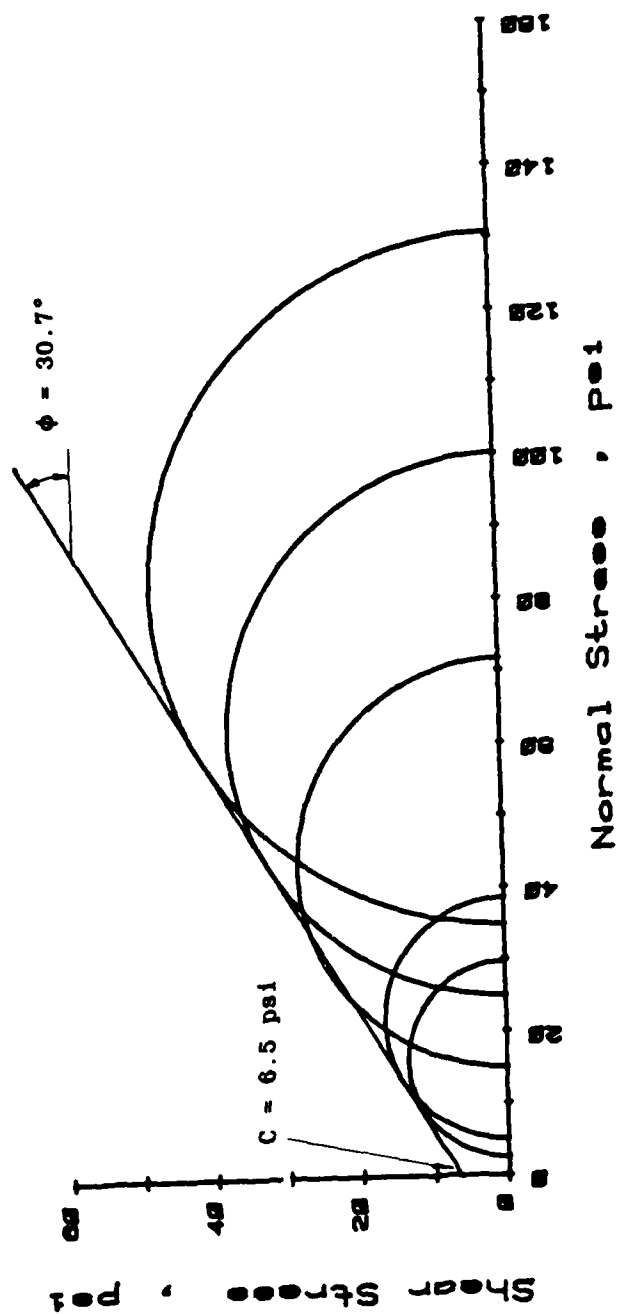


Figure 2.5 Mohr Circle Diagram

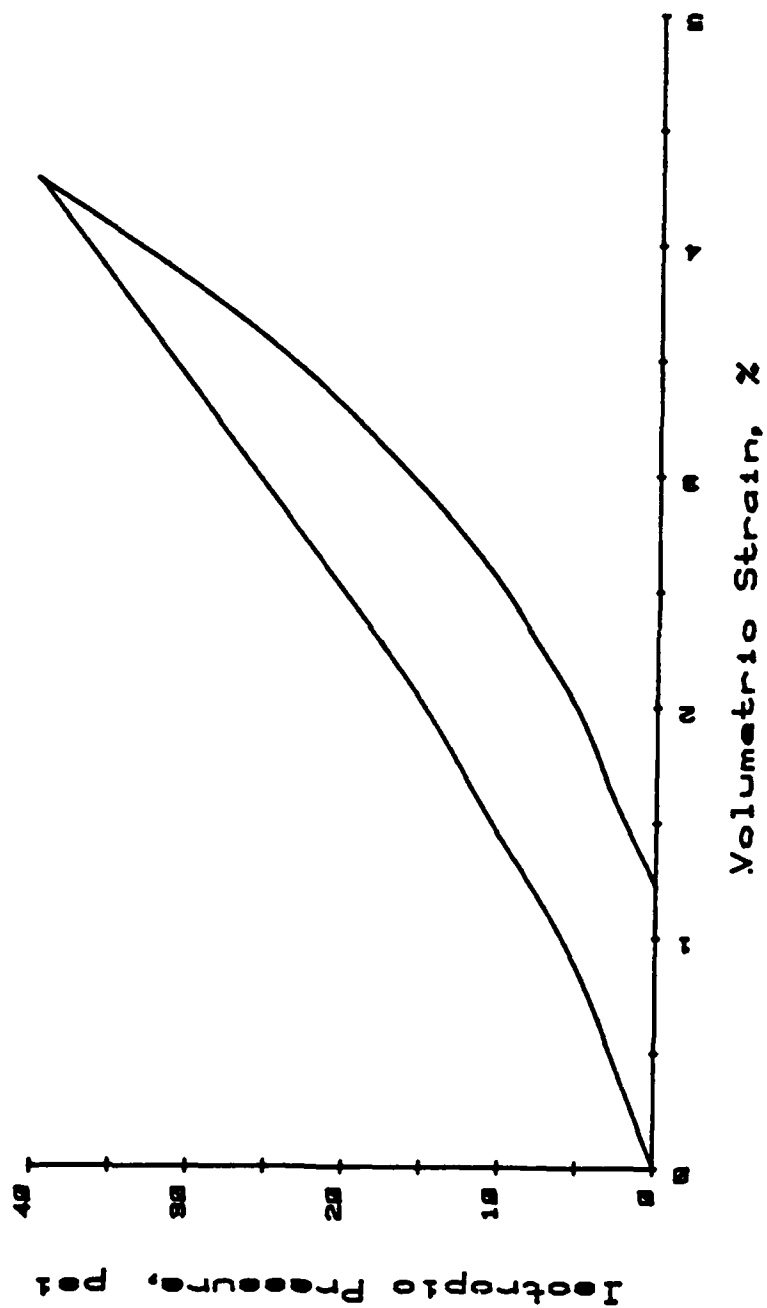


Figure 2.6 Isotropic Pressure vs Volumetric Strain from  
Isotropic Compression Test

## CHAPTER III

### DESCRIPTION OF EQUIPMENT

#### 3.1 Description of the Centrifuge

The Department of Civil, Environmental and Architectural Engineering at the University of Colorado in Boulder acquired its 10g-ton centrifuge in May of 1978. Specifications and dimensions of this equipment are given in Table 3.1. The schematic of the centrifuge in the flight position is shown in Figure 3.1.

The payload capacity represents the weight of soil container and soil multiplied by the g-level at the mass center of payload. The modification of the swinging basket for the experimental package in 1983 increased the payload capacity from 20,000 g-lbs to 35,000 g-lbs, which was verified in the summer of 1984.

The sample basket serves to carry the soil container which includes the soil-culvert system and will be explained in Section 3.6.

#### 3.2 Culvert and Strain Gauge

##### 3.2.1 Culvert and Its Properties

A thin aluminum circular cylinder was chosen for the soil-culvert interaction problem. The tube is 4 inches in O.D. and

TABLE 3.1 - University of Colorado Centrifuge Specifications  
(De Donati, 1981)

Manufacturer	Genisco
Model	1230-5
G-Range	Variable 1 to 262 g at 42 in nominal radius
Driving System	25 HP hydraulic
Working Radii	42.0 in - center to basket hinge 11.5 in - hinge to basket floor
RPM Range	0-470 RPM
Payload Capacity	35,000 g lbs (350 lb at 100 g)
Test Package Size	18 in x 18 in x 18 in maximum
Electrical Pick-ups	56 slip rings
Fluid Transfer	2 hydraulic slip rings
Test Recording	Closed circuit TV 35 mm SLR camera

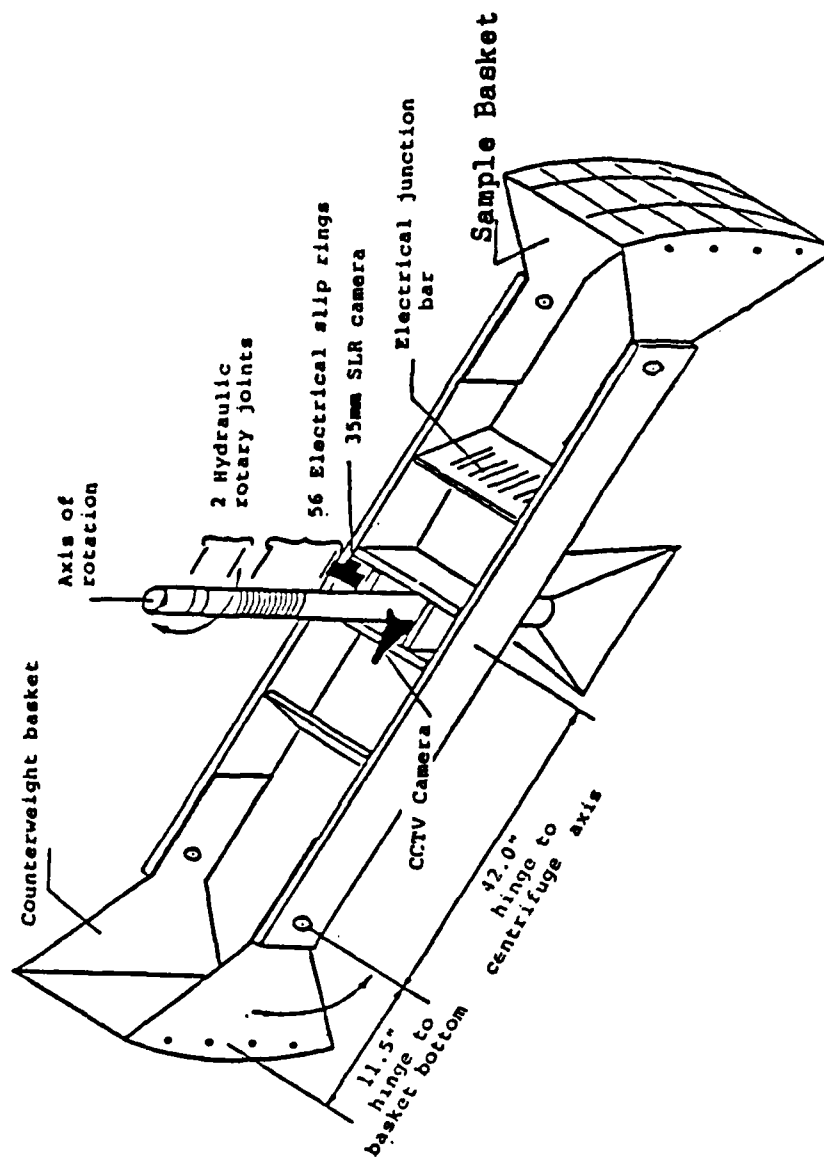


Figure 3.1 - Schematic of the Centrifuge (Ko et al., 1982)

0.025 inch wall thickness, and was obtained from the TUBESALES Company of Salt Lake City.

This thin tube is made of 5052 O-Temper aluminum which is alloyed with 2.5% magnesium, with very good corrosion resistance, good workability, weldability and strength. Its properties are listed in the Table 3.2. The length of tube used in the centrifuge is 16.9 inches.

### 3.2.2 Selection of Strain Gauge

There are many types of strain gauges which can be found in manufacturers' catalogs. For different problems only certain types of gauge are appropriate. Selection of the best strain gauge is difficult and is more of an art than science. In general the considerations for the selection of strain gauge include: gauge grid area, gauge resistance, self-temperature-compensation, gauge series, heat-sink property of the mounting surface, and optimum strain gauge excitation level. The detailed description of each factor can be found in the manufacturer's catalog. Based on the above considerations, the type of strain gauge chosen was CEA - 13 - 015CK - 120, Option W, made by Micromeasurements Inc.

### 3.2.3 Gauge Installation

Eleven gauges were installed each on the inside and outside of the tube. Figure 3.2 shows the schematic of the 22 strain gauges and their relative positions. The installation procedure is described in the following steps:



TABLE 3.2 - Engineering Properties of Tube

Alloy-Temper	Ultimate Strength (psi)	Yield Strength (psi)	Brinell Hardness	Shear Strength (psi)	Endurance Limit (psi)	Elastic Modulus (psi)	Poisson's Ratio
5052-0	28,000	13,000	47	18,000	16,000	$10.2 \times 10^6$	0.334

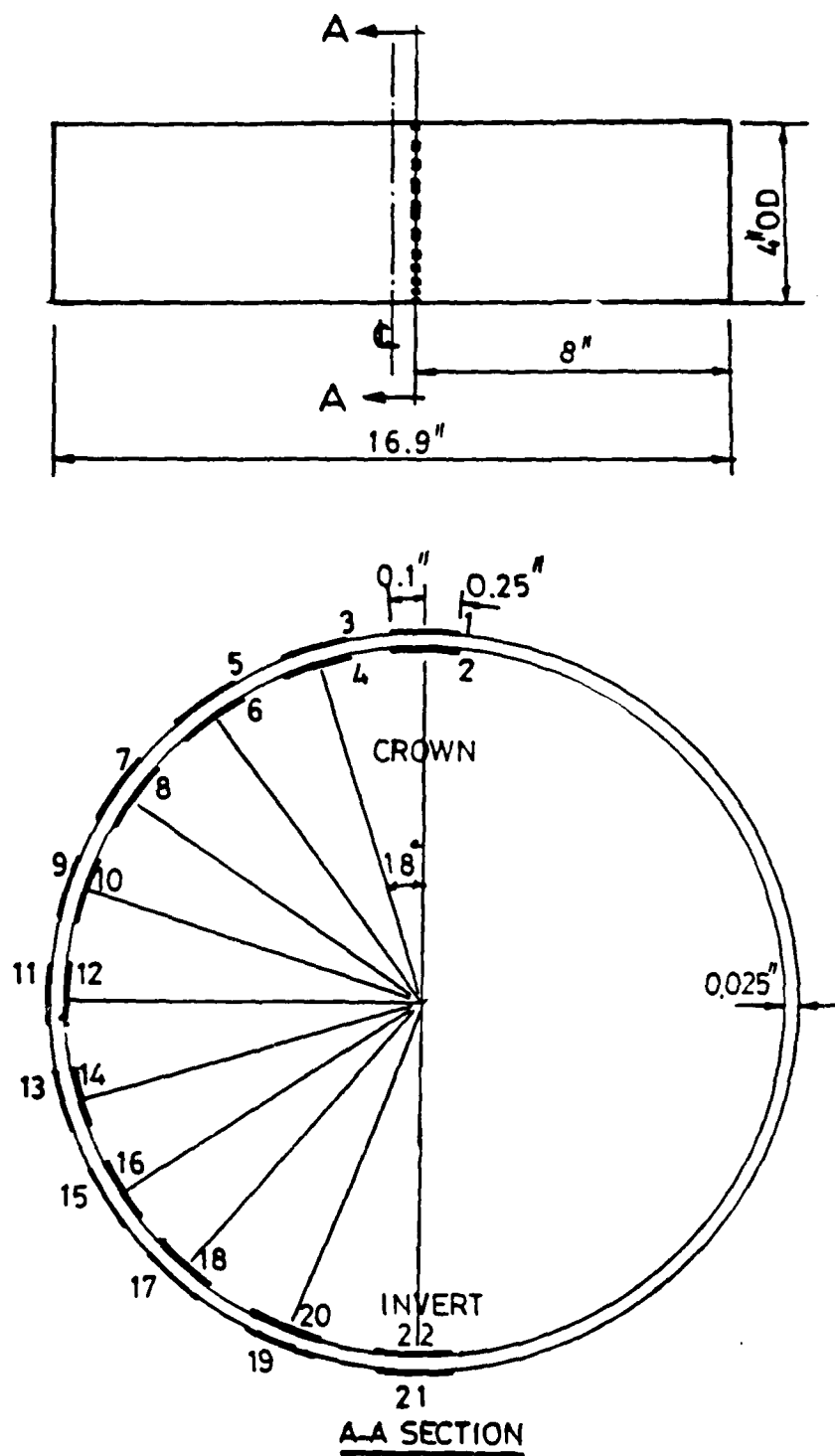


Figure 3.2 Locations of 22 Strain Gauges

(1) Two rectangular paper sheets are cut as shown in Figure 3.3. One with size of 8" x 6.205" is used on the inside of the tube, the other of 8" x 6.283" is used on the outside of the tube. Eleven notches are cut in each sheet with a specified spacing so that 18° is spanned between each pair of gauges, one on the outside and the other on the inside.

(2) The ends of the tube are filed and sanded such that the plane determined by the end surface is perpendicular to the longitudinal direction.

(3) The 6.205" and 6.283" sides of the sheets are aligned with the end surface of the tube, and the 8" sides are aligned longitudinally at the inside and the outside, respectively. These two sheets are taped in position.

(4) The gauge application technique as detailed in the manufacturer's catalog is followed carefully. The locations of the inside gauges are repeatedly checked through a mirror by examining whether the gauge is correctly oriented and fitted in the notch before the M-Bond 200 adhesive is applied. Then firm thumb pressure is applied to the gauge and terminal area for about 5 minutes to minimize the possibility of the trapped voids in the glue line.

(5) Step (4) is repeated until all the gauges are glued on. Then the two paper sheets are removed, completing the gauge installation.

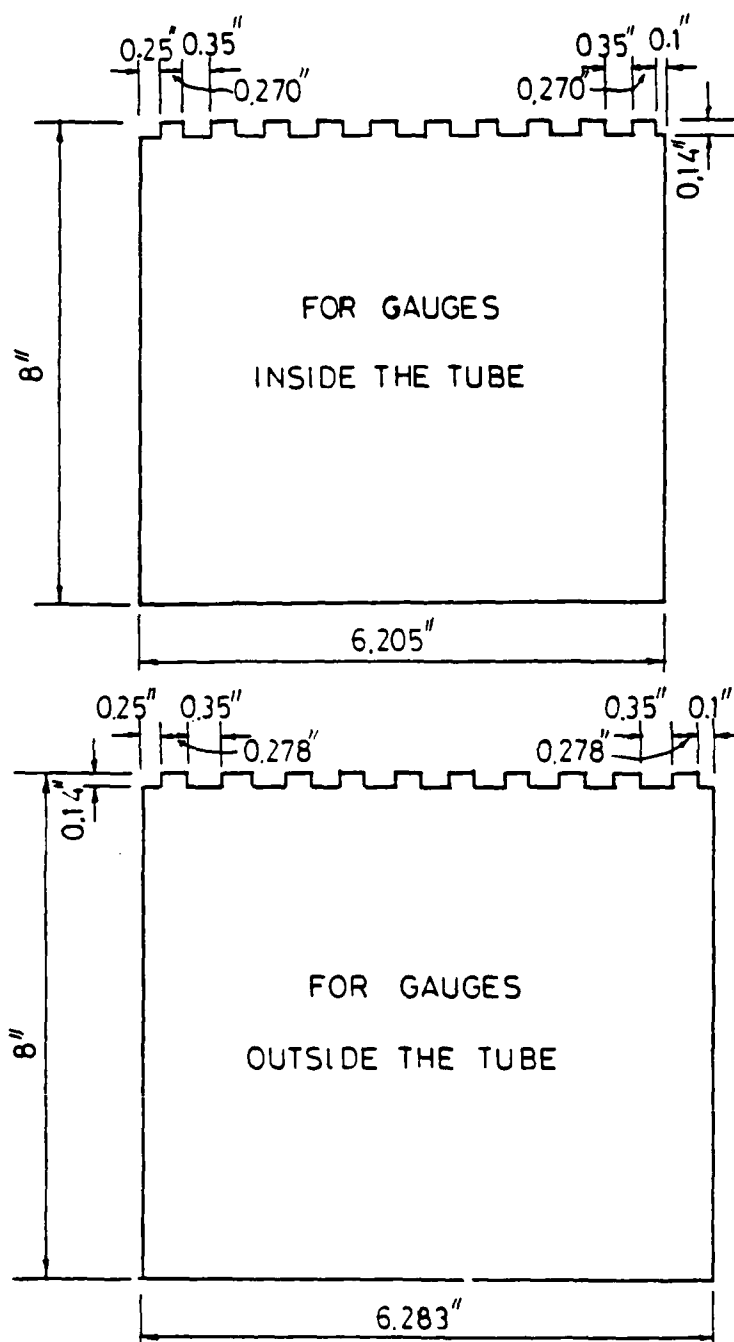


Figure 3.3 Gauge Locators

#### 3.2.4 Wiring Technique

The wire leads to the terminals of outside gauges have to go through the wall of the tube immediately if the smooth condition of the outside surface is to be maintained. Therefore 22 small holes were drilled. The location and the diameter of these holes were chosen with the following considerations. First, the proper size of wire will not break easily at the soldering spot. Second, the location of the hole is far enough from the gauge grid so that the stress concentration will not affect the actual gauge reading. From linear elasticity if the hole is 6 times the diameter of the hole away from the gauge grid, this disturbance can be neglected (Poulos and Davis, 1973). Figure 3.4 shows the position of a hole and its size in relation to a strain gauge. By the above consideration, these numbers are reasonable choices.

Labeled wire leads pass through these holes and collect at one side of the tube after the other ends of the wire leads are soldered to the terminals of the inside gauges. Next, the labeled wire leads are soldered to the terminals of outside gauges. The resistance of each gauge is checked to verify the conditions and the labeling of the gauges. M-coating A is applied to each gauge to protect the gauge and the adhesive from the penetration of sand grain during the test. The wiring procedure is now completed. Figure 3.5 shows the gauged and wired tube.

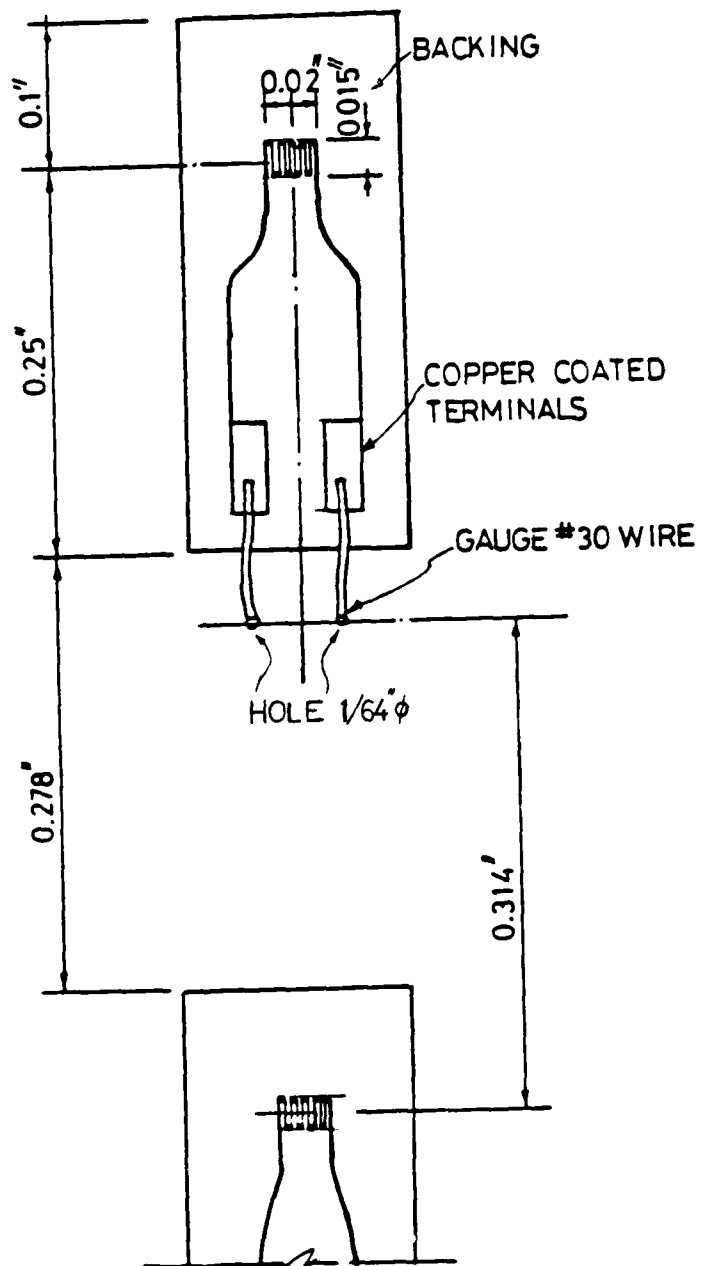


Figure 3.4 Wired Strain Gauge System

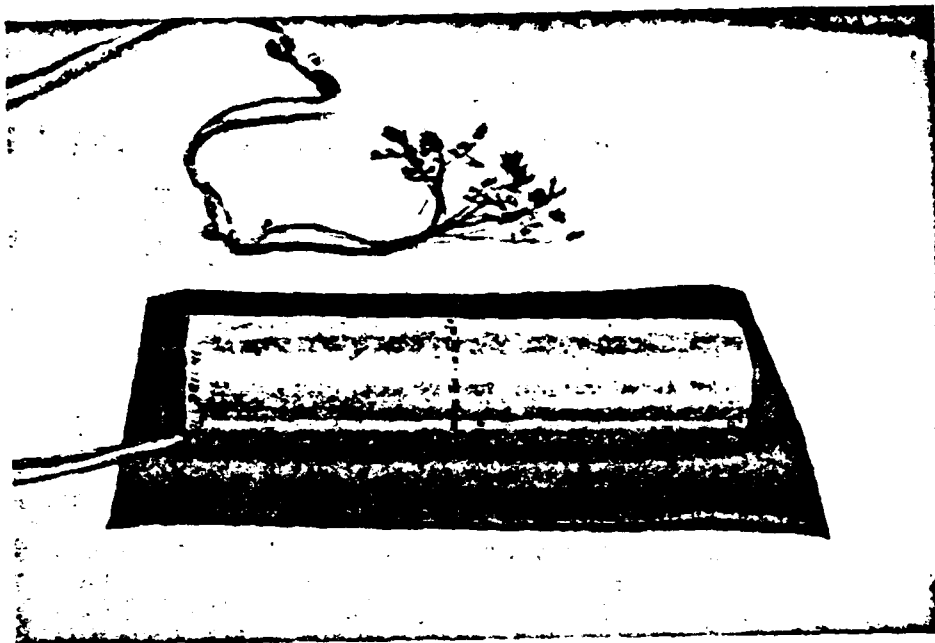


Figure 3.5 The Tube with Strain Gauges and Wire Leads

### 3.2.5 Gauge Circuit and Amplification

The one-quarter wheatstone bridge circuit is adopted as shown in Figure 3.6. Three dummy gauges,  $R_1 = R_2 = R_4 = 120 \Omega$ , and one active gauge,  $R_3 = 120\Omega$ , complete one bridge with a 3.8 VDC power supply  $V_{CA}$ . The strain calculated from the measurement of voltage variation across the bridge,  $\Delta V_{DB}$ , is expressed as follows:

$$\epsilon = \frac{-4 \Delta V_{DB}}{2.08 (2 \Delta V_{DB} + V_{CA})} \quad (3.1)$$

where gauge factor = 2.08.

All the dummy gauges to complete the wheatstone bridges are housed in an aluminum box which is mounted close to the rotating shaft in the centrifuge and is wrapped with duct tape to avoid the effect of temperature fluctuation in the centrifuge on the bridge balancing as shown in Figure 3.7. The Jones strips serve as the connectors between the one-quarter active gauge and the three-quarter dummy gauges to complete the wheatstone bridge as shown in Figure 3.8.

Since the slip rings at the top of the shaft shown in Figure 3.1 will generate noise when the centrifuge is spinning, the power supplies for gauge excitation and amplifiers are mounted inside the centrifuge. In order to produce a higher signal-to-noise ratio amplification of the signal is necessary before passing through the slip ring. The amplifier box is placed between the cross-bridge wires and the slip rings.



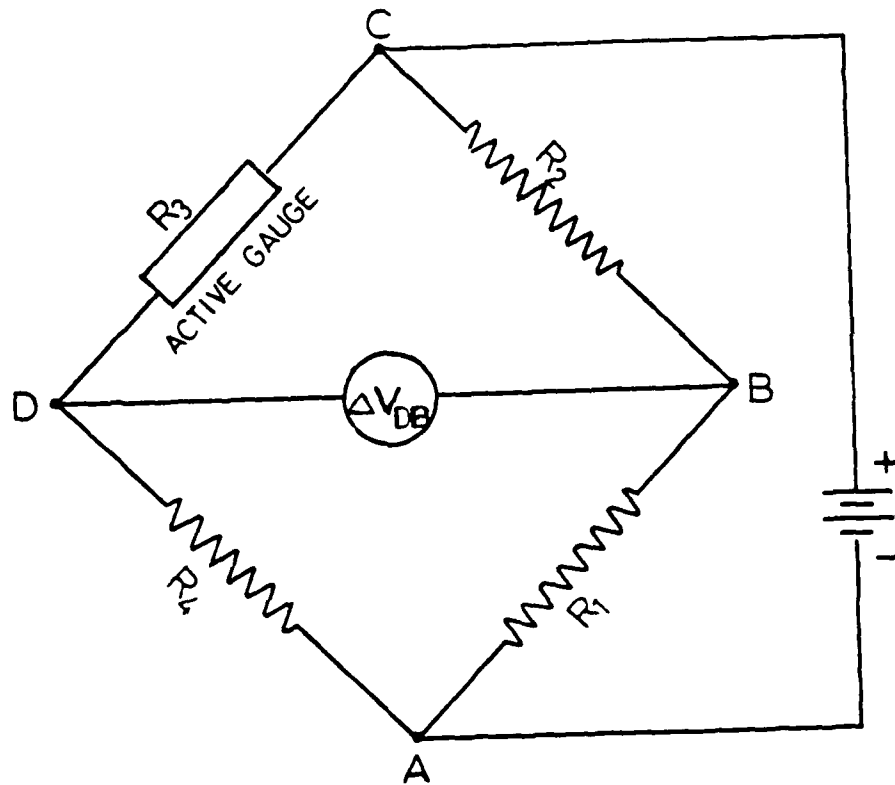


Figure 3.6 Wheatstone Bridge



Figure 3.7 Amplifier, Dummy Gauge and LVDT Signal Module Boxes



Figure 3.8 Jones' Strips on the Arm in the Centrifuge

A general purpose, 25 channel amplifier system has been built and housed in an aluminum box. To minimize the increased gravity effect on each soldering joint and, in turn on the bridge balancing, the amplifier box is mounted as close as possible to the rotating shaft in the centrifuge. The calibration of amplifier powered by  $\pm 10\text{VDC}$  is performed for each channel by measuring the same signal with and without amplification three times with the centrifuge in the stationary condition. The average ratio of amplified signal to unamplified signal is the amplification. It is assumed that operating the centrifuge will not change the amplification. The amplifications of all 25 channels are shown in Table 3.3.

#### 3.2.6 Zero Stability

Zero stability is also called no-load stability, which is essential to the accuracy of strain measurement. When the soil container with the gauged tube buried in the soil is subjected to the loads imposed by the centrifuge running at a constant angular speed, the gravitational forces applied on the tube are constant, and therefore, the cross-bridge output voltage reading should be stable.

After several trial experiments the optimum warm-up time was found to range between 30 and 40 minutes. However, due to the possibility of trapped air bubbles or the hot-spot effect in the gauge installation, perfect zero stability could never be

TABLE 3.3 - Amplification of Amplifiers

Channel Number	Amplification	Channel Number	Amplification
1	980	13	952
2	970	14	946
3	976	15	963
4	977	16	943
5	955	17	950
6	959	18	931
7	940	19	930
8	969	20	964
9	947	21	973
10	936	22	945
11	981	23	958
12	980	24	970
		25	987

achieved. Also, the drifting of signal was so erratic and irregular that it was decided that the best way to obtain accurate data was to shorten the test duration. The test duration of two cycles of loading-unloading and data recording was around four minutes for which an error in the recorded voltage output was about 10 millivolts. Compared with the actual signal output, this error indicates that good accuracy is obtained from the data acquisition.

### 3.2.7 Zero Shift

The strain states around the tube when the latter is loaded by external pressure under 50g are desired and constitute the primary data to be collected. The differences between the strain readings under 1g (no spinning) and under 50g (198 rpm) reflect the strain states of the tube caused by the soil self-weight under an increased gravitational force field. Certainly these data are useful for comparing with the analytical solution, but these readings were not reproducible because a zero shift occurred on the gauge circuits and amplifiers.

The zero shift occurs because of the gravitational effect on the electronic parts in the amplifiers and the variation in heat-sink conditions among gauges in the bridge circuit. Therefore the attempt to get the initial strain readings under the soil selfweight in the 50g gravitational force field was abandoned.

### 3.3 LVDT System

The deflections of the tube under surcharge loading are desired for comparison with the analytical solution.

Plane strain conditions should be adhered to in the centrifugal model test as closely as possible. Any end friction between the soil and the model container would violate this plane strain condition. To avoid these unknown end effects the deflection measurements were made as close as possible to the center section of the tube so that the influence of the friction on these measurements can be minimized.

Twelve LVDT's were used to measure the tube deflections from the inside. They were anchored on two hollow rings mounted on a stiff rod that ran along the center line of the tube and was mounted on the soil container at both ends. This is shown in Figure 3.9. The twelve LVDT's are oriented to measure the radial deflections of the tube as shown in Figure 3.10.

The relative position of the strain gauge section and LVDT section along the tube is shown in Figure 3.11. The wires from the LVDT's go to one end of the tube and the wires from the gauges go to the other end, such that two measuring systems can have the best location to make the proper measurements without interference.

The choice of the LVDT type is governed by two factors. First, the range and the precision, and second, the weight and volume must be considered. The units selected are the Schaevis

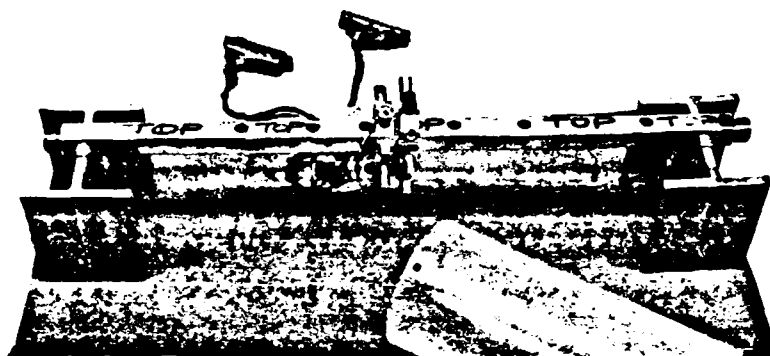


Figure 3.9 Stiff Rod with 12 LVDT's



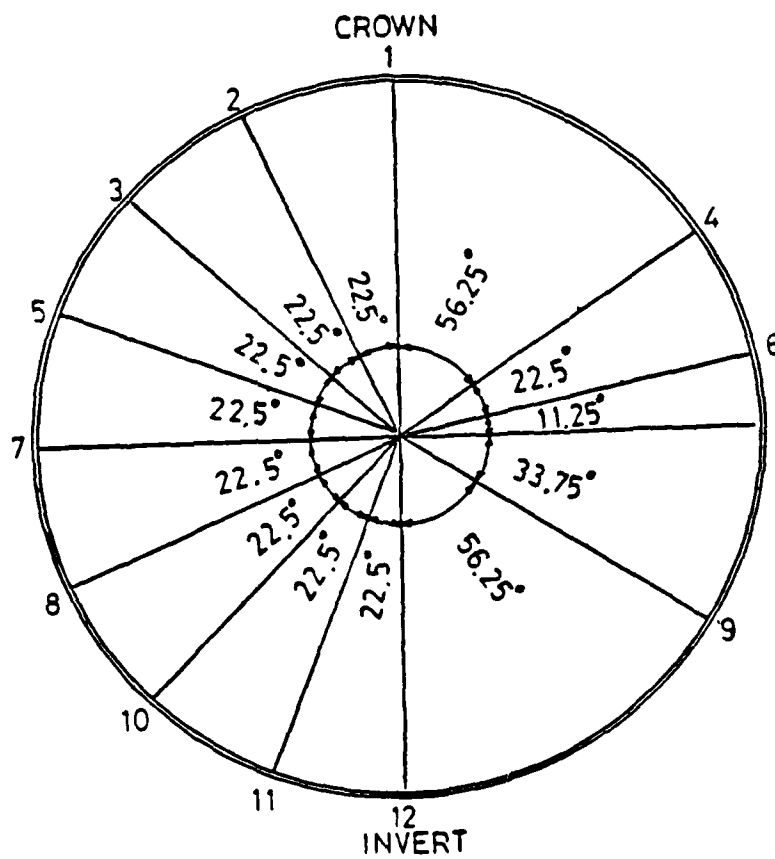
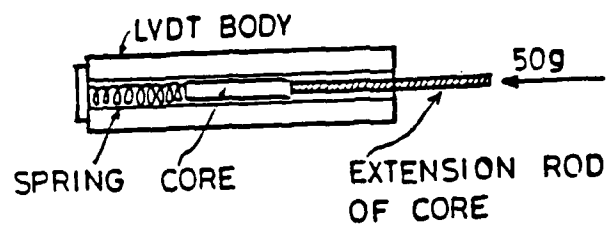


Figure 3.10 Locations of 12 LVDTs

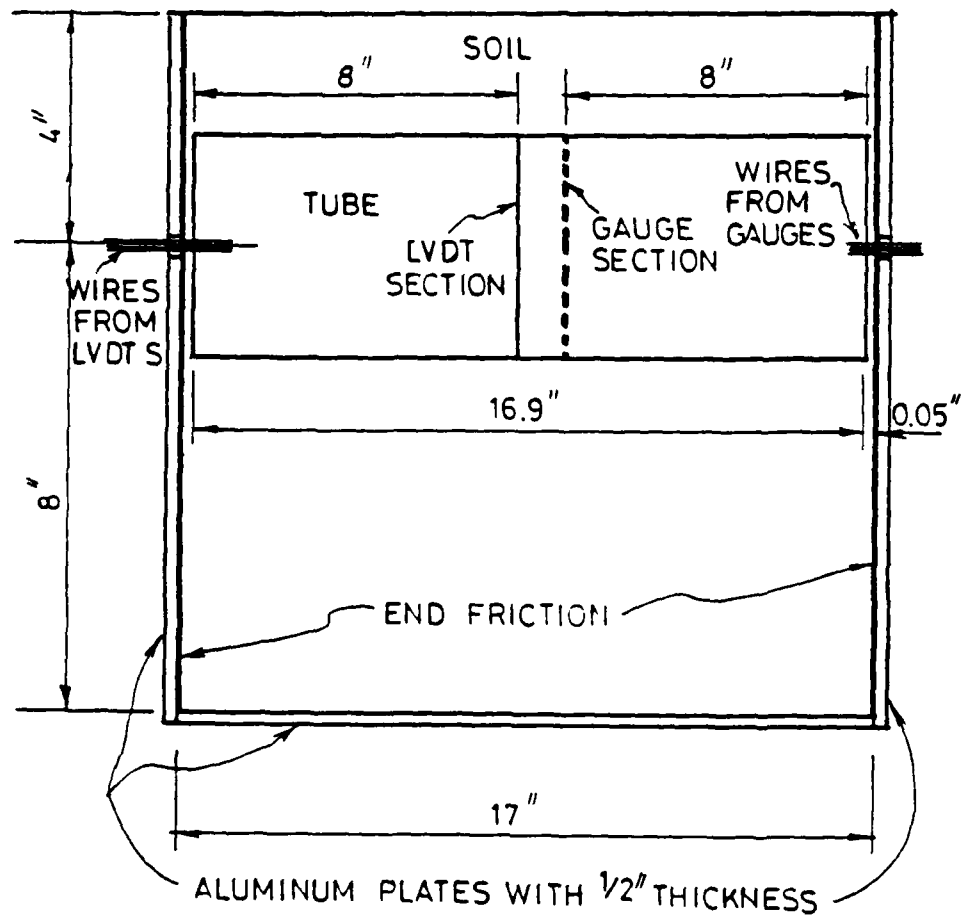


Figure 3.11 Schematic of Buried Culvert

miniature LVDT's, model 100 MHR with a  $\pm 0.100$  inch range. They were calibrated with a  $\pm 15$  VDC power supply to produce a response of 1 volt per 0.01 inch. The signal conditioning units for these LVDT's were mounted close to the rotating shaft of the centrifuge during the model test.

The radial displacements at the measurement locations are either inward or outward. The LVDT's core has to contact the tube at all times. This was accomplished by using a spring to push the LVDT core, with an extension rod in front, against the tube. The stiffness of the spring cannot be too large to contribute an extra resistance to the deflection of the tube and should not be so small that it cannot sustain the weight of the LVDT's core and extension rod under 50g as shown in Figure 3.10. By such consideration the size of eigiLOY wire used to form the spring was determined to be 0.008" in diameter. The springs were made on the lathe by simply wrapping the wire on a 1/16" diameter rod at a zero pitch. When the spring was released from the rod it would extend to its normal shape by itself.

The range of the miniature LVDT is limited to  $\pm 0.1$ ". In order to utilize the whole range and to maintain the LVDT operating within this range in monitoring the tube deflections which may vary around the tube, the position of the LVDT core must be preset by adjusting the length of the extension rod attached to it. The proper setting was determined by trial and error.

### 3.4 Data Acquisition System and Polarity Check

The twelve LVDT signals and twenty-two strain gauge signals were passed through the slip rings and taken to the control panel. Then these signals were transmitted to a Hewlett-Packard Data Acquisition System, HP3597A, which is monitored by a HP9825B computer. This is shown in Figure 3.12.

To make sure that the correct data were recorded, it was essential to perform a polarity check on the strain gauges and LVDT's through the data acquisition system. By bending a flexible plate on which a single gauge was glued, compression or tension was generated and the associated signal was checked. Similarly by translating the core inward or outward the sign of the LVDT signal was checked. The results are shown in Table 3.4.

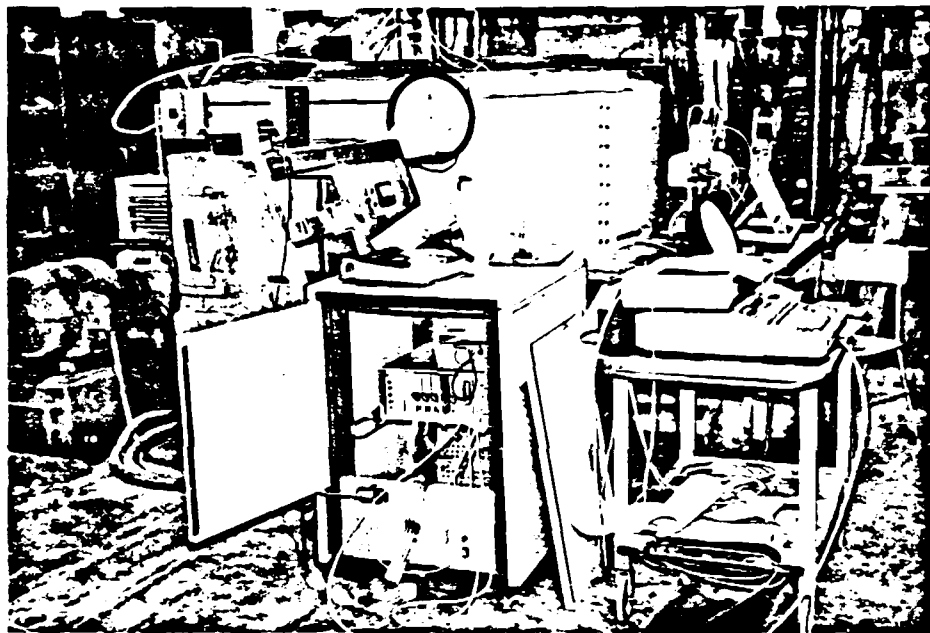
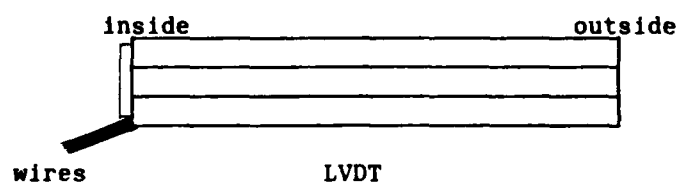


Figure 3.12 Data Acquisition and Computer System

TABLE 3.4 - Sign Convention of Strain Gauge and LVDT

Cross-bridge voltage output	gauge's strain	sign
$\Delta V_{DB} < 0$	tension	+
$\Delta V_{DB} > 0$	compression	-



Core Position	LVDT Voltage output
inside	+
outside	-

### 3.5 Line Load Test

Although the strain gauges were selected and installed carefully and the repeated zero-load stability and polarity tests indicated that all the strain gauges were in fair condition, it would still be advisable to double check the exact performance of gauges through comparison with a known situation. For this purpose, a line load test was performed on the instrumented tube. This loading situation was chosen because a closed form solution is available from the theory of elasticity.

The test procedure is described as follows. The gauged tube was laid on a flat platform and was loaded vertically through a  $\frac{1}{2}$ " diameter steel rod which ran the whole length of the tube and was clamped to the tube tightly at both ends to simulate the line force reaction as shown in Figure 3.13. The load consisted of metal plates about the length of the tube and was placed on top of the tube. Strain readings were taken after each increment of load. Typical test results are shown in Figure 3.14, and are compared with the analytical solution of thin ring under diametrical loading as shown in Figure 3.15. The agreement was excellent except that a slightly larger moment was measured at the crown. This may be caused by the imperfection of line load at the top of the tube. Elastic behavior of the tube was observed throughout these line load tests. Therefore, the performance of the gauges is considered to be satisfactory.

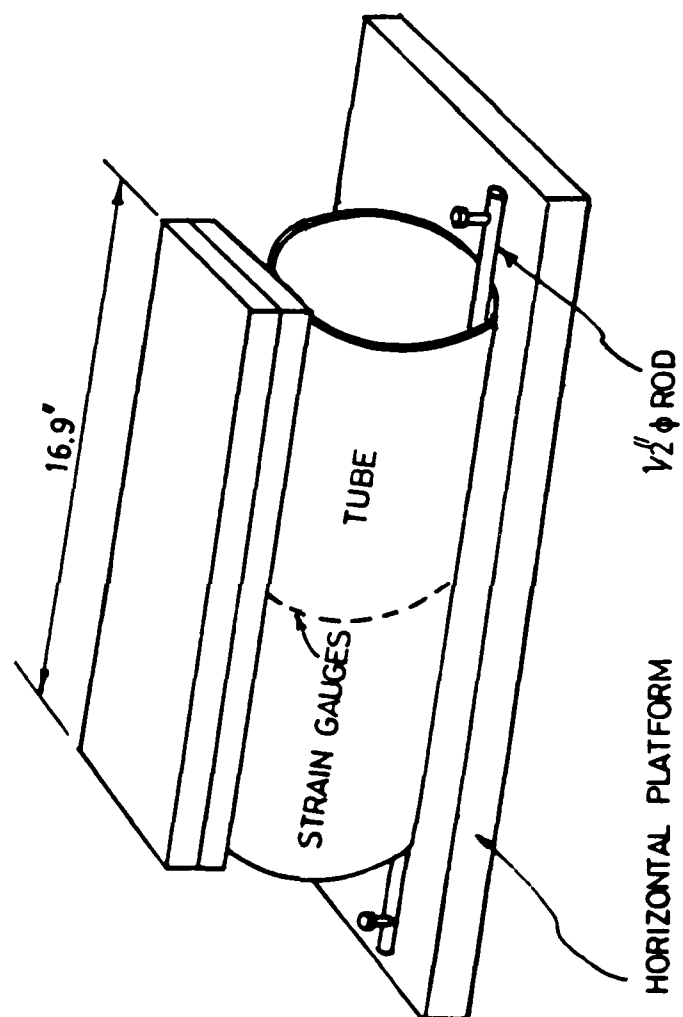


Figure 3.13 Schematic of Line Load Test



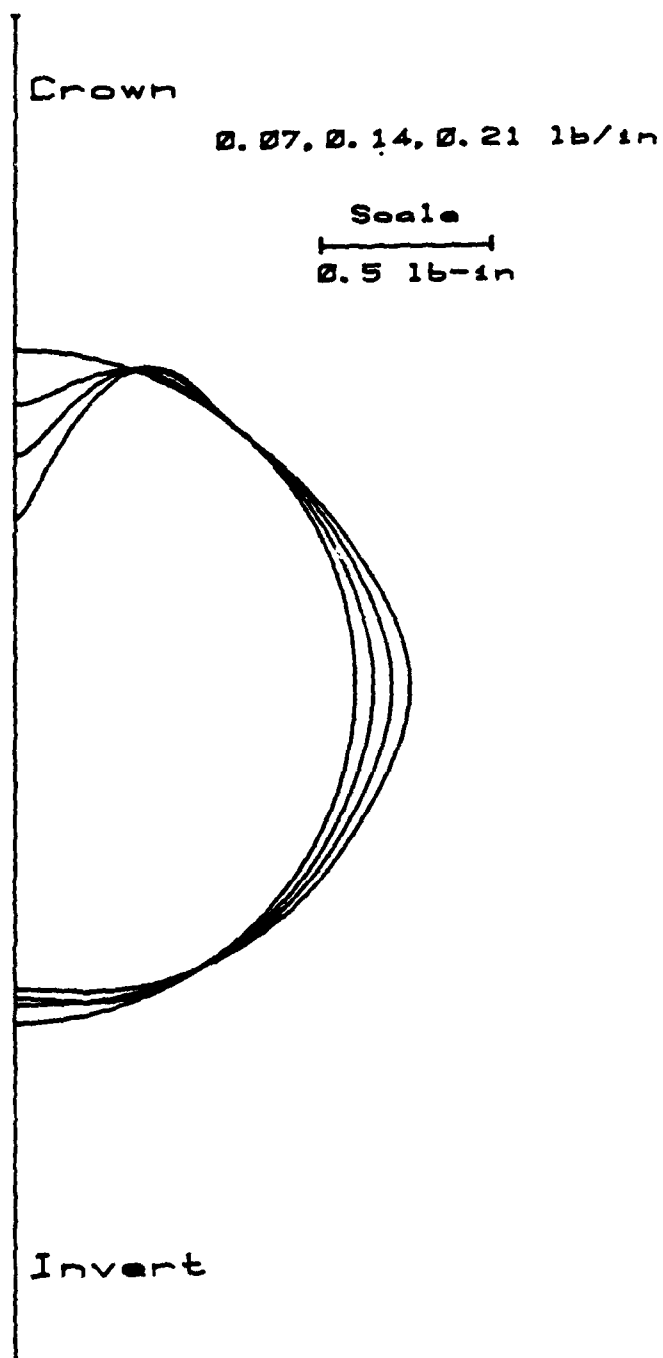


Figure 3.14 Moment Diagram in Line Load Test

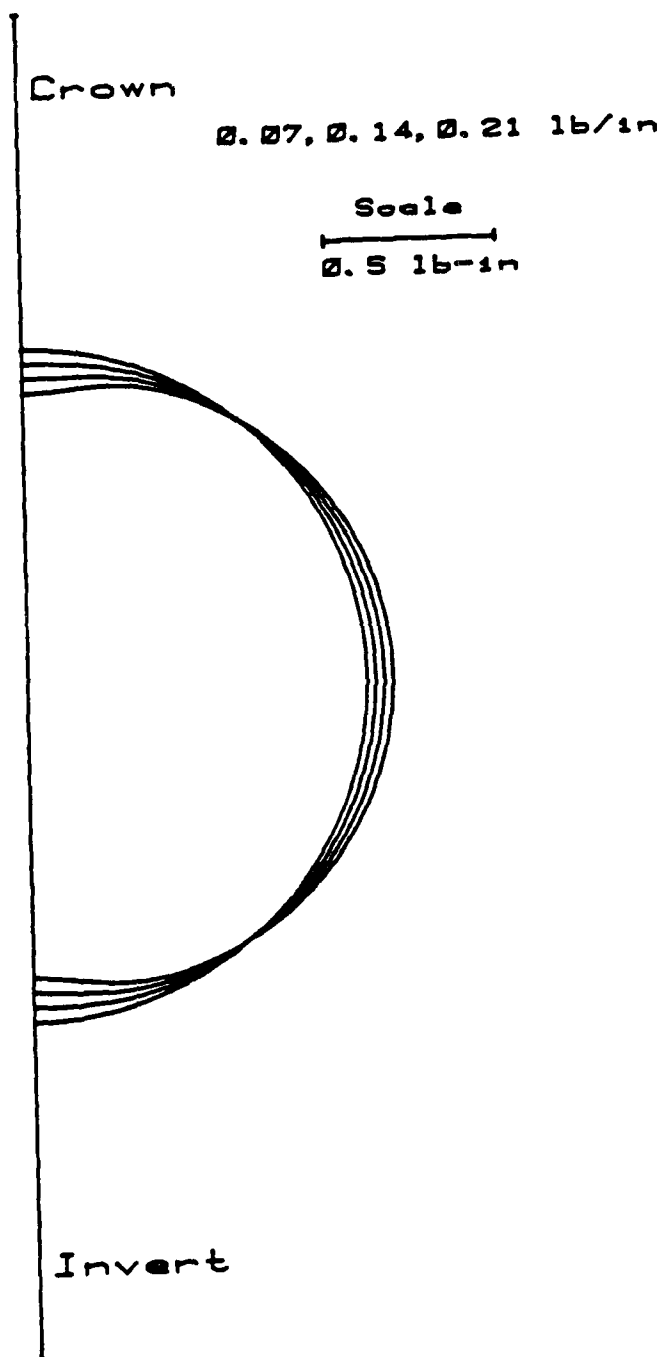


Figure 3.15 Analytical Solution of Thin Ring

### 3.6 Soil Container

The container in which the soil-culvert interaction problem was simulated was placed in the sample basket of the centrifuge as shown in Figure 3.1. The container consists of two rectangular boxes made of 0.5 inch thick aluminum plates with four half-circular openings shown in Figure 3.16. After the completion of compaction in both boxes (to be assembled later), two half-circular trenches were cut out. The gauged tube was placed in the lower trench before the two boxes were assembled together. With this technique the uniform soil density around the tube was maintained. The loading apparatus was mounted on the top surface of soil to apply the surface loading.

### 3.7 Loading Apparatus

The loading apparatus consists of three parts, a, b and c, as shown in Figure 3.17. A silicone rubber membrane is compressed by part b and c by tightening the assembly screws. Compressed air supplied through the 1/8" NPT fitting inflates the membrane to apply the pressure on the soil surface and causes the deflection of the tube. The width of the effective loading area is 2.9 inches. This loading apparatus can be positioned at several locations on the soil surface for the symmetrical and unsymmetrical cases. Through minor modifications the same apparatus was used as the mold for making the silicone rubber membrane.

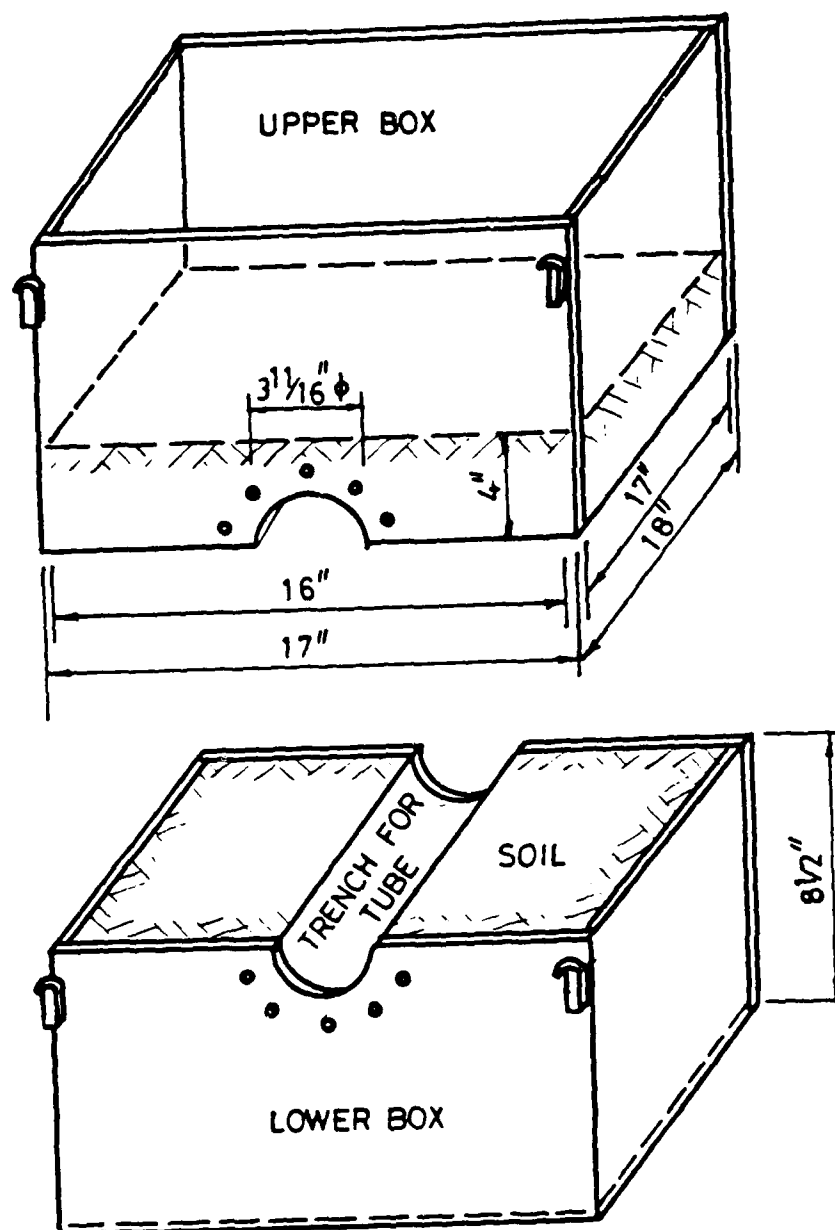


Figure 3.16 Schematic of Two Soil Boxes

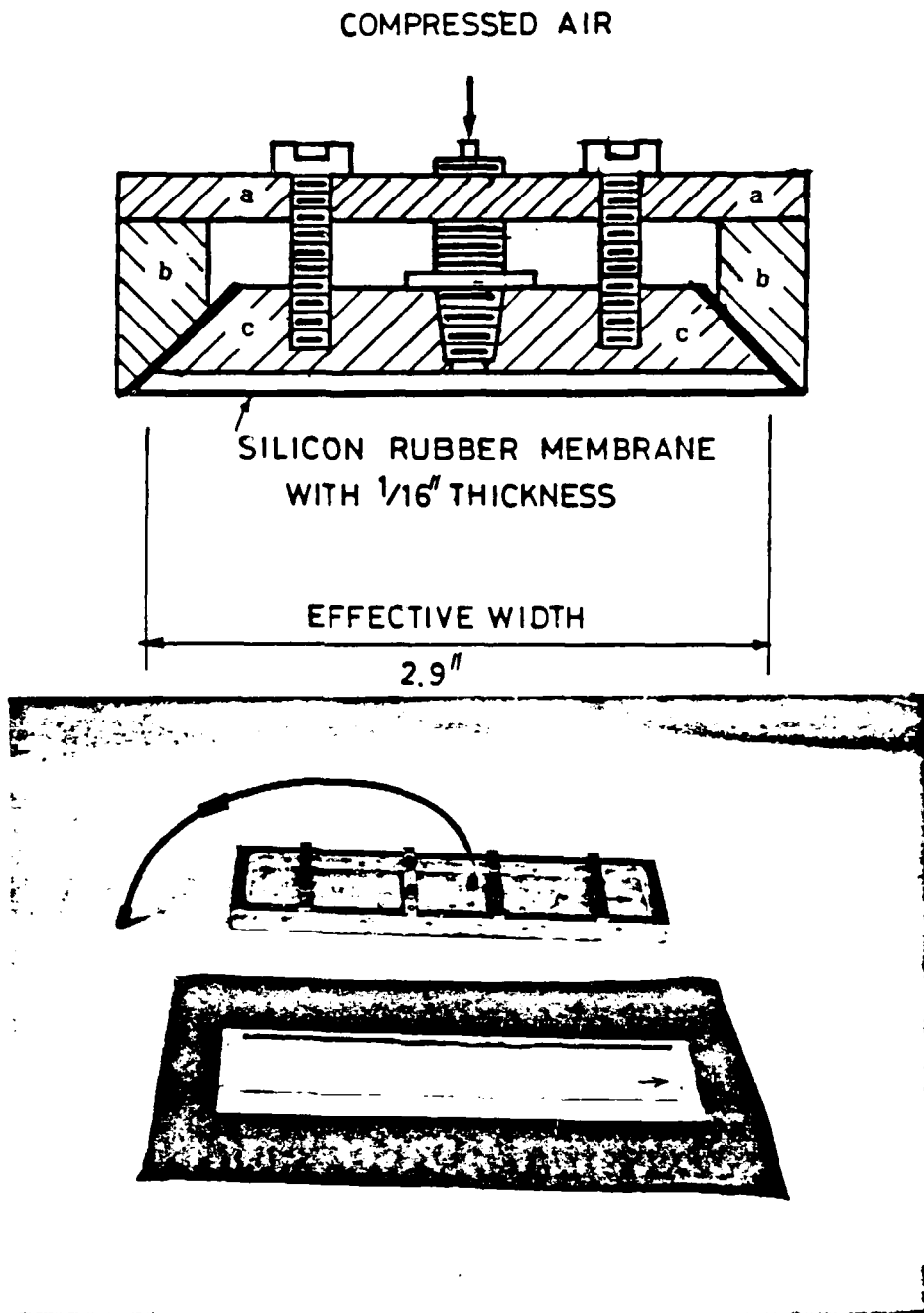


Figure 3.17 Loading Apparatus

### 3.8 Model Preparation

The procedure for soil preparation, compaction, trench making, and the assemblage is described in the following steps:

(1) Weigh twenty-four units of oven-dried soil and spread them individually on plates to cool down, as shown in Figure 3.18. The weight of each unit is governed by the density of the soil to be achieved by compaction.

(2) Mix the dry soil with the proper amount of distilled water calculated to produce 10.8% of moisture content, as shown in Figure 3.19.

(3) Store the mixed wet soil unit for one day in a can whose inner surface is coated with wax to prevent the loss of moisture, as shown in Figure 3.20.

(4) Compact the soil in the lower container box in sixteen layers and in the top box in eight layers with 0.5 inch thickness for each layer as shown in Figure 3.21. The under compaction technique (Ladd, 1978) was used to achieve a uniform density throughout the depth of soil. The compaction of the last layer should stop when the soil surface is flush with the top surface of the container. The average compaction effort for each layer is listed in Table 3.5.

(5) Trim any extra soil away with a very flat cutter to have the top surfaces of soil and box co-planed, see Figure 3.22.



Figure 3.18 Oven Dried Soil is Cooling Off

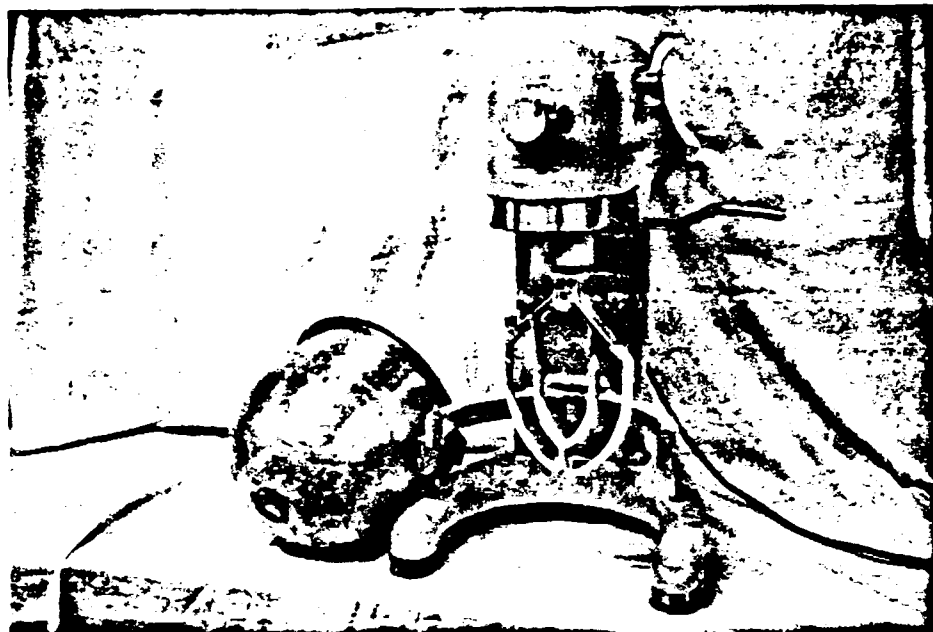


Figure 3.19 Mixing Equipment





Figure 3.20 Waxed Cans



Figure 3.21 Soil Compaction on the Press Machine

TABLE 3.5 - Average Compaction Effort for Centrifuge Soil Model

T o p  C o n t a i n e r	Layer Order	Vertical Pressure (psi)
	1	68
	2	83
	3	81
	4	79
	5	76
	6	71
	7	64
	8	63

B o t t o m  C o n t a i n e r	Layer Order	Vertical Pressure (psi)
	16	59
	15	60
	14	60
	13	61
	12	60
	11	64
	10	66
	9	63
	8	65
	7	67
	6	74
	5	70
	4	66
	3	65
	2	71
	1	58

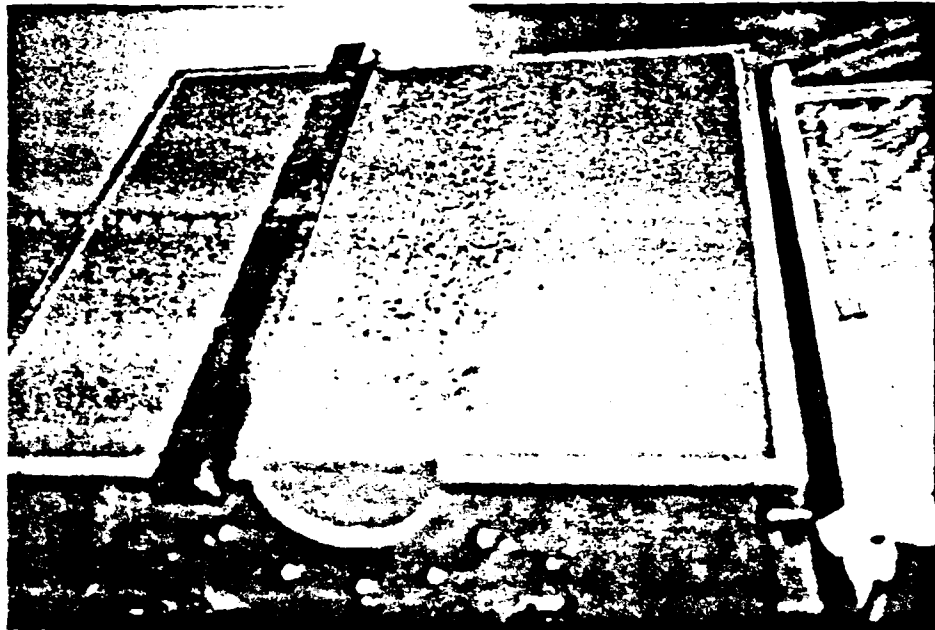


Figure 3.22 A Flat Cutter to Trim Extra Soil Away

(6) Cut a half-circular trench from each box. First, a rough cutting was made by the device shown in Figure 3.23. Second, a precise cutting was made by the device shown in Figure 3.24. The cutter could slide along the rod and rotate with the rod around the adapters which were fitted at the center of the circular plates that were mounted on the end wall of the soil box. With this technique the exact size and location of the trench could be reproducible from test to test. Figure 3.25 shows the final result of the cutting. The distinct edges and the smooth surface in the trench fully demonstrate the high quality of this trench cutting technique.

(7) Place the gauged tube in the trench at the lower soil box with the right orientation after a band of soil at the longitudinal section where the strain gauges were located was removed. Then the top soil box was placed on top of the lower box.

(8) Place the LVDT cores into matched LVDT bodies mounted on the stiff rod. This stiff rod with 12 LVDT's was inserted into the tube and each core was pushed against the tube by the spring in the LVDT body. Both ends of this stiff rod were anchored at the center of the circular plates which connected the two soil boxes into one soil container. The leadwires from strain gauges and LVDTs passed through the opening separately at each end.

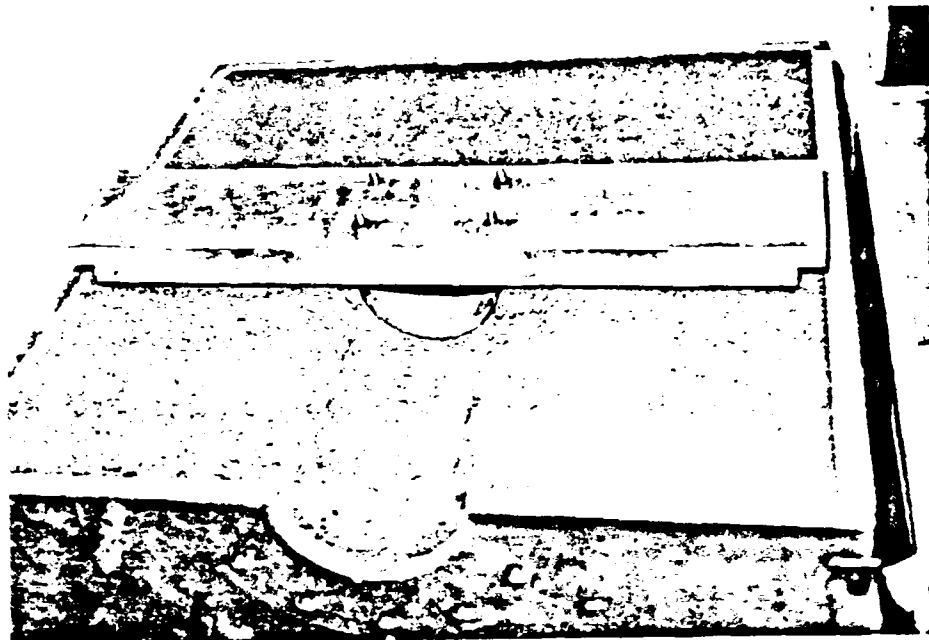


Figure 3.23 Trench Cutter for Rough Shape

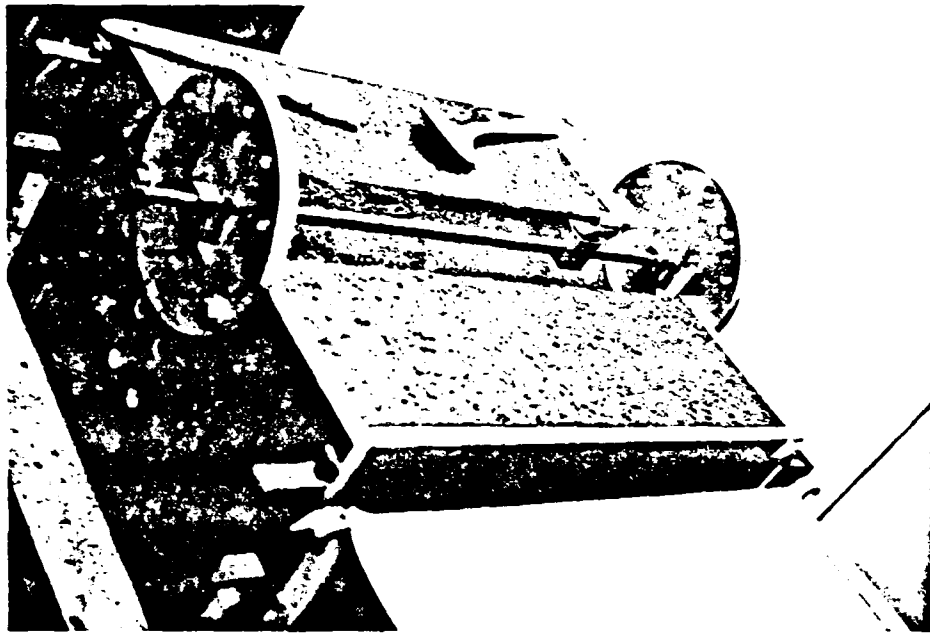


Figure 3.24 Trench Cutter for Precise Shape

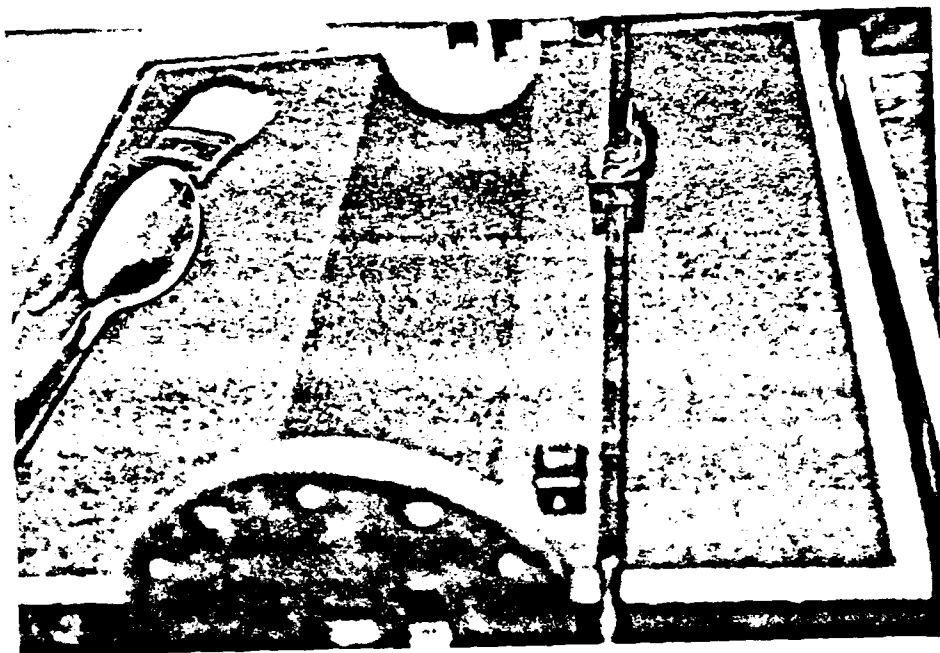


Figure 3.25 The Completed Trench



(9) Place the loading apparatus on the soil surface and fix it at both ends against the wall of the soil container. The uncovered soil surface was covered by two plastic sheets which were taped against the container wall so that the soil would not dry up when it was spun in the centrifuge. Figure 3.26 shows the final product of assembly.

The soil container was moved into the centrifuge and made ready for the test.

(10) After the centrifuge test, the soil was dug out and placed in a big pan to air dry. Then a crusher adjusted to have the right size of opening was used to breakup the soil crumb. This recycling equipment is shown in Figure 3.27.

This completes the preparation of one test.

### 3.9 Test Procedure

The test procedure used in each centrifuge test is described in the following:

(1) The soil container was assembled in the sample basket with the LVDT leadwires facing outside.

(2) The connector from LVDT leadwires was plugged into the connector leading to the signal conditioning modules. After the power was on, all the output signals were checked for loose



Figure 3.26 The Completed Assembly

AD-A172 482

CENTRIFUGAL AND ANALYTICAL MODELING OF A BURIED  
FLEXIBLE CONDUIT (U) COLORADO UNIV AT BOULDER DEPT OF  
CIVIL ENVIRONMENTAL AND ARCH J C NT 31 OCT 85

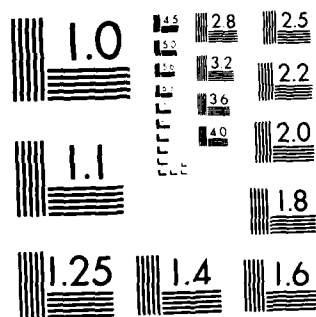
2/3

UNCLASSIFIED

AFOSR-TR-86-0850 AFOSR-84-0300

F/G 13/13

NL



CROCOPY RESOLUTION TEST CHART  
NATIONAL BUREAU OF STANDARDS 1963 A

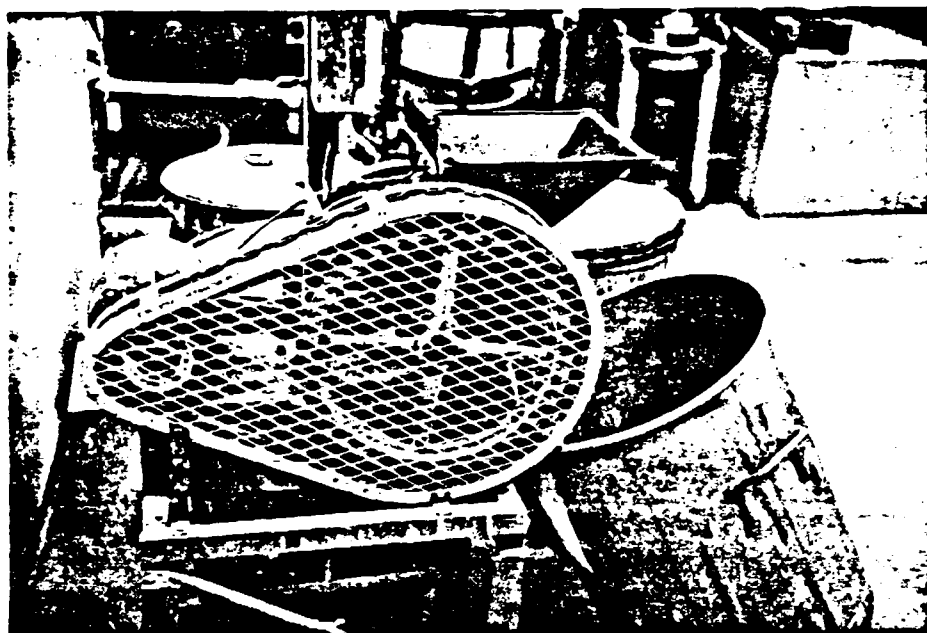


Figure 3.27 Soil Crusher

wires. The initial readings of all LVDTs were compared with the preset reading in Section 3.3.2 to make sure the starting position of each LVDT core was satisfactory.

(3) Connect all the gauge leads to the ordered Jones Strips which lead to the dummy gauge box. Power was then turned on. When all the bridges were balanced and the readings found to locate within the effective range, the power was turned off to avoid overheating. The Jones Strips were wrapped with plastic sheet to keep the exposed wires and posts from the fluctuating temperature during spinning as shown in Figure 3.8. This enhanced the zero stability of all bridges.

(4) The polyflo tubing leading to the loading apparatus was connected to one of the hydraulic lines, so that the compressed air supplied through the hydraulic rotary joint would pressurize the rubber membrane to generate the surface loading. Outside the centrifuge, the same pressure line was connected to a pressure regulator and a pressure gauge.

(5) The data acquisition system was connected to the front control panel. The signals from the gauges and the LVDT's were checked for polarity.

(6) With both baskets being locked in the in-flight position, weights were put in the counterweight basket until the centrifugal arm was leveled. After the arm was locked, the baskets were let down.

(7) Turn on the power for gauges and LVDTs and monitor for one-half hour. When stable gauge readings were observed, data recording under 1 g condition was performed. The centrifuge was then spun up slowly to minimize the undesirable tangential acceleration, taking 6 minutes to go from 0 to 198 rpm.

(8) When a speed of 198 rpm was reached, data recording was executed once.

(9) Incremental pressure of 10 psi was quickly applied and was followed by the data recording. It took about 15 seconds for each step of load. Two cycles of loading to a maximum pressure of 40 psi and unloading were performed within 4 minutes.

(10) The last set of data was recorded after the centrifuge was stopped.

(11) All the data were printed out and sorted, any indication of out of balance or abnormal signal was written down. Based on this, the correcting procedure was set up in the centrifuge.

(12) After the correction in the centrifuge, the soil container was released and disassembled. The gauges on the tube were checked by an Ohmmeter to see if there was any physical damage or significant increase in resistance on the gauges. All the cores and springs for LVDTs were collected for reuse in the future.

### 3.10 Centrifuge Test Results

After going through zero stability, zero shift and polarity checks in the centrifuge, two series of centrifugal tests on buried culvert were conducted. In the first series test, a uniform strip loading (Figure 3.17) was applied on the ground surface through the loading apparatus which was positioned symmetrically above the center line of the culvert. In the second series test, the uniform loading was shifted to one side so that the edge of this strip loading coincided with the center line, i.e., unsymmetrical loading case. The rest of the soil-culvert system and the test procedure were exactly the same in those two series tests. The testing continued until at least three repeatable test results were obtained in each series. The test results in terms of the strains, deflections, hoop stresses and bending moments in each series test are listed in Appendix A.

The hoop stresses,  $\sigma_h$ , and the bending moments,  $M$ , induced in the pipe walls with the linear elastic material law by a plane strain loading can be calculated from the measured strains using the following relations:

$$\sigma_h = \frac{1-\nu}{(1+\nu)(1-2\nu)} \cdot \frac{(\epsilon_0 + \epsilon_1) E}{2} \quad (3.2)$$

$$M = \frac{1-\nu}{(1+\nu)(1-2\nu)} \cdot \frac{(\epsilon_0 - \epsilon_1) E t^2}{12} \quad (3.3)$$



where  $E$  = Young's modulus of the culvert material  
 $\nu$  = Poisson's ratio of the culvert material  
 $t$  = thickness of culvert wall  
 $\epsilon_0$  = circumferential strain measured from the gauge on  
the external face of the culvert  
 $\epsilon_1$  = circumferential strain measured from the gauge on  
the internal face of the culvert

Due to the symmetry, the test results in the first series were plotted on one half of the tube. Figure 3.28 shows the deflected shape of the culvert under 10, 20, 30 and 40 psi surface loading. The largest inward deflection is located at the crown where the pressure-deflection relation is plotted in Figure 3.29. The largest outward deflection is located at the springline where the pressure-deflection behavior is shown in Figure 3.30. The hoop stresses are demonstrated in Figure 3.31 with the compressive stresses being plotted inside the half circle. The bending moments which cause the sagging of the culvert are plotted inside the half circle and the hogging moments are plotted outside as shown in Figure 3.32.

In the second series test, the gauged culvert was accidentally overloaded to cause buckling failure. A spare culvert without strain gauges was used to continue the test. Therefore, only the deflected shapes of the culvert were available and are shown in Figure 3.33.

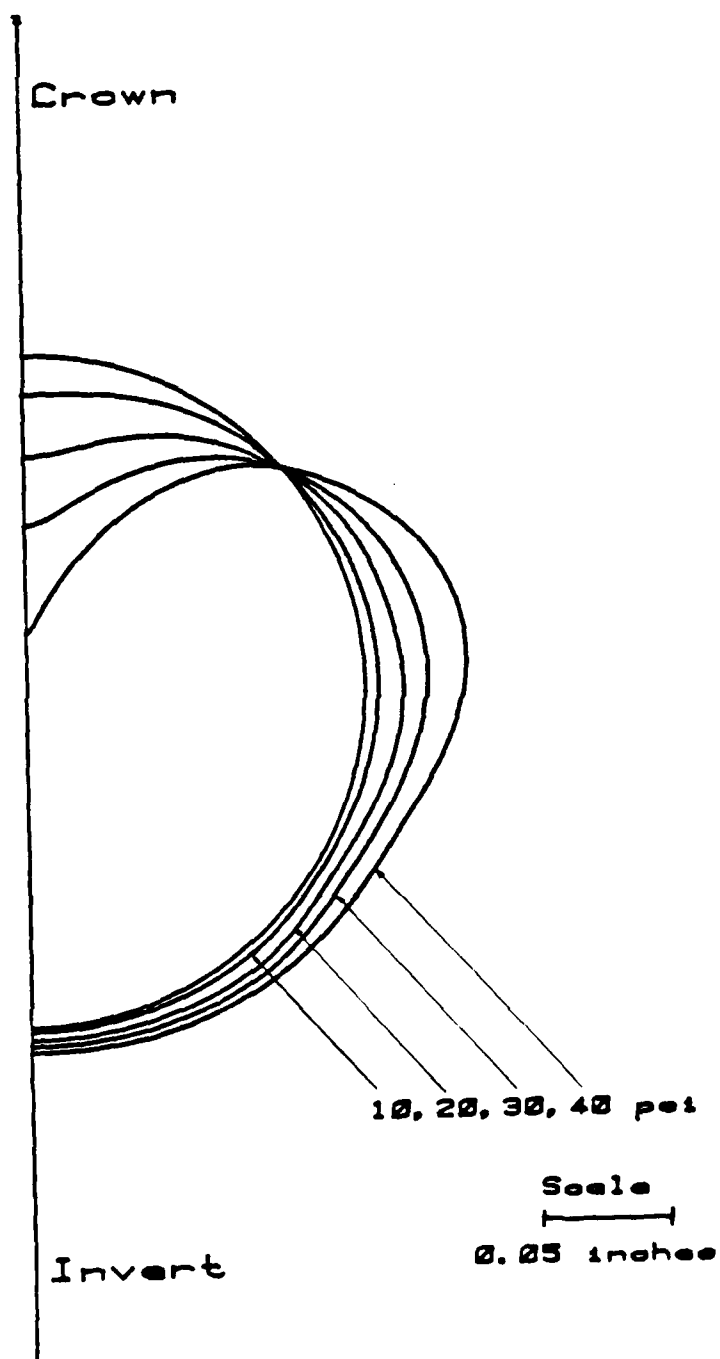


Figure 3.28 Deflected Culvert Under Symmetrical Loading

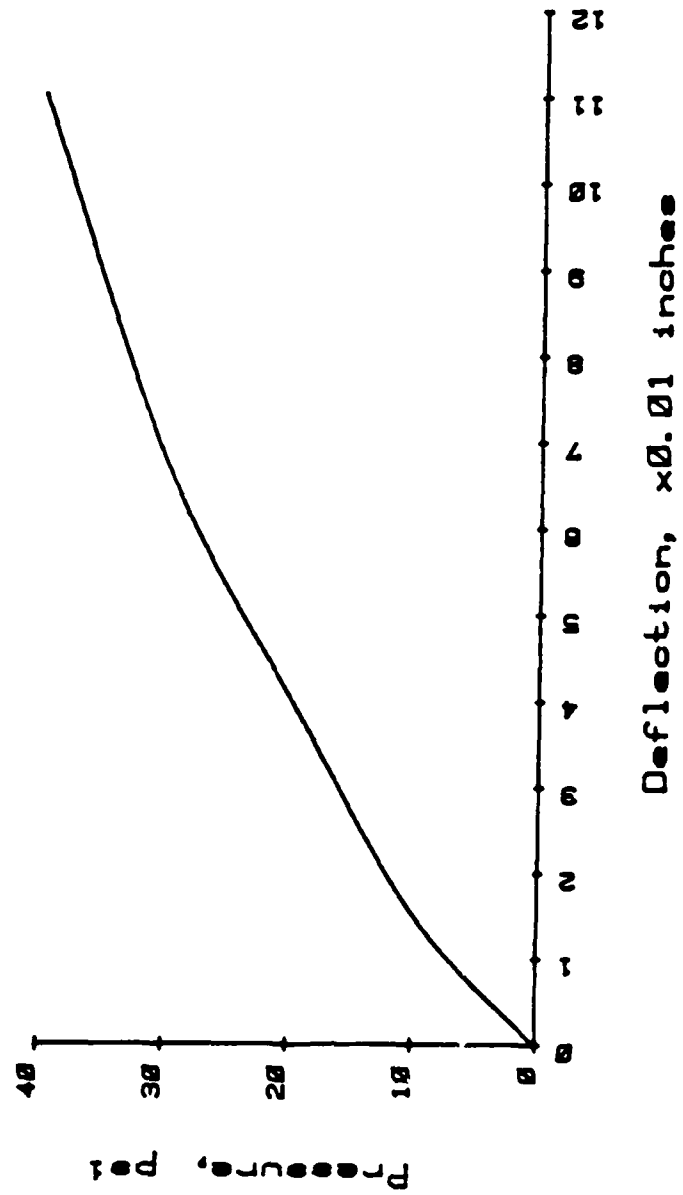


Figure 3.29 Deflection at Crown Under Symmetrical Loading .

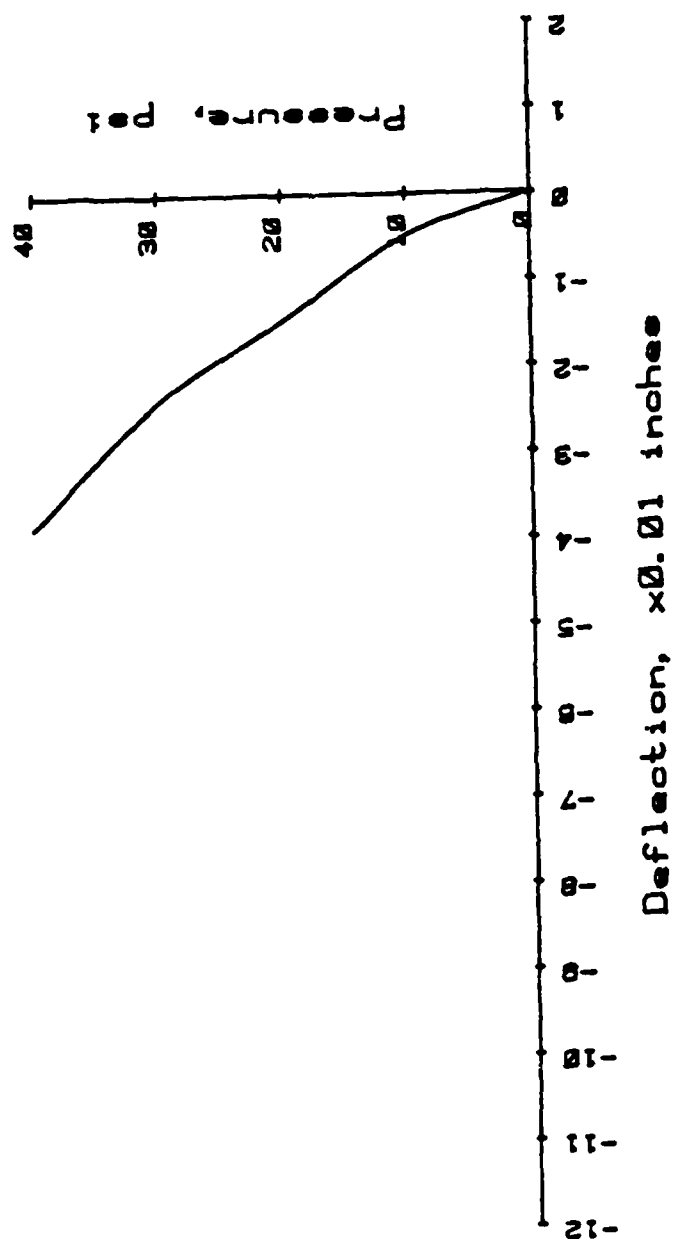


Figure 3.30 Deflection at Springline Under Symmetrical Loading

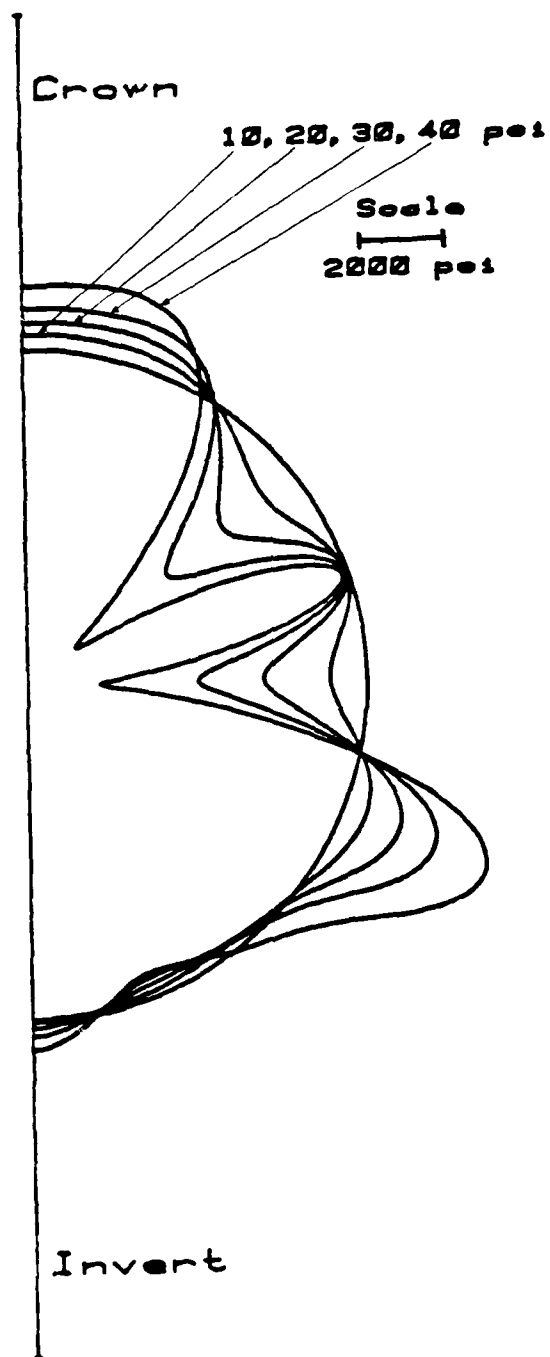


Figure 3.31 Hoop Stresses Under Symmetrical Loading



Figure 3.32 Bending Moments Under Symmetrical Loading

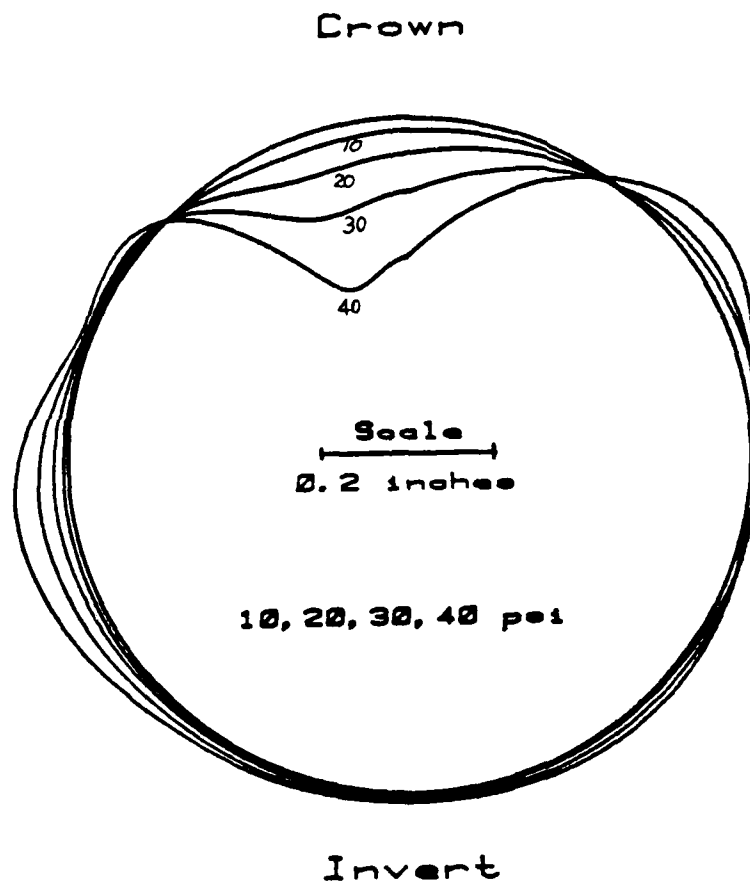


Figure 3.33 Deflected Culvert Under Unsymmetrical Loading

## CHAPTER IV

### CONSTITUTIVE RELATIONS

#### 4.1 General

The constitutive relations of soil and culvert used in the finite element analysis are described herein. The stress-strain relations of aluminum can be accurately described by isotropic linear elasticity until the yield stress is reached. Since the stress state in the culvert is maintained below the yield stress throughout the model test, isotropic linear elasticity is a good choice as the material law for the aluminum culvert. On the other hand soil is probably the most difficult material the civil engineer has to deal with, due to the dependency of its properties on the stress-strain history, stress path, density, water content, etc. In general, these features produce such physical behaviors as nonlinearity, inelasticity, anisotropy and time-dependency. The up-to-date development of constitutive laws for soil can be founded in the review paper presented by Ko and Sture (1980). The important ingredient to connect the equilibrium and compatibility conditions is the stress-strain law, including the failure condition. The soil deformation from its initial stress-strain state through failure and beyond can be predicted accurately provided that the stress-strain-strength behavior is modeled correctly. In



this work three models are adopted to examine their individual capability in modeling the soil-structure interaction of a culvert system. They are 1) isotropic linear elastic stress-strain relation, 2) hyperbolic stress-strain relation, and 3) Lade's elastoplastic relation.

## 4.2 Isotropic Linear Elastic Stress-Strain Relation

### 4.2.1 General Description

This relation is also named as generalized Hooke's Law for the three-dimensional case, whereas Hooke's Law is used for uniaxial state of stress and strain. This three-dimensional linear elasticity can be written as:

$$\sigma_{ij} = C_{ijkl} \epsilon_{kl} \quad (4.1)$$

in which  $\sigma_{ij}$  and  $\epsilon_{kl}$  are second order tensors and  $C_{ijkl}$  is a fourth order tensor with 81 constants. Since both  $\sigma_{ij}$  and  $\epsilon_{kl}$  are symmetrical, one has the following symmetrical conditions:

$$C_{ijkl} = C_{jikl} = C_{ijlk} = C_{jilk} \quad (4.2)$$

Hence the maximum number of independent constants is reduced to 36. Further, if we specify isotropic symmetry, that is the properties along any direction are identical, then the number of independent constants is reduced to two. There are several combinations of these two constants. See for instance Chen and Saleeb, 1982, p. 155. The most commonly used combination consists of Young's modulus,  $E$  and the Poisson's ratio,  $\nu$ .

The stress-strain relation can be expressed in matrix forms. These forms are suitable for use in solutions by the finite element method. In matrix form equation 4.1 is expressed as follows:

$$\begin{Bmatrix} \sigma_x \\ \sigma_y \\ \sigma_z \\ \tau_{xy} \\ \tau_{yz} \\ \tau_{zx} \end{Bmatrix} = \frac{E}{(1+\nu)(1-2\nu)} \begin{bmatrix} 1-\nu & \nu & \nu & 0 & 0 & 0 \\ \nu & 1-\nu & \nu & 0 & 0 & 0 \\ \nu & \nu & 1-\nu & 0 & 0 & 0 \\ 0 & 0 & 0 & \frac{1-2\nu}{2} & 0 & 0 \\ 0 & 0 & 0 & 0 & \frac{1-2\nu}{2} & 0 \\ 0 & 0 & 0 & 0 & 0 & \frac{1-2\nu}{2} \end{bmatrix} \begin{Bmatrix} \epsilon_x \\ \epsilon_y \\ \epsilon_z \\ \gamma_{xy} \\ \gamma_{yz} \\ \gamma_{zx} \end{Bmatrix} \quad (4.3)$$

or

$$\begin{Bmatrix} \epsilon_x \\ \epsilon_y \\ \epsilon_z \\ \gamma_{xy} \\ \gamma_{yz} \\ \gamma_{zx} \end{Bmatrix} = \frac{1}{E} \begin{bmatrix} 1 & -\nu & -\nu & 0 & 0 & 0 \\ -\nu & 1 & -\nu & 0 & 0 & 0 \\ -\nu & -\nu & 1 & 0 & 0 & 0 \\ 0 & 0 & 0 & 2(1+\nu) & 0 & 0 \\ 0 & 0 & 0 & 0 & 2(1+\nu) & 0 \\ 0 & 0 & 0 & 0 & 0 & 2(1+\nu) \end{bmatrix} \begin{Bmatrix} \sigma_x \\ \sigma_y \\ \sigma_z \\ \tau_{xy} \\ \tau_{yz} \\ \tau_{zx} \end{Bmatrix} \quad (4.4)$$

Plane strain conditions in the xy plane ( $\epsilon_z = \gamma_{yz} = \gamma_{zx} = 0$ ) are assumed in the present finite element analyses. By deleting three columns and three rows associated with  $\epsilon_z$ ,  $\gamma_{yz}$  and  $\gamma_{zx}$  from equation 4.3 the resulting stress-strain equations can be written as:

$$\begin{Bmatrix} \sigma_x \\ \sigma_y \\ \tau_{xy} \end{Bmatrix} = \frac{E}{(1+\nu)(1-2\nu)} \begin{bmatrix} 1-\nu & \nu & 0 \\ \nu & 1-\nu & 0 \\ 0 & 0 & \frac{1-2\nu}{2} \end{bmatrix} \begin{Bmatrix} \epsilon_x \\ \epsilon_y \\ \gamma_{xy} \end{Bmatrix} \quad (4.5)$$

The strain-stress equations cannot be obtained simply by deletion from equation 4.4. This is because  $\sigma_z \neq 0$  although  $\tau_{yz} = \tau_{zx} = 0$ . Instead, they can be found by inverting the relation of equation 4.5.

$$\begin{Bmatrix} \epsilon_x \\ \epsilon_y \\ \gamma_{xy} \end{Bmatrix} = \frac{1+\nu}{E} \begin{bmatrix} 1-\nu & -\nu & 0 \\ -\nu & 1-\nu & 0 \\ 0 & 0 & 2 \end{bmatrix} \begin{Bmatrix} \sigma_x \\ \sigma_y \\ \tau_{xy} \end{Bmatrix} \quad (4.6)$$

By manipulating equations 4.3 and 4.6 with  $\epsilon_z = 0$  it can be shown that

$$\sigma_z = \nu(\sigma_x + \sigma_y) \quad (4.7)$$

Equations 4.5 and 4.7 are used in the displacement based finite element code to form the stiffness matrix and find the stress state. To define these equations for soil and an aluminum culvert it is necessary to find the two parameters,  $E$  and  $\nu$ , through laboratory experiments.

#### 4.2.2 Parameter Evaluation of Soil

A series of conventional triaxial CTC tests were performed for parameter evaluation. The results are shown in Chapter II.

In the CTC test  $\sigma_1 > \sigma_2 = \sigma_3$ . From equation 4.4

$$\epsilon_1 = \frac{1}{E} (\sigma_1 - 2\nu\sigma_3) = \frac{\sigma_1 - \sigma_3}{E} + \frac{1-2\nu}{E}\sigma_3 \quad (4.8)$$

where  $\sigma_3$  is a constant.

By differentiating equation 4.8 the following equation can be obtained

$$\frac{d(\sigma_1 - \sigma_3)}{d\epsilon_1} = E \quad (4.9)$$

In the CTC test, the volumetric strain can be expressed as  $\epsilon_v = (1-2\nu)\epsilon_1$ . The slope of  $\epsilon_v$  vs  $\epsilon_1$  at the origin is  $1-2\nu$  and is evaluated for each confining pressure. The average value of  $1-2\nu$  can be obtained. The Young's modulus is the slope of the deviator stress-strain curve and it varies with the axial strain,  $\epsilon_1$ , and the confining pressure,  $\sigma_3$ . Therefore the constant values chosen for  $E$  and  $\nu$  have to be averaged over these variations. In this work the following values are chosen

$$E = 2500 \text{ psi} \quad (4.10)$$

$$\nu = 0.3 \quad (4.11)$$

#### 4.2.3 Prediction of Triaxial Test

From equations 4.4, 4.10 and 4.11 the analytical prediction of CTC test results can be obtained. Figures 4.1a and 4.1b show the comparison between the laboratory results and the prediction from isotropic linear elastic stress-strain relation. The poor agreement is attributed to the constant modulus and Poisson's ratio and the simple stress-strain relations. Therefore, the nonlinearity of volume change and stress-strain relation and dilatancy cannot be modeled.

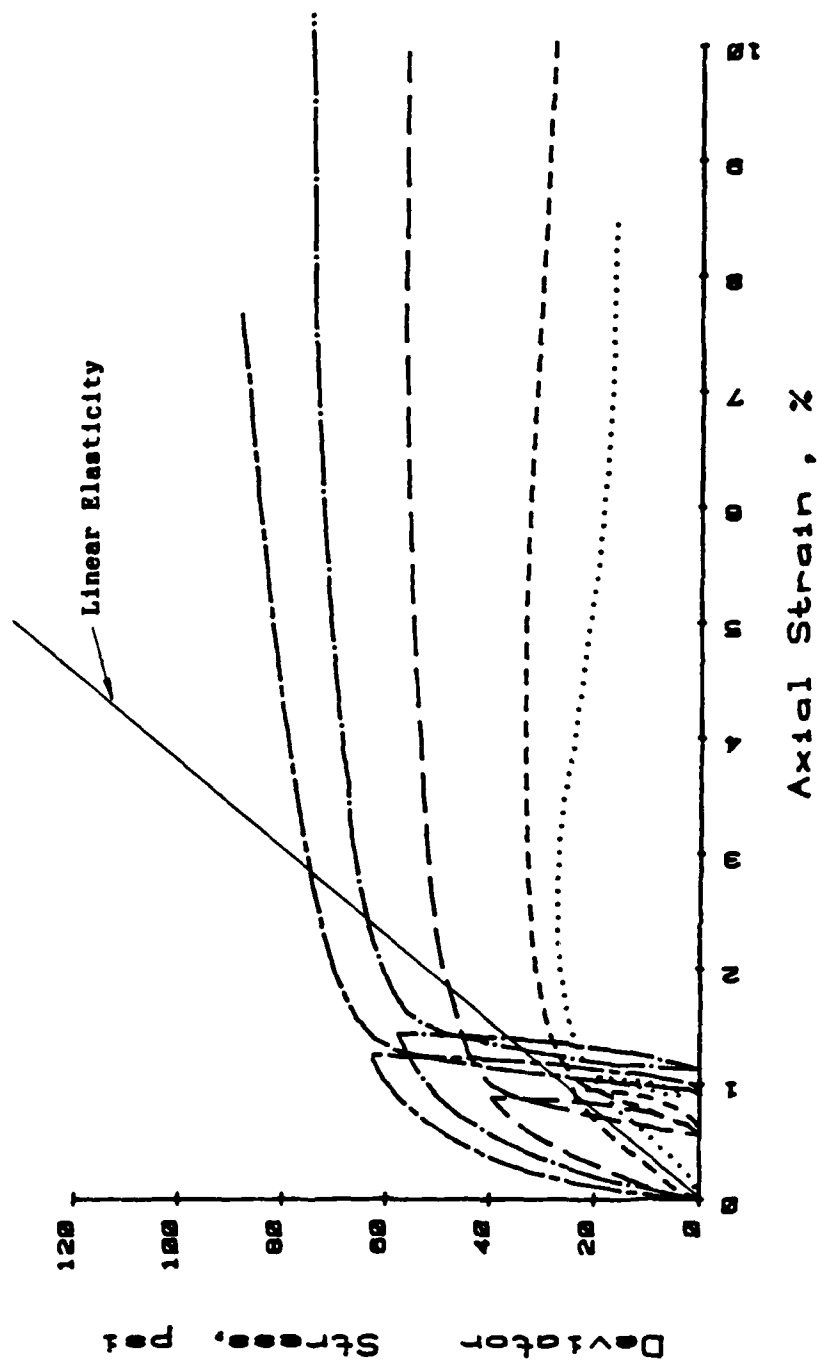


Figure 4.1a Comparisons Between Predictions of Linear Elastic Relation and Experimental Results of Conventional Triaxial Compression Tests.  $\sigma_1 - \sigma_3$  vs  $\epsilon_1$  Plot

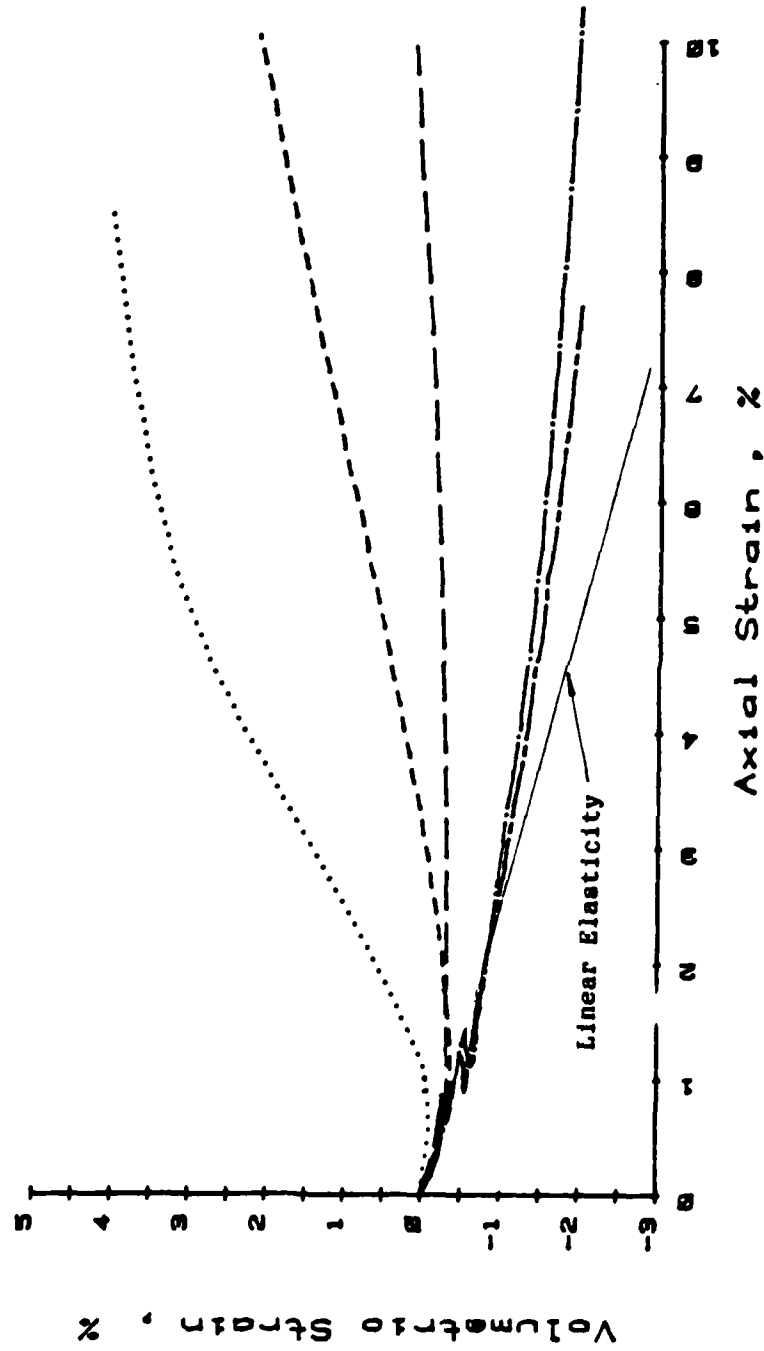


Figure 4.1b Comparisons Between Predictions of Linear Elastic Relation and Experimental Results of Conventional Triaxial Compression Tests.  $\epsilon_v$  vs  $\epsilon_1$  Plot

#### 4.2.4 Parameter Evaluation of an Aluminum Culvert

The culvert is made of 5052, 0-Temper aluminum. This alloy is made with 2.5% magnesium so that it has many features like good corrosion resistance, good workability, weldability, and strength.

The engineering properties of this kind of material can be found in most textbooks on strength of materials.

$$E = 10.2 \times 10^6 \text{ psi} \quad (4.12)$$

$$\nu = 0.334 \quad (4.13)$$

These values have been well established and the re-evaluation of these values is not necessary.

#### 4.3 Hyperbolic Stress-Strain Relation

##### 4.3.1 General Description

The hyperbolic constitutive relation proposed by Duncan and Chang (1970) has been widely used in finite element analyses of a number of different types of static soil mechanics problems (Clough and Duncan, 1971; Clough, 1972; Duncan and Chang, 1970; Duncan and Clough, 1971; Duncan and Lefebvre, 1973; Kulhawy and Duncan, 1972; Lefebvre et al, 1973; Duncan, 1977; McVay, 1982) and the values of the hyperbolic parameters were determined for about 150 different soils (Duncan et al, 1980).

The hyperbolic relations account for three important characteristics of the stress-strain behavior of soils, namely nonlinearity, stress dependence and inelasticity. However, the material is still regarded as isotropic. Therefore, for each stress increment only two parameters are needed to uniquely determine the stress-strain relation and in general these two parameters vary from increment to increment. The parameters have easily understood physical significance and the coefficients are easily evaluated from CTC tests. Those advantages made this model very popular. On the other hand, there are some significant limitations inherent in this model. Shear dilatancy, strain-softening and the intermediate principal stress effects are not modeled in these stress strain relations.

There are three versions of hyperbolic stress-strain relations. In all those, the tangential Young's modulus,  $E_t$ , is used. In the first version a constant Poisson's ratio is used. Nonlinear tangential Poisson's ratio,  $\nu_t$ , is used in the second version. Nonlinear tangential bulk modulus,  $B_t$ , is used in the last version. They are presented in the following.

Hyperbolas were used first by Kondner (1963) and Knodner and Zelasko (1963) to represent the nonlinear stress-strain curves obtained from CTC tests. These hyperbolas have the equation:

$$\sigma_1 - \sigma_3 = \frac{\epsilon_1}{\frac{1}{E_t} + \frac{\epsilon_1}{(\sigma_1 - \sigma_3)_{ult}}} \quad (4.14)$$



where  $E_1$  is the tangent Young's modulus at the origin and  $(\sigma_1 - \sigma_3)_{ult}$  is the asymptotic value of stress difference at large values of the axial strain,  $\epsilon_1$ .

$R_f$ , called the failure ratio, is used to define the relative value between failure and ultimate stress difference

$$R_f = \frac{(\sigma_1 - \sigma_3)_f}{(\sigma_1 - \sigma_3)_{ult}} \quad (4.15)$$

The stress dependent stress-strain behavior can be represented by varying  $E_1$  and  $(\sigma_1 - \sigma_3)_{ult}$  with confining pressure. The variation of  $E_1$  with  $\sigma_3$  is modeled by an equation of the following form suggested by Janbu (1963):

$$E_1 = K P_a \left( \frac{\sigma_3}{P_a} \right)^n \quad (4.16)$$

where  $P_a$  is a reference pressure usually chosen as the atmospheric pressure, and  $K$  and  $n$  are two parameters. By using the Mohr-Coulomb failure criterion

$$(\sigma_1 - \sigma_3)_f = \frac{2C \cos\phi + 2\sigma_3 \sin\phi}{1 - \sin\phi} \quad (4.17)$$

the variation of  $(\sigma_1 - \sigma_3)_{ult}$  with  $\sigma_3$  is accounted for with the combination of equations 4.15 and 4.17.

$$(\sigma_1 - \sigma_3)_{ult} = \frac{2C \cos\phi + 2\sigma_3 \sin\phi}{R_f(1 - \sin\phi)} \quad (4.18)$$

The instantaneous slope of the stress-strain curve,  $E_t$ , is needed for the constitutive relation in the finite element method. By differentiating equation 4.14 with respect to  $\epsilon_1$

$$E_t = \frac{\partial (\sigma_1 - \sigma_3)}{\partial \epsilon_1} = \frac{\frac{1}{E_1}}{\left[ \frac{1}{E_1} + \frac{\epsilon_1}{(\sigma_1 - \sigma_3)_{ult}} \right]^2} \quad (4.19)$$

and substituting equations 4.16 and 4.18 into equation 4.19, the following equation can be derived:

$$E_t = \left[ 1 - \frac{R_f (1 - \sin \phi) (\sigma_1 - \sigma_3)}{2C \cos \phi + 2\sigma_3 \sin \phi} \right]^2 K P_a \left( \frac{\sigma_3}{P_a} \right)^n \quad (4.20)$$

which is used during loading.

The inelastic behavior is represented by the use of different modulus values for loading and unloading. The same value of unloading-reloading modulus,  $E_{ur}$ , is used for both unloading and reloading. The stress dependent  $E_{ur}$  is represented by the following equation:

$$E_{ur} = K_{ur} P_a \left( \frac{\sigma_3}{P_a} \right)^n \quad (4.21)$$

where  $K_{ur}$  is the unloading-reloading modulus number. The value of  $K_{ur}$  is always larger than the value of  $K$  (for primary loading), so  $E_{ur}$  is always larger than  $E_t$ .

A very simple loading-unloading criterion has been used in which unloading-reloading is indicated when the current value of the stress level  $(\sigma_1 - \sigma_3)/(\sigma_1 - \sigma_3)_f$  is less than the maximum previous value. A more detailed discussion about this criterion is shown in Appendix B.

The second part of the hyperbolic constitutive relation is the axial strain-volumetric strain relationship. In the first work by Duncan and Chang (1970), a constant Poisson's ratio  $\nu$  was assumed. In the CTC test  $\epsilon_2 = \epsilon_3 = -\nu\epsilon_1$ . Thus,

$$\epsilon_v = (1-2\nu) \epsilon_1 \quad (4.22)$$

Equation 4.22 represents the linear relation between the compressive volume strain and axial strain.

A subsequent extension developed by Kulhawy and Duncan (1972) allows for nonlinear volumetric strain. A hyperbolic curve fitting for the Poisson's ratio is used with a similar approach as for the axial stress-strain relationship. The bulk modulus,  $B$ , can be written in terms of  $E$  and  $\nu$  as

$$B = \frac{E}{3(1-2\nu)} \quad (4.23)$$

Since the Poisson's ratio approaches 0.5 when the slope of the curve  $\epsilon_v$  vs  $\epsilon_1$  tends to become horizontal, the bulk modulus increases rapidly. This means that volumetric response changes with shearing and this disagrees with the fact observed in the laboratory. To overcome this problem Duncan et al. (1980) proposed the latest version of hyperbolic model in which nonlinear volume change is accounted for by using a constant bulk modulus,  $B$ . The bulk modulus is assumed independent of shear stress level ( $\sigma_1 - \sigma_3$ ) and dependent on the confining pressure:

$$B = K_b P_a \left( \frac{\sigma_3}{P_a} \right)^m \quad (4.24)$$

where  $K_b$  and  $m$  are two parameters.

By eliminating  $\nu$  from equations 4.22 and 4.23 the following equation can be derived

$$\epsilon_v = \frac{E}{3B} \epsilon_1 \quad (4.25)$$

This equation implies the nonlinearity between  $\epsilon_v$  and  $\epsilon_1$  is generated by the nonlinear relation of  $E$  and  $\epsilon_1$ .

The latest version of the hyperbolic model with Young's and bulk moduli is adopted (see equation 5.15). The next section shows the procedure to calibrate the model.

#### 4.3.2 Parameter Evaluation

A series of conventional triaxial tests are necessary to calibrate this model. The laboratory tests must be performed using specimens compacted to the same density and water content as in the centrifugal physical model. The same drainage condition is also used in the laboratory tests and the centrifugal test. The confining pressures used in the CTC tests cover the pressure range experienced by the soil elements in the centrifuge model, i.e.,  $\sigma_3 = 2.5, 5, 15, 25$ , and  $35$  psi.

The  $E_1$  value from each CTC test is first determined. The evaluation of parameters  $K$  and  $n$  is performed by plotting  $E_1/P_a$  versus  $\sigma_3/P_a$  on log-log scales. The best fitting straight line can be determined, as shown in Figure 4.2. The value of  $K$  is equal to the value of  $E_1/P_a$  at the point where  $\sigma_3/P_a$  is equal to unity on the best fitting line mentioned above. The value of  $n$  is equal to the slope of this best fitting line.

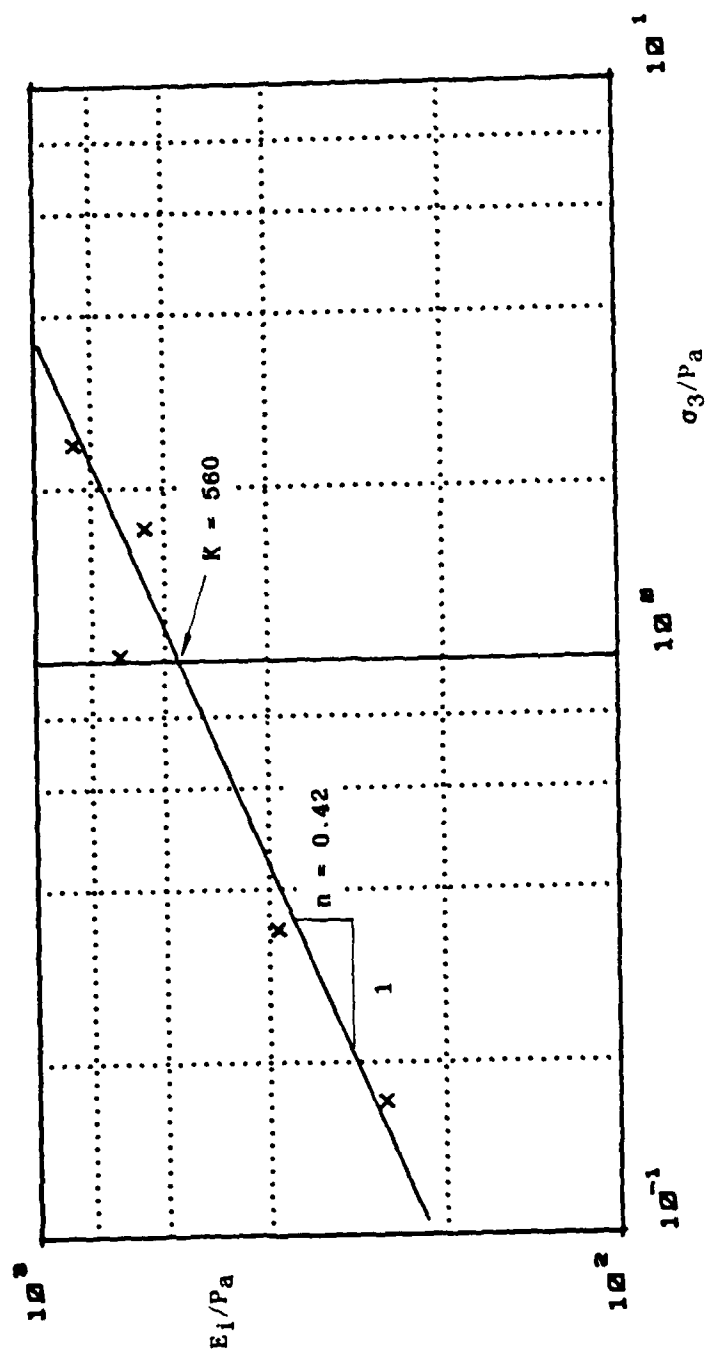


Figure 4.2 Hyperbolic Relation Calibration.  
 $E_1/Pa$  vs  $\sigma_3/Pa$  Plot

The value of  $K_{ur}$  is usually determined by assuming that the modulus exponent  $n$  for unloading-reloading (equation 4.21) is the same as that for primary loading (equation 4.16). Equation 4.21 can be transformed to the following form

$$K_{ur} = \frac{E_{ur}}{P_a \left(\frac{\sigma_3}{P_a}\right)^n} \quad (4.26)$$

where  $n$  is the value evaluated from the previous step and the unloading modulus  $E_{ur}$  can be measured from each test. Then, the corresponding value of  $K_{ur}$  can be determined from equation 4.26. The scattered values of  $K_{ur}$  are averaged to give the representative value of  $K_{ur}$ .

Two steps are involved in determining the values of  $K_b$  and  $m$ . The first is to determine the value of  $B$  from the CTC test data. For soils with volume change curves which do not reach horizontal tangents prior to the stage at which 70% of the strength is mobilized, the value of  $B$  is determined by using the following equation

$$B = \frac{(\sigma_1 - \sigma_3)}{3\epsilon_v} \quad (4.27)$$

together with  $(\sigma_1 - \sigma_3) = 0.7(\sigma_1 - \sigma_3)_f$  and the corresponding value of  $\epsilon_v$ . For highly dilatant soils having volumetric strain curves that reached horizontal tangents prior to the stage of the test at which 70% of the strength is mobilized, the data corresponding to the stage at which the volumetric strain curves become horizontal

are used in calculating values of  $B$ . The second step is to plot values of  $B/P_a$  against  $\sigma_3/P_a$  on log-log scales to determine the values of  $K_b$  and  $m$  as shown in Figure 4.3.

The selected value of parameter  $R_f$  is the average value of the results from equation 4.15 for each CTC test after the  $(\sigma_1 - \sigma_3)_{ult}$  and  $(\sigma_1 - \sigma_3)_f$  are evaluated from equations 4.14 and 4.17, respectively.

The Mohr's circles are plotted for the failure stress conditions in the CTC tests and the value of strength parameters  $C$  and  $\phi$  are determined by drawing the failure envelope and measuring the intercept and angle of inclination as shown in Figure 2.5.

The values of these nine parameters evaluated for the sandy silts used in this study are listed in Table 4.1

#### 4.3.3 Prediction of Triaxial Test

The hyperbolic model, calibrated in the fashion just described, is implemented in a constitutive driven computer program which is used to predict the CTC test response of the soil. Figures 4.4 and 4.5 show the comparison between the laboratory test results and the model's prediction. As expected the stress-strain behavior is in good agreement. However, the dilatant behavior observed at the low confining pressures is not modeled accurately.

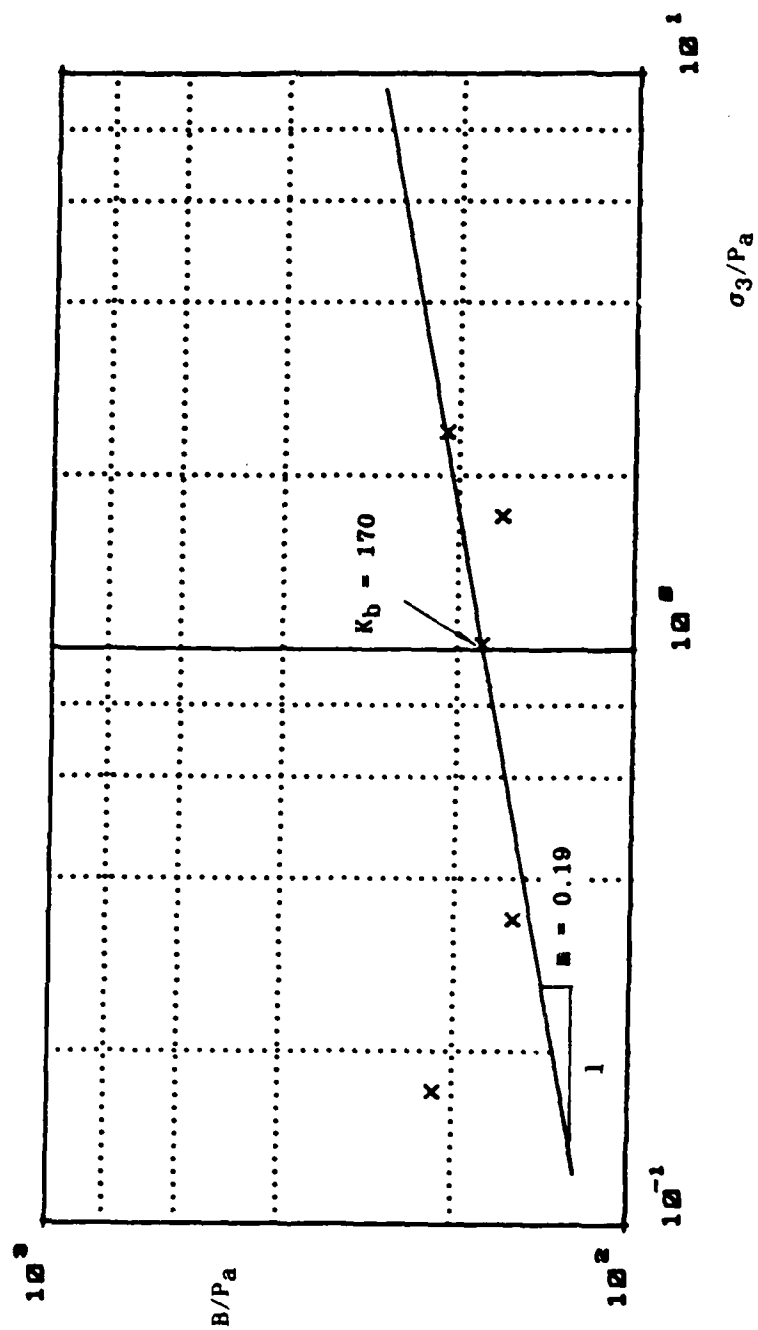


Figure 4.3 Hyperbolic Relation Calibration.  
 $B/Pa$  vs  $\sigma_3/Pa$  Plot



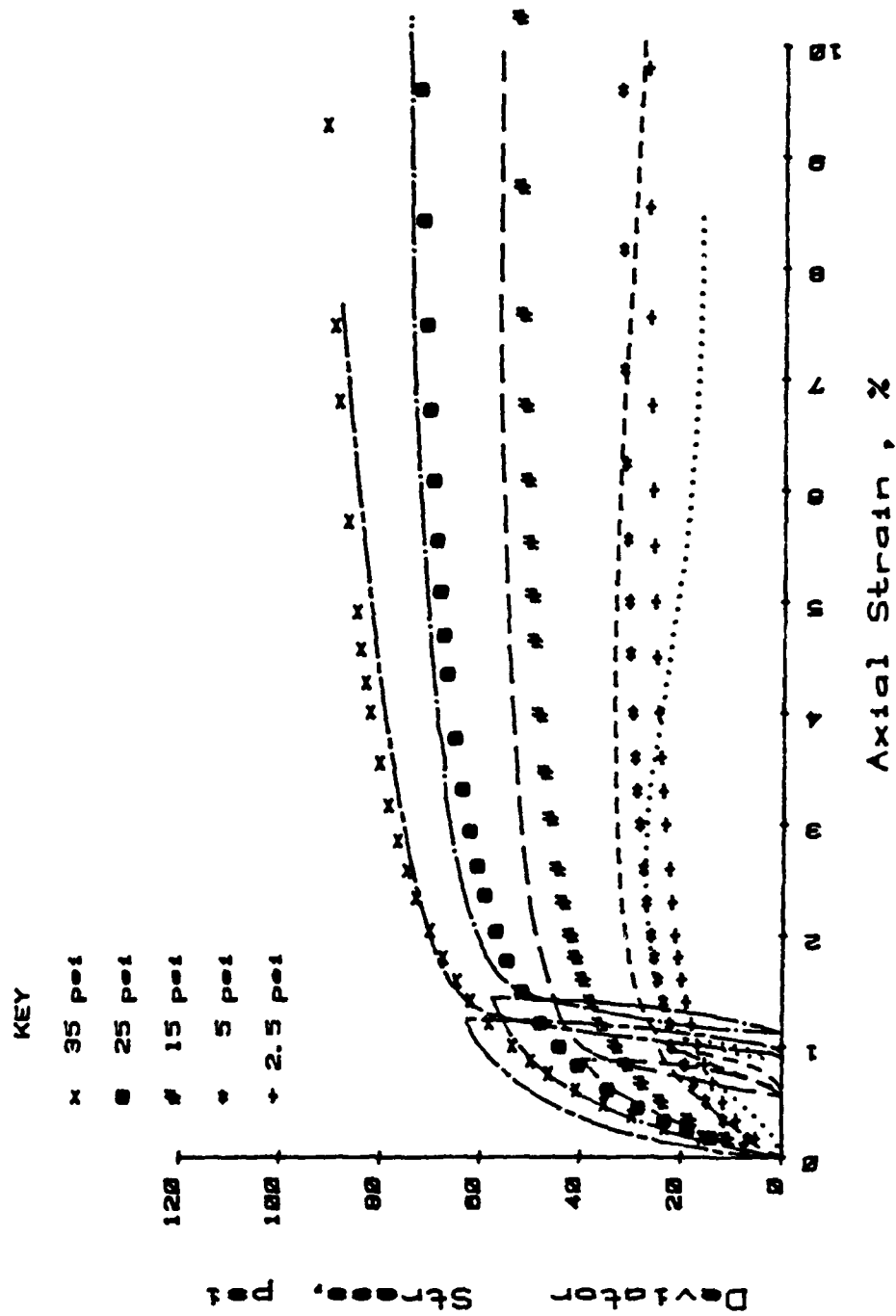


Figure 4.4 Comparisons Between Predictions of Hyperbolic Relation and Experimental Results of Conventional Triaxial Compression Tests.  $\sigma_1 - \sigma_3$  vs  $\epsilon_1$  Plot.

Table 4.1 - Parameters in Hyperbolic Constitutive Relations

Stress-Strain	loading	$K = 560$ $n = 0.42$ $R_f = 0.95$ $c = 6.5 \text{ psi}$ $\phi = 30.7^\circ$
	unloading	$K_{ur} = 820$
Strain Direction		$K_b = 170$ $m = 0.19$

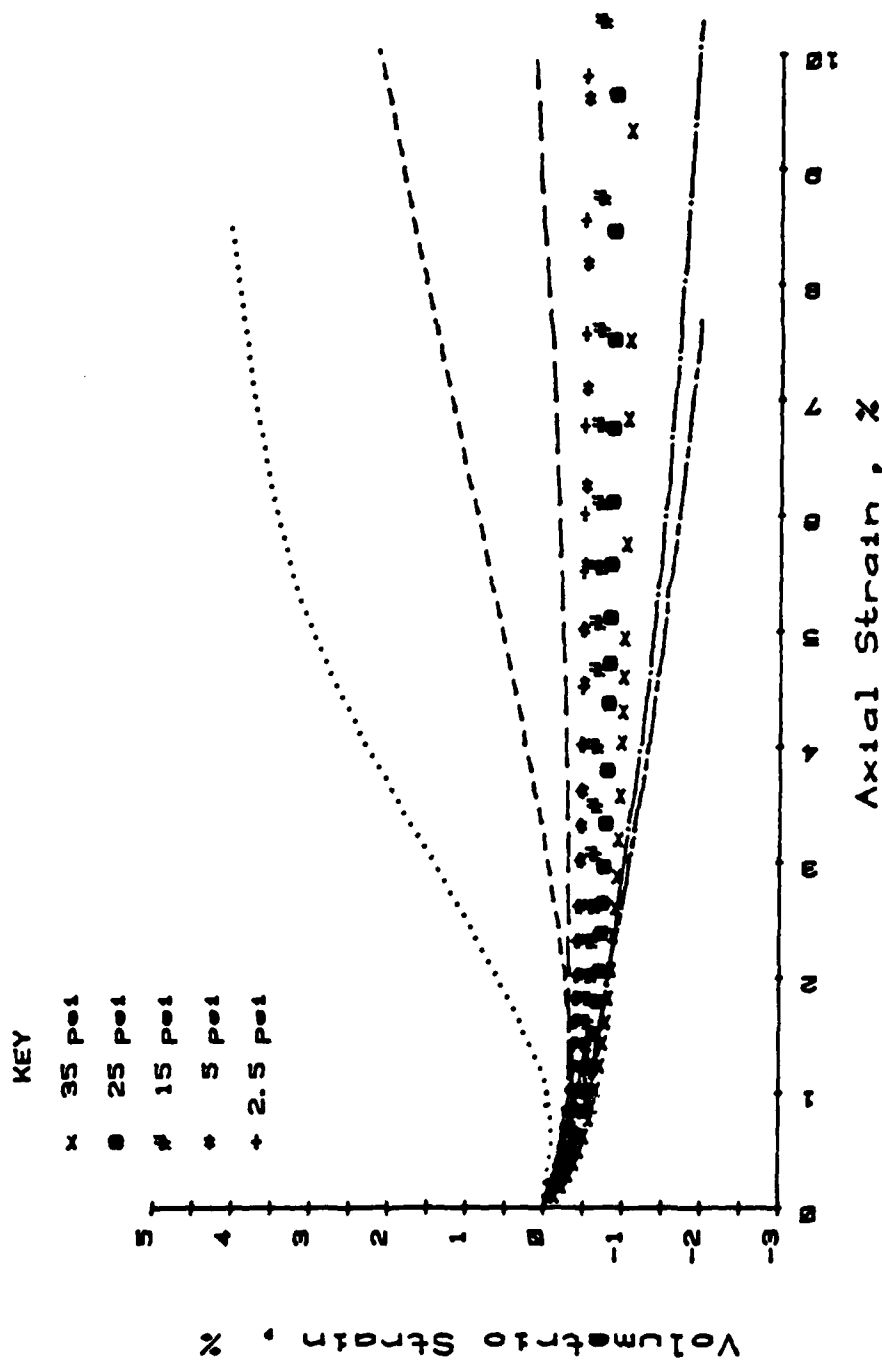


Figure 4.5 Comparison Between Predictions of Hyperbolic Relation and Experimental Results of Conventional Triaxial Compression Tests.  $\epsilon_v$  vs  $\epsilon_1$  Plot

#### 4.4 Lade's Elasto-Plastic Relation

##### 4.4.1 General Description

An elasto-plastic constitutive model for three-dimensional stress-deformation analysis for monotonic loading only was proposed by Lade (1972, 1977) for cohesionless soil. Later Lade (1979) predicted the behavior of normally consolidated clays with this model. The analytical description of this model is based on conventional work-hardening incremental plasticity theory. A semi-empirically developed work-hardening rule was incorporated into the yield function in the model. The resulting constitutive equation relates the effective stress increments to the total strain increments.

This model is capable of simulating several essential features of the behavior of soil: nonlinearity, stress-path dependency, shear dilatancy, the influence of  $\sigma_2$ , and the coincidence of strain increment and stress increment axes at low stress levels with the transition to the coincidence of strain increment and stress axes at high stress levels. It also has some refined features, like the prediction of plastic strain in proportional loading and the curved yield and ultimate strength surfaces.

Lade's model assumes that the total strain increment ( $d\epsilon$ ) is divided into three components: an elastic strain increment ( $d\epsilon^e$ ), a plastic collapse increment ( $d\epsilon^C$ ), and a plastic expansive increment ( $d\epsilon^P$ ), so that

$$(de) = (de^e) + (de^c) + (de^p) \quad (4.28)$$

Figure 4.6 illustrates schematically these three strain components in a conventional triaxial compression test.

The elastic strain increment is calculated by generalized Hooke's law and is recoverable upon unloading. Two elastic moduli  $E_{ur}$  and  $\nu$  are used to give this component:

$$E_{ur} = K_{ur} P_a \left( \frac{\sigma_3}{P_a} \right)^n \quad (4.29)$$

$$\nu = \text{constant} \quad (4.30)$$

where  $K_{ur}$  and  $n$  are material parameters and  $P_a$  is the atmospheric pressure.

The plastic collapse strains are calculated from a plastic stress-strain theory which includes a cap-type spherical yield surface, as shown in Figure 4.7.

The yield function is given by

$$F_C((\sigma), W_C) = f'_C((\sigma)) - f''_C(W_C) = 0 \quad (4.31)$$

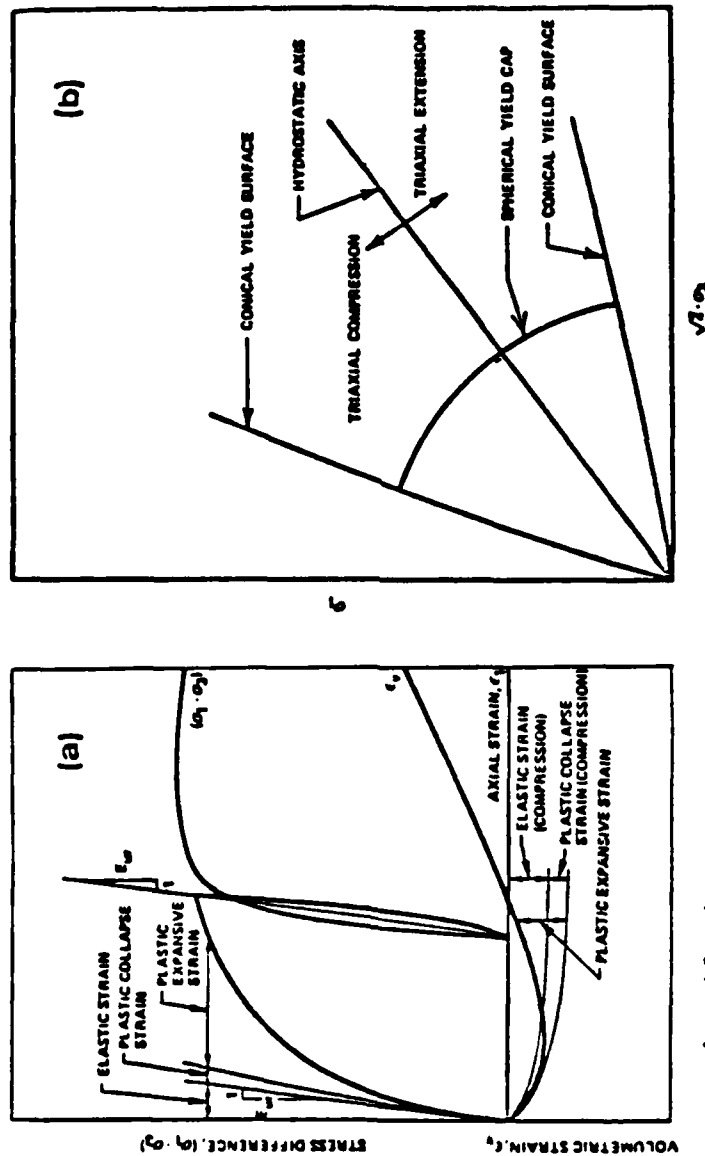
$$\text{where } f'_C((\sigma)) = f_C = I_1^2 + 2 I_2 = g_C \quad (4.32)$$

$$\text{and } I_1 = \sigma_x + \sigma_y + \sigma_z$$

$$I_2 = \tau_{yx}\tau_{xy} + \tau_{xz}\tau_{zx} + \tau_{yz}\tau_{zy} - (\sigma_x\sigma_y + \sigma_y\sigma_z + \sigma_x\sigma_z) \quad (4.33)$$

$W_C$  is a work-hardening parameter.

A work-hardening relationship can be defined experimentally by the inverse function of  $f''_C(W_C)$ .



$$\dot{\epsilon}_{ij} = \dot{\epsilon}_{ij}^e + \dot{\epsilon}_{ij}^c + \dot{\epsilon}_{ij}^p$$

Figure 4.6 Schematic Illustrations of (a) Elastic, Plastic Collapse, and Plastic Expansive Strain Components in Drained Triaxial Compression Test, and (b) Conical and Spherical Cap Yield Surfaces in Triaxial Plane (Lade, 1977)

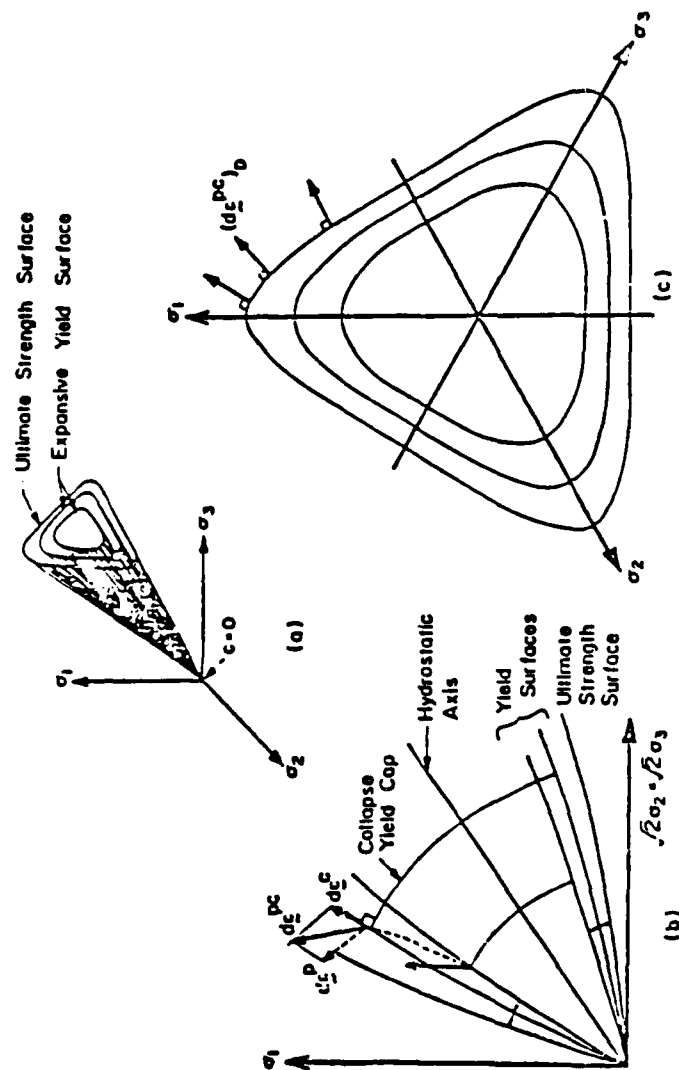


Figure 4.7 Ultimate Strength and Yield Surfaces (Lade, 1977)

$$W_C(f_C) = C P_a \left( \frac{f_C}{P_a} \right)^P \quad (4.34)$$

where C and P are material parameters. The incremental plastic work is expressed by

$$dW_C = \{\sigma\}^T \{d\epsilon^C\} \quad (4.35)$$

The associated flow rule is defined by

$$\{d\epsilon^C\} = \lambda_C \left\{ \frac{\partial f_C}{\partial \sigma} \right\} \quad (4.36)$$

Substituting equation 4.36 into equation 4.35 the following is given

$$\lambda_C = \frac{dW_C}{\{\sigma\}^T \left\{ \frac{\partial f_C}{\partial \sigma} \right\}} = \frac{dW_C}{2f_C} \quad (4.37)$$

where  $dW_C$  can be derived from equation 4.34, i.e.

$$dW_C = C P P_a \left( \frac{P_a}{f_C} \right)^{1-P} d\left( \frac{f_C}{P_a} \right) \quad (4.38)$$

The collapse strain increments can be derived by eliminating  $\lambda_C$  from equations 4.36 and 4.37

$$\begin{pmatrix} d\epsilon_x^C \\ d\epsilon_y^C \\ d\epsilon_z^C \\ d\gamma_{xy}^C \\ d\gamma_{xz}^C \\ d\gamma_{yz}^C \end{pmatrix} = \frac{dW_C}{f_C} \begin{pmatrix} \sigma_x \\ \sigma_y \\ \sigma_z \\ 2\tau_{xy} \\ 2\tau_{xz} \\ 2\tau_{yz} \end{pmatrix} \quad (4.39)$$

The plastic expansive strain increments are derived in the following steps.



The ultimate strength surface which remains stationary in principal stress space during loading and unloading has the appearance of the irregularly shaped hexagonal pyramid (Figure 4.7). The yield surface was assumed to have the same shape as the ultimate strength surface. The yield function is assumed as:

$$F_p((\sigma), W_p) = f_p'((\sigma)) - f_p'(W_p) = 0 \quad (4.40)$$

$$\text{where } f_p'((\sigma)) = f_p = \left( \frac{I_1^3}{I_3} - 27 \right) \left( \frac{I_1}{P_a} \right)^m \quad (4.41)$$

$$I_3 = \sigma_x \sigma_y \sigma_z + \tau_{xy} \tau_{yz} \tau_{xz} + \tau_{yx} \tau_{zy} \tau_{zx} - \\ (\sigma_x \tau_{yz} \tau_{zy} + \sigma_y \tau_{xz} \tau_{zx} + \sigma_z \tau_{xy} \tau_{yx}) \quad (4.42)$$

When  $f_p = \eta_1$ , the corresponding surface is the ultimate strength surface.

The plastic potential function  $g_p$  is defined through experimental observation.

$$g_p = I_1^3 - \left( 27 + \eta_2 \left( \frac{P_a}{I_1} \right)^m \right) I_3 \quad (4.43)$$

where  $\eta_2$  is constant at given values of  $\sigma_3$  and  $f_p$ .

$$\eta_2 = S f_p + R \sqrt{\sigma_3 / P_a} + t \quad (4.44)$$

in which  $S$ ,  $R$  and  $t$  are material parameters. Through the observation in the laboratory, the relation between  $W_p$  and  $f_p$  can be expressed by

$$f_p = a e^{-b w_p} (w_p/P_a)^{1/q}, \quad q > 0 \quad (4.45)$$

$$\text{where } a = \eta_1 \left( \frac{e P_a}{w_{p \text{ peak}}} \right)^{1/q} \quad (4.46)$$

$$b = \frac{1}{q w_{p \text{ peak}}} \quad (4.47)$$

$$w_{p \text{ peak}} = P P_a (\sigma_3/P_a)^f \quad (4.48)$$

$$q = \alpha + \beta (\sigma_3/P_a) \quad (4.49)$$

A nonassociated flow rule defines the relation between stress and strain increments by the following expression:

$$\{d\epsilon^p\} = \lambda_p \{\partial g_p / \partial \sigma\} \quad (4.50)$$

where the  $\lambda_p \geq 0$ .

The incremental plastic work is expressed by

$$dw_p = \{\sigma\}^T \{d\epsilon^p\} \quad (4.51)$$

Substituting equation 4.50 into equation 4.51 gives

$$\lambda_p = \frac{dw_p}{\{\sigma\}^T \{\partial g_p / \partial \sigma\}} \quad (4.52)$$

$$\text{where } \{\sigma\}^T \{\partial g_p / \partial \sigma\} = 3g_p + m \eta_2 \left( \frac{P_a}{I_1} \right)^m I_3 \quad (4.53)$$

Based on equation 4.45 the increment in plastic work can be expressed as follows:

$$dW_p = \frac{df_p}{f_p} \frac{1}{\left(\frac{1}{q W_p} - b\right)} \quad (4.54)$$

Substituting equations 4.53 and 4.54 into equation 4.52 the resulting expression is then used to eliminate  $\lambda_p$  from equation 4.50. The following is obtained

$$(d\epsilon^p) = \frac{\frac{df_p}{f_p} \frac{1}{\left(\frac{1}{q W_p} - b\right)}}{3 g_p + \eta_2 \left(\frac{P_a}{I_1}\right)^n I_3} (\partial g_p / \partial \sigma) \quad (4.55)$$

where  $(\partial g_p / \partial \sigma)$  is obtained by differentiating equation 4.43 with respect to  $(\sigma)$ .

The plastic expansive stress-strain relationship is obtained as

$$\begin{Bmatrix} d\epsilon_x^p \\ d\epsilon_y^p \\ d\epsilon_z^p \\ d\gamma_{yz}^p \\ d\gamma_{zx}^p \\ d\gamma_{xy}^p \end{Bmatrix} = \frac{\frac{df_p}{f_p} \frac{1}{\left(\frac{1}{q W_p} - b\right)}}{3 g_p + \eta_2 (P_a / I_1)^n I_3} \left[ - [27 + \eta_2 \left(\frac{P_a}{I_1}\right)^n] \begin{Bmatrix} \sigma_y \sigma_z - \tau_{yz}^2 \\ \sigma_x \sigma_z - \tau_{xz}^2 \\ \sigma_x \sigma_y - \tau_{xy}^2 \\ -2\sigma_x \tau_{yz} + 2\tau_{xy} \tau_{zx} \\ -2\sigma_y \tau_{zx} + 2\tau_{yz} \tau_{xy} \\ -2\sigma_z \tau_{xy} + 2\tau_{zx} \tau_{yz} \end{Bmatrix} \right] +$$

$$\left[ 3I_1^2 + \frac{I_3}{I_1} m \eta_2 \left( \frac{P_a}{I_1} \right)^m \right] \begin{Bmatrix} 1 \\ 1 \\ 1 \\ 0 \\ 0 \\ 0 \end{Bmatrix} \quad (4.56)$$

where  $W_p$ ,  $f_p$  and  $g_p$  are evaluated by equations 4.45, 4.41 and 4.43, respectively, and those material parameters are obtained in the next section on model calibration. The total strain increment can be obtained by summing up three strain components calculated from equations 4.4, 4.39 and 4.56 as shown in Figure 4.7.

The Lade's stress-strain-strength theory described above can only model sand and normally consolidated, remolded cohesive soils. That means it cannot model soils that exhibit cohesive properties and tensile strength. However, the soil used in this research shows a nonzero cohesion (Figure 2.5). Some modification of the theory is necessary for this soil. Lade (1981) and Kim and Lade (1984) proposed a simple way to include this effect into the strength evaluation for concrete and rock. In order to include the cohesion and the tension which can be sustained by soil, a translation of the principal stress space along the hydrostatic axis is performed as illustrated in Figure 4.8. Thus, a constant stress  $a \cdot P_a$  is added to the normal stresses before substitution in equation 4.41:

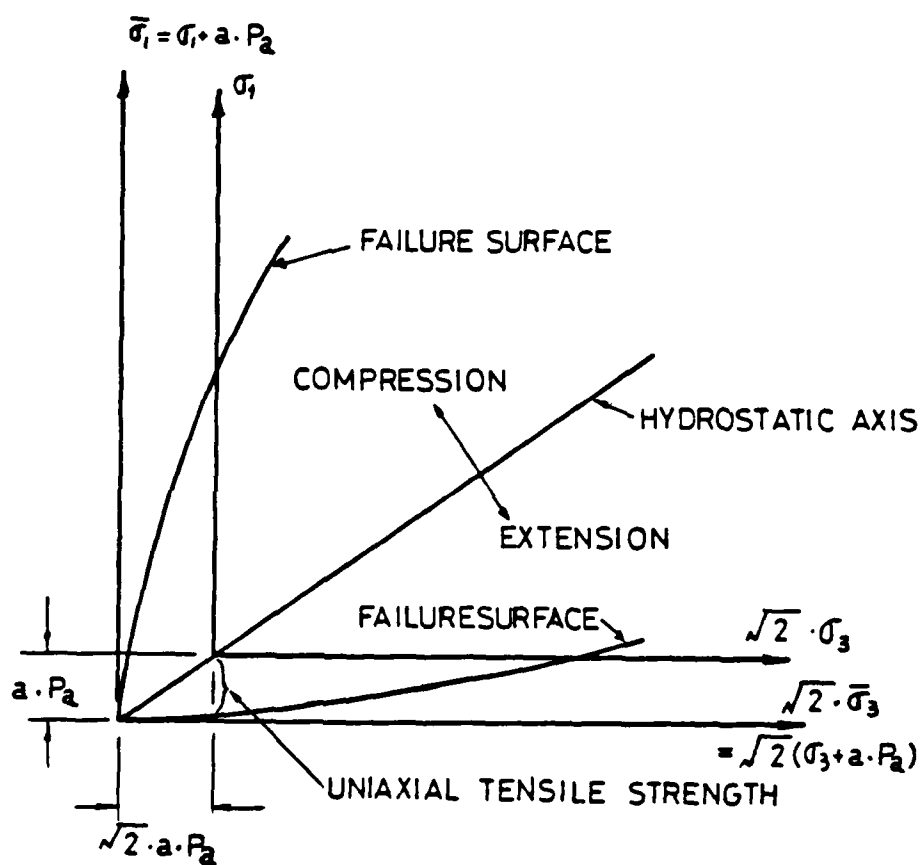


Figure 4.8 Translation of Principal Stress Space Along Hydrostatic Axis to Include Effect of Tensile Strength in Failure Criterion

$$\overline{\sigma}_x = \sigma_x + a \cdot P_a \quad (4.57a)$$

$$\overline{\sigma}_y = \sigma_y + a \cdot P_a \quad (4.57b)$$

$$\overline{\sigma}_z = \sigma_z + a \cdot P_a \quad (4.57c)$$

where "a" is a dimensionless parameter and  $P_a$  is atmospheric pressure in the same units as  $\sigma_x$ ,  $\sigma_y$  and  $\sigma_z$ . The value of  $a \cdot P_a$  reflects the effect of the tensile strength of the material. The stress-strain relations within the region bounded by  $0 \leq \overline{\sigma}_1 \leq a \cdot P_a$  and yield surfaces, i.e., tensile region, are assumed to behave in the same way as in the compressive region.

#### 4.4.2 Parameter Evaluation

Since the uniaxial tensile strength of the soil used is not available, the only way left for the estimation of parameter "a" is by trial and error. With the assumption of parameter "a" in equation 4.57, the plot of  $(I_1^3/I_3 - 27)$  vs  $(P_a/I_1)$  on the log-log scale can be drawn. The value of parameter "a" is picked such that the best fitted straight line using this "a" value passes through all the data points as shown in Figure 4.9. This gives  $a = 0.544$ ,  $\eta_1 = 26$ , and  $m = 0.137$ . Then three steps are followed to complete the parameter evaluation procedure.

##### a. Elastic Parameters

The unloading modulus  $E_{ur}$  is measured from the experimental data curve and  $E_{ur}/P_a$  vs  $\sigma_3/P_a$  is plotted on log-log diagram for each CTC test. From the best fitted straight line, the slope

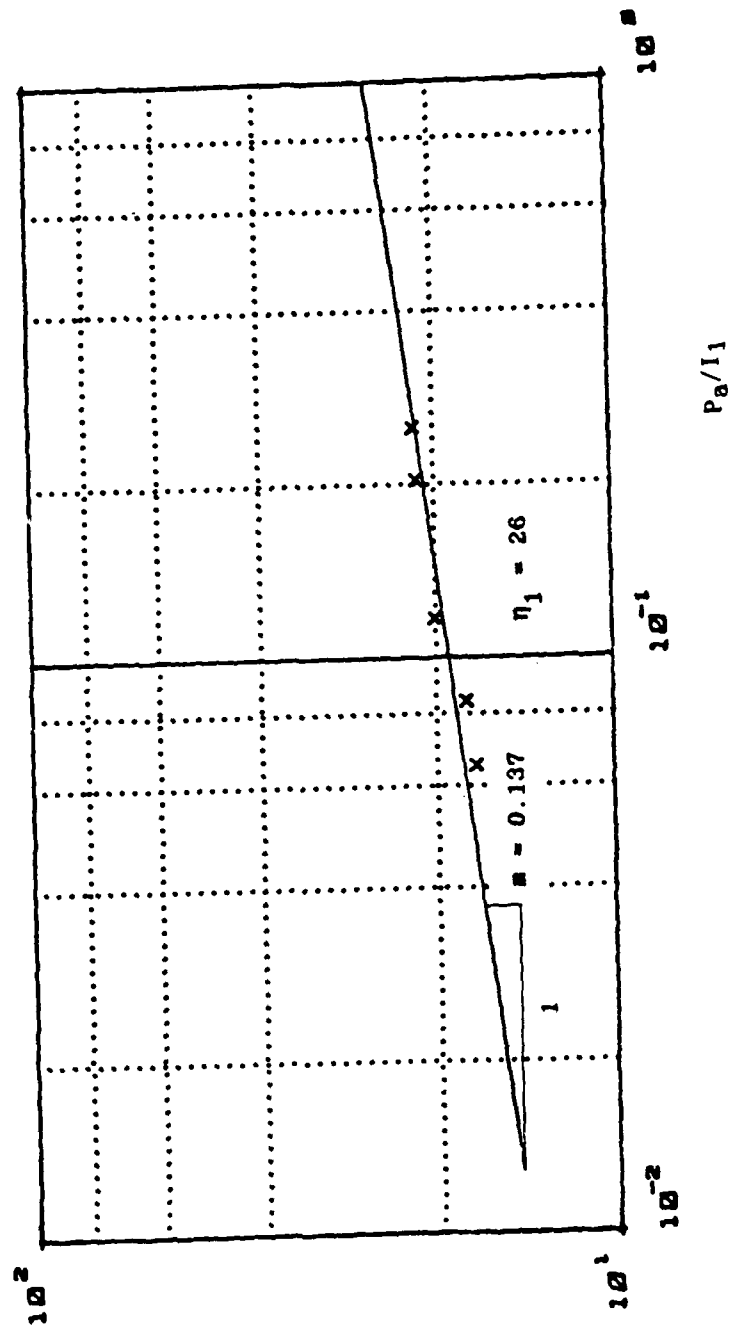


Figure 4.9 Lade's Relation Calibration.  
 $I_1^3/I_3-27$  vs  $P_a/I_1$  Plot

defines the parameter  $n$  and the intercept with  $\sigma_3/P_a = 1$  defines the parameter  $K_{ur}$ , as shown in Figure 4.10. The constant parameter  $\nu$  is chosen as 0.2 through a trial and error process with  $K_{ur} = 490$  and  $n = 0.95$ .

$K_{ur}$  and  $n$  are also calculated by using the unloading path in the hydrostatic compression test. Due to the nonlinearity of this relation, the incremental form of equation 4.4 is used to give

$$d\epsilon_v = d\epsilon_1 + d\epsilon_2 + d\epsilon_3 = \frac{3(1-2\nu)}{E_{ur}} d\sigma_3 \quad (4.58)$$

Equation 4.58 is combined with equation 4.29 to give

$$d\epsilon_v = \frac{3(1-2\nu)}{K_{ur} P_a} \left(\frac{\sigma_3}{P_a}\right)^{-n} d\sigma_3 \quad (4.58)$$

Integrating equation 4.58 gives

$$\epsilon_v = \frac{3(1-2\nu)}{(1-n) K_{ur}} \left(\frac{\sigma_3}{P_a}\right)^{1-n} \quad (4.59)$$

or

$$\log_{10}(\epsilon_v) = \log_{10} \left[ \frac{3(1-2\nu)}{(1-n) K_{ur}} \right] + (1-n) \log_{10} \left( \frac{\sigma_3}{P_a} \right) \quad (4.60)$$

Data points  $(\epsilon_v, \sigma_3/P_a)$  of the unloading path in the hydrostatic compression test are plotted in the log-log coordinate, Figure 4.11. The best fitted straight line has a slope equal to  $(1-n)$  and an intercept  $\sigma_3/P_a = 1$  equal to  $3(1-2\nu)/[(1-n)K_{ur}]$ . With the assumed Poisson's ratio, the value of  $K_{ur}$  and  $n$  can be found. The experimental data for the test give  $K_{ur} = 185$ ,  $n = 0.252$ .



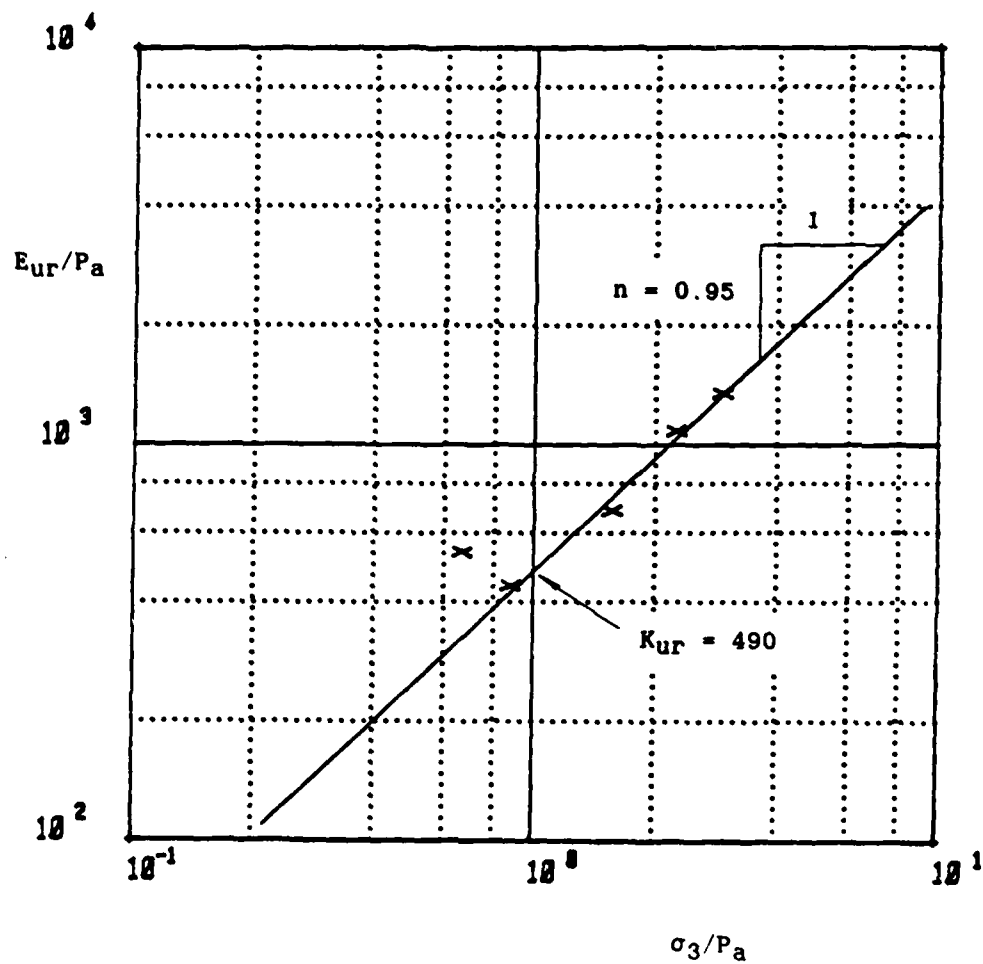


Figure 4.10 Lade's Relation Calibration.  
 $E_{ur}/P_a$  vs  $\sigma_3/P_a$  Plot

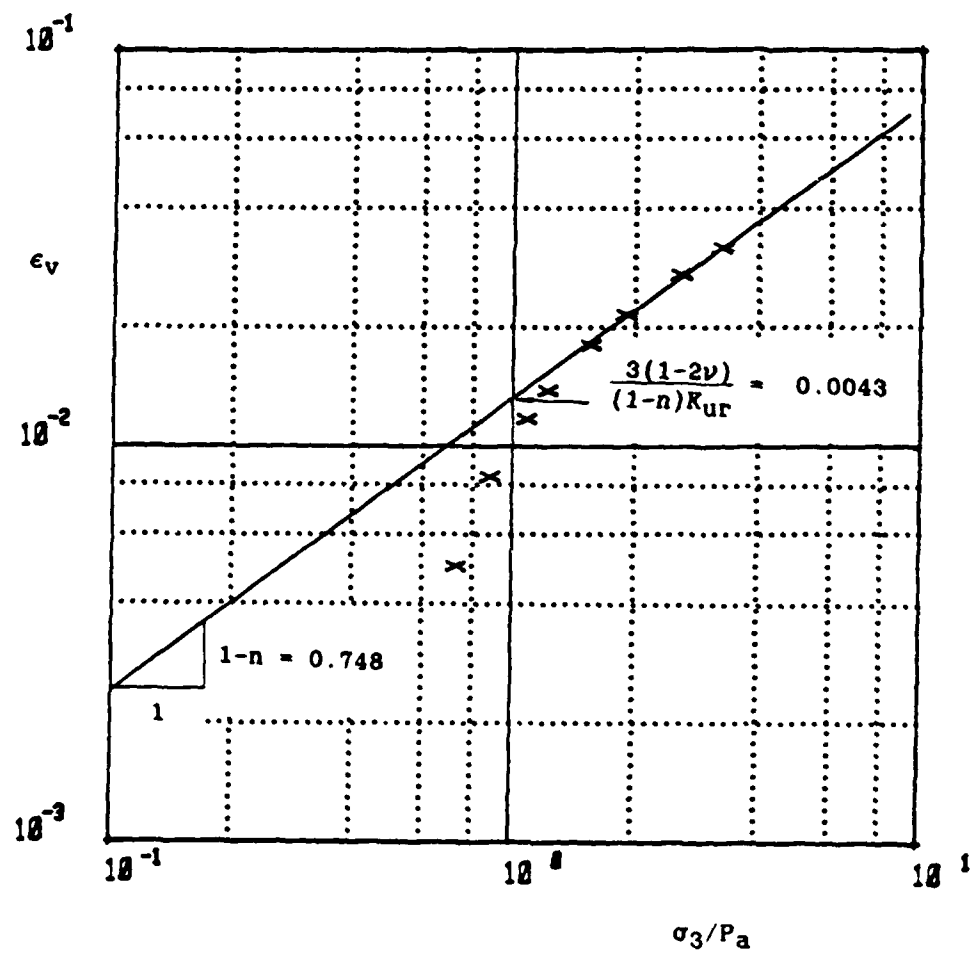


Figure 4.11 Lade's Relation Calibration.  
 $\epsilon_v$  vs  $\sigma_3/P_a$  Plot

Ideally, if this soil is isotropic the values of  $K_{UR}$  and  $n$  from the CTC test and isotropic compression test should be the same. However, they are quite different. Because the soil samples were compacted vertically with an average stress of 60 psi before triaxial tests, stress-induced anisotropy exists which makes the vertical Young's modulus larger than the horizontal one. Therefore the fact that the elastic Young's moduli evaluated from CTC tests are larger than those from isotropic compression tests is reasonable. In order to simulate the stress-strain relation closely, a trial and error procedure is used to find out the optimum values for  $K_{UR}$  and  $n$ . Values of  $K_{UR}$  and  $n$  are chosen and the rest of the calibration procedure is followed until all the parameters are evaluated. Then CTC test results are produced numerically based on these parameters values. If these results match those from the lab, the calibration is done. Otherwise new values of  $K_{UR}$  and  $n$  are chosen and the whole procedure is repeated until CTC test results are predicted well numerically. It was found that  $K_{UR}=409$  and  $n=0.95$  gave the best results.

#### b. Plastic Collapsible Parameters

The stress path in the isotropic compression test only induces the elastic and plastic collapsive strains while expansive plastic strains are zero. Thus,

$$\epsilon_v = \epsilon^e + \epsilon^c \quad (4.61)$$

or

$$\epsilon^c = \epsilon_v - \epsilon^e \quad (4.62)$$

The collapsive volumetric strain can be used to obtain the collapsive plastic work through the following equation

$$W_C = \int \sigma_3 d\epsilon_V^C \approx \sum (\sigma_3 \cdot \Delta \epsilon_V^C) \quad (4.63)$$

The associated collapsive stress level,  $f_C$ , can be expressed as:

$$f_C = I_1^2 + 2 I_2 = 3\sigma_3^2 \quad (4.64)$$

Equation 4.34 can be written as:

$$\log_{10}(W_C/P_a) = \log_{10} C + p \log_{10}(f_C/P_a^2) \quad (4.65)$$

The data  $(W_C/P_a, f_C/P_a^2)$  can be plotted on a log-log scale as shown in Figure 4.12 where the slope of the best fitted straight line is the value of parameter  $P$  and the intercept with line  $f_C/P_a^2 = 1$  is the value of parameter  $C$ .

There is a great deal of difficulty in evaluating these collapsive plastic parameters. If the values of  $C$  and  $P$  evaluated from the isotropic compression tests result marked as "x" points in the Figure 4.12 were used, the subsequent calibration in step c will be impossible, because the variation of  $\eta_2$  is so erratic that almost no function can be used to model it. After picking several different values of  $C$  and  $P$  throughout the trial and error procedure, the properly picked values of  $C$  and  $P$  are represented by the straight line in Figure 4.12. Obviously, the chosen relationship between  $W_C/P_a$  and  $f_C/P_a^2$  is very much different from the experimental observation. This is due to the fact that horizontal Young's modulus is much smaller than the vertical one.

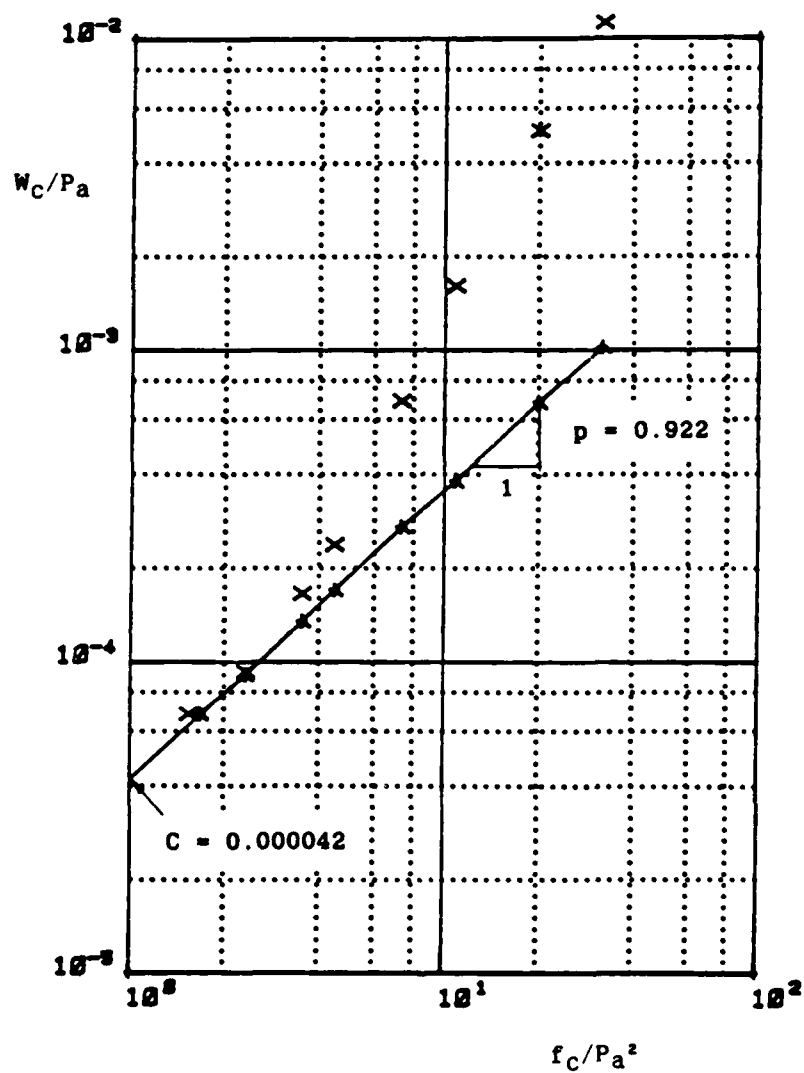


Figure 4.12 Lade's Relation Calibration.  
 $W_c/P_a$  vs  $f_c/P_a^2$  Plot

### c. Expansive Parameters

The failure envelope parameters  $\eta_1$  and  $m$  were determined previously in step a.

Next the plastic potential parameters  $S$ ,  $R$  and  $t$  are evaluated through the following concept. By assuming

$$\nu^p = - \frac{\Delta \epsilon_3^p}{\Delta \epsilon_1^p} \quad (4.66)$$

then substituting expressions for  $\Delta \epsilon_1^p$  and  $\Delta \epsilon_3^p$  from equation 4.56 into equation 4.66 and solving for  $\eta_2$  gives:

$$\eta_2 = \frac{3(1+\nu^p) I_1^2 - 27 \sigma_3 (\sigma_1 + \nu^p \sigma_3)}{(P_a/I_1)^m \left[ \sigma_3 (\sigma_1 + \nu^p \sigma_3) - \frac{I_3}{I_1} m(1+\nu^p) \right]} \quad (4.67)$$

All the variables which appear in the above expression are known for a given state of stress except  $\nu^p$ . However the elastic and collapsive strains are already known, the expansive plastic strain can be derived by subtracting the  $\Delta \epsilon^e$  and  $\Delta \epsilon^c$  from the total strain increment,  $\Delta \epsilon$ , measured in the CTC tests.  $\nu^p$  and  $\eta_2$  can then be calculated for each stress level. This procedure involves a great deal of calculation and is executed through a computer program.

The variation of  $\eta_2$  as shown in Figure 4.13 can be modeled by a simple expression

$$\eta_2 = S f_p + R \sqrt{\sigma_3/P_a} + t \quad (4.68)$$

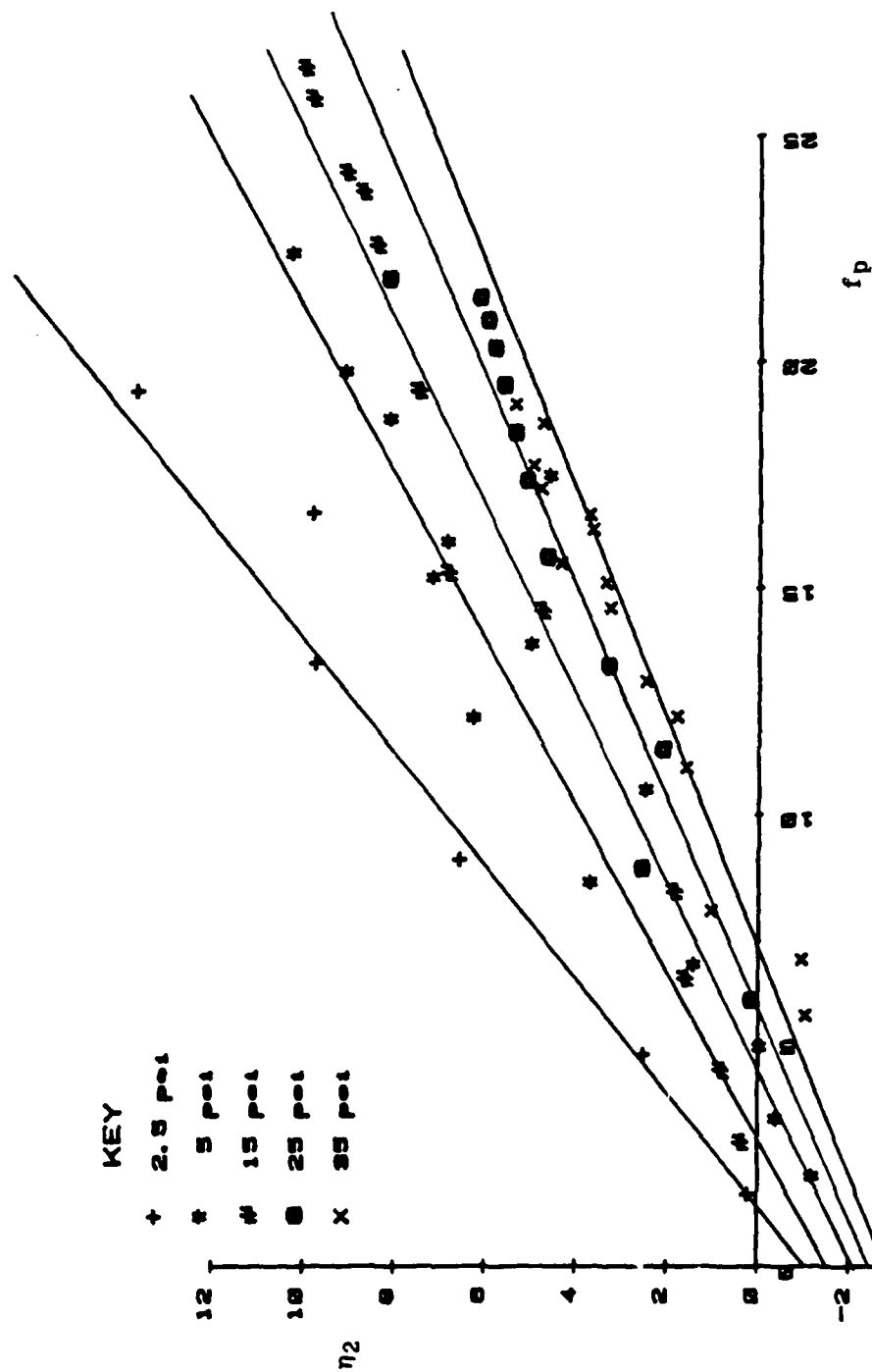


Figure 4.13 Lade's Relation Calibration.  
 $\eta_2$  vs  $f_p$  Plot

where

$$S = S_1 + S_2 \sqrt{\sigma_3/P_a} \quad (4.69)$$

The measured slope for each approximated straight line with an associated confining pressure is plotted in Figure 4.14 where the intercept gives the value of  $S_1$  and the slope of that best fitted straight line equals the value of  $S_2$ .

The intercepts in the Figure 4.13 and the associated  $\sqrt{\sigma_3/P_a}$  are replotted in figure 4.15 where the slope of best fitted straight line offers the value of parameter  $R$  and the intercept at  $\sqrt{\sigma_3/P_a} = 0$  gives the value of parameter  $t$ .

The work-hardening parameters  $p$ ,  $l$ ,  $\alpha$  and  $\beta$  are evaluated through the following process. The expansive plastic work at each stage of the CTC tests is calculated from

$$W_p = \int (\sigma)^T (d\epsilon^p) \approx \sum (\sigma_1 \Delta\epsilon_1^p + 2 \sigma_3 \Delta\epsilon_3^p) \quad (4.70)$$

as well as the value of  $f_p$  from equation 4.41. These calculations of  $W_p$  vs  $f_p$  can be used to evaluate the values of  $W_p$  peak and  $W_{p60}$  where

$W_p$  peak = the value of  $W_p$  at the peak point

and

$W_{p60}$  = the value of  $W_p$  at  $f_p = 0.6\eta_1$

The parameters  $p$  and  $l$  can be evaluated by plotting ( $W_p$  peak/ $P_a$ ,  $\sigma_3/P_a$ ) in a log-log scale as shown in Figure 4.16.



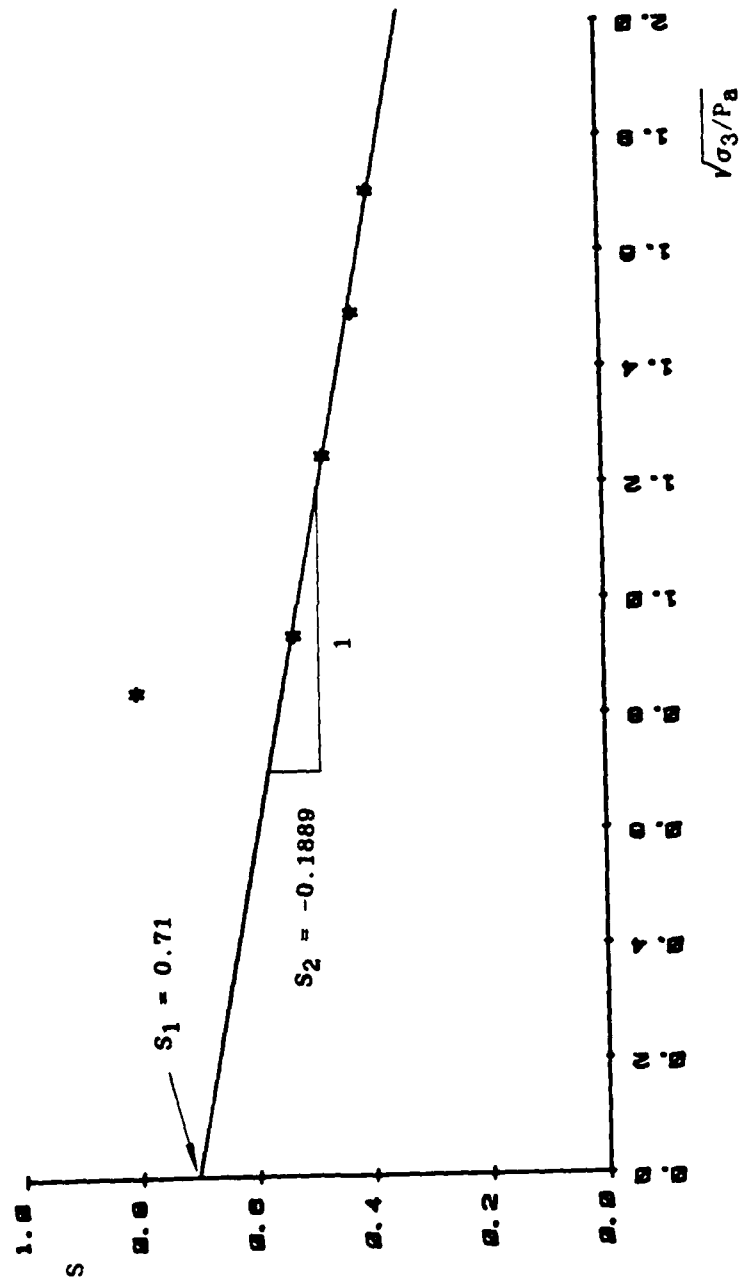


Figure 4.14 Lade's Relation Calibration.  
 $S$  vs  $\sqrt{\sigma_3/Pa}$  Plot

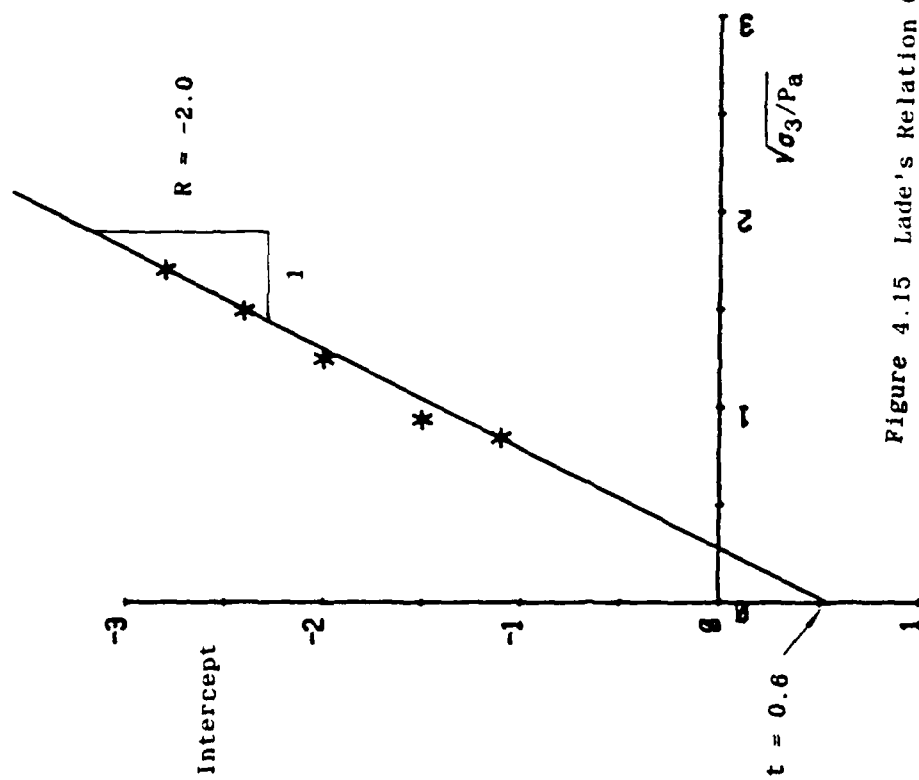


Figure 4.15 Lade's Relation Calibration.  
Intercept vs  $\sqrt{\sigma_3/P_a}$  Plot

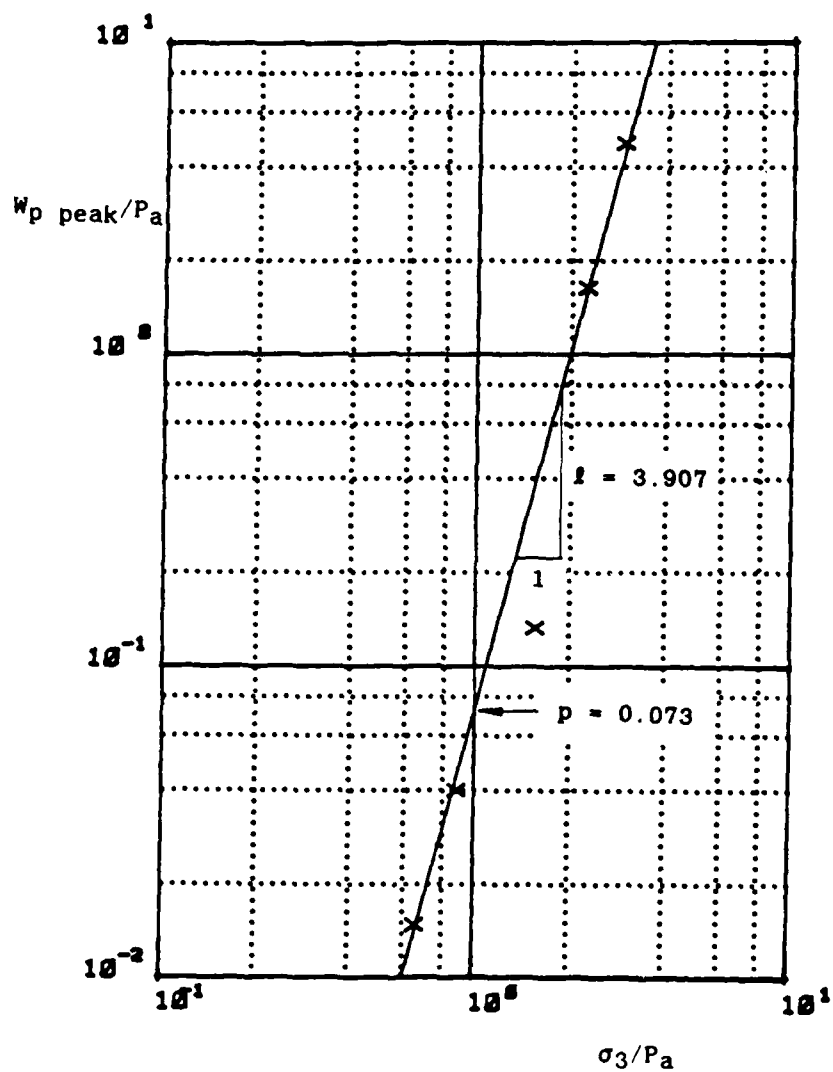


Figure 4.16 Lade's Relation Calibration.  
 $w_p \text{ peak}/P_a$  vs  $\sigma_3/P_a$  Plot

Finally the parameters  $\alpha$  and  $\beta$  are evaluated from the plot of  $q$  vs  $\sigma_3/P_a$  in Figure 4.17

$$\text{where } q = \frac{\log_{10} \left( \frac{w_{p \text{ peak}}}{w_{p60}} \right) - \left( 1 - \frac{w_{p60}}{w_{p \text{ peak}}} \right) \log_{10} e}{\log_{10} \left( \frac{\eta_1}{f_{p60}} \right)} \quad (4.71)$$

#### 4.4.3 Predictions of Triaxial Tests

All the 16 evaluated parameters are listed in Table 4.2. Prediction of conventional triaxial and isotropic compression test results using these parameter values in Lade's model are shown in Figures 4.18, 4.19 and 4.20. Features like nonlinearity, dilatancy and transition from a highly dilatant behavior for low  $\sigma_3$  to a highly compressive behavior for high  $\sigma_3$  are reasonably simulated and the agreement is pretty good. Since the Lade's theory is based on an isotropic hardening rule, the unloading is considered to be elastic. Therefore, the decreasing volume change during unloading observed in the CTC test cannot be predicted correctly. For monotonic loading, Lade's theory is a pretty simple and accurate model.

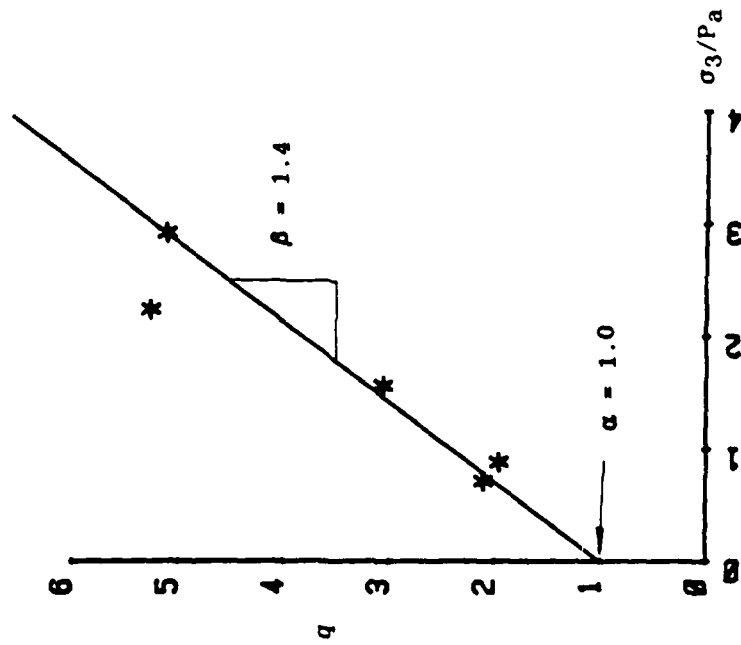


Figure 4.17 Lade's Relation Calibration.  
 $q$  vs  $\sigma_3/P_a$  Plot

TABLE 4.2 - Lade's Elasto-Plastic Relation

Cohesion Correction			$a \cdot P_a = 8 \text{ psi}$
ELASTIC			$K_{ur} = 409$ $n = 0.95$ $\nu = 0.2$
P L A S T I C	Collapsive		$c = 0.000042$ $p = 0.922$
	E X P A N S I V E	Failure Envelope	$\eta_1 = 26$ $m = 0.137$
		Plastic Potential	$S_1 = 0.71$ $S_2 = -0.1889$ $t = 0.6$ $R = -2.0$
		Work Hardening	$p = 0.073$ $f = 3.907$ $\alpha = 1.0$ $\beta = 1.4$

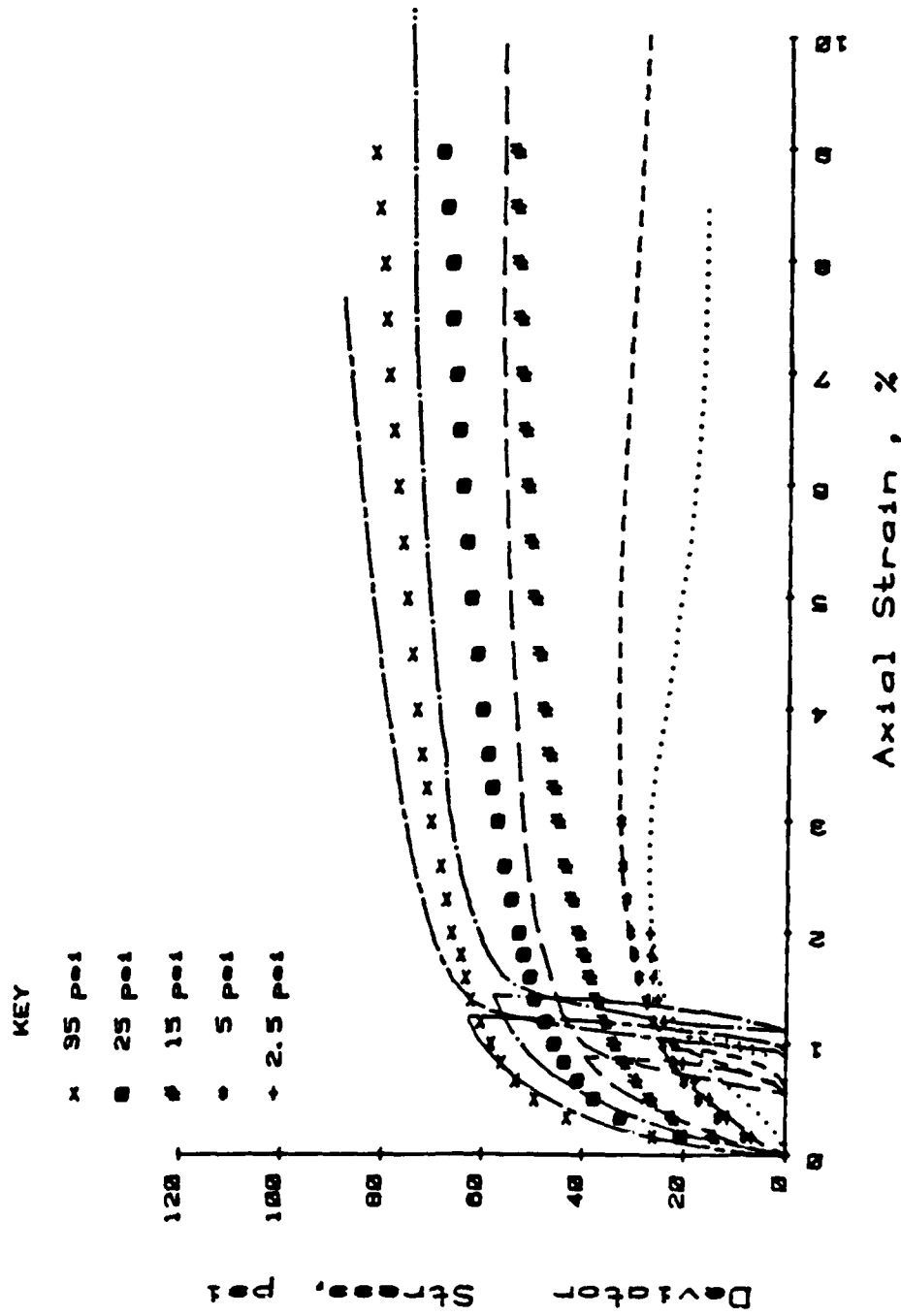


Figure 4.18 Comparison Between Predictions of Lade's Relation and Experimental Results of Conventional Triaxial Compression Tests.  $\sigma_1 - \sigma_3$  vs  $\epsilon_1$  Plot

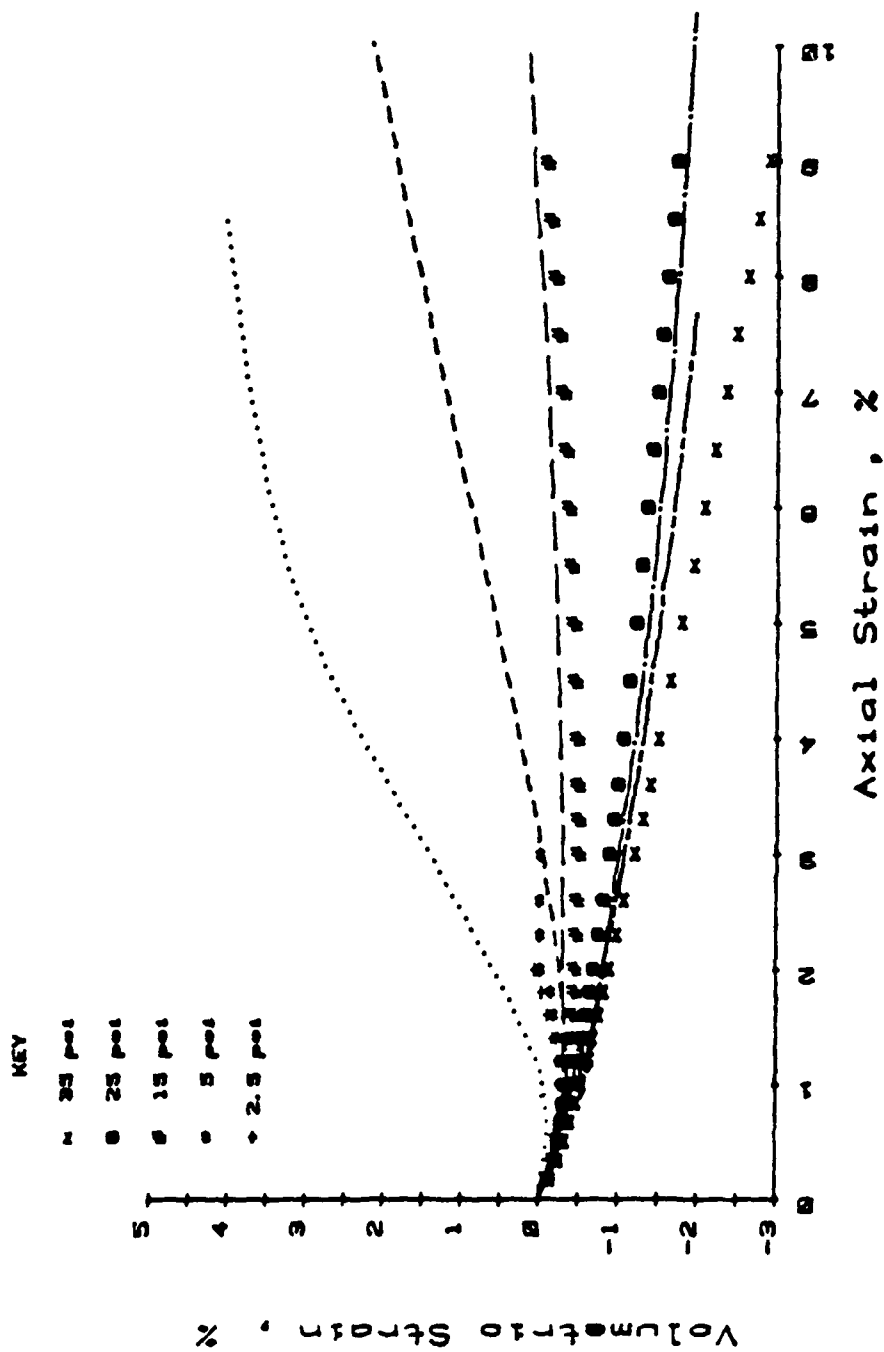


Figure 4.19 Comparison Between Predictions of Lade's Relation and Experimental Results of Conventional Triaxial Compression Tests.  $\epsilon_v$  vs  $\epsilon_1$  Plot



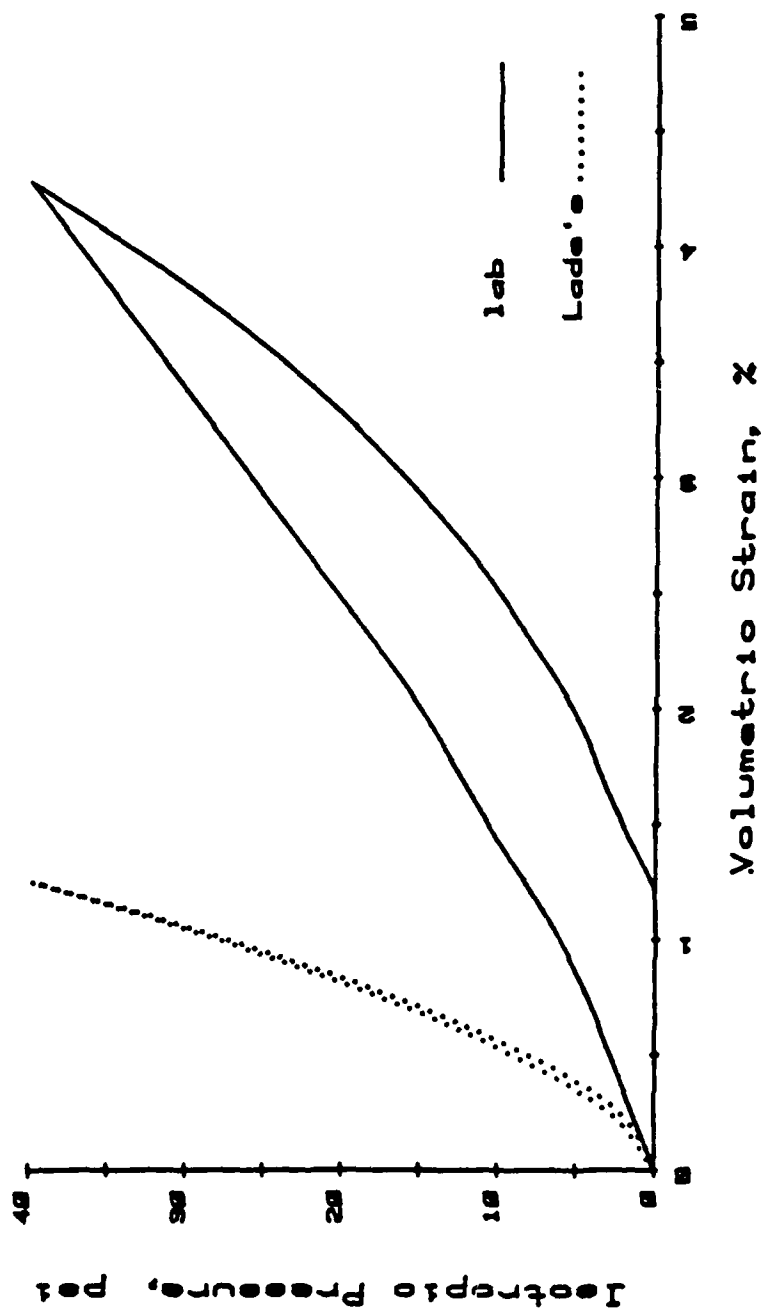


Figure 4.20 Comparison Between Predictions of Lade's Relation and Experimental Results of Isotropic Compression Tests.  $\sigma_3$  vs  $\epsilon_v$  Plot

## CHAPTER V

### NUMERICAL MODELING

#### 5.1 General

The numerical model mentioned in Table 1.1 is a finite element model based on small deformation theory and plane strain conditions. Since the development of the finite element method in the 1950's, numerous books have been written about the subject. The availability of the high speed digital computer combined with the development of sophisticated constitutive relations to describe the properties of soil materials have made it possible to apply the finite element method to the analyses of different geotechnical problems. In this chapter, only the important parts of the numerical modeling procedure using finite elements will be described.

#### 5.2 Numerical Modeling Procedure

Since the results from centrifugal and numerical modeling will be compared for the purpose of selecting a soil model, the closer the simulation of numerical modeling to the centrifuge model, the better the base of judgement. The simulation was divided into three stages, starting with the soil preparation for centrifugal model test, through the loading generated by the 50g gravitation field associated with 198 rpm rotating speed of the

centrifuge, to the uniform surface strip loading applied under the elevated gravity conditions. Those steps have been described in sections 3.8 and 3.9.

In the first stage of the experiment, the soil mass with uniform density is made under 1 g conditions. Then the tube is buried in the soil trench, so the self weight of soil is applied on the tube instantly. The above procedure is called the "gravity turn on" procedure. This stage is simulated numerically by the method of direct iteration as follows. The initial stress states in all the elements in the finite element model are assumed to be in the  $K_0$  condition. The corresponding stiffness matrix is then calculated and is followed by the calculation of displacement vector under the load vector due to the parallel 1 g gravitational force field. The load vector is derived as in the next stage and given by Equation 5.10. The updated stress state is obtained and is input for the next iteration. This iteration process is continued until the input and output stress states are sufficiently close, indicating that convergence has occurred.

In the second stage, the gradually increased gravitation force from 1 g to 50g is applied to the soil-culvert system as shown in Figure 5.1. The direction in which gravity acts on each element will be defined by specifying the angle measured counter clockwise from the positive y axis. To obtain the equivalent nodal forces, the virtual work concept is employed. If  $a$  is the centrifugal acceleration and the material mass density is  $\rho$ , then

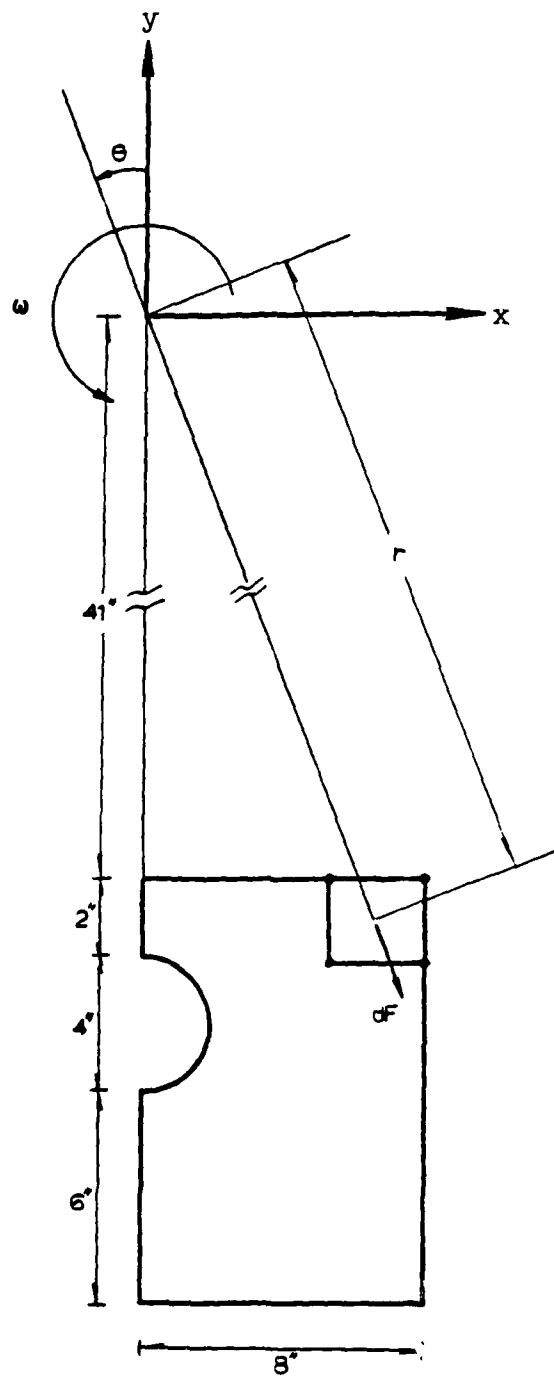


Figure 5.1 Analytical Modeling of Soil-Culvert System in the Centrifuge

the gravity force  $dF$  acting on the element volume  $dV$  is

$$dF = \rho a dV \quad (5.1)$$

which acts in the direction away from the center of rotation. The relation between centrifugal acceleration and angular velocity is

$$a = r\omega^2 \quad (5.2)$$

where  $r$  is the radius to the element under consideration. The centrifugal acceleration can be expressed as follows

$$a = ng \quad (5.3)$$

where  $g = 32.2 \text{ ft/sec}^2$  (earth gravitational acceleration) (5.4)

and  $n$  is the gravity ratio and is chosen as 50 in this research.

Eliminating  $a$  from Equations 5.2 and 5.3 gives

$$n = \frac{\omega^2 r}{g} \quad (5.5)$$

Substituting Equations 5.3 and 5.5 into 5.1 gives

$$\begin{aligned} dF &= \rho g \frac{\omega^2 r}{g} dV \\ &= \gamma \frac{\omega^2 r}{g} dV \end{aligned} \quad (5.6)$$

where  $\gamma$  is the unit weight under normal gravity.

The components acting in the x and y directions respectively are

$$\begin{aligned} dF_x &= \gamma \frac{\omega^2 r}{g} dV \sin \theta \\ dF_y &= -\gamma \frac{\omega^2 r}{g} dV \cos \theta \end{aligned} \quad (5.7)$$

The virtual displacements  $u$  and  $v$  in the  $x$  and  $y$  directions respectively are applied simultaneously to each node. Applying the principle of virtual work results in the following expression for the equivalent nodal forces  $P_{xi}$  and  $P_{yi}$  where  $i$  ranges from 1 to 4 in this case

$$\begin{aligned} P_{xi} u &= \int_V (N_i u \gamma \omega^2 r \sin \theta) / g dV \\ P_{yi} v &= -\int_V (N_i v \gamma \omega^2 r \cos \theta) / g dV \end{aligned} \quad (5.8)$$

where  $N_i$  are shape functions.

Since equation 5.8 holds for any value of  $u$  and  $v$ ,  $u$  and  $v$  can be factored out to give

$$\begin{Bmatrix} P_{xi} \\ P_{yi} \end{Bmatrix} = \int_V (N_i \gamma \omega^2 r / g) \begin{Bmatrix} \sin \theta \\ -\cos \theta \end{Bmatrix} dV \quad (5.9)$$

For practical purposes, the integration shown in the above equation is executed by the Gaussian numerical integration technique resulting in equation 5.9 being replaced by

$$\begin{Bmatrix} P_{xi} \\ P_{yi} \end{Bmatrix} = (t \gamma \omega^2 / g) \begin{Bmatrix} \sin \theta \\ -\cos \theta \end{Bmatrix} \sum_{n=1}^{N_{GAUS}} \sum_{m=1}^{N_{GAUS}} r(\xi_n, \eta_m) N_i(\xi_n, \eta_m) W_n W_m \det[J(\xi_n, \eta_m)] \quad (5.10)$$

where  $t$  is the element thickness, NGAUS is the number of Gaussian points,  $[J]$  is the Jacobian matrix, and  $W_n, W_m$  are the Gaussian weighting functions.

Due to the nonlinear behavior of the soil-structure interaction problem, the midpoint Runge-Kutta incremental scheme is used to simulate the selfweight loading from  $1g$  to  $50g$  in the soil-culvert system. So far the construction procedure of the centrifugal model has been faithfully simulated. If the material constitutive law used in the numerical model is correct, then the computed initial stress state before the external surface loading should be very close to the condition existing in the centrifuge model.

In the third stage the uniform surface loading is modeled numerically with the equivalent nodal forces. A point load,  $P$ , is applied to a node of the 4-node isoparametric plane strain element with the local coordinate of the point,  $\xi = \xi_p$  and  $\eta = 1$ . The principle of virtual work is applied again here with the virtual displacement  $u$  and  $v$  in the  $x$  and  $y$  directions respective at node  $i$ :

$$\begin{aligned} P_{xi} u &= P_x N_i(\xi_p, 1)u \\ P_{yi} v &= P_y N_i(\xi_p, 1)v \end{aligned} \quad (5.11)$$

where  $P_x$  and  $P_y$  are the components of the point load  $p$  acting in the  $x$  and  $y$  directions, respectively. Since equation 5.11 holds

for any value of  $u$  and  $v$ , it is equivalent to

$$\begin{Bmatrix} P_{xi} \\ P_{yi} \end{Bmatrix} = N_i(\xi_{p,1}) \begin{Bmatrix} P_x \\ P_y \end{Bmatrix} \quad (5.12)$$

where  $N_i$  are the shape functions which are used to relate the displacements at nodes to that at intermediate points. Again, the midpoint Runge-Kutta incremental scheme is used in the modeling of this external loading where the number of load increments can be specified by the program user.

The Gaussian integration scheme for the stiffness matrix used in the previous three stages is applied with 2x2 full-integration for the soil elements and with 1x1 under-integration for the culvert elements. The importance of under-integration on culvert stiffness is demonstrated in the following.

Four-node isoparametric elements are attractive because they are simple and have only corner nodes. But in bending they are too stiff. In Figure 5.2 the rectangular element with  $\xi = 2x/L$  and  $\eta = 2y/H$  is given the prescribed displacements  $\bar{u}$ . The element is deformed in pure bending as shown in Figure 5.2(b) because its sides must remain straight. Its deformation field is given by

$$u = \bar{u}\xi\eta \text{ and } v = 0 \quad (5.13)$$

The correct shape under pure bending is shown in Figure 5.2(c) and is expressed by

$$u = \bar{u}\xi\eta \text{ and } v = \frac{L\bar{u}}{2H} (1-\xi^2) + \nu \frac{H\bar{u}}{2L} (1-\eta^2) \quad (5.14)$$



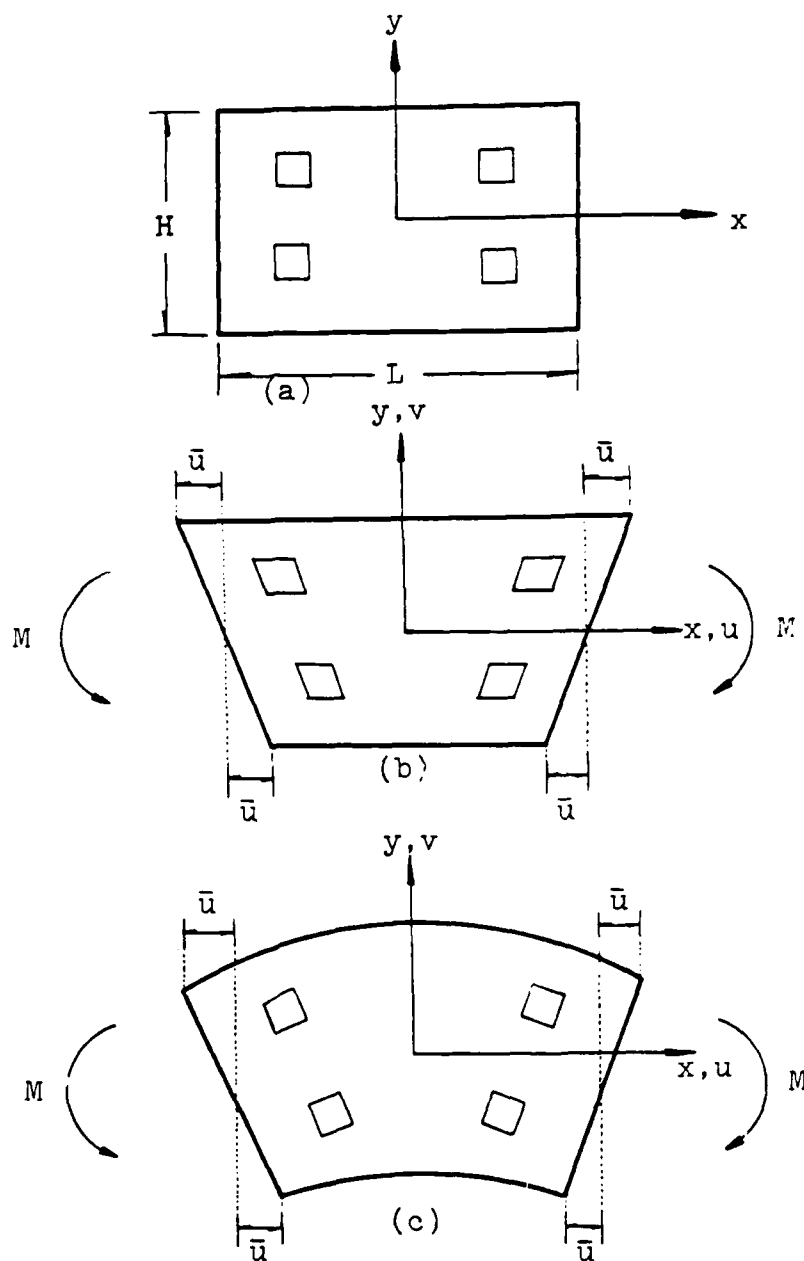


**Figure 5.2** A Rectangular Linear Element. Quadrilaterals Within the Element Represent Initial and Deformed Shapes at Gauss Points of a 2-by-2 Quadrature Rule (a) Undeformed Shape. (b) Prescribed d.o.f.  $\bar{u}$  Deform the Element in a Bending Mode. (c) The Correct Shape of a Beam Segment in Bending.

Equation 5.14 (from Cook, 1977) yields the correct value of shear strain,  $\gamma_{xy} = 0$ , but equation 5.13 yields a nonzero shear strain. The extra distortion due to shear is introduced by using this 4-node element so that this element becomes stiffer in the bending mode. This effect is called shear locking or parasitic shear. Its influence is disastrous if the aspect ratio,  $L/H$ , is large where  $L$  and  $H$  are defined in Figure 5.2. This is exactly the case for the buried flexible culvert whose deformed shape suggests that the bending mode is dominant. The aspect ratio used in the finite element analysis in this work range from 25 to 50 depending on the coarse or fine mesh layout. Therefore, shear locking is expected to play an important role in this soil and thin culvert system, and under-integration on the stiffness of culvert elements is utilized.

### 5.3 Numerical Formulations for Constitutive Laws

#### 5.3.1 Hyperbolic Constitutive Relations

The hyperbolic stress-strain relations were developed in section 4.3 for use in nonlinear incremental analysis of soil deformations. In each increment of such analysis the stress-strain behavior of the soil is treated as being linear, which can be expressed as follows for conditions of plane strain:

$$\begin{Bmatrix} \Delta\sigma_x \\ \Delta\sigma_y \\ \Delta\tau_{xy} \end{Bmatrix} = \frac{3B}{9B-E} \begin{bmatrix} 3B+E & 3B-E & 0 \\ 3B-E & 3B+E & 0 \\ 0 & 0 & E \end{bmatrix} \begin{Bmatrix} \Delta\epsilon_x \\ \Delta\epsilon_y \\ \Delta\gamma_{xy} \end{Bmatrix} \quad (5.15)$$

in which

$$B = K_b P_a \left( \frac{\sigma_3}{P_a} \right)^m \quad (4.24)$$

$$E = \left[ 1 - \frac{R_f (1 - \sin \phi) (\sigma_1 - \sigma_3)}{2c \cos \phi + 2 \sigma_3 \sin \phi} \right]^2 K P_a \left( \frac{\sigma_3}{P_a} \right)^n \quad (4.20)$$

for primary loading.

$$E = K_{ur} P_a \left( \frac{\sigma_3}{P_a} \right)^n \quad (4.21)$$

for unloading or reloading.

The values of the eight parameters appearing in the hyperbolic model are listed in Table 4.1.

Equation 5.15 is equivalent to Equation 4.5, and can be obtained by substituting

$$\nu = 0.5 - \frac{E}{6B} \quad (5.16)$$

into the latter.

The loading and unloading criteria are defined as follows:

$$\text{Primary loading, if } \left[ \frac{\sigma_1 - \sigma_3}{(\sigma_1 - \sigma_3)_f} \right]_{i+1} > \left[ \frac{\sigma_1 - \sigma_3}{(\sigma_1 - \sigma_3)_f} \right]_i \quad (B.1)$$

$$\text{Reloading \& unloading, if } \left[ \frac{\sigma_1 - \sigma_3}{(\sigma_1 - \sigma_3)_f} \right]_{i+1} \leq \left[ \frac{\sigma_1 - \sigma_3}{(\sigma_1 - \sigma_3)_f} \right]_i \quad (B.2)$$

$i$  = current increment

$i+1$  = subsequent increment.

### 5.3.2 Lade's Constitutive Relation

The numerical implementation of Lade's constitutive relations to solve boundary value problems has been quite limited so far. Ozawa (1973) and Ozawa and duncan (1976) were the first to apply the Lade's constitutive relation with one yield surface (Lade, 1972) to a passive earth pressure problem by the finite element method. The same work was further studied by Wong (1978) and Evgin (1981). The latest version of the Lade's relation (Lade, 1977) was first implemented by Aubry and Des Croix (1979, 1981). Lade and Nelson (1981, 1984) published an explicit formulation suitable for numerical implementation. Azevedo (1983) used this kind of numerical formulation in a finite element code to analyze excavations in sand.

In order to incorporate this constitutive model with two yield surfaces in a finite element code, it is necessary to develop an incremental stress- incremental strain relationship of the form

$$\{d\sigma\} = [Cep] \{d\epsilon\} \quad (5.17)$$

where

$$\{d\sigma\}^T = \{d\sigma_x \ d\sigma_y \ d\sigma_z \ d\tau_{xy} \ d\tau_{xz} \ d\tau_{yz}\} \quad (5.18)$$

and

$$\{d\epsilon\}^T = \{d\epsilon_x \ d\epsilon_y \ d\epsilon_z \ d\gamma_{xy} \ d\gamma_{xz} \ d\gamma_{yz}\} \quad (5.19)$$

Each of these two yield surfaces is assumed to produce plastic strain increments whose sum, together with the elastic strain increments, makes up the total strain increments

$$\{d\epsilon\} = \{d\epsilon^e\} + \{d\epsilon^c\} + \{d\epsilon^p\} \quad (4.28)$$

The incremental form of Equation 4.3 gives the relation of incremental elastic strain and incremental stress:

$$\{d\sigma\} = [C^e] \{d\epsilon^e\} \quad (5.20)$$

For the work-hardening material, the yield functions of collapse and expansive plastic strains are expressed as

$$F_c (\{\sigma\}, W_c) = 0 \quad (4.31)$$

and

$$F_p (\{\sigma\}, W_p) = 0 \quad (4.40)$$

respectively. The consistency condition states that loading from a plastic state must again lead to another plastic state, which means that

$$F_c + dF_c = 0, \quad F_p + dF_p = 0 \quad (5.21)$$

Eliminating  $F_c$  and  $F_p$  from Equations 5.21, 4.31 and 4.40, we obtain

$$dF_c (\{\sigma\}, W_c) = 0 \quad (5.22)$$

and

$$dF_p (\{\sigma\}, W_c) = 0 \quad (5.23)$$

The flow rules used for collapsive and expansive plastic strains are

$$\{d\epsilon^C\} = \lambda_C \left\{ \frac{\partial g_C}{\partial \sigma} \right\}, \quad \lambda_C \geq 0 \quad (4.36)$$

and

$$\{d\epsilon^P\} = \lambda_P \left\{ \frac{\partial g_P}{\partial \sigma} \right\}, \quad \lambda_P \geq 0 \quad (4.50)$$

respectively.

Equations 5.22 and 5.23 can be expressed in the following forms:

$$\left\{ \frac{\partial F_C}{\partial \sigma} \right\}^T \{d\sigma\} + \left\{ \frac{\partial F_C}{\partial \epsilon^C} \right\}^T \{d\epsilon^C\} = 0 \quad (5.24)$$

$$\left\{ \frac{\partial F_P}{\partial \sigma} \right\}^T \{d\sigma\} + \left\{ \frac{\partial F_P}{\partial \epsilon^P} \right\}^T \{d\epsilon^P\} = 0$$

From Equation 5.20 and 4.28:

$$\{d\sigma\} = [C\epsilon] (\{d\epsilon\} - \{d\epsilon^C\} - \{d\epsilon^P\}) \quad (5.25)$$

Substituting Equation 5.25 into Equation 5.24 gives:

$$\left\{ \frac{\partial F_C}{\partial \sigma} \right\}^T [C\epsilon] (\{d\epsilon\} - \{d\epsilon^C\} - \{d\epsilon^P\}) + \left\{ \frac{\partial F_C}{\partial \epsilon^C} \right\}^T \{d\epsilon^C\} = 0 \quad (5.26)$$

$$\left\{ \frac{\partial F_P}{\partial \sigma} \right\}^T [C\epsilon] (\{d\epsilon\} - \{d\epsilon^C\} - \{d\epsilon^P\}) + \left\{ \frac{\partial F_P}{\partial \epsilon^P} \right\}^T \{d\epsilon^P\} = 0$$

Equation 5.25 can be represented by using Equations 4.36 and 4.50

$$\left\{ \frac{\partial F_C}{\partial \sigma} \right\}^T [C\epsilon] (\{d\epsilon\} - \lambda_C \left\{ \frac{\partial g_C}{\partial \sigma} \right\} - \lambda_P \left\{ \frac{\partial g_P}{\partial \sigma} \right\}) + \left\{ \frac{\partial F_C}{\partial \epsilon^C} \right\}^T \left\{ \frac{\partial g_C}{\partial \sigma} \right\} \lambda_C = 0 \quad (5.27)$$

$$\left\{ \frac{\partial F_P}{\partial \sigma} \right\}^T [C\epsilon] (\{d\epsilon\} - \lambda_C \left\{ \frac{\partial g_C}{\partial \sigma} \right\} - \lambda_P \left\{ \frac{\partial g_P}{\partial \sigma} \right\}) + \left\{ \frac{\partial F_P}{\partial \epsilon^P} \right\}^T \left\{ \frac{\partial g_P}{\partial \sigma} \right\} \lambda_P = 0$$

These equations may be written in matrix form as

$$\left[ \frac{\partial F}{\partial \sigma} \right]^T [C\epsilon] (\{d\epsilon\} - \left[ \frac{\partial g}{\partial \sigma} \right] \{\lambda\}) + [D] \{\lambda\} = \{0\} \quad (5.28)$$

where

$$\left[ \frac{\partial F}{\partial \sigma} \right]_{6 \times 2}^T = \left[ \left\{ \frac{\partial F_C}{\partial \sigma} \right\}_{6 \times 1} \left\{ \frac{\partial F_P}{\partial \sigma} \right\}_{6 \times 1} \right]^T \quad (5.29)$$

$$\left[ \frac{\partial g}{\partial \sigma} \right]_{6 \times 2} = \left[ \left\{ \frac{\partial g_C}{\partial \sigma} \right\}_{6 \times 1} \left\{ \frac{\partial g_P}{\partial \sigma} \right\}_{6 \times 1} \right] \quad (5.30)$$

$$\{\lambda\}_{2 \times 1} = \begin{Bmatrix} \lambda_C \\ \lambda_P \end{Bmatrix} \quad (5.31)$$

and

$$[D]_{2 \times 2} = \begin{bmatrix} \left\{ \frac{\partial F_C}{\partial \epsilon^C} \right\}^T \left\{ \frac{\partial g_C}{\partial \sigma} \right\} & 0 \\ 0 & \left\{ \frac{\partial F_P}{\partial \epsilon^P} \right\}^T \left\{ \frac{\partial g_P}{\partial \sigma} \right\} \end{bmatrix} \quad (5.32)$$

From Equations 4.31 and 4.35

$$\left\{ \frac{\partial F_C}{\partial \epsilon^C} \right\} = \left\{ \frac{\partial f_C''}{\partial \epsilon^C} \right\} = \frac{\partial f_C''}{\partial w_C} \{\sigma\} \quad (5.33)$$

where  $f_C''$  is a function of  $w_C$  only.

Similarly, from Equations 4.40 and 4.51

$$\left\{ \frac{\partial F_p}{\partial \epsilon_p} \right\} = \left\{ \frac{\partial f_p''}{\partial \epsilon_p} \right\} = \frac{\partial f_p''}{\partial w_p} \{ \sigma \} \quad (5.34)$$

where  $f_p''$  is a function of  $w_p$  only.

[D] can be expressed in the following form:

$$[D]_{2 \times 2} = \begin{bmatrix} \frac{\partial f_c''}{\partial w_c} \{ \sigma \}^T \left\{ \frac{\partial g_c}{\partial \sigma} \right\} & 0 \\ 0 & \frac{\partial f_p''}{\partial w_p} \{ \sigma \}^T \left\{ \frac{\partial g_p}{\partial \sigma} \right\} \end{bmatrix} \quad (5.35)$$

Similarly Equation 5.29 can be rewritten as follows

$$\left[ \frac{\partial F}{\partial \sigma} \right]_{2 \times 6}^T = \left[ \frac{\partial f}{\partial \sigma} \right]^T = \left[ \left\{ \frac{\partial f_c'}{\partial \sigma} \right\} \left\{ \frac{\partial f_p'}{\partial \sigma} \right\} \right]^T \quad (5.36)$$

where  $f_c'$  and  $f_p'$  depend on stress only.

Equation 5.28 may be written as:

$$\left( \left[ \frac{\partial f}{\partial \sigma} \right]^T [C^e] \left[ \frac{\partial g}{\partial \sigma} \right] - [D] \right) \{ \lambda \} = \left[ \frac{\partial f}{\partial \sigma} \right]^T [C^e] \{ d\epsilon \} \quad (5.37)$$

or

$$\{ \lambda \} = [L]^{-1} \left[ \frac{\partial f}{\partial \sigma} \right]^T [C^e] \{ d\epsilon \} \quad (5.38)$$



in which

$$[L]_{2 \times 2} = \left[ \frac{\partial f}{\partial \sigma} \right]^T [c^e] \left[ \frac{\partial g}{\partial \sigma} \right] - [D] \quad (5.39)$$

From Equations 5.25, 4.36 and 4.50

$$\{d\sigma\} = [c^e] (\{d\epsilon\} - \left[ \frac{\partial g}{\partial \sigma} \right] \{\lambda\}) \quad (5.40)$$

Substituting Equation 5.38 into Equation 5.40 gives:

$$\{d\sigma\} = ([c^e] - [c^e] \left[ \frac{\partial g}{\partial \sigma} \right] [L]^{-1} \left[ \frac{\partial f}{\partial \sigma} \right]^T [c^e]) \{d\epsilon\} \quad (5.41)$$

Thus

$$[c^e p] = [c^e] - [c^e] \left[ \frac{\partial g}{\partial \sigma} \right] [L]^{-1} \left[ \frac{\partial f}{\partial \sigma} \right]^T [c^e] \quad (5.42)$$

or

$$[c^e p] = [c^e] - \frac{[c^e]}{A} \left( \left\{ \frac{\partial g_c}{\partial \sigma} \right\} \{b_c\}^T + \left\{ \frac{\partial g_p}{\partial \sigma} \right\} \{b_p\}^T \right) [c^e] \quad (5.43)$$

$$\text{where } A = L_{11} \cdot L_{22} - L_{12} \cdot L_{21} \quad (5.44)$$

$$\{b_c\} = L_{22} \cdot \left\{ \frac{\partial f'_c}{\partial \sigma} \right\} - L_{12} \cdot \left\{ \frac{\partial f'_p}{\partial \sigma} \right\} \quad (5.45)$$

$$\{b_p\} = L_{11} \cdot \left\{ \frac{\partial f'_p}{\partial \sigma} \right\} - L_{21} \cdot \left\{ \frac{\partial f'_c}{\partial \sigma} \right\} \quad (5.46)$$

$$\left\{ \frac{\partial f'_C}{\partial \sigma} \right\} = \left\{ \frac{\partial g_C}{\partial \sigma} \right\} = 2 \begin{Bmatrix} \sigma_x \\ \sigma_y \\ \sigma_z \\ 2\tau_{xy} \\ 2\tau_{zx} \\ 2\tau_{yz} \end{Bmatrix} \quad (5.47)$$

$$\left\{ \frac{\partial f'_p}{\partial \sigma} \right\} = \frac{I_1^2}{I_2^3} \left( \frac{I_1}{P_a} \right)^m \begin{Bmatrix} 3I_3 - (\sigma_y \sigma_z - \tau_{yz}^2) I_1 \\ 3I_3 - (\sigma_z \sigma_x - \tau_{zx}^2) I_1 \\ 3I_3 - (\sigma_x \sigma_y - \tau_{xy}^2) I_1 \\ 2(\sigma_z \tau_{xy} - \tau_{zx} \tau_{yz}) I_1 \\ 2(\sigma_y \tau_{zx} - \tau_{yz} \tau_{xy}) I_1 \\ 2(\sigma_x \tau_{yz} - \tau_{xy} \tau_{zx}) I_1 \end{Bmatrix} + \left( \frac{I_1^3}{I_3} - 27 \right) \frac{I_1}{P_a} \left( \frac{I_1}{P_a} \right)^{m-1} \begin{Bmatrix} 1 \\ 1 \\ 1 \\ 0 \\ 0 \\ 0 \end{Bmatrix} \quad (5.48)$$

and

$$\left\{ \frac{\partial g_p}{\partial \sigma} \right\} = -(27 + \eta_2 \left( \frac{P_a}{I_1} \right)^m) \begin{Bmatrix} \sigma_y \sigma_z - \tau_{yz}^2 \\ \sigma_z \sigma_x - \tau_{zx}^2 \\ \sigma_x \sigma_y - \tau_{xy}^2 \\ -2(\sigma_z \tau_{xy} - \tau_{zx} \tau_{yz}) \\ -2(\sigma_y \tau_{zx} - \tau_{yz} \tau_{xy}) \\ -2(\sigma_x \tau_{yz} - \tau_{xy} \tau_{zx}) \end{Bmatrix} + \left( 3I_1^2 + \frac{I_3}{I_1} \eta_2 \left( \frac{P_a}{I_1} \right)^m \right) \begin{Bmatrix} 1 \\ 1 \\ 1 \\ 0 \\ 0 \\ 0 \end{Bmatrix} \quad (5.49)$$

From Equations 5.39 and 5.35

$$L_{11} = \left\{ \frac{\partial f'_C}{\partial \sigma} \right\}^T [C^e] \left\{ \frac{\partial g_C}{\partial \sigma} \right\} + \frac{\partial f'_C}{\partial w_C} \{\sigma\}^T \left\{ \frac{\partial g_C}{\partial \sigma} \right\} \quad (5.50)$$

$$L_{22} = \left\{ \frac{\partial f_p'}{\partial \sigma} \right\}^T [C^e] \left\{ \frac{\partial g_p}{\partial \sigma} \right\} + \frac{\partial f_p''}{\partial w_p} \{\sigma\}^T \left\{ \frac{\partial g_p}{\partial \sigma} \right\} \quad (5.51)$$

$$L_{12} = \left\{ \frac{\partial f_c'}{\partial \sigma} \right\}^T [C^e] \left\{ \frac{\partial g_p}{\partial \sigma} \right\} \quad (5.52)$$

$$L_{21} = \left\{ \frac{\partial f_p'}{\partial \sigma} \right\}^T [C^e] \left\{ \frac{\partial g_c}{\partial \sigma} \right\} \quad (5.53)$$

Using Equation 4.38

$$\frac{\partial f_c''}{\partial w_c} = \frac{P_a}{CP} \left( \frac{f_c'}{P_a^2} \right)^{1-P} \quad (5.54)$$

from Equation 4.54

$$\frac{\partial f_p''}{\partial w_p} = f_p \left( \frac{1}{q w_p} - b \right) \quad (5.55)$$

Thus, the implementation of this incremental procedure can be carried out by using those equations from 5.43 to 5.55.

## CHAPTER VI

### COMPARISON BETWEEN CENTRIFUGAL AND ANALYTICAL RESULTS

In this chapter, comparisons are made between the centrifuge test results and analytical results obtained from the finite element analysis. The accuracy of the finite element program used is first demonstrated by using it to analyze a boundary value problem that has an exact, closed form solution.

#### 6.1 Verification of Analytical Model

The boundary value problem chosen for verification of the finite element program is shown in Figure 6.1. It consists of a linearly elastic soil mass loaded in plane strain conditions by its self weight as in a centrifuge. The loading considered acts only in y-direction and is therefore by the unit weight of the soil as

$$\gamma = \gamma_g \frac{\omega^2 y}{g} \quad (6.1)$$

where  $\omega$  = angular velocity = 198 rpm

$g$  = earth's gravity = 32.2 ft/sec<sup>2</sup>

$\gamma_g$  = unit weight of soil under earth's gravity

$y$  = radius to point under consideration.

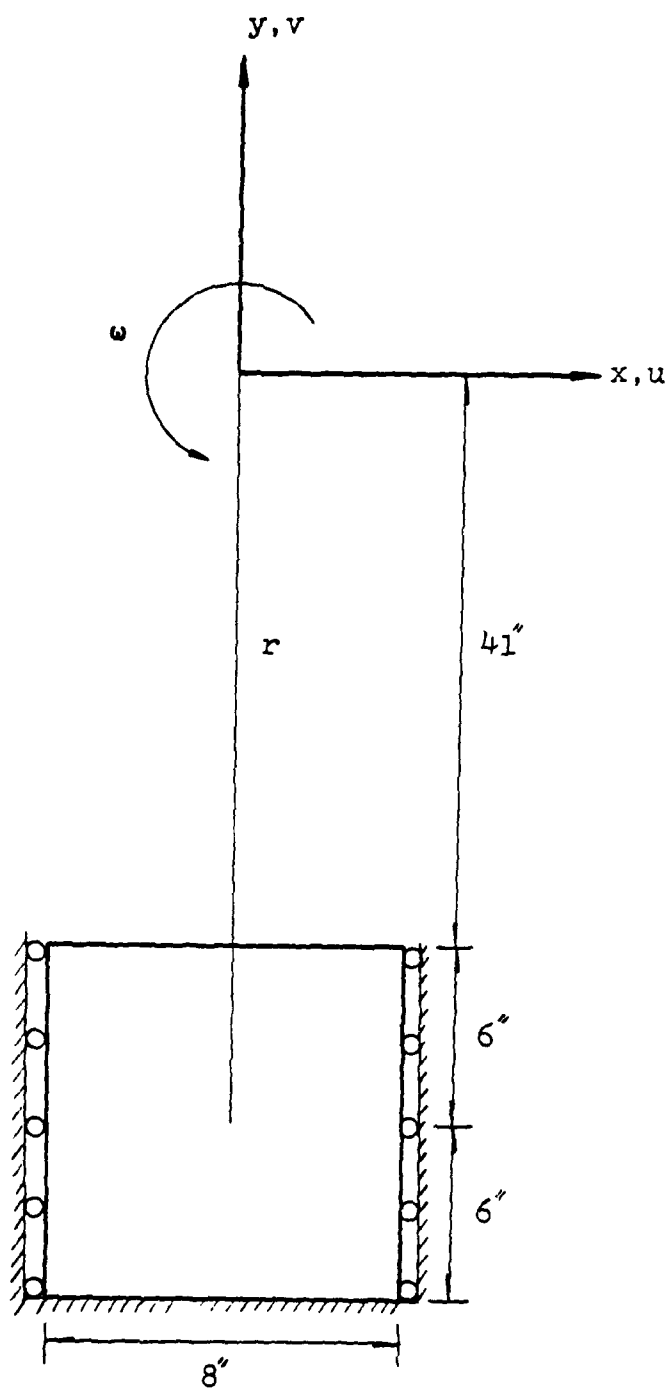


Figure 6.1 Idealized Problem I

For this analysis, it is assumed that  $\gamma_g$  acts in the y-direction. The close form solution to this problem is given by

$$v = \frac{A}{6} (-y^3 + 3L_1^2 y - 3L_1^2 L_2 + L_2^3) \quad (6.2)$$

$$\epsilon_y = \frac{A}{2} (L_1^2 - y^2) \quad (6.3)$$

$$\sigma_y = \frac{\gamma_g \omega^2}{2g} (L_1^2 - y^2) \quad (6.4)$$

where  $A = \frac{(1+\nu)(1-2\nu)\gamma_g \omega^2}{E(1-\nu)g}$

$$L_1 = -41 \text{ inches}$$

$$L_2 = -53 \text{ inches}$$

$$v = \text{displacement in the y-direction}$$

$$E = \text{Young's modulus} = 2500 \text{ psi}$$

$$\nu = \text{Poisson's ration} = 0.3$$

This problem is also analyzed by a finite element method in which the continuum is modeled by one 4 node element with the same boundary conditions. The comparison between the close form solution and finite element solution is listed in Table 6.1.

The acceleration force is correctly simulated in the finite element code. The stress and displacement are almost the same as the true solution with error 2.2% and 4.5%, respectively. This discrepancy arises because the displacement field is modeled by bilinear function whereas the true displacement is cubic function as shown in Equation 6.2. To prove this, another problem is

TABLE 6.1 Comparison Between Close Form and Numerical Solutions of an Idealized Problem I

item method	vertical stress at center (psi)	displacement at top surface (inches)	acceleration force (lb)
true solutions	-22.8	-0.6778	-365
numerical solutions	-23.3	-0.0813	-365

considered. A close form solutions of the same continuum (but weightless) with a linear elastic constitutive law under plane strain, no side friction, and uniform surface loading conditions (Figure 6.2) are expressed in the following

$$v = - \frac{p(1+\nu)(1-2\nu)}{E(1-\nu)} (y - L_2) \quad (6.5)$$

$$\sigma_y = p$$

$$\epsilon_y = p \frac{(1+\nu)(1-2\nu)}{E(1-\nu)} \quad (6.7)$$

Equation 6.5 is linear function which can be correctly modeled by the bilinear shape functions of 4 node quadrilateral elements. The comparison between the true solutions and numerical solutions is shown in Table 6.2. The stresses and displacements are exactly evaluated by the finite element method. Therefore, the analytical model with linear elasticity is correctly established.

The hyperbolic and Lade's relation implementations are checked next. First, a stress-controlled program for each constitutive relation is developed. The prediction from these program for CTC tests are pretty good except that the hyperbolic model can not catch the dilatant behavior as shown in Figures 4.4, 4.5, 4.18 and 4.19. Furthermore, Azevedo (1983) checked the similar algorithm by comparing the solution from a stress-controlled program with the solution from finite element program for the plane



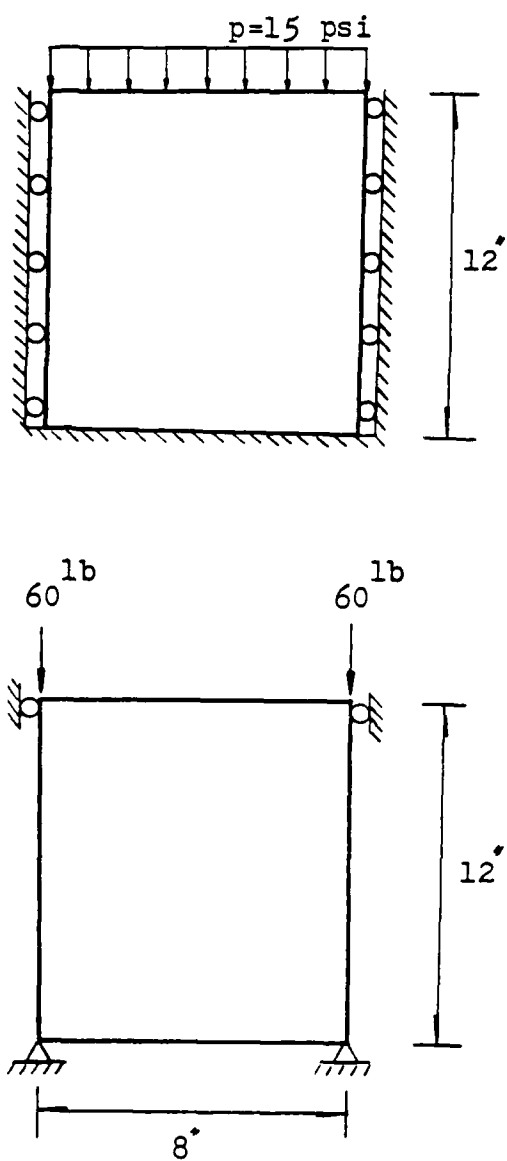


Figure 6.2 Idealized Problem II

TABLE 6.2 Comparison Between Close Form and Numerical Solutions  
of an Idealized Problem II

<u>item</u> <u>method</u>	vertical stress at center (psi)	displacement at top surface (inches)	acceleration force (lb)
true solutions	-15	-0.05348	-6.429
numerical solutions	-15	-0.05348	-6.429

strain triaxial compression. The agreement is very good, thus leading to the conclusion that the analytical models were properly implemented.

## 6.2 Convergence Studies

Two studies were carried out to investigate the convergence of the numerical solutions. Firstly, to study the influence of the mesh size on the accuracy and stability of the numerical solution, three meshes with progressively smaller element size and increasing degree of freedom were used to analyze the buried culvert. Secondly, the number of load increments used to obtain the nonlinear solutions of hyperbolic and Lade's models was progressively increased with the same mesh configuration in order to see if the convergence could be achieved.

Mesh 1 with 43 elements, mesh 2 with 76 elements, and mesh 3 with 122 elements are shown in Figures 6.3, 6.4 and 6.5, respectively. The deflections at the crown and the springline used to study the convergence of the analysis with the hyperbolic soil model are shown in Figures 6.6 and 6.7, respectively. Monotonic convergence to the true solution is obvious. Similarly, Figures 6.8 and 6.9 show the same feature of monotonic convergence of the analytical solutions with Lade's soil model.

To study the influence of the number of load increments, 2, 8 and 16 load increments were used for mesh 3. Figure 6.10 shows the relation between the deflection at the crown and the

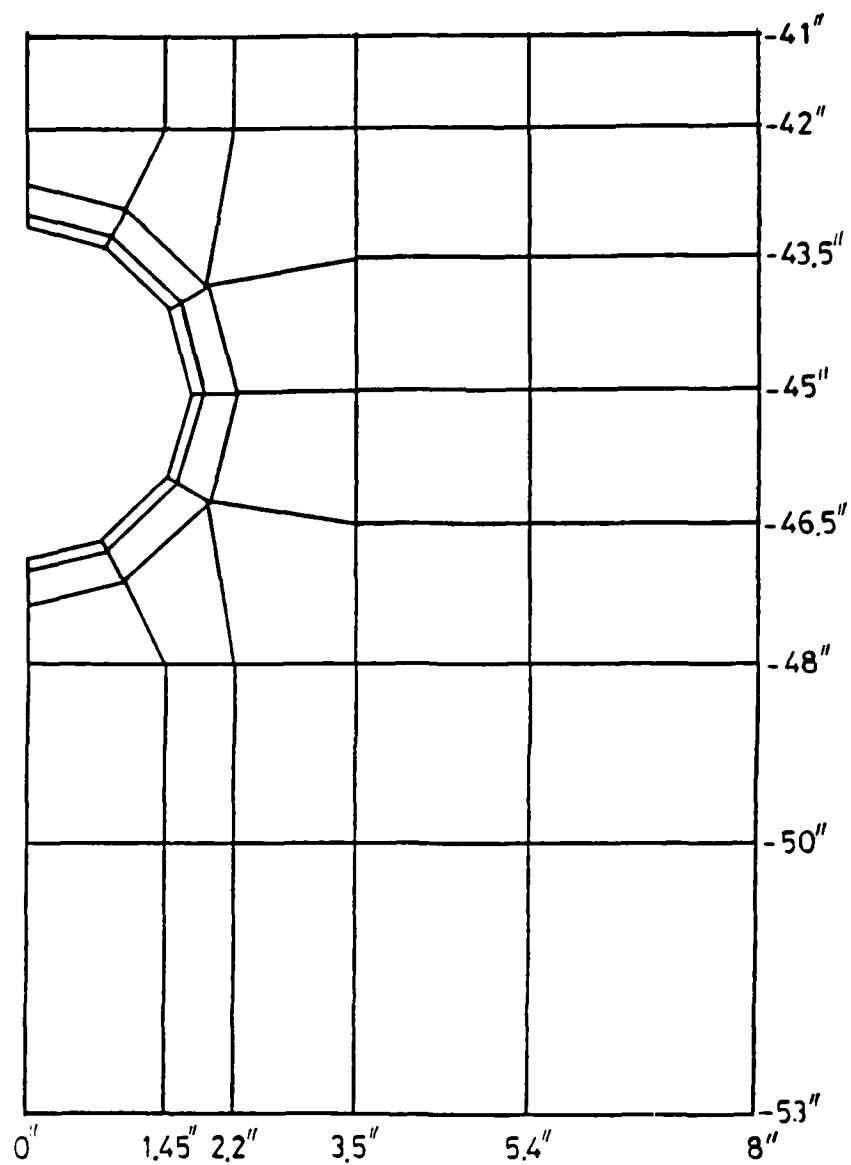


Figure 6.3 Mesh 1 with 43 Elements

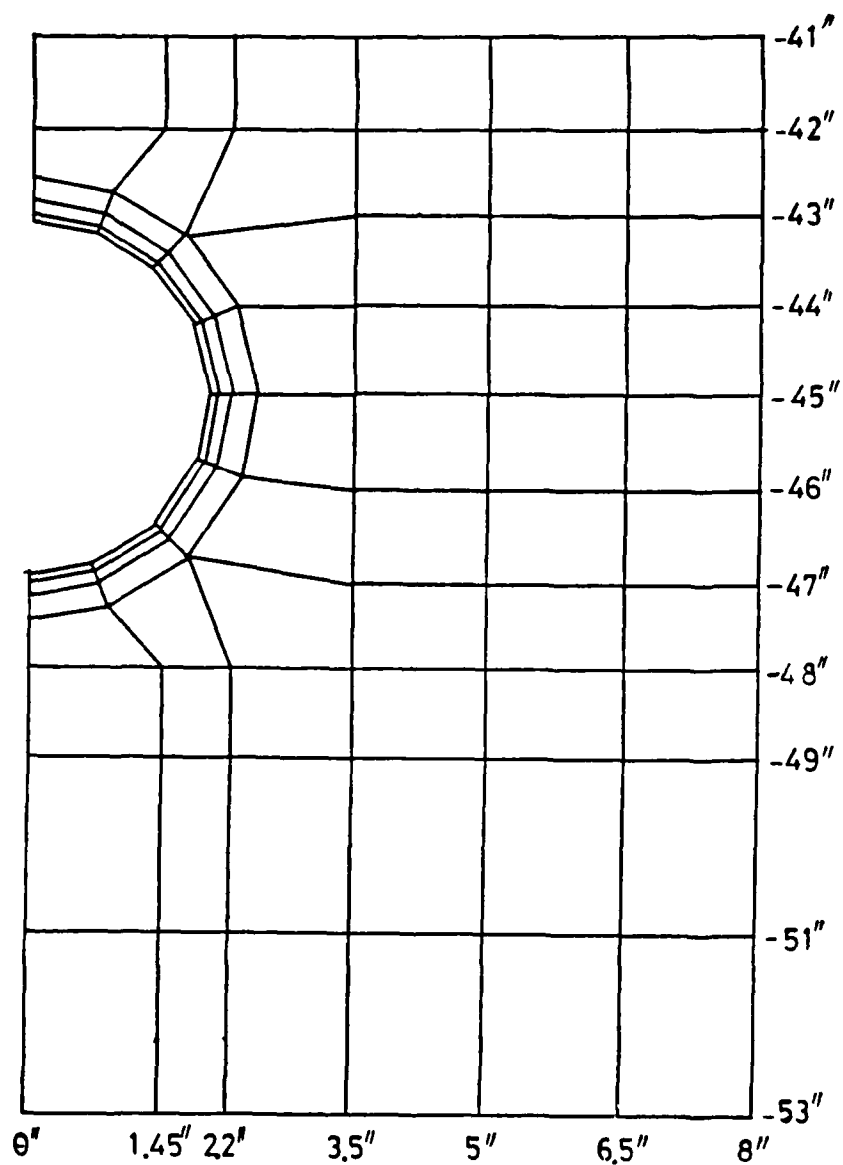


Figure 6.4 Mesh 2 with 76 Elements

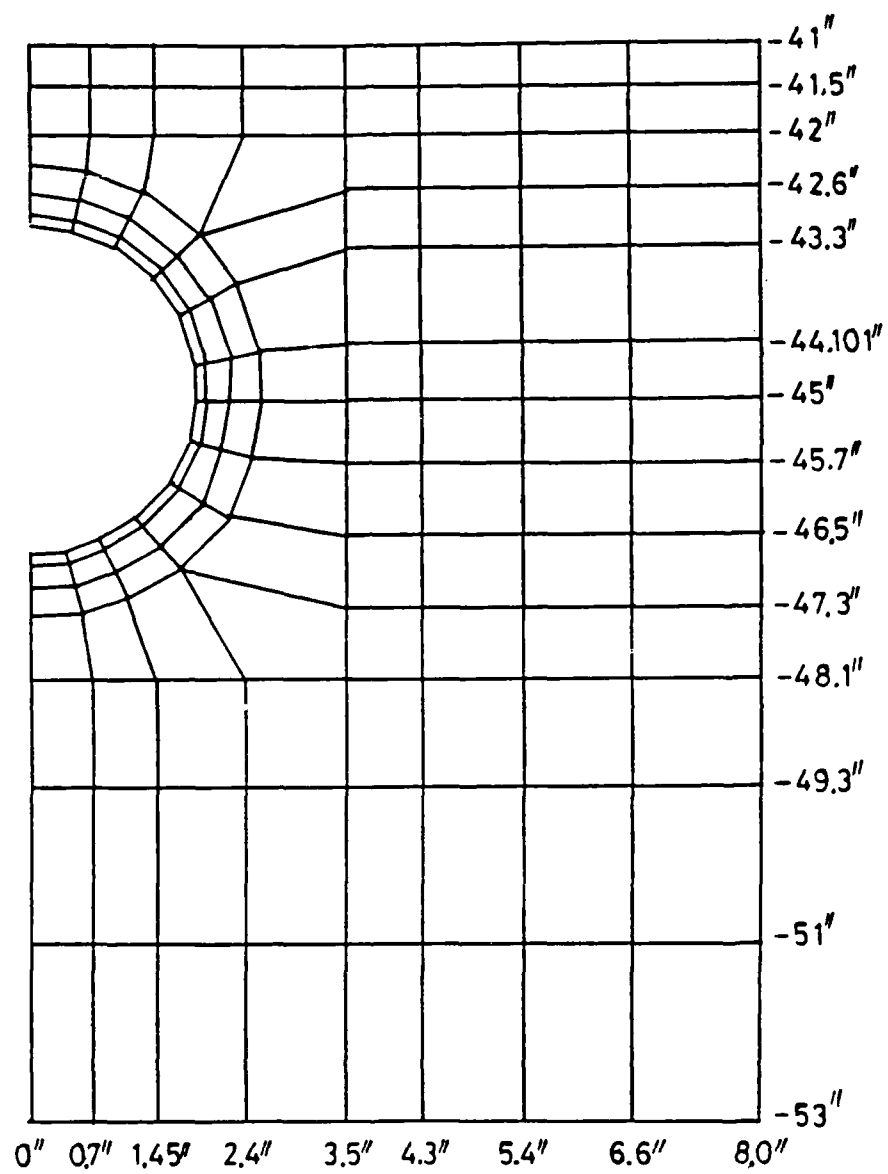


Figure 6.5 Mesh 3 with 122 Elements

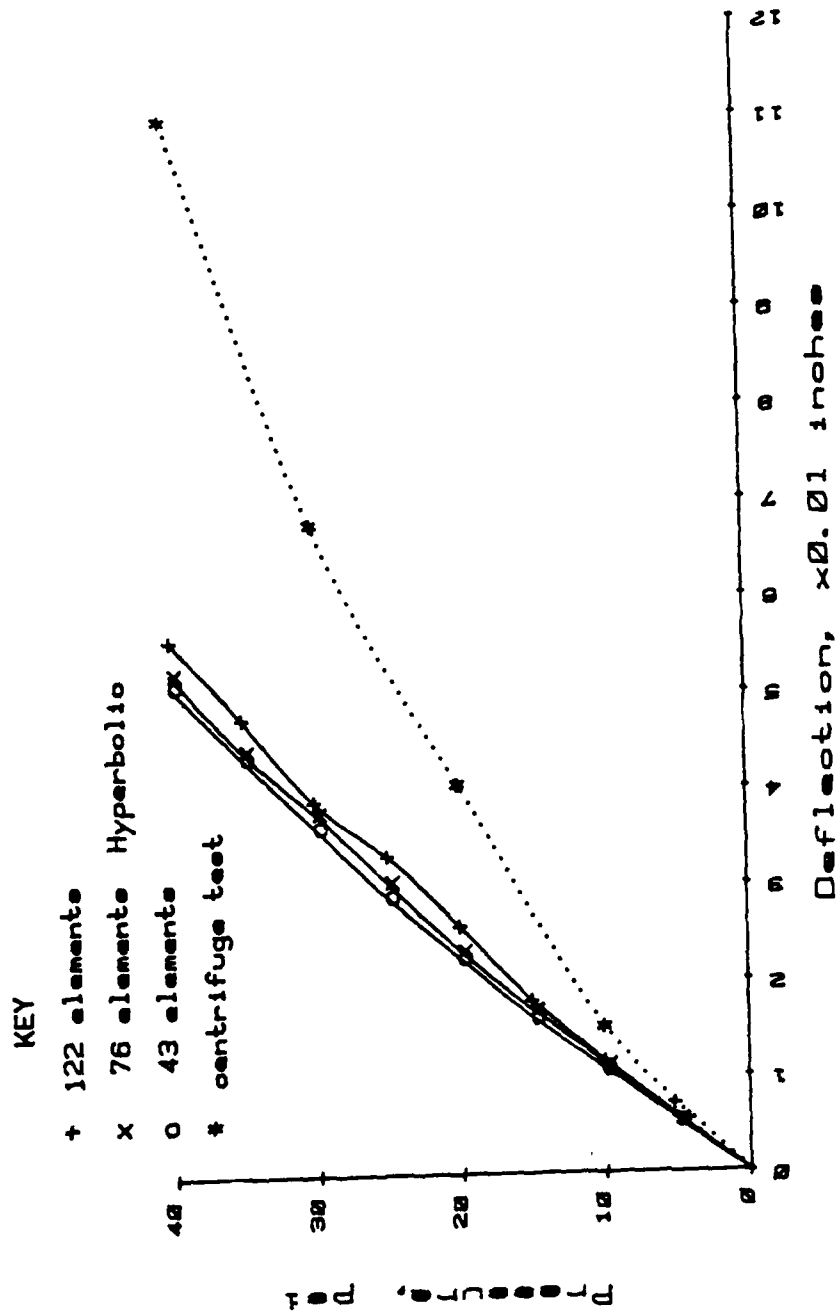


Figure 6.6 Convergence Study on Refined Meshes.  
Deflection at Crown. Hyperbolic Soil Model

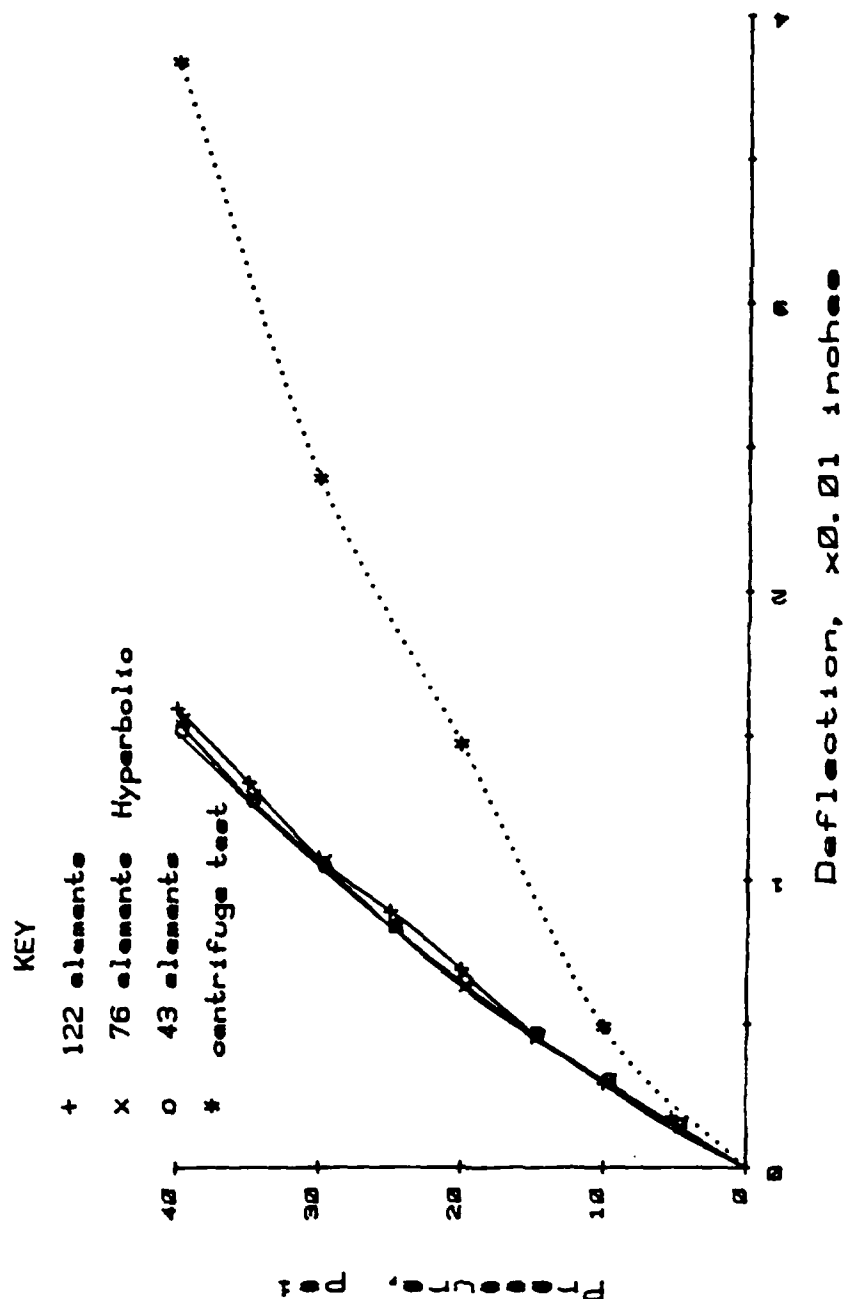


Figure 6.7 Convergence Study on Refined Meshes.  
Deflection at Springline. Hyperbolic Soil Model.



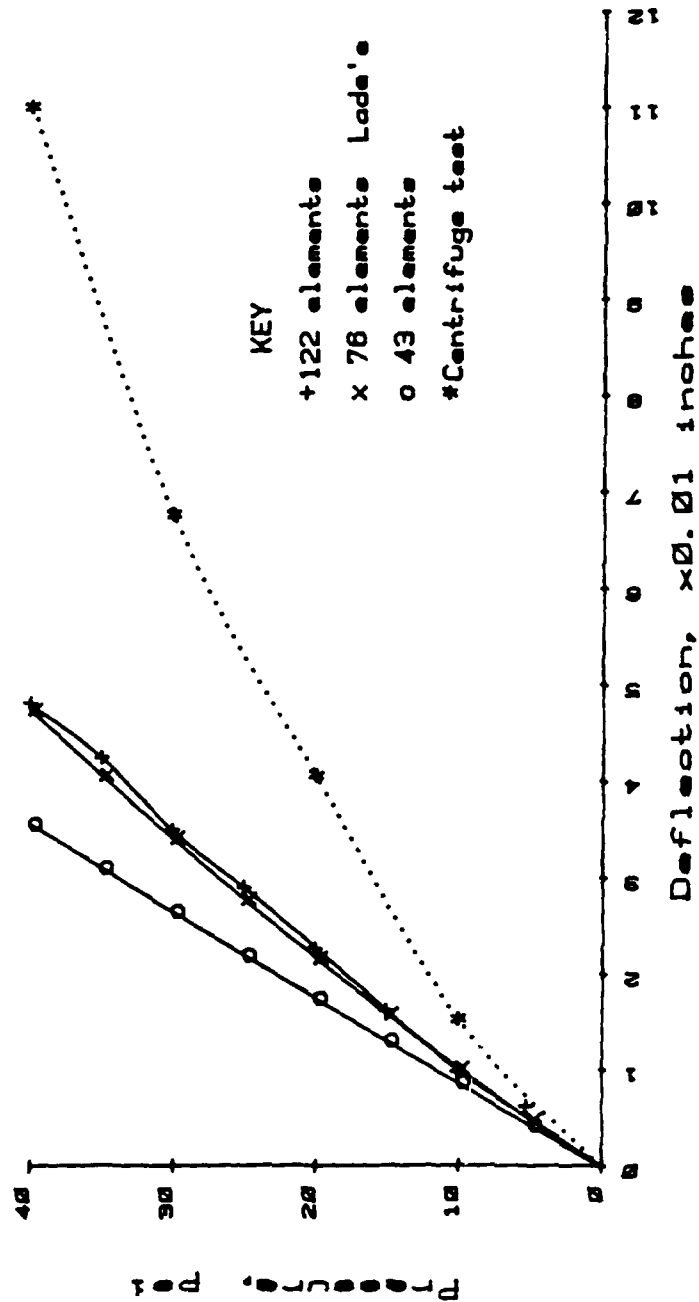


Figure 6.8 Convergence Study on Refined Meshes.  
Deflection at Crown. Lade's Soil Model

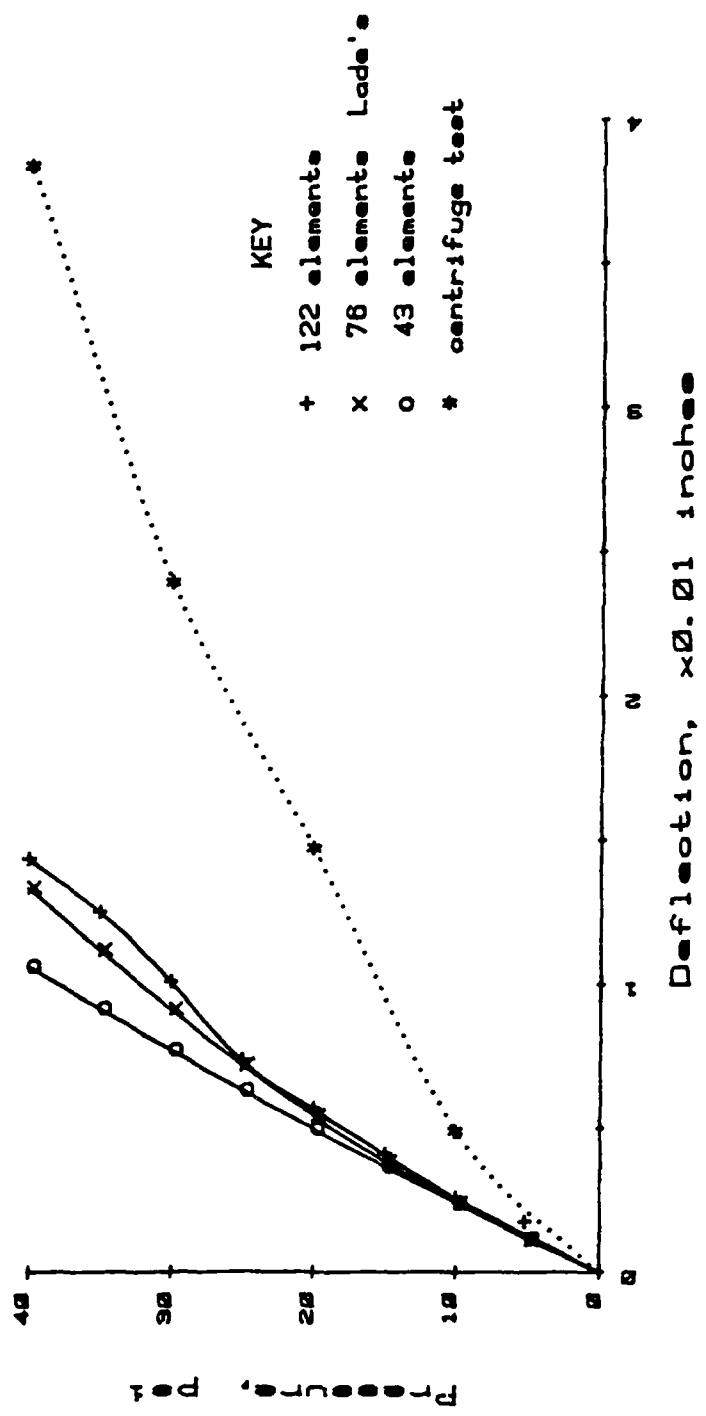


Figure 6.9 Convergence Study on Refined Meshes.  
Deflection at Springline. Lade's Soil Model

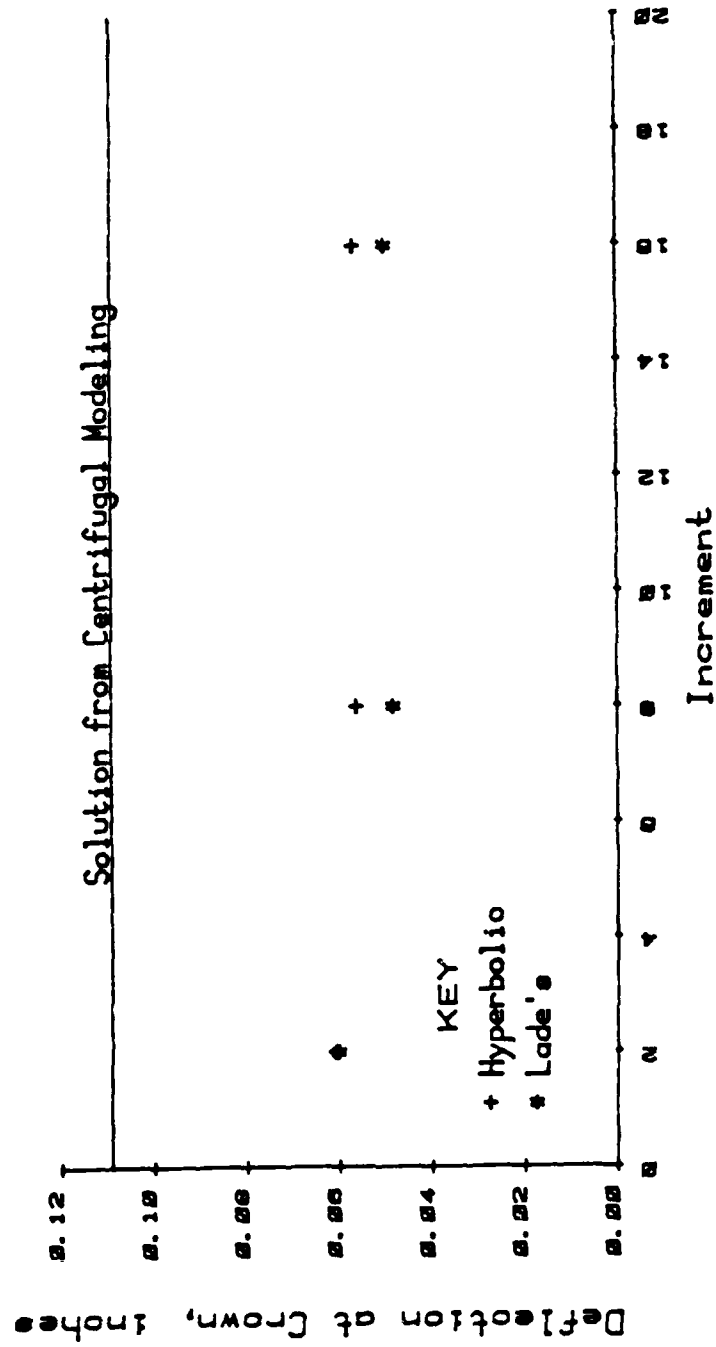


Figure 6.10 Convergence Study on Load Increment

load increment. The more the number of load increments, the stiffer the soil-culvert system. This seems to contradict what is expected, i.e., softer behavior with more increments. The reason for this is the key in this study and is explained as follows.

The horizontal stresses are smaller than the vertical stresses due to self weight loading in the soil-culvert system before the surface loading is applied. During surface loading, the horizontal stresses in the region shaded in Figure 6.11 increase at a higher rate than the vertical stresses. This type of stress path will only generate collapsive plastic strain in the Lade's soil model with only the cap-type yield surface (Figure 4.7) being activated. The predicted collapsive plastic volumetric strain by Lade's constitutive relation is much smaller than the real value as shown in Figure 4.20. This is because the soil prepared by static compaction possesses very high anisotropy which causes the soil to be softer when the applied major principal stress is acting perpendicularly to the direction of compaction (Budiman, 1985). However, since Lade's constitutive relation can only deal with isotropic materials, it was calibrated by using laboratory test results obtained from the CTC test in which the major principal stress acts in the same direction as soil compaction during sample preparation. The use of the constitutive relation thus calibrated results in very small collapsive plastic strain in the shaded region in Figure 6.11, so that the soil-culvert system becomes stiffer during the surface loading stage.

AD-A172 482

CENTRIFUGAL AND ANALYTICAL MODELING OF A BURIED  
FLEXIBLE CONDUIT (U) COLORADO UNIV AT BOULDER DEPT OF  
CIVIL ENVIRONMENTAL AND ARCH J C MI 31 OCT 85

3/3

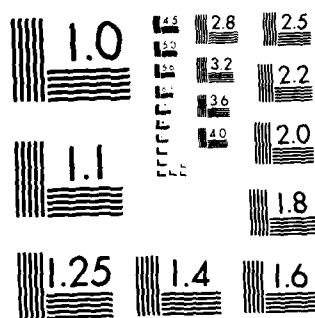
UNCLASSIFIED

AFOSR-IR-86-0050 AFOSR-84-0300

F/C 13/13

NL

END  
DATE  
FILMED  
11 86  
DTIC



XEROCOPY RESOLUTION TEST CHART  
NATIONAL BUREAU OF STANDARDS 1963 A

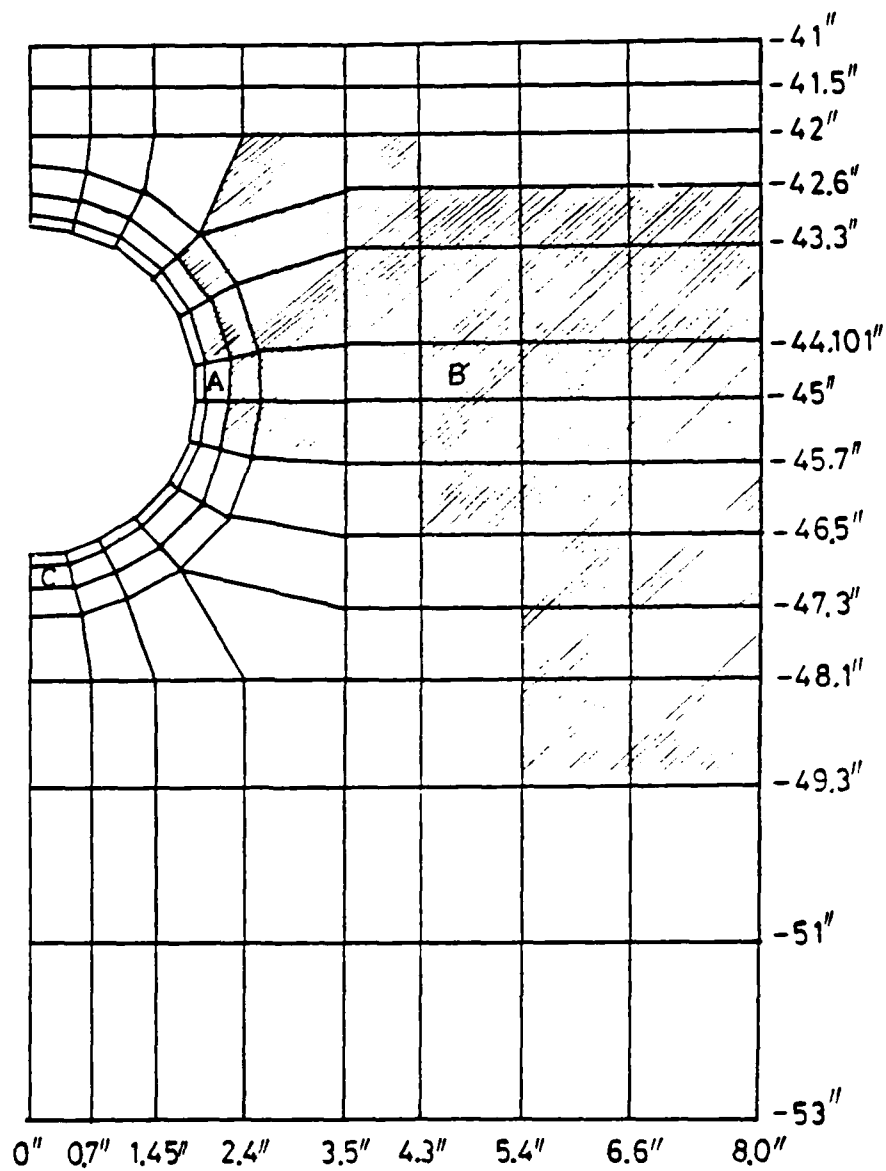


Figure 6.11 Stiffer Elements in Mesh 3

That is why "the more number of the load increments, the stiffer the soil-culvert system". The same phenomena are observed in the analytical solution with hyperbolic soil relation, i.e.,

$$\frac{\Delta\sigma_3}{\Delta\sigma_1} > \frac{\sigma_3}{\sigma_1} \quad (6.8)$$

where  $\sigma_1$  and  $\sigma_3$  are the stresses before the surface loading, and  $\Delta\sigma_1$  and  $\Delta\sigma_3$  are incremental stresses during the surface loading stage. By applying the loading and unloading criteria (Equations B.9 and B.10) the unloading or reloading Young's modulus is activated. Those shaded elements with higher stiffness during surface loading stage pose like a constraint which explains the fact that the soil-culvert system becomes stiffer numerically during surface loading. The above comment indirectly demonstrates that the convergence study on the load increment is correct. To prove this directly, an unconfined compression tests with plane strain boundary condition were simulated with Lade's and hyperbolic constitutive relations. Continuous hardening behavior was observed while the load increment was increased. Therefore, all the above description demonstrates that the convergence studies of these analytical solutions are valid.

### 6.3 Comparisons Between Centrifugal and Analytical Results

The importance of under-integration in computing the stiffness response of a flexible, buried tube is demonstrated first. The crown of the tube deflects linearly regardless of the



type of nonlinear soil model if the full-integration of stiffness matrix is used. This is shown in Figure 6.12. Due to the shear locking, the tube is hardly deflected in the numerical analysis. Figure 6.12 also shows that the deflection calculated with the under-integration technique is a more reasonable solution than the value from full-integration. Next, the deflection curve predicted by linear elasticity shows the importance of choices of  $E$  and  $\nu$ . In this study, we assume the true solution is given by the results of the centrifuge test. By adjusting the values of  $E$  and  $\nu$ , a reasonable solution could be obtained that would match the centrifuge results. In reality, however, the true solution for each different boundary value problem is unknown. The proper selection of  $E$  and  $\nu$  to match the solution, therefore, also becomes impossible. The use of linear elasticity to represent soil behavior is not realistic. Therefore, only the analytical methods with hyperbolic and Lade's constitutive relations for soil and with under-integration scheme will be demonstrated from now on.

#### 6.3.1 Symmetrical Loading

The mesh shown in Figure 6.5 was used in analyzing the symmetrical loading case. The predicted deflections of the buried culvert from using the analytical methods with hyperbolic and Lade's constitutive relations, together with centrifugal test results under 10, 20, 30 and 40 psi surface loading, are shown in Figures 6.13, 6.14, 6.15 and 6.16, respectively. Except at the invert, the analytical methods always underestimate the deflection. The analytical solutions from the hyperbolic soil relation

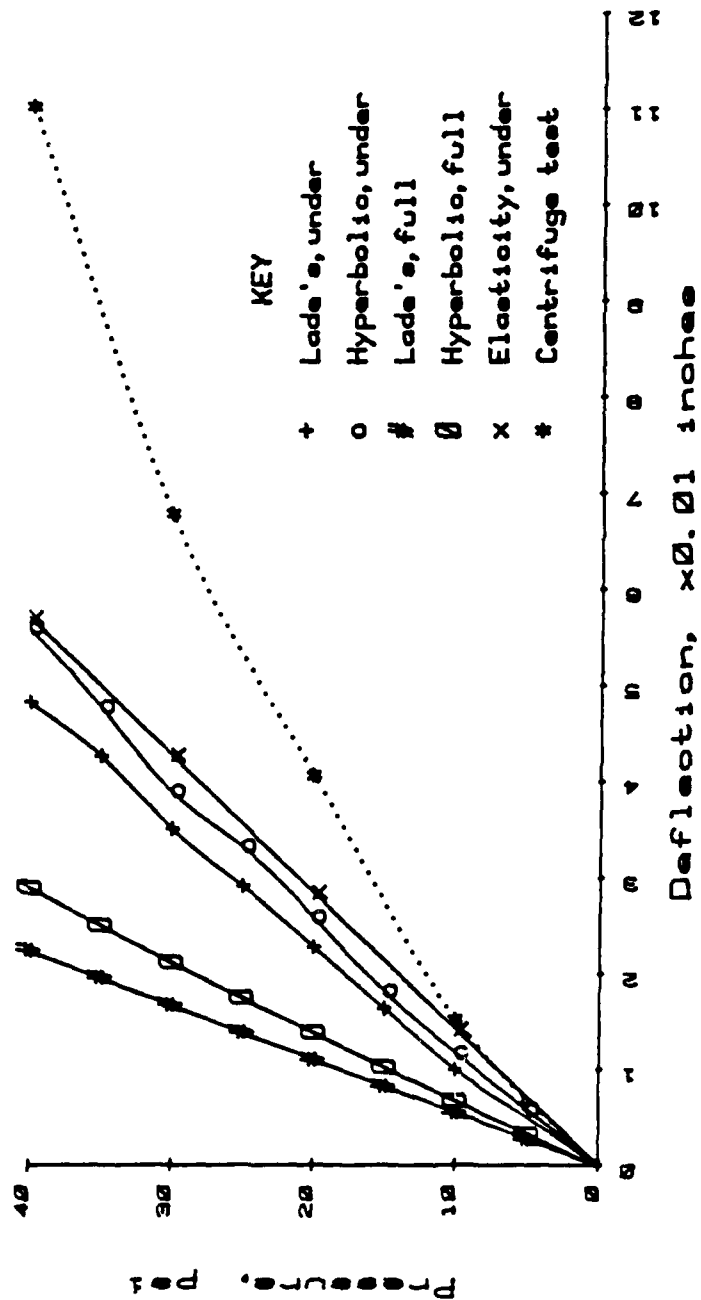


Figure 6.12 Comparison Between Under- and Full-Integration

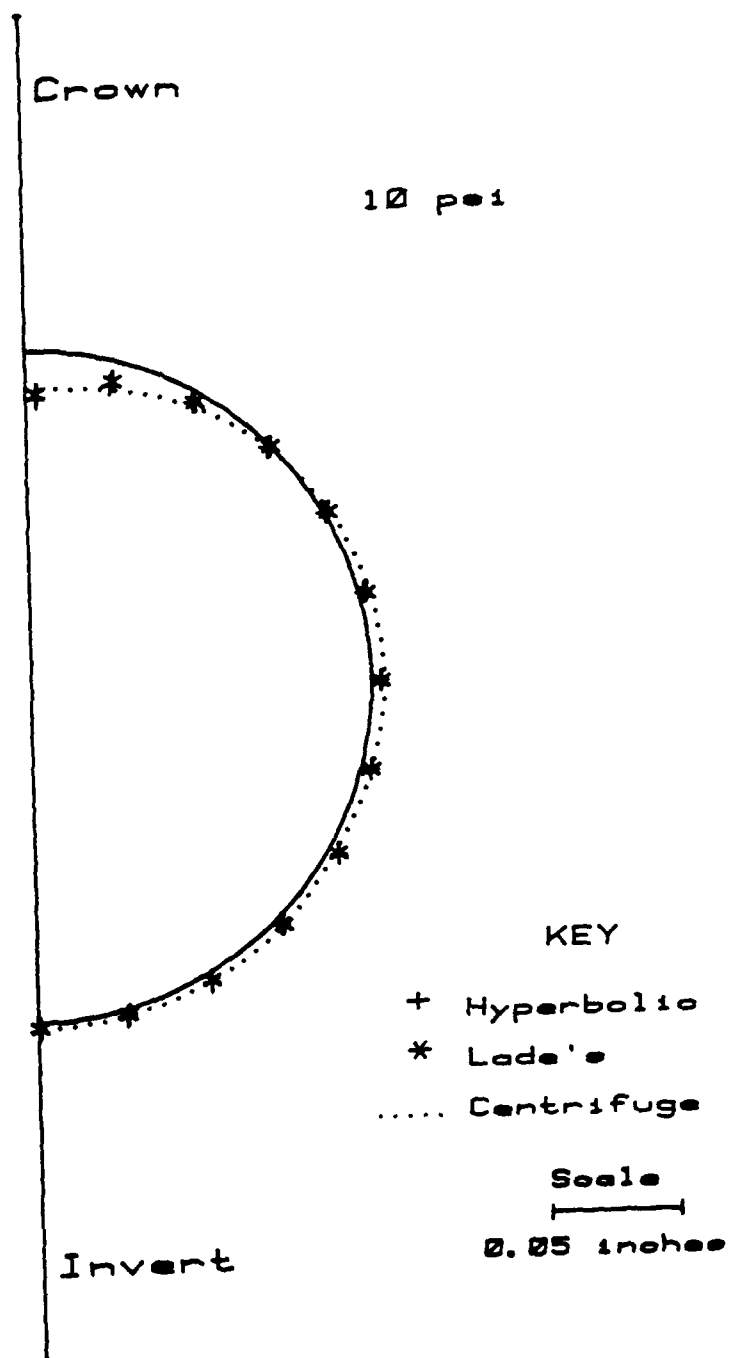


Figure 6.13 Comparison of Deflections.  
Symmetrical Load 10 psi

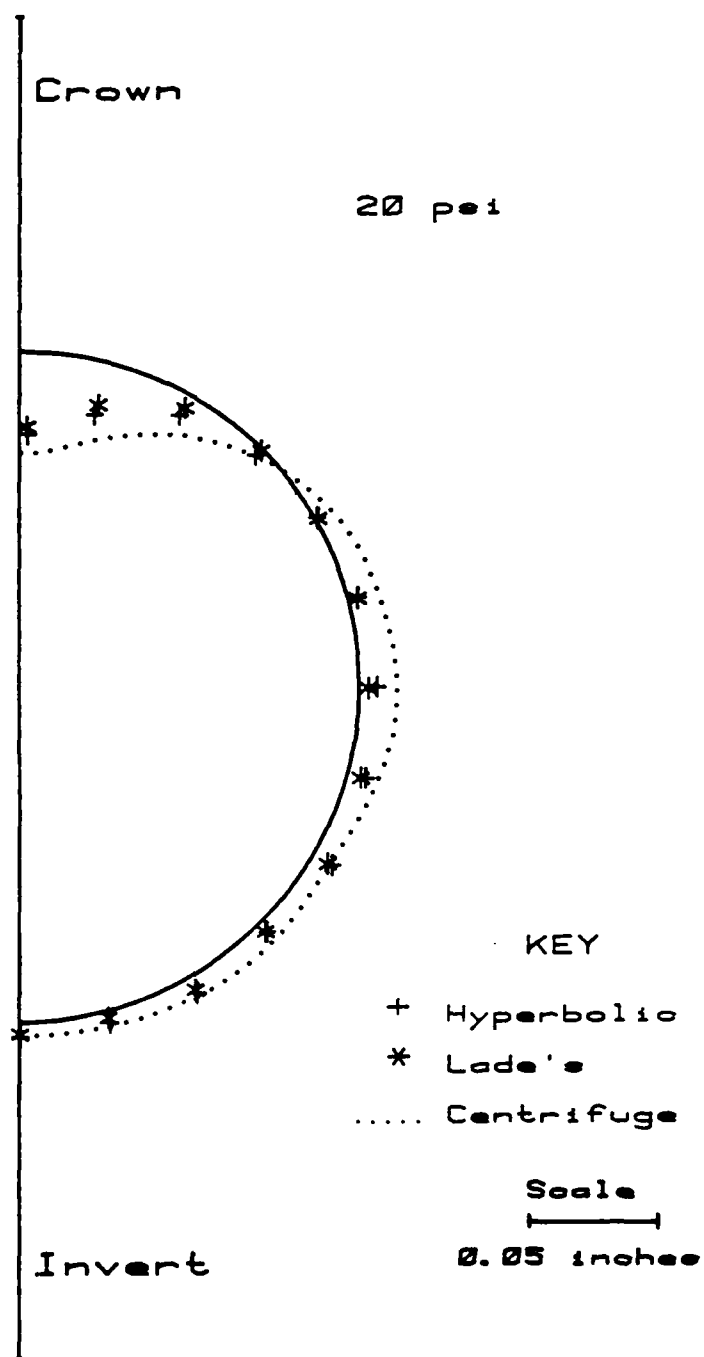


Figure 6.14 Comparison of Deflections.  
Symmetrical Load 20 psi

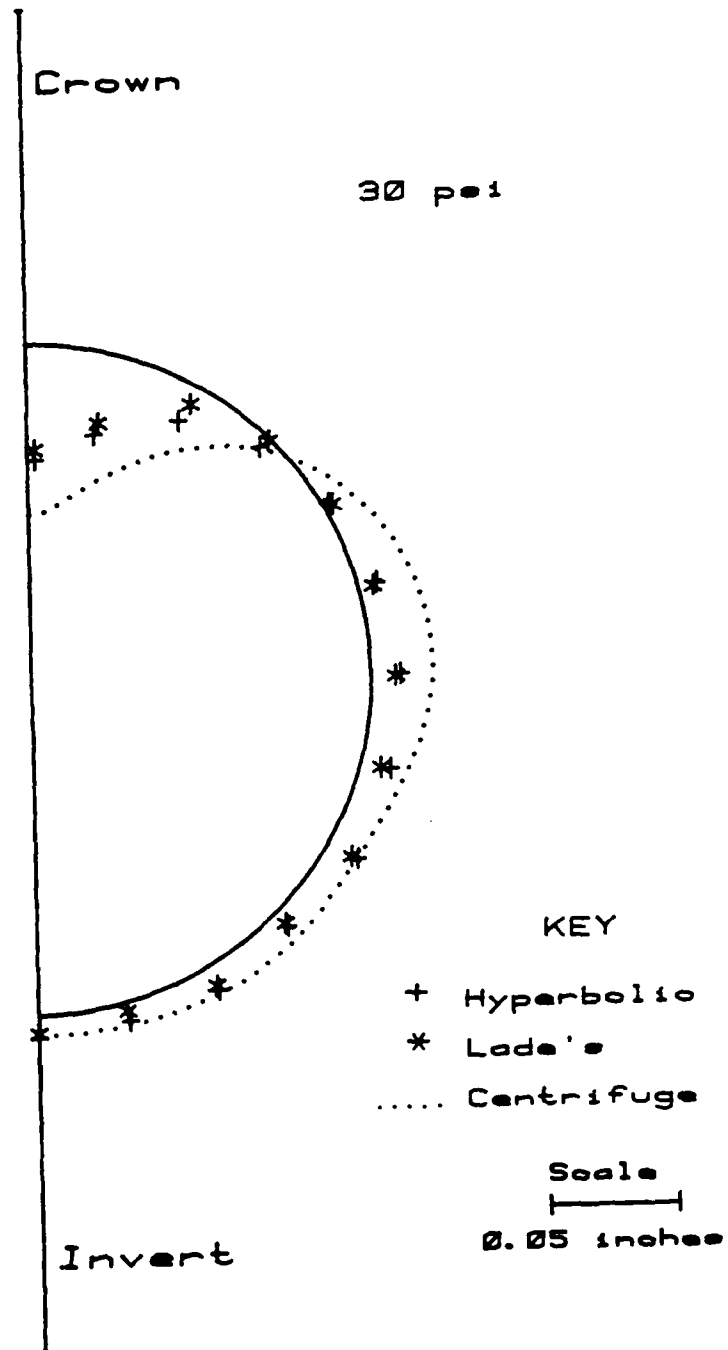


Figure 6.15 Comparison of Deflections.  
Symmetrical Load 30 psi

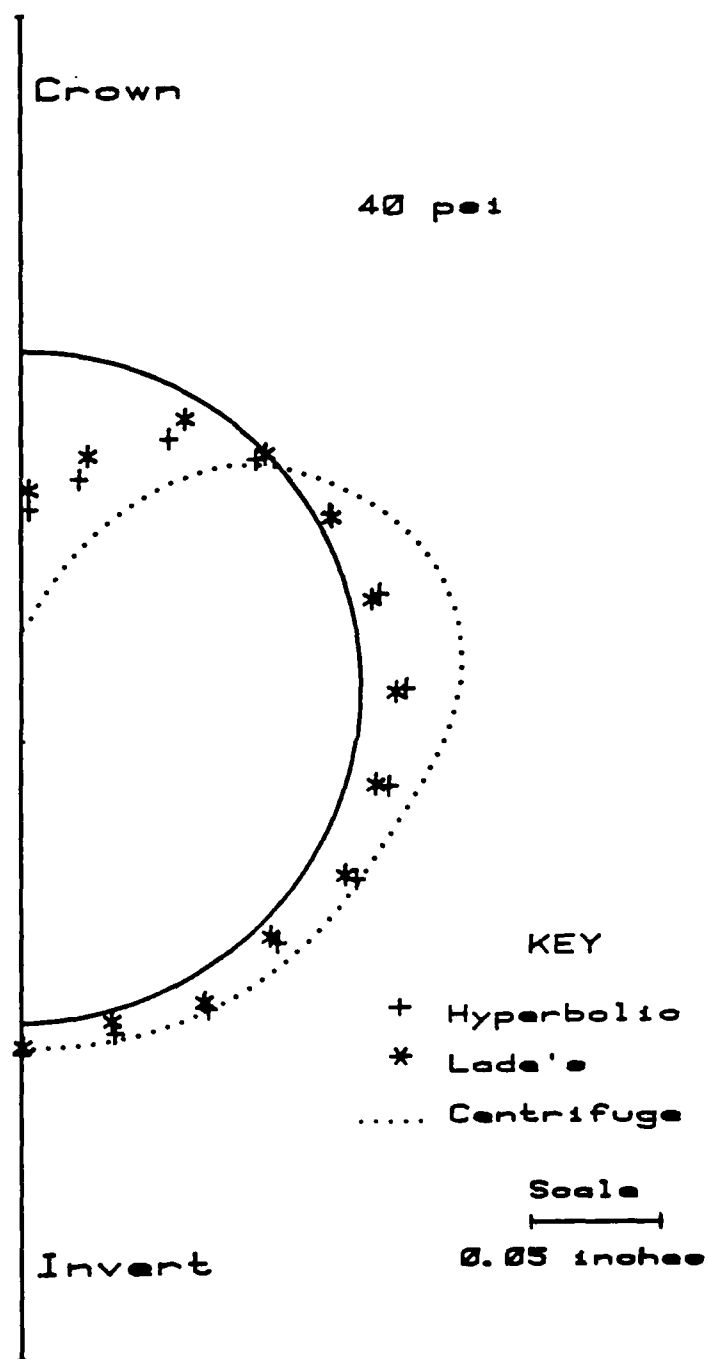


Figure 6.16 Comparison of Deflections.  
Symmetrical Load 40 psi

show better results than that from Lade's soil relation. The important features like the largest inward deflection at the crown and outward deflection at the springline have been correctly predicted. The deflection curve at each point along the circumference of the tube is very similar to those at the crown (Figure 6.12) except for different magnitudes of deflections.

The hoop stresses calculated by both soil models under the self weight loading at 50g are very similar, with the largest hoop stress at the haunch and the smallest at the crown as shown in Figures 6.17 and 6.18 where compressive value is plotted inside the tube. The centrifugal test data for the hoop stresses are not available due to problems with the strain gauge amplifiers. Under the surface loading of 10, 20, 30 and 40 psi, the corresponding hoop stresses are drawn in Figures 6.19 and 6.20 for both soil models. The largest hoop stress are found at the shoulder and the smallest at the invert. Again, the results are very similar. However, the centrifugal test results in Figure 3.31 show completely different hoop stresses from those two analytical solutions. The solutions from the centrifuge tests were believed to be wrong although all the gauges have been checked to function correctly. The following explanation is offered. To protect the gauges from the penetration of sand grain, a circumferential strip of soil, 0.18" width and running half way around the tube from the crown to the invert, was removed (Step 7, section 3.8). This is shown in figure 6.21. This eliminated the contact between the soil the gauges, preventing any damages of the latter from impinge-

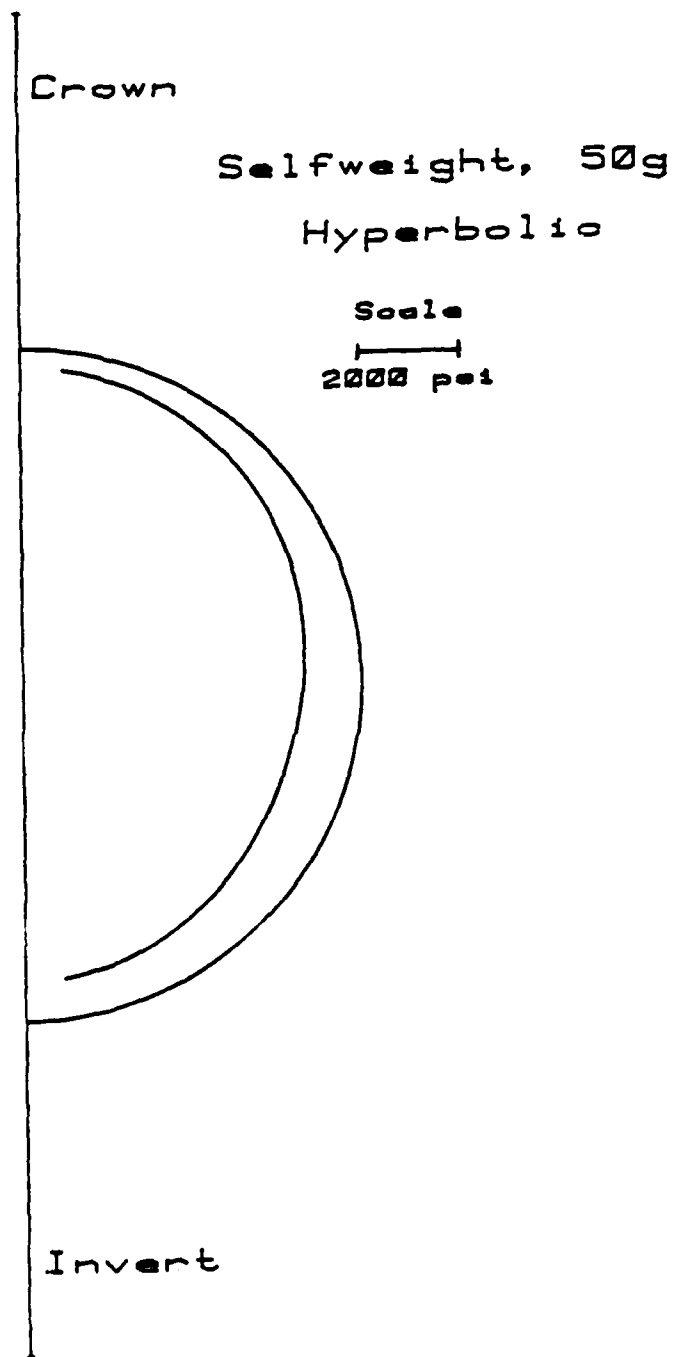


Figure 6.17 Hoop Stresses Under Selfweight.  
Hyperbolic Soil Model



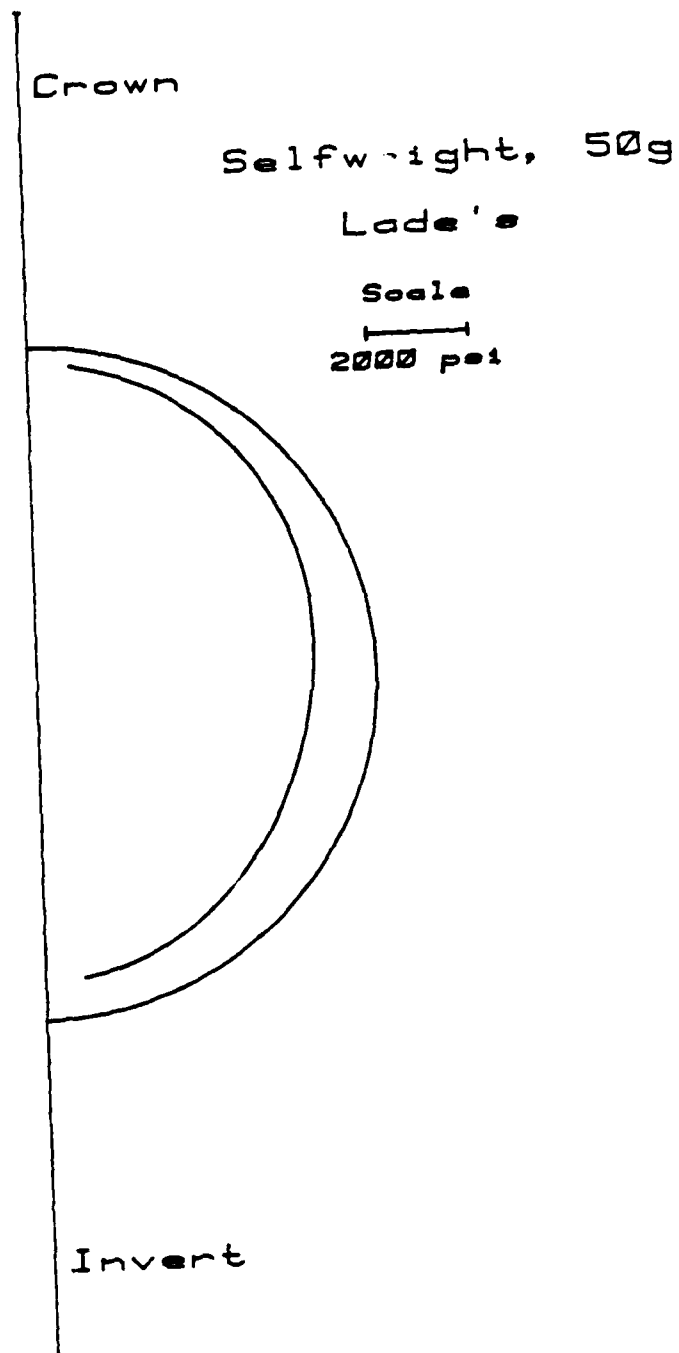


Figure 6.18 Hoop Stresses Under Selfweight.  
Lade's Soil Model

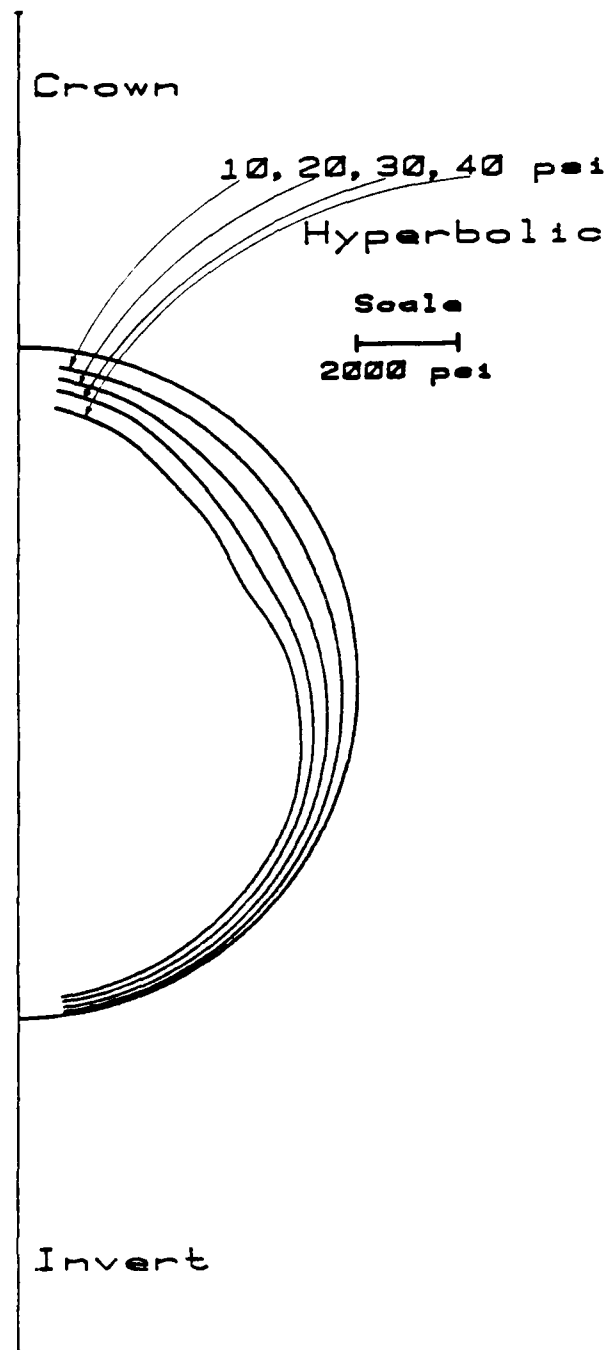


Figure 6.19 Hoop Stresses Under Symmetrical Load.  
Hyperbolic Soil Model

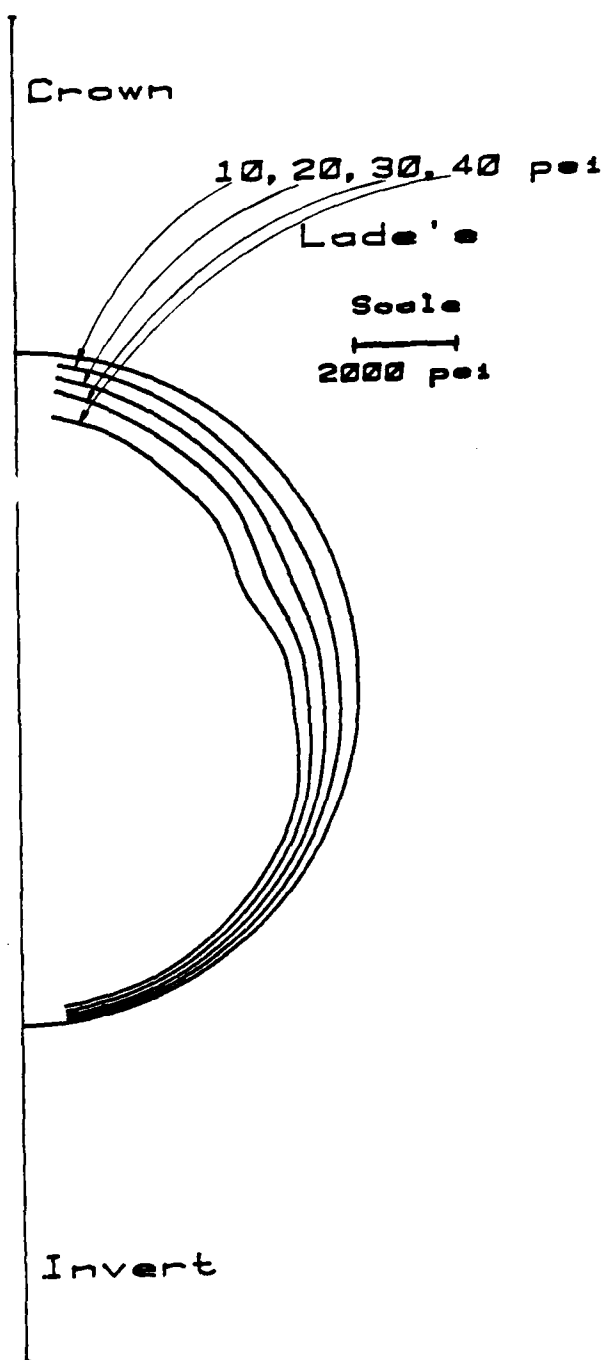


Figure 6.20 Hoop Stresses Under Symmetrical Load.  
Lade's Soil Model

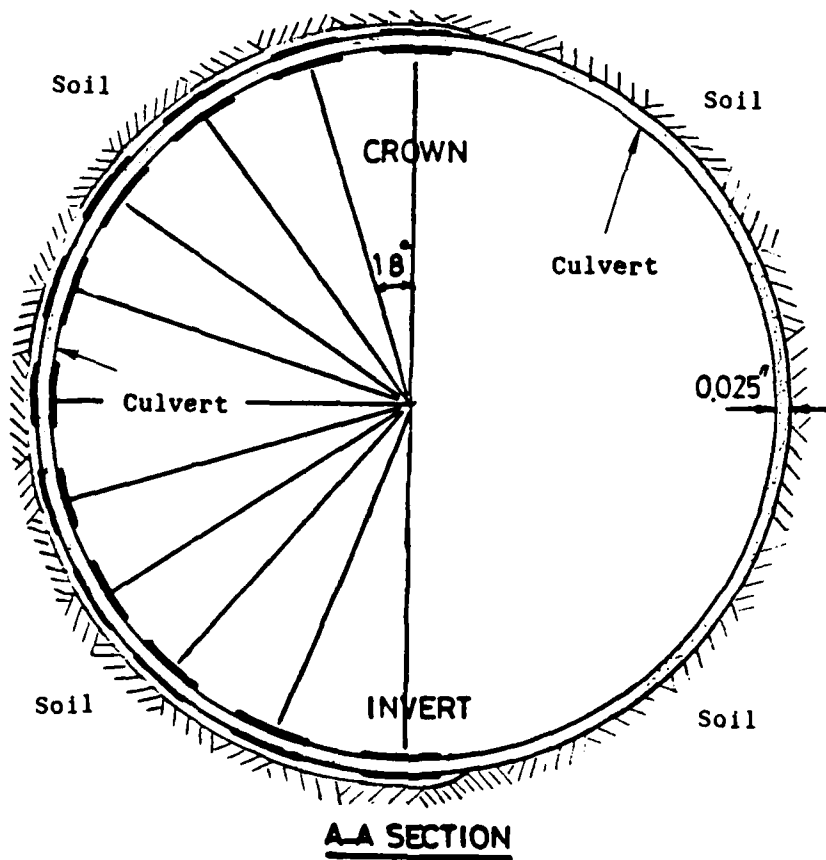
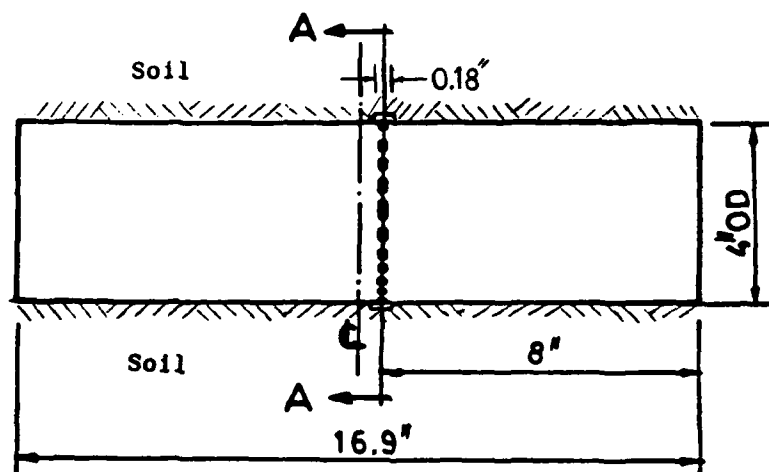


Figure 6.21 Gauged Tube in the Soil Trench

ment by the soil grains. However, in retrospect, because these gauges are now located at areas of the tube that are not loaded by soil, a peculiar stress and strain state exists at these gauge locations which is reflected by meaningless strain gauge data. When this problem with the data was discovered several months later, an attempt was made to repeat the same tests but with better soil conditions at the gauge locations. It was discovered that the aging in the gauge epoxy has caused deterioration which made the gauges to malfunction. Henceforth, the attempt to acquire better data was abandoned.

#### 6.3.2 Unsymmetrical Loading

The whole mesh in Figure 6.22 was used to analyze the behavior of buried culvert under unsymmetrical loading. The deflected shapes of the tube from the centrifuge test and the analytical solutions under 10, 20, 30 and 40 psi surface loading are shown in Figures 6.23, 6.24, 6.25 and 6.26, respectively. All the deflections are underestimated by both analytical solutions, while the analytical solution with the hyperbolic soil model shows better results than that with Lade's soil model. The largest inward deflection occurs at the shoulder which is on the same side of the surface loading. The largest outward deflections are located at the shoulder on the opposite side and at the haunch on the same side. These features are correctly predicated by both analytical solutions.

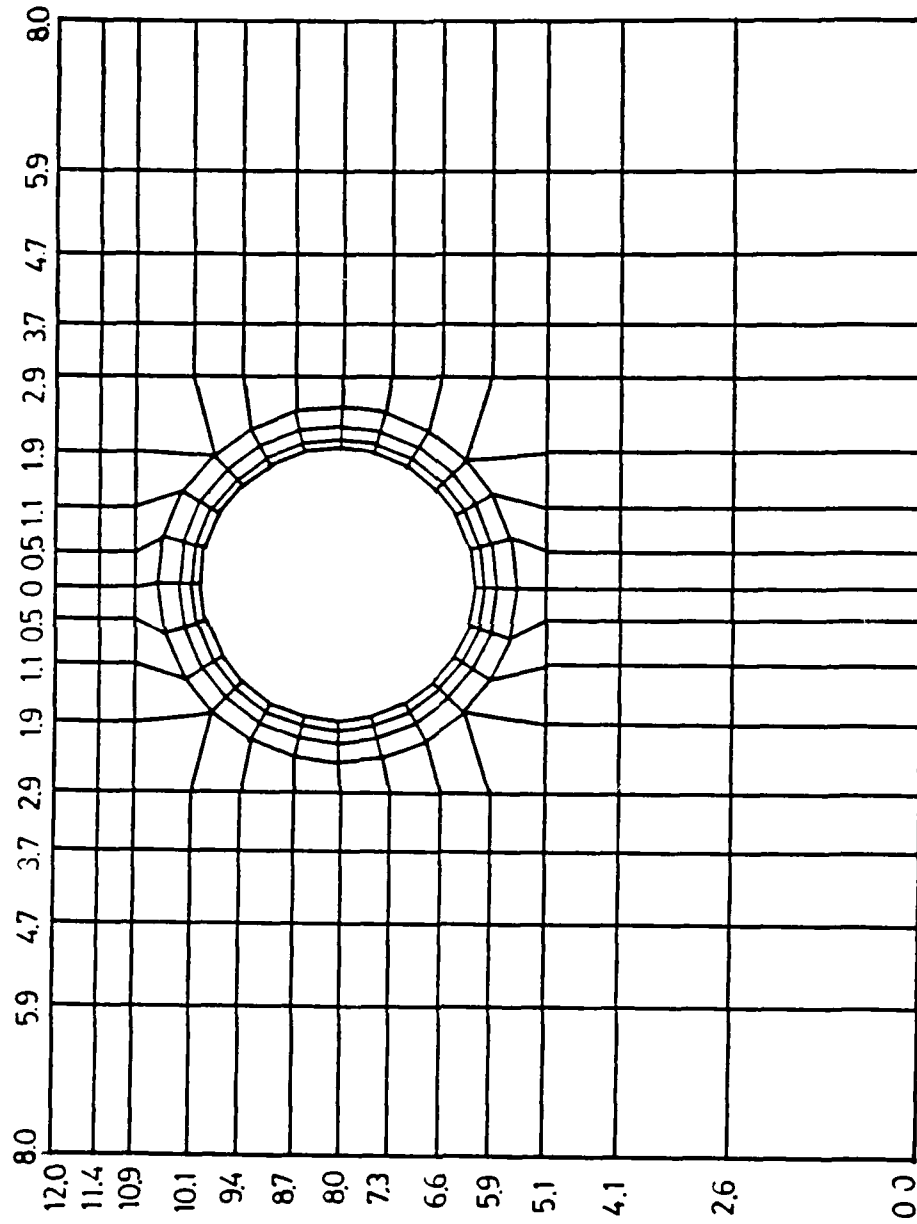


Figure 6.22 Mesh 4 for Unsymmetrical Load

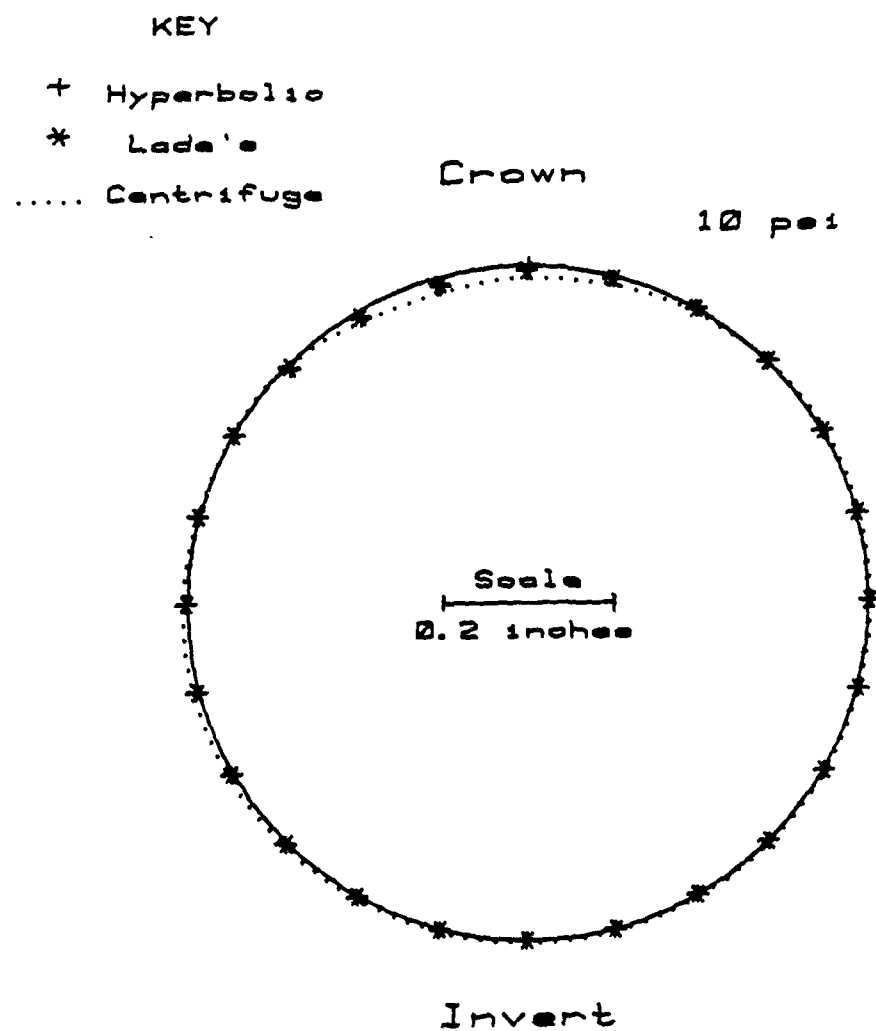


Figure 6.23 Comparison of Deflections.  
Unsymmetrical Load 10 psi

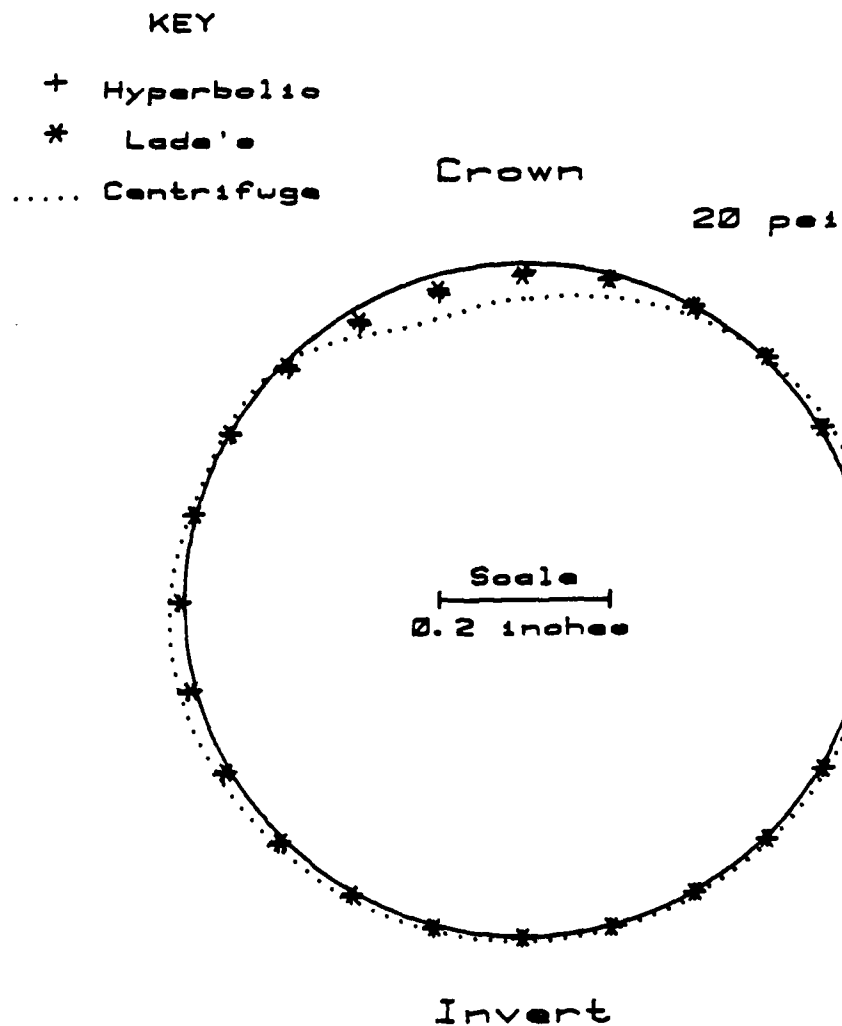


Figure 6.24 Comparison of Deflections.  
Unsymmetrical Load 20 psi



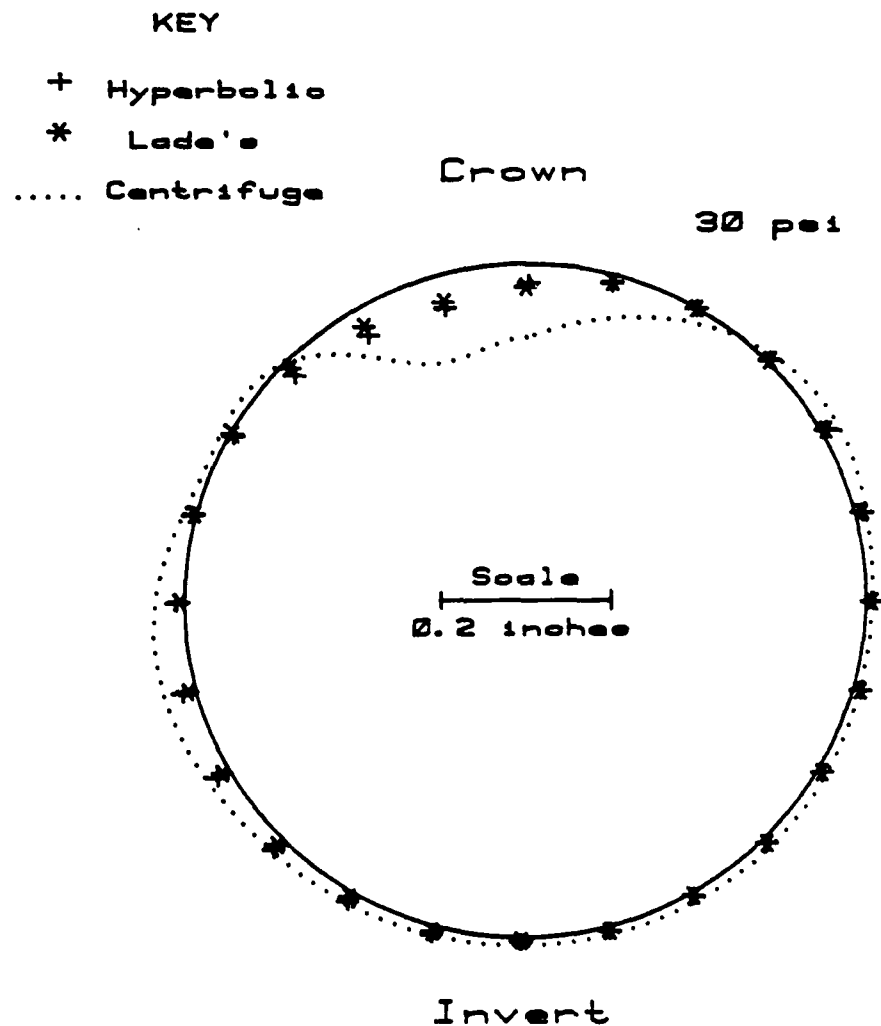


Figure 6.25 Comparison of Deflections.  
Unsymmetrical Load 30 psi

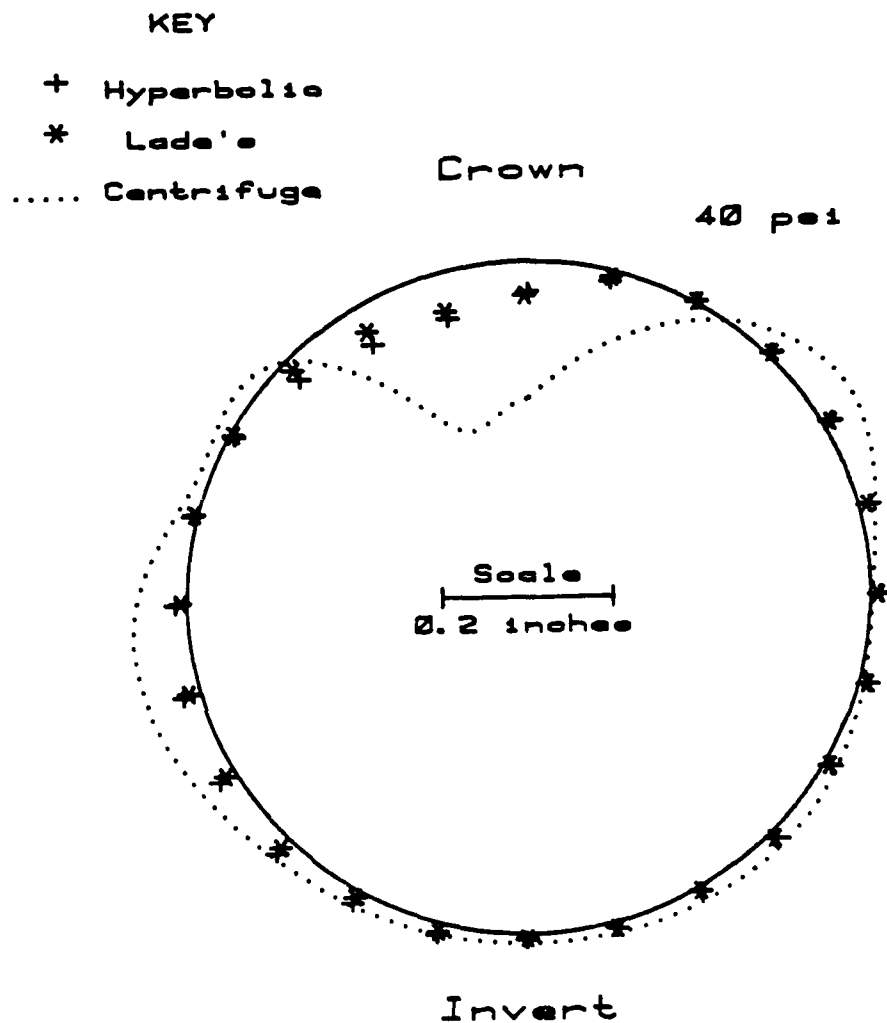


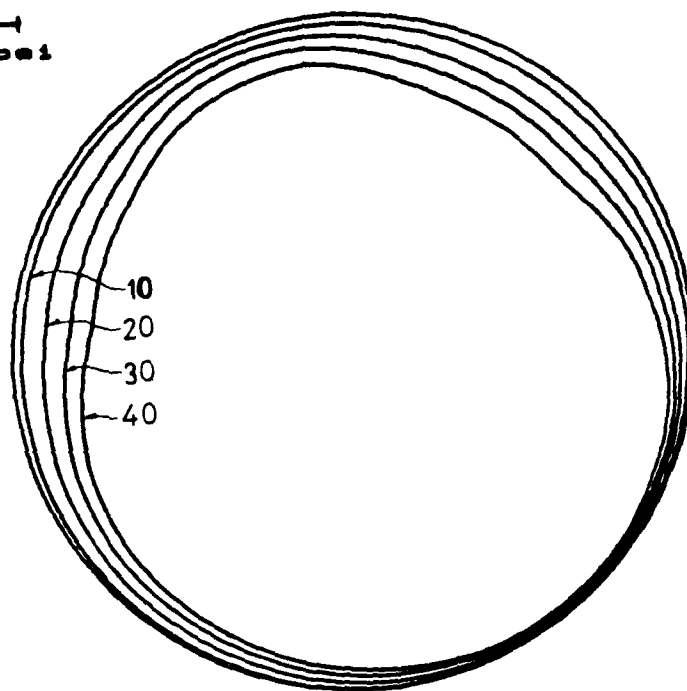
Figure 8.26 Comparison of Deflections.  
Unsymmetrical Load 40 psi

10, 20, 30, 40 psi

Hyperbolic

Crown

Scale  
2000 psi



Invert

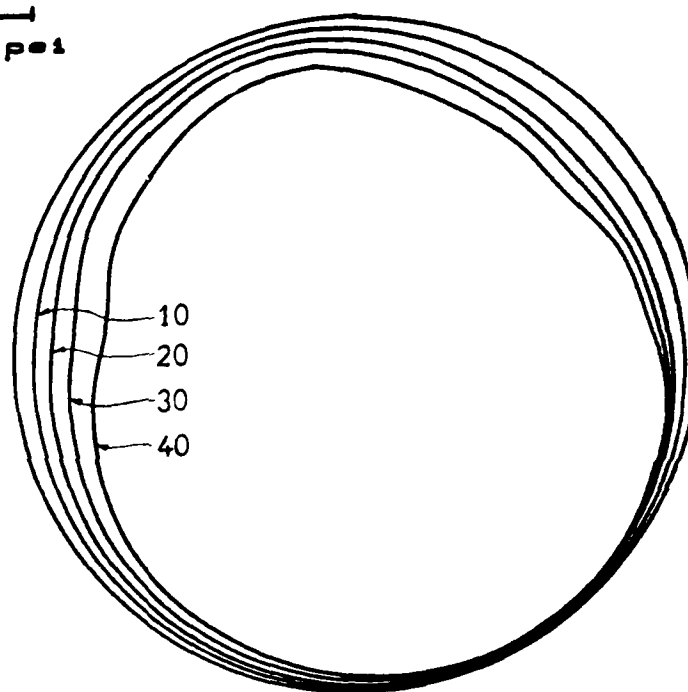
Figure 6.27 Hoop Stresses Under Unsymmetrical Load.  
Hyperbolic Soil Model

10, 20, 30, 40 psi

Lade's

Crown

Scale  
2000 psi



Invert

Figure 6.28 Hoop Stresses Under Unsymmetrical Load.  
Lade's Soil Model

The hoop stresses predicated by the analytical solutions with hyperbolic and Lade's soil models under surface loading are very similar as shown in Figures 6.27 and 6.28. The distribution of hoop stresses around the tube is rotated counterclockwise from the case of symmetrical surface loading. During this experiment, the gauged tube was accidentally overloaded by an excessive surface pressure and was destroyed by buckling failure. The buckled tube is shown in Figure 6.29.

#### 6.4 Discussion of the Results

Due to the uncertainty in the strain measurement as explained in Section 6.3.1, the deflections of the culvert were used to study the suitability of hyperbolic and Lade's constitutive relations in the analysis of the buried culvert system. Both analytical solutions predict the shape of the deflected culvert very well, however, the magnitude of deflection is always underestimated except at the invert in either the symmetrical or unsymmetrical loading case. This phenomenon can be explained in terms of the stress path experienced at each location along the circumference of the tube. The stress paths in the three elements shown in Figure 6.11 are used for the following demonstration.

The soil element C under the invert of the buried tube experienced a stress path similar to the one in the CTC test as shown in Figures 30 and 31. The stress-strain relation in the CTC test results can be simulated very well by both soil models, as shown in Figures 4.4 and 4.18. Therefore, the deflection at

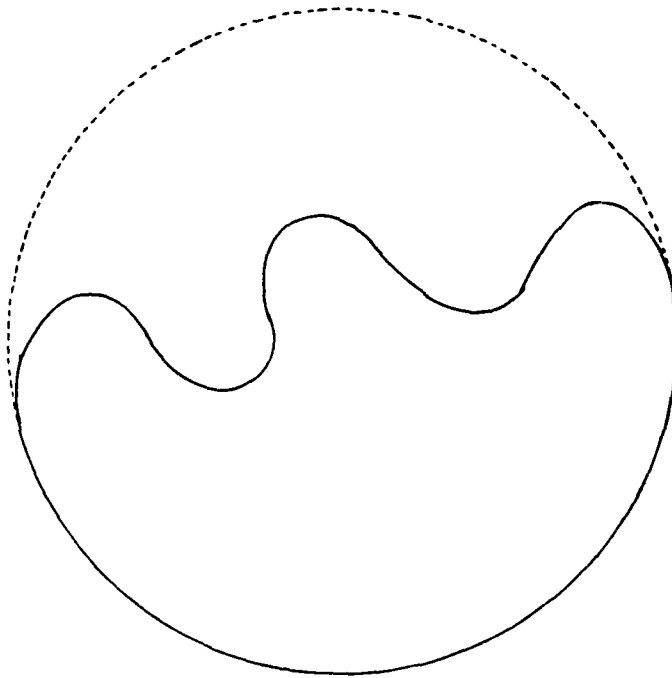


**Figure 6.29 Buckling Failure of the Flexible Culvert**

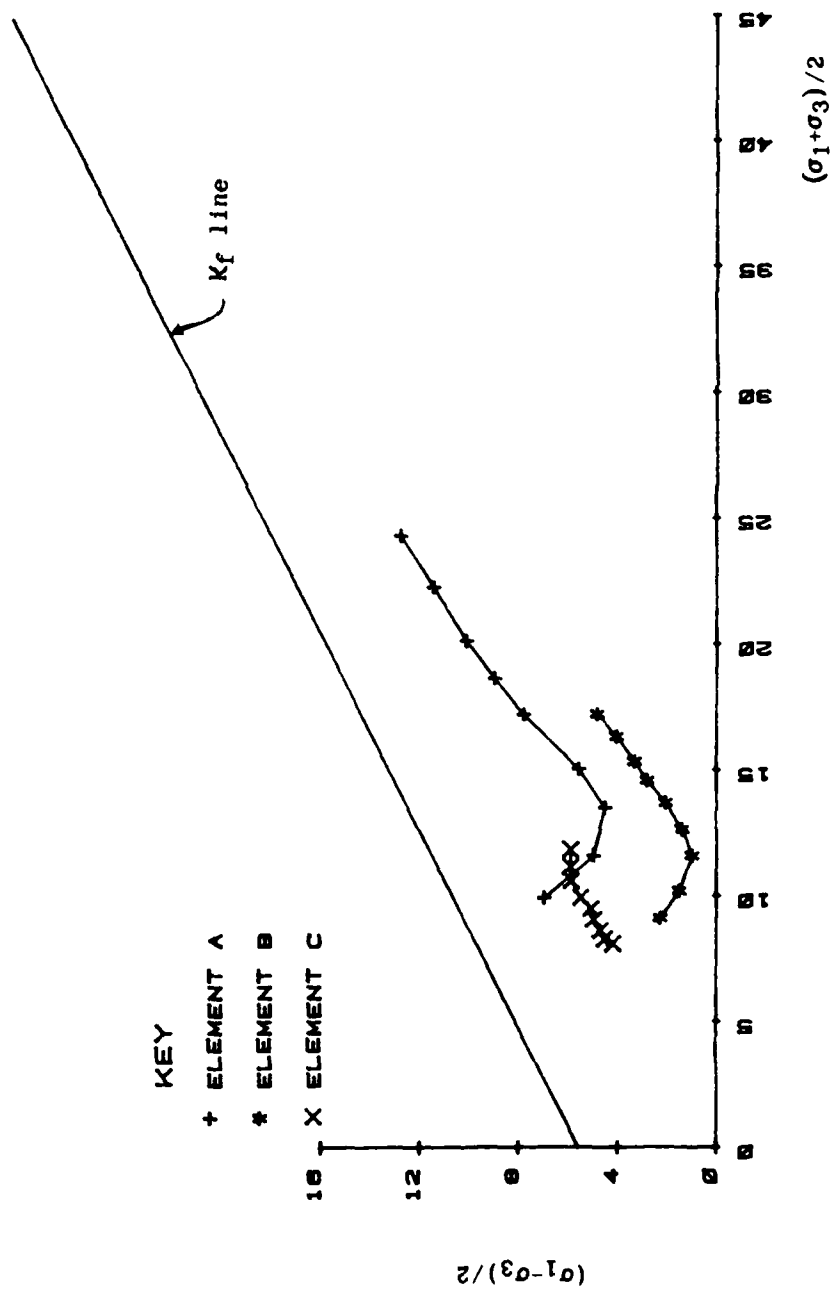


Figure 6.30 Stress Paths. Hyperbolic Soil Model

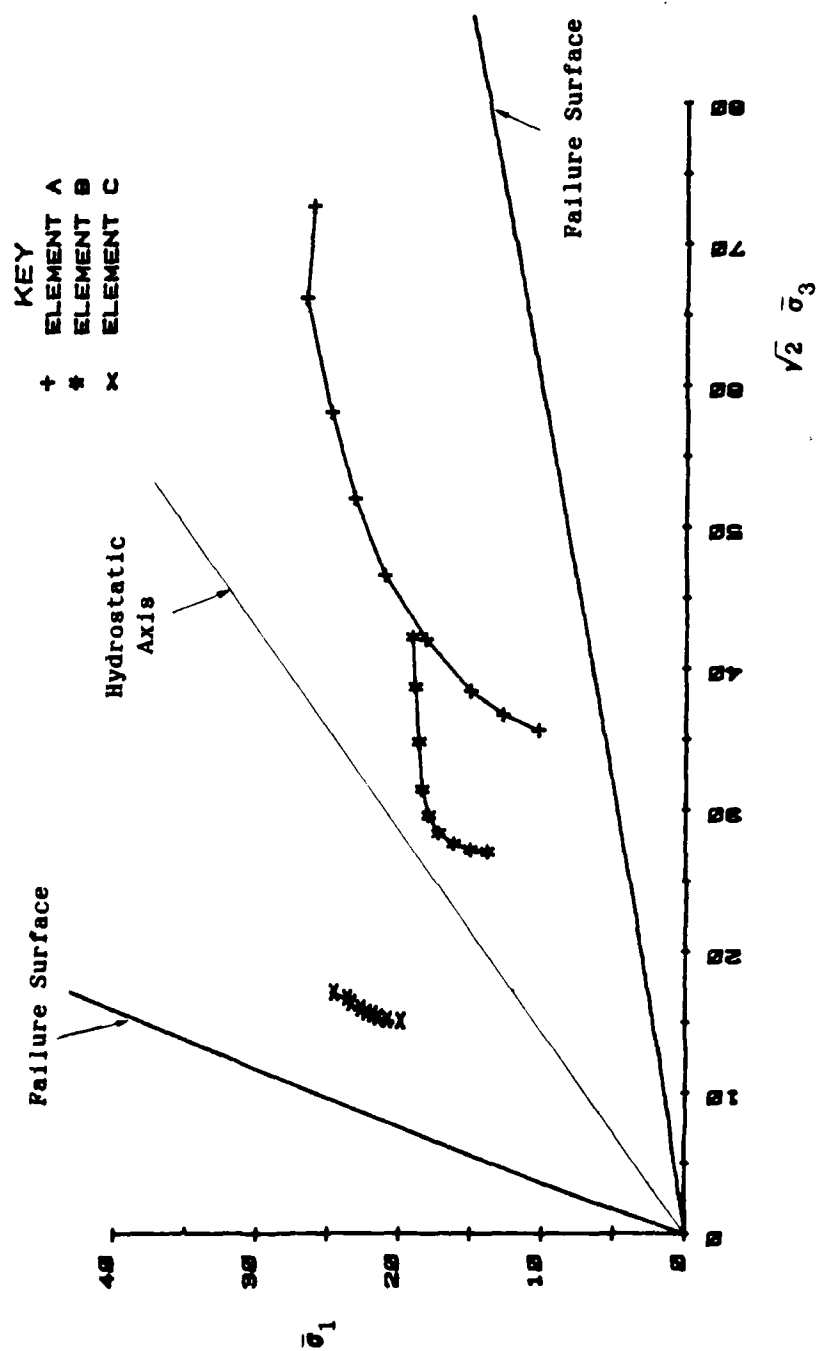


Figure 6.31 Stress Paths. Lade's Soil Model



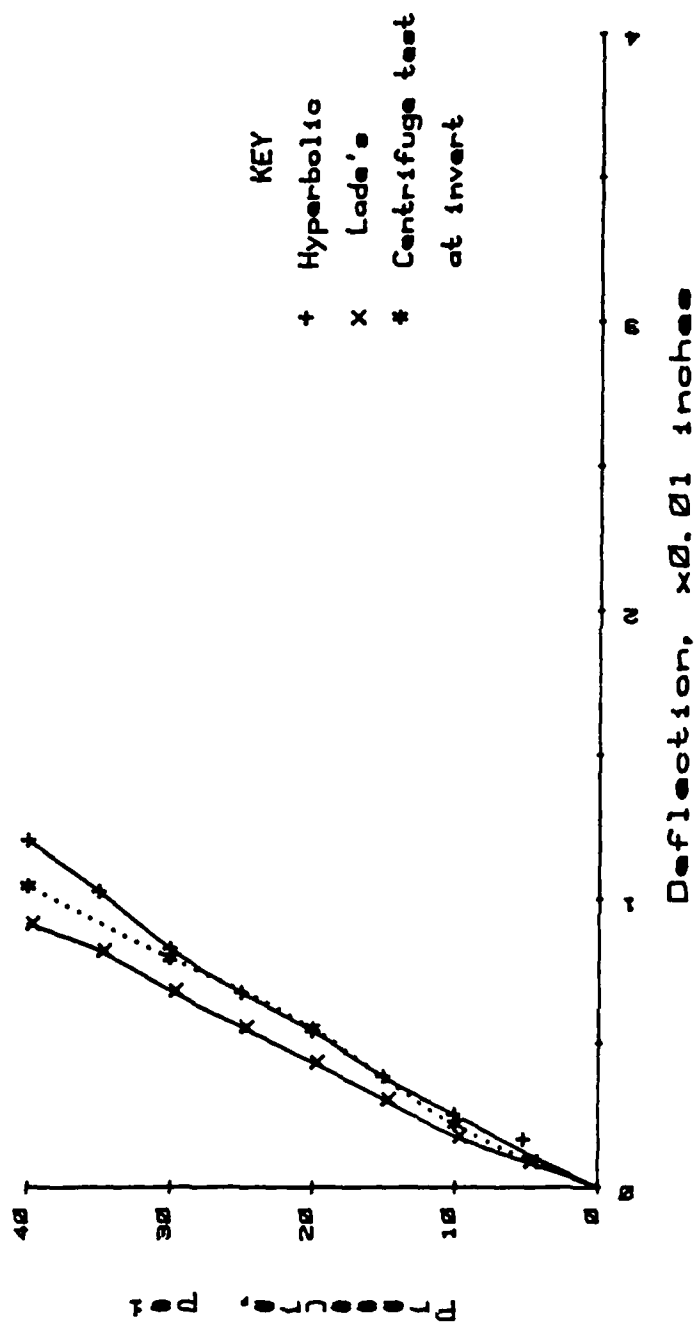


Figure 6. Comparison of Deflection at Invert

invert is also very accurately predicted by both soil models (Figure 6.32).

At the springline and the crown the deflections are underestimated in both soil models. The underestimated deflection at the crown is caused by the underestimated deflection at the springline. The stress paths experienced in the soil elements in the region between the springline to the vertical boundary offer the clue to explaining the discrepancy on the deflections.

First, the analytical solutions with a hyperbolic soil model are studied. The major principal stresses in the shaded elements in Figure 6.11 are acting in the vertical direction before the surface loading. During the surface loading these major principal stresses gradually rotate  $90^\circ$  to align with the horizontal direction. The corresponding stress path implies that the incremental stress ratio due to surface loading is larger than the total stress ratio before the loading. According to the loading and unloading criteria in Equation B.10, either unloading or reloading is activated. This is proved by the fact that the stress level is decreasing at the element A and B. Thus the unloading Young's modulus is chosen for those elements. This makes the stiffness of the soil-culvert system too high. These stress paths with total stress ratio ranging from 0.4 to 0.8 cannot be predicted well by the hyperbolic soil model (Lade, 1972). The strains predicted for primary loading are too large and those for unloading and reloading are too small. Since unloading and

reloading are induced in those shaded elements in Figure 6.11 the whole system is too stiff and therefore the deflection at the springline is underestimated. If the primary loading criterion, instead of unloading, is imposed on those elements the predicted deflection at the crown is improved but is still underestimated as shown in Figure 6.33. This discrepancy is a result of the anisotropy of the soil which is compacted vertically in layers. The strain response caused by rotating the major principal stress from the vertical to the horizontal shows progressively decreasing stiffness (Sture, Ko, Budiman and Ontuna, 1985). Therefore, the soil near the springline will deform a lot more than the prediction which is based on isotropic soil properties. The application of a hyperbolic soil model on the buried, flexible culvert with the backfill soil being compacted in layers will not be satisfactory because of the anisotropy of the soil and the stress paths experienced by the soil which cannot be predicted by this soil model.

Second, the analytical solutions obtained from Lade's soil model are studied herein. The stress paths induced in the shaded elements (Figure 6.11) during surface loading will only activate the cap-type yield surface. This can be explained by the stress paths of the elements A and B in Figure 31. Lade's constitutive relations are derived under the assumption of isotropic materials. However, the soil used in the centrifugal modeling is anisotropic. This can be proved by the fact that the predicted volumetric strains are much smaller than the measured values in the isotropic

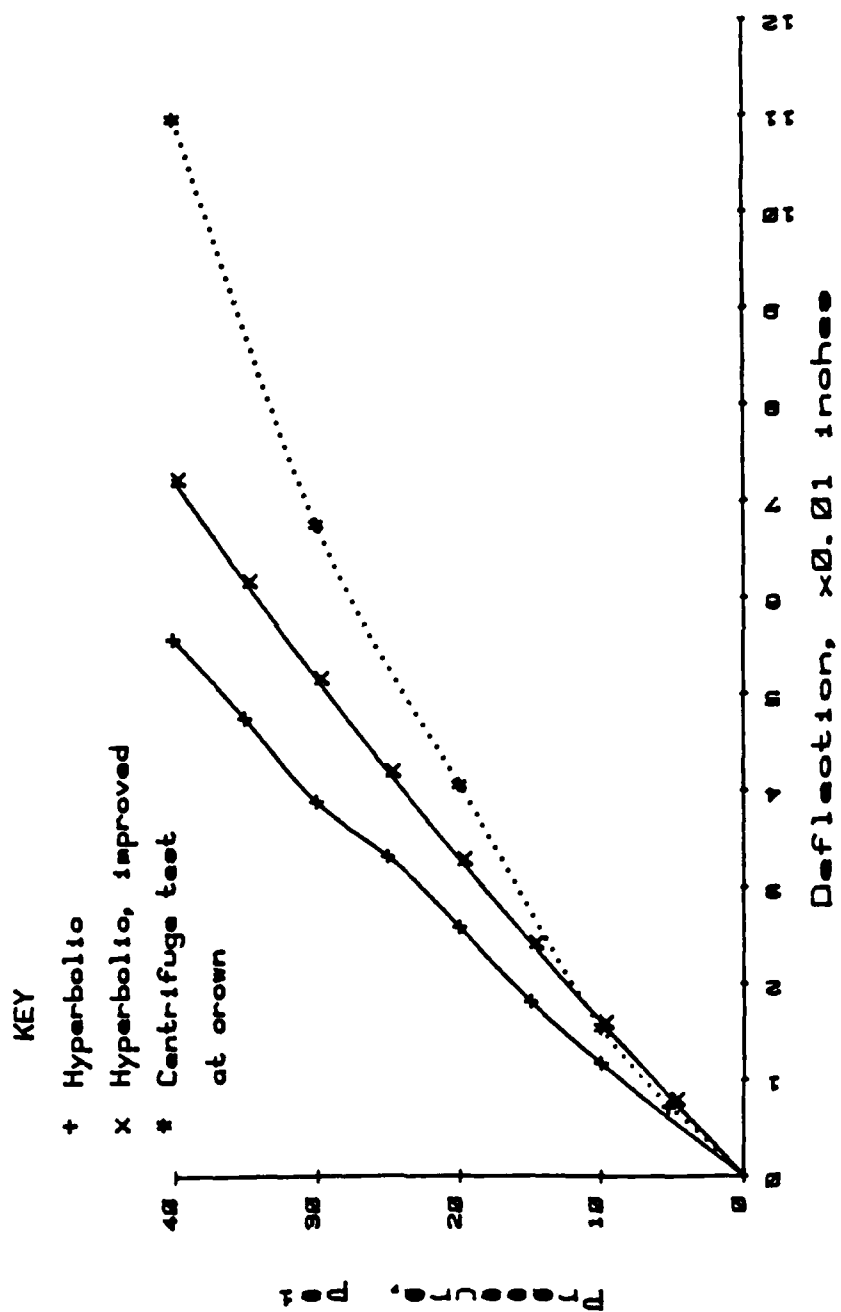


Figure 6.3 Comparison of Deflection at Crown.  
Improved Hyperbolic Soil Model

compression tests when the parameters calibrated from the CTC tests are used (Figure 4.20). Lade's soil model predicts the CTC test results very well, as shown in Figures 4.18 and 4.19. Since the collapsive plastic strain is so small that the stress-strain relations behave like unloading and reloading when only the cap yield surface is activated. While the surface loading gradually increases to 40 psi the shaded area with the abnormal high stiffness will move toward the vertical boundary at a slower speed than in the hyperbolic soil model. Therefore, the calculated deflections from Lade's soil model are always smaller than those from the hyperbolic model. In view of the above argument, Lade's isotropic soil model is not suitable for the analyses of flexible culverts buried in a layered compacted soil. The more flexible the culvert, the larger the passive zone around the springline. Then the anisotropy plays a more important role.

Those comments mentioned in connection with the symmetrical loading case also hold for the unsymmetrical loading. Figure 6.34 shows the shaded elements where only the cap yield surface is activated. The softer area is located at the haunch on the left hand side of the tube where the calculated outward deflection is the largest and this is proved by centrifugal test results as shown in Figure 6.26. In the analytical model the stiffer area resides at the shoulder on the right hand side, where the deflection is underestimated again. Therefore, an anisotropic soil model with the ability to incorporate the principal stress rotation is required to account for the directional soil stiffness.

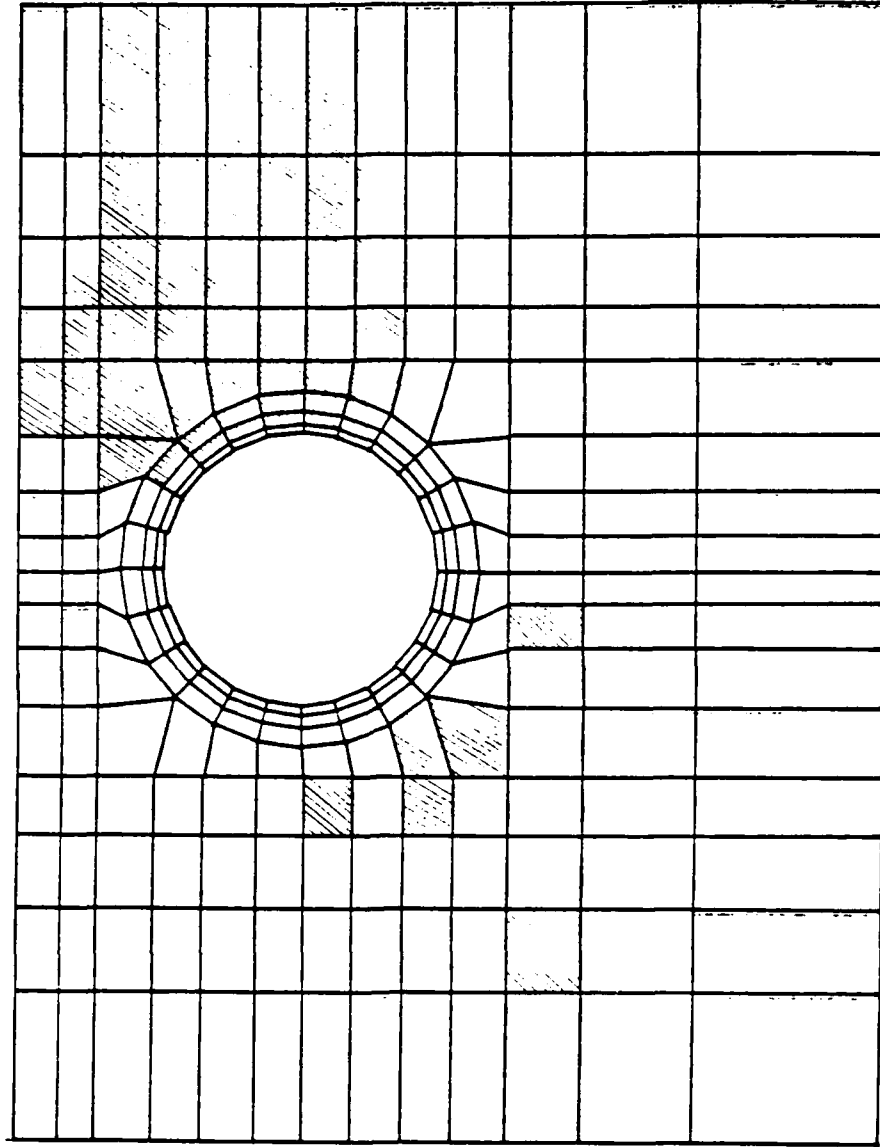


Figure 6.31 Stiffer Elements in Mesh 4

culvert. On the other hand, the culvert behaved linearly regardless of what type of nonlinear soil models if full-integration was applied.

4. The hyperbolic and Lade's constitutive relations through the mid-point incremental algorithm could simulate the hardening or stiffening system.

5. The hyperbolic relation was able to represent the stress-strain behavior but not the dilatant behavior in the test soil. Lade's relation could simulate both aspects fairly well.

6. Due to the fact that the behavior along some stress paths was poorly predicted by the hyperbolic soil model and to the inability to represent the anisotropic behavior, the analytical solution with the hyperbolic relation underestimated the deflections along the circumference of the tube except at the invert.

7. Lade's constitutive relation could not represent the anisotropic behavior with its soil parameters obtained from calibration with CTC test results. The predicted culvert deflections, therefore, are always smaller than the measured values except at the invert.

8. The accuracy of the predicted deflections from hyperbolic relation was slightly better than that from Lade's relation. But the simplicity of the hyperbolic model and the much shorter computer runtime gave this model an advantage over Lade's relation

in this study. Especially when no other models are available, the improved hyperbolic soil model can predict the deflections fairly well and with less expense in the computation.

9. To properly portray the rotation of the major principal stress in the soil adjacent to the culvert's springline, an anisotropic soil model with the ability to represent the rotation of principal stresses is required in order to have an accurate prediction on the behavior of a buried culvert.

### 7.3 Recommendations for Future Work

The experience gained in this study led to the following recommendations for future work in this line of research.

1. Amplifiers and signal condition modules with high quality are essential for producing repeatable and stable signals under a high gravitational field. With such improved instrumentation, the induced strains in the culvert under selfweight in the centrifuge could then be measured.

2. The application of a soft, protective material, such as Play-Doh, around the strain gauges along the interface between the soil and the structure is important to protect the gauges against the penetration of sand grains; and to model the constrained condition of the buried structure in order to have the correct information from the strain gauges.



3. Other constitutive models, such as the bounding surface model, with the ability to account for the rotation of principal stresses may be necessary to analyze a very flexible tube buried in a transversely isotropic soil.

4. The utilization of a 9-node isoparametric element to represent the soil and the culvert provides the ability to model the curved geometrical shape inherent in a culvert system.

5. The utilization of curved beam elements for the culvert may have better performance than the 4-node and 9-node elements. Data manipulation to obtain the bending moment can then be avoided.

6. Similar modeling, both centrifugal and numerical, of rigid tubes and the application of dynamic loading is possible and warrants pursuit.

## BIBLIOGRAPHY

- Abel, J.F., Mark, R., and Richards, R. (1973): "Stresses Around Flexible Elliptic Pipes", *Journal of Soil Mechanics and Foundations Division, ASCE*, No. SM7, July, pp. 509-526
- Allgood, J.R. and Ciani, J.B. (1968): "The Influence of Soil Modulus on the Behavior of Cylinders in Sand", *Highway Research Record No. 249, HRB, National Academy of Sciences, Washington, DC*
- Anand, S.C. (1974): "Stress Distributions around Shallow Buried Rigid Pipes", *Proc. ASCE*, Vol. 100, No. ST1, Jan., pp. 161-174.
- Anderson, J.E. (1974): "A Model for Evaluating the Response of Buried Circular Concrete Pipe", *Dissertation presented to Northwestern University at Evanston, IL*
- Aubry, D. and Des Croix, Ph. (1979): "Numerical Algorithm for an Elasto-Plastic Constitutive Equation with Two Yield Surfaces", *Proceedings of the Third International Conference on Numerical Methods in Geomechanics, Vol. 1, Aachen, 1979, pp. 283-288*
- Aubry, D. and Des Croix, Ph. (1981): "Implementation of Lade-Theory with Finite Elements", *Implementation of Computer Procedures and Stress-Strain Laws in Geotechnical Engineering, Proceedings of the Symposium held at Chicago, IL, 1981, pp. 619-630*
- Azevedo, R. (1983): "Centrifugal and Analytical Modeling of Excavations in Sand", *Ph.D. Thesis, University of Colorado*
- Brown, C.B. (1967): "Forces on Rigid Culverts Under High Fills", *Journal of the Structural Division, ASCE*, Vol. 93, No. ST5, pp. 195-215
- Brown, C.B., Green, D.R., and Pawsey, S. (1968): "Flexible Culverts Under High Fills", *Proceedings ASCE*, Vol. 94, No. ST4, April, pp. 905-917
- Budiman, J.S. (1985): "Analytical and Experimental Characterization of Stress Induced Anisotropy in a Weak and Soft Soil", *Ph.D thesis, University of Colorado, pp. 87-100.*

## CHAPTER VII

### SUMMARY, CONCLUSIONS AND RECOMMENDATIONS

#### 7.1 Summary

The complex problem of the reaction of a buried culvert to loads applied at the ground surface is studied by analytical modeling and centrifugal modeling. The increased body forces in the centrifuge can correctly reproduce the initial stress state of an earth structure whose response is mainly governed by the self-weight induced stresses. Under well controlled conditions, centrifuge modeling can offer accurate data to validate the constitutive relations used in the analytical method.

The principal objective of this study was to investigate the suitability of the hyperbolic and Lade's constitutive relations in the analysis of a buried culvert. A sandy silt was utilized and its stress-strain and strength characteristics were determined by conventional soil testing. The same soil was used in the centrifugal modeling test in which a gauged tube was loaded by symmetrical and unsymmetrical loads. The induced strains and displacements were measured at the midsection of the tube.

A finite element code was written to simulate the construction of a soil-culvert system outside the centrifuge and the

gravitational field in the centrifuge. Linear elasticity was used to model the tube while the hyperbolic and Lade's constitutive relations were implemented to model the soil.

Based on the soil test results, the constitutive relations were calibrated and used in the analytical model. The analytical solutions were compared with the results obtained in the centrifugal model. It was found that the behavior of the buried tube was predicted well enough qualitatively but not quantitatively.

## 7.2 Conclusions

Based on the above studies, several conclusions can be drawn.

1. Consistent reproducibility of centrifuge test results indicates that strain gauge and LVDT instrumentation performed satisfactorily. The preparation procedure for the soil-culvert centrifuge model was satisfactory except that the strain gauges should have been in full contact with the adjacent soil.

2. The finite element code was found to perform satisfactorily under the monotonic convergence tests with the refined meshes and increased number of load increments.

3. Under-integration was essential for the 4-node quadrilateral elements which were used to model the flexible, buried

- Burns, J.Q. (1964): "An Analysis of Circular Cylindrical Shells Embedded in Elastic Media", Ph.D. Thesis, University of Arizona, Tucson, AZ
- Chang, C.S., Espinoza, J.M. and Selig, E.T. (1980): "Computer Analysis of Newtown Creek Culvert", Journal of the Soil Mechanics and Foundation Division, ASCE, No. SM5, pp. 531-556
- Chang, C-Y. and Duncan, J.M. (1970): "Analysis of Soil Movements Around a Deep Excavation", Journal of Soil Mechanics and Foundations Division, ASCE, Vol. 96, No. SM5, Proceeding Paper 7512, September, pp. 1655-1681
- Chen, W-F. and Saleeb, A.F. (1983): "Constitutive Equations for Engineering Materials, Elasticity and Modeling", Vol. 1, John Wiley & Sons, Inc.
- Clough, G.W. (1972): "Application of the Finite Element Method to Earth-Structure Interaction", State-of-the-Art Report, Proceedings of the Symposium on Applications of the Finite Element Method in Geotechnical Engineering, U.S. Army Engineers Waterways Experiment Station, Vicksburg, MS, May
- Clough, G.W. and Duncan, J.M. (1971): "Finite Element Analyses of Retaining Wall Behavior", Journal of the Soil Mechanics and Foundations Division, ASCE, Vol. 97, No. SM12, December.
- Cook, R.D. (1981): "Concepts and Applications of Finite Element Analysis", John Wiley & Sons.
- Dar, S.M. and Bates, R.C. (1974): "Stress Analysis of Hollow Cylindrical Inclusions", Proc. ASCE, Vol. 100, No. GT2, Feb., pp. 123-138.
- Doderer, E.S. (1970): "Elastic Interaction Fields for Buried Pipe", Ph.D. Thesis, Princeton University.
- Duncan, J.M. (1977): "Behavior and Design of Long-Span Metal Culvert Structures", ASCE Convention in San Francisco.
- Duncan, J.M., P. Byrne, K.S. Wont and P. Mabry (1980): "Strength, Stress-Strain and Bulk Modulus Parameters For Finite Element Analyses of Stresses and Movements in Soil Masses", Report No. UCB/GT/80-01, August, 1980
- Duncan, J.M. and Change, C-Y (1970): "Nonlinear Analysis of Stress and Strain in Soils", Journal of the Soil Mechanics and Foundations Division, ASCE, Vol. 96, No. SM5, pp. 1629-1653

- Duncan, J.M. and Clough, G.W. (1971): "Finite Element Analyses of Port Allen Lock", Journal of the Soil Mechanics and Foundations Division, ASCE, No. SM8, pp. 1053-1068
- Duncan, J.M. and Lefebvre, G. (1973): "Earth Pressures on Structures Due to Fault Movement", Journal of the Soil Mechanics and Foundations Division, ASCE, Vol. 99, No. SM12, pp. 1153-1163
- Duns, C.S. and Butterfield, R. (1970): "Flexible Buried Cylinders, Part 1 - Static Response", Int. Journal Rock Mech. Min. Society, Vol. 8, pp. 577-600.
- Evgin, E. (1981): "Evaluation of an Elasto-Plastic Model", Ph.D. Thesis, University of Alberta, Edmonton
- Fugro National, Inc. (1979): "MX Siting Investigation Geotechnical Evaluation", for Space and Missile Systems Organization, Norton Air Force Base, CA 92409
- Hoeg, K. (1966): "Pressure Distribution on Underground Structural Cylinders", Air Force Weapons Laboratory, Technical Report No. AFWL TR-65-98, Kirtland Air Force Base, NM, April
- Hoeg, K. (1968): "Stresses Against Underground Structural Cylinders", Journal of the Soil Mechanics and Foundations Division, ASCE, Vol. 94, No. SM4, July, pp. 833-858
- Howard, A.K. (1972): "Laboratory Load Tests on Buried Flexible Pipes", Paper presented on June 6th, 1972 at the 92nd Annual Conference of the AWWA, Chicago, IL
- Hughs, T., Cohen, M. and Haroun, M. (1978): "Reduced and Selective Integration Techniques in the Finite Element Analysis of Plates", Nuclear Engineering and Design 46, pp. 203-222
- Janbu, N. (1963): "Soil Compressibility as Determined by Oedometer and Triaxial Tests", Proceedings of European Conference on Soil Mechanics and Foundation Engineering, Vol. 1, Wiesbaden, pp. 19-25
- Katona, M.G., Smith, J.M., Odello, R.J. and Allgood, J.R. (1976): "CANDE: Engineering Manual - A Modern Approach for the Structural Design and Analysis of Buried Culverts", Report to the Federal Highway Administration, Civil Engineering Laboratory, Port Hueneme, CA
- Kim, M.K. and Lade, P.V. (1984): "Modeling Rock Strength in Three Dimensions", International Journal Rock Mechanics, Mining Society & Geomechanics, Vol.21, No. 1, pp. 21-33

- Ko, H.Y. and Sture, S. (1981): "State of the Art: Data Reduction and Application for Analytical Modeling", Laboratory Shear Strength of Soil, ASTM STP 740, pp. 329-386.
- Kondner, R.L. (1963): "Hyperbolic Stress-Strain Response: Cohesive Soils", Journal of the Soil Mechanics and Foundation Division, ASCE, No. SM1, pp. 115-143
- Kondner, R.L. and Zelasko, J.S. (1963): "A Hyperbolic Stress-Strain Formulation for Sands", Proceedings of the Second Pan-American Conference on Soil Mechanics and Foundation Engineering, Vol. 1, Brazil, pp. 289-324
- Krizek, R.J. and McQuade, P.V. (1978): "Behavior of buried Concrete Pipe", Journal of Soil Mechanics and Foundations division, ASCE, No. SM7, July, pp. 815-836.
- Kulhawy, F.H. and Duncan, J.M. (1972): "Stresses and Movements in Oroville Dam", Journal of the Soil Mechanics and Foundations Division, ASCE, Vol. 98, No. SM7, Proceeding Paper 9016, July 1972, pp. 653-665
- Ladd, R.S. (1978): "Preparing Test Specimens Using Undercompaction", Geotechnical Testing Journal, Vol. 1, pp. 16-23.
- Lade, P.V. (1972): "Nonlinear Analysis of Stress and Strain in Soil", Proc. ASCE, SM5, pp. 495-498.
- Lade, P.V. (1972): "The Stress-Strain and Strength Characteristics of Cohesionless Soil", Ph.D. Thesis, University of California, Berkeley
- Lade, P.V. (1977): "Elasto-Plastic Stress-Strain Theory for Cohesionless Soil with Curved Yield Surfaces", International Journal of Solids and Structures, Vol. 13, pp. 1019-1035
- Lade, P.V. (1979): "Stress-Strain Theory for Normally Consolidated Clay", Third International Conference on Numerical Methods in Geomechanics, Aachen, April
- Lade, P.V. (1981): "Three-Parameter Failure Criterion for Concrete", Joint ASME/ASCE Mechanics Conference, Boulder, CO, June 22-24.
- Lade, P.V. and Nelson, R.B. (1981): "Incrementalization Procedure for Elasto-Plastic Constitutive Model with Multiple, Simultaneous Yield Surfaces: Implementation of Computer Procedures and Stress-Strain Laws in Geotechnical Engineering, pp. 503-518.

- Lade, P.V. and Nelson, R.B. (1984): "Incrementalization Procedure for Elasto-Plastic Constitutive Model with Multiple Intersecting Yield Surfaces", International Journal for Numerical and Analytical Methods in Geomechanics, Vol. 8, pp. 311-323
- Larsen, H. (1977): "Earth Pressure Around Buried Pipes", Ph.D. Thesis, University of Cambridge.
- Lefebvre, G., Duncan, J.M. and Wilson, E.L. (1973): "Three Dimensional Finite Element Analyses of Dams", Journal of the Soil Mechanics and Foundation Division, ASCE, Vol. 99, No. SM7, Proceeding Paper 9857, July 1973, pp. 495-507
- Leonards, G.A. and Stetkar, R.A. (1978): "Performance of Buried Flexible Conduits", Joint Highway Research Project, Civil Engineering, Purdue University, December.
- Luscher, U. (1966): "Buckling of Soil-Surrounded Tubes", Journal of the Soil Mechanics and Foundations Division, ASCE, Vol. 92, No. SM6, November, 1966.
- Malishev, M.V. (1965): "Calculations of Soil Pressure in Pipelines in Embankments", Proceedings of 6th International Conference on SM & FE, Montreal, Vol. 2, pp. 401-404
- Marston, A. (1922): "Second Progress Report to the Joint Concrete Culvert Pipe Committee", Engineering Experiment Station, Iowa State College, April 1922
- Marston, A. (1930): "The Theory of External Loads on Closed Conduits in the Light of the Latest Experiments", Proceeding HRB, Vol. 9, pp. 138-170
- McNeal, R.H. (1978): "A Simple Quadrilateral Shell Element", Computers & Structures, Vol. 8, pp. 175-183
- McVay, M.C. (1982): "Evaluation of Numerical Modeling of Buried Conduits", Ph.D. Thesis, University of Massachusetts
- Mitchell, J.K. (1976): "Fundamentals of Soil Behavior", John Wiley & Sons Inc., pp. 112-134
- Ozawa, Y. (1973): "Elasto-Plastic Finite Element Analysis of Soil Deformation", Ph.D. Thesis, University of California, Berkeley
- Ozawa, Y. and Duncan, J.M. (1976a): "Elasto-Plastic Finite Element Analysis of Sand Deformations", Proceedings of the Second International Conference on Numerical Methods in Geomechanics, Vol. 1, Virginia, pp. 243-263



- Ozawa, Y. and Duncan, J.M. (1976b): "Corrections to Elasto-Plastic Finite Element Analysis of Sand Deformations", Proceedings of the Second International Conference on Numerical Methods in Geomechanics, Vol. 3, Virginia, pp. 1477-1479
- Poulos H.G. and Davis E.H. (1973): "Elastic Solutions for Soil and Rock Mechanics". John Wiley & Sons, Inc.
- Prathap, G. and Bhashyam, G.R. (1982): "Reduced Integration and the Shear-Flexible Beam Element", International Journal for Numerical Methods in Engineering, Vol. 18, pp. 195-210
- Reimers, C. (1975): "Beskrivelse af Geoplane, et brugerprogram til beregning af plane elastiske problemer ved finite element metoden", Exam Project at Danmarks Ingeniørhøjskole, Bygningsafdelingen, Copenhagen
- Savin, G.N. (1961): "Stress Concentration Around Holes Which are Strengthened by Elastic Rings", International Series of Monographs in Aeronautics and Astronautics, Vol. 1, Div. 1, Chapter V, pp. 324-352
- Simpson, B. (1973): "Finite Elements Applied to Problems of Plane Deformation in Soils", Ph.D. Thesis, University of Cambridge
- Spangler, M.G. (1926): "A Preliminary Experiment on the Supporting Strength of Culvert Pipes in an Actual Embankment", Bull. No. 76, Engineering Experiment Station, Iowa State College
- Spangler, M.G. (1941): "The Structural Design of Flexible Pipe Culverts", Bull. No. 153, Engineering Experiment Station, Iowa State College
- Sture, S., Ko, H.Y., Budiman, J. and Ontuna, A. (1985): "Constitutive Behavior of Cohesive and Cohesionless Soils During Continuous and Discrete Jump Rotations of Principal Stress Directions in a Directional Shear Cell", Proceedings 11th ICSMFE, San Francisco, CA
- Timoshenko, S. (1963): "Strength of Materials", John Wiley & Sons Inc., p. 81
- Trott, J.J. and Gaunt, J. (1972): "Experimental Work on Large Steel Pipeline at Kirtling", Transport and Road Research Laboratory, Report LR472

- White, H.L. and Layer, J.P. (1960): "The Corrugated Metal Conduit as a Compression Ring", Proceedings HRB, Vol. 39, 1960, pp. 389-397
- Whitman, R.V. and Luscher, U. (1962): "Basic Experiment of Soil-Structure Interaction", Journal of the Soil Mechanics and Foundations Division, ASCE, Vol. 88, No. SM6, December, pp. 135-167
- Wong, K.S. (1978): "Elasto-Plastic Finite Element Analysis of Passive Earth Pressure Tests", Ph.D. Thesis, University of California, Berkeley
- Zienkiewicz, O.C. (1977): "The Finite Element Method", McGraw-Hill Book Co Ltd.

**APPENDIX A**

**Centrifugal Test Results**

-----  
 DISPLACEMENT (Inches) FOR SYMMETRICAL LOADING  
 -----

	10psi	20psi	30psi	40psi
1	-0.015405	-0.040807	-0.067958	-0.110469
2	-0.009392	-0.025809	-0.044920	-0.075536
3	-0.001486	-0.004655	-0.007343	-0.009983
4	0.001200	0.004101	0.006902	0.011003
5	0.003320	0.009792	0.016944	0.028467
6	0.004539	0.012525	0.022740	0.038597
7	0.004943	0.014760	0.023985	0.038501
8	0.003379	0.009649	0.015187	0.022909
9	0.002749	0.007473	0.012538	0.019692
10	0.003488	0.008919	0.013079	0.017826
11	0.002790	0.007123	0.010326	0.013577
12	0.002177	0.005522	0.007976	0.010486

	30psi	20psi	10psi	0psi
1	-0.111176	-0.107735	-0.101928	-0.090517
2	-0.075762	-0.072830	-0.068516	-0.061191
3	-0.009699	-0.008511	-0.008218	-0.009206
4	0.012004	0.011804	0.010200	0.007401
5	0.029116	0.028862	0.027247	0.023763
6	0.039224	0.038426	0.036622	0.033349
7	0.038843	0.037901	0.036143	0.032890
8	0.022873	0.021901	0.020967	0.019366
9	0.019430	0.018571	0.017754	0.016901
10	0.017479	0.016580	0.015781	0.014520
11	0.013186	0.012449	0.012056	0.011439
12	0.009980	0.009239	0.008844	0.008348

HOOP STRESSES (psi) FOR SYMMETRICAL LOADING

	10psi	20psi	30psi	40psi
1	364.81903	647.91372	993.07051	1515.66240
2	365.95433	697.93055	1037.33026	1602.34387
3	-63.37096	-214.11593	-355.25302	-1318.62629
4	-870.43527	-2048.65818	-3751.32037	-6429.33413
5	-39.20840	-23.13563	-67.79976	-157.13244
6	-870.15870	-2437.96839	-3981.85337	-6297.72763
7	455.01387	1120.75446	1803.02483	2669.83523
8	123.76207	392.74257	827.05744	1698.09270
9	-213.31000	-275.17937	-255.82715	-23.33279
10	-133.40577	-272.83018	-404.91715	-514.54865
11	-46.62773	140.72828	340.84332	672.40434

	30psi	20psi	10psi	0psi
1	1391.31046	1184.30650	879.99442	333.43253
2	1500.60783	1300.92191	988.50310	455.62252
3	-1651.50179	-1872.64272	-2123.33530	-1990.64841
4	-6512.40247	-6204.63673	-5628.25049	-4576.07184
5	-50.91346	35.39955	103.42415	197.10466
6	-6134.52087	-5745.23223	-5159.18277	-4423.38332
7	2655.80861	2576.06372	2355.32414	1894.97280
8	1739.61205	1708.14951	1678.12761	1650.81682
9	27.86890	-3.07624	34.43615	107.53026
10	-393.83613	-280.40152	-152.98573	-18.99501
11	733.90408	765.21964	806.28124	841.07928

\*\*\*\*\*  
 MOMENT (lb-in) FOR SYMMETRICAL LOADING  
 \*\*\*\*\*

	10psi	20psi	30psi	40psi
1	-0.33727	-0.77293	-1.18533	-1.83726
2	-0.09490	-0.28327	-0.58742	-1.20315
3	0.03203	0.07617	0.12824	0.31117
4	0.07750	0.18476	0.35090	0.61409
5	0.06296	0.21367	0.36349	0.52804
6	0.06548	0.18961	0.32166	0.51995
7	-0.03042	-0.08988	-0.14778	-0.21780
8	0.02014	0.01695	-0.00092	-0.05433
9	0.02019	0.02765	0.02699	0.00785
10	0.01156	0.03101	0.04633	0.06121
11	-0.00043	-0.03053	-0.05393	-0.09310

	30psi	20psi	10psi	0psi
1	-1.87020	-1.85668	-1.81124	-1.59073
2	-1.25143	-1.21031	-1.12603	-0.93780
3	0.33676	0.34468	0.34750	0.27293
4	0.60909	0.56989	0.50581	0.39282
5	0.56388	0.57699	0.59191	0.61555
6	0.50336	0.46617	0.40988	0.34192
7	-0.22242	-0.21707	-0.20201	-0.16943
8	-0.07423	-0.08672	-0.10418	-0.12434
9	0.00040	0.00210	-0.00384	-0.01272
10	0.05071	0.04114	0.03107	0.02126
11	-0.09818	-0.10045	-0.10333	-0.10745

## BURIED CULVERT TEST RESULTS UNDER 50g IN THE CENTRAI JOE

## STRAIN OUTPUT FOR SYMMETRICAL LOADING

	10psi	20psi	30psi	40psi
1	-0.00010701	-0.00044152	-0.00067710	-0.00105109
2	0.00023487	0.00052600	0.00080662	0.00124872
3	-0.00003554	-0.00013179	-0.00030002	-0.00064856
4	0.00008225	0.00022280	0.00043528	0.00085749
5	0.00001591	0.00003372	0.00005710	0.00010878
6	-0.00002418	-0.00006163	-0.00010342	-0.00028072
7	-0.00000824	-0.00001793	-0.00002495	-0.00003482
8	-0.00010526	-0.00024920	-0.00046419	-0.00080351
9	0.00003678	0.00013222	0.00022308	0.00032025
10	-0.00004190	-0.00013524	-0.00023192	-0.00034074
11	-0.00001575	-0.00004027	-0.00005828	-0.00008516
12	-0.00009771	-0.00027762	-0.00046092	-0.00073601
13	0.00001063	0.00001681	0.00002506	0.00003775
14	0.00004870	0.00012933	0.00021004	0.00031038
15	0.00002067	0.00003621	0.00005335	0.00007671
16	-0.00000454	0.00001500	0.00005450	0.00014471
17	-0.00000127	-0.00000064	0.00000021	0.00000339
18	-0.00002654	-0.00003525	-0.00003357	-0.00000643
19	-0.00000146	0.00000162	0.00000260	0.00000476
20	-0.00001593	-0.00003720	-0.00005540	-0.00007186
21	-0.00000331	-0.00000993	-0.00001153	-0.00001443
22	-0.00000277	0.00002828	0.00005598	0.00010211

	30psi	20psi	10psi	0psi
1	-0.00107981	-0.00103484	-0.00107625	-0.00097386
2	0.00126123	0.00123927	0.00119099	0.00101734
3	-0.00068541	-0.00067269	-0.00064031	-0.00055725
4	0.00088108	0.00084232	0.00076920	0.00061666
5	0.00010310	0.00009364	0.00007906	0.00004104
6	-0.00031844	-0.00033782	-0.00035592	-0.00030060
7	-0.00004337	-0.00004783	-0.00005036	-0.00005248
8	-0.00080580	-0.00076120	-0.00068351	-0.00054420
9	0.00034960	0.00036343	0.00037721	0.00039311
10	-0.00035624	-0.00035882	-0.00036372	-0.00037241
11	-0.00008490	-0.00008280	-0.00007982	-0.00007438
12	-0.00071499	-0.00066633	-0.00059289	-0.00050239
13	0.00003394	0.00003209	0.00002712	0.00001750
14	0.00031235	0.00030381	0.00027999	0.00022959
15	0.00006696	0.00005709	0.00004420	0.00002980
16	0.00015987	0.00016564	0.00017461	0.00018545
17	0.00000207	0.00000111	-0.00000016	-0.00000095
18	0.00000157	-0.00000151	0.00000465	0.00001437
19	0.00000606	0.00000747	0.00000947	0.00001207
20	-0.00005741	-0.00004403	-0.00002942	-0.00001455
21	-0.00001360	-0.00001298	-0.00001210	-0.00001241
22	0.00010930	0.00011276	0.00011724	0.00012208

## BURIED CULVERT TEST RESULTS UNDER 50g IN THE CENTRIFUGE

\*\*\*\*\*  
DISPLACEMENT (inches) FOR UNSYMMETRICAL LOADING  
\*\*\*\*\*

	10psi	20psi	30psi	40psi
1	-0.014183	-0.042129	-0.087248	-0.164064
2	-0.016942	-0.047745	-0.096336	-0.181091
3	-0.008046	-0.023281	-0.047692	-0.092017
4	0.001200	0.004101	0.006902	0.011003
5	0.001644	0.003941	0.007619	0.012785
6	0.003488	0.012769	0.012891	0.013002
7	0.005520	0.016446	0.033496	0.058432
8	0.006116	0.016027	0.032441	0.057321
9	0.002257	0.006331	0.011331	0.016635
10	0.003686	0.009394	0.017543	0.028316
11	0.002358	0.006258	0.010961	0.015265
12	0.001385	0.004120	0.007322	0.009810

	30psi	20psi	10psi	0psi
1	-0.178505	-0.176051	-0.168949	-0.154886
2	-0.194933	-0.192794	-0.185769	-0.170977
3	-0.099315	-0.097666	-0.093257	-0.086074
4	0.012004	0.011804	0.010200	0.007401
5	0.013608	0.013568	0.013260	0.012008
6	0.013015	0.013000	0.013012	0.013041
7	0.061776	0.060947	0.059089	0.056380
8	0.060706	0.060116	0.058543	0.056761
9	0.017087	0.017026	0.016458	0.015478
10	0.029479	0.029322	0.028506	0.027915
11	0.015534	0.015618	0.015326	0.014974
12	0.009885	0.010193	0.009944	0.009774



## APPENDIX B

The loading and unloading criteria used in the hyperbolic constitutive relation are defined as follows

$$\text{Primary loading, if } \left[ \frac{\sigma_1 - \sigma_3}{(\sigma_1 - \sigma_3)_f} \right]_{i+1} > \left[ \frac{\sigma_1 - \sigma_3}{(\sigma_1 - \sigma_3)_f} \right]_i \quad (\text{B.1})$$

$$\text{Reloading and unloading, if } \left[ \frac{\sigma_1 - \sigma_3}{(\sigma_1 - \sigma_3)_f} \right]_{i+1} \leq \left[ \frac{\sigma_1 - \sigma_3}{(\sigma_1 - \sigma_3)_f} \right]_i \quad (\text{B.2})$$

where  $i$  = current increment  
 $i + 1$  = subsequent increment  
 $(\sigma_1 - \sigma_3)$  = failure stress difference

However, the physical meaning of these criteria is difficult to interpret. Another way to represent these criteria is derived herein, so that the loading or unloading can be explained through the stress path. By using Equation 4.17

$$\frac{\sigma_1 - \sigma_3}{(\sigma_1 - \sigma_3)_f} = \frac{\sigma_1 - \sigma_3}{\frac{2C \cos \phi + 2 \sigma_3 \sin \phi}{1 - \sin \phi}} = \frac{(\sigma_1 - \sigma_3)(1 - \sin \phi)}{2C \cos \phi + 2 \sigma_3 \sin \phi} \quad (\text{B.3})$$

For cohesionless soil,  $C=0$ , Equation B.3 becomes

$$\left[ \frac{\sigma_1 - \sigma_3}{(\sigma_1 - \sigma_3)_f} \right]_i = a \frac{\sigma_1 - \sigma_3}{\sigma_3} \quad (\text{B.4})$$

$$\text{where } a = \frac{1 - \sin \phi}{2 \sin \phi} \quad (\text{B.5})$$

After the next increment, the stress level becomes

$$\left[ \frac{\sigma_1 - \sigma_3}{(\sigma_1 - \sigma_3)_f} \right]_{i+1} = a \frac{(\sigma_1 + \Delta\sigma_1) - (\sigma_3 + \Delta\sigma_3)}{\sigma_3 + \Delta\sigma_3} \quad (\text{B.6})$$

where  $\Delta\sigma_1$  and  $\Delta\sigma_3$  are the incremental stresses due to the  $i+1^{\text{th}}$  load increment.

For the case of neutral loading Equation B.4 is equivalent to Equation B.6 and gives

$$a \frac{\sigma_1 - \sigma_3}{\sigma_3} = a \frac{(\sigma_1 + \Delta\sigma_1) - (\sigma_3 + \Delta\sigma_3)}{\sigma_3 + \Delta\sigma_3} \quad (\text{B.7})$$

This equation can be simplified to the following form

$$\frac{\Delta\sigma_3}{\Delta\sigma_1} = \frac{\sigma_3}{\sigma_1} \quad (\text{B.8})$$

with the constant value of friction angle.

The loading and unloading criteria expressed by Equations B.1 and B.2 can then be represented as follows

$$\text{primary loading, if } \frac{\Delta\sigma_3}{\Delta\sigma_1} < \frac{\sigma_3}{\sigma_1} \quad (\text{B.9})$$

$$\begin{array}{l} \text{reloading, if } \frac{\Delta\sigma_3}{\Delta\sigma_1} > \frac{\sigma_3}{\sigma_1} \\ \text{unloading, if } \frac{\Delta\sigma_3}{\Delta\sigma_1} > \frac{\sigma_3}{\sigma_1} \end{array} \quad (\text{B.10})$$

That means the loading or unloading at the current load increment is determined by the relative value of the incremental stress ratio and the previous total stress ratio.

DATE  
FILMED  
8